X_b Search and Measurement of the $\Upsilon(1S)$, $\Upsilon(2S)$ and $\Upsilon(3S)$ Polarization

Zur Erlangung des akademischen Grades eines
DOKTORS DER NATURWISSENSCHAFTEN
von der Fakultät für Physik des
Karlsruher Institut für Technologie (KIT)

genehmigte

DISSERTATION

von

Dipl.-Phys. Claudia Marino
aus Karlsruhe

Tag der mündlichen Prüfung: 30.10.2009

Referent: Prof. Dr. M. Feindt, Institut für Experimentelle Kernphysik

Korreferent: Prof. Dr. G. Quast, Institut für Experimentelle Kernphysik

Contents

Chapter 1

Quarkonium Spectroscopy

Spectroscopy represents one main area of study in particle physics. It comprises all experiments which are designed to study the spectra of bound states. With such kind of experiments one can probe the properties of bound states and the interaction forces between their constituent parts.

Typical excitation energies of atoms are of the order of magnitude of $10\,\mathrm{eV/c^2}$ which corresponds to a size of $1\,\text{Å} = 10^{-10}\,\mathrm{m}$. The excitation energy of the atomic nucleus is around $40\,\mathrm{MeV/c^2} = 4{\cdot}10^7\,\mathrm{eV/c^2}$ which translates to a size of $10\,\mathrm{fm} = 10^{-14}\,\mathrm{m}$, and their constituents like protons or neutrons have masses of the order of $1\ \mathrm{GeV/c^2} = 10^9\ \mathrm{eV/c^2}$ and a size of $1\ \mathrm{fm} = 10^{-15}\ \mathrm{m}$. Attention should be paid to the very different energy scales for each of the previously given examples. The smaller the length dimension is, the larger is the necessary energy to study such tiny objects. Such energies can be achieved using highly accelerated stable particles which are brought to collision, either with each other or with some fixed target. According to Einstein's equation, $E = mc^2$, their available center of mass energy can be used to create other massive particles. If the colliding particles provide enough energy, it is even possible to produce highly exited states. Nowadays, huge circular particle accelerators with circumferences of several kilometers are able to produce such high energies that it is possible to resolve structures smaller than a billionth of the size of a nucleus.

Commonly known bound states are the hydrogen atom and the positronium. Hydrogen consists of a proton and an electron which form the first atomic element in the periodic table of chemical elements. Positronium is a bound state of an electron and a positron. The positron is the anti-particle of the electron. Thus the positronium is a bound state of a particle and its anti-particle. In high energy physics it is also possible to find such analogue particle and anti-particle bound states made up of a quark and its antiquark. Pure bound states exist only for quark-flavors with high mass, as it is the case for the strange, charm and bottom quark[a]. Such kind of compositions of charm and bottom quarks are called 'quarkonia'. The quarkonium

[a]The ϕ resonance is nearly a pure $s\bar{s}$ state. However, it containts some minor contributions from $u\bar{u}$ and $d\bar{d}$

with bottom quark content is called 'bottomonium'. The first three spin one states of the bottomonium, which are called Υ-states, are one main research field in this analysis.

This introductory chapter presents shortly our current understanding of matter. Some basic terminology that is important in particle physics and in particular in the context of this analysis, will be introduced. The theory that describes the fundamental particles and the forces that act between them is shortly explained. Especially the possibility how the fundamental blocks of matter can be combined to one system is exemplary discussed for the quarkonium states as well as for other molecule or tetraquark compositions, and their theoretical predicted masses will be presented. Finally, theoretical predictions of the polarization of the Υ-states at the Tevatron are presented.

1.1 The History of Matter

For the Greek natural philosopher Democritus the world was built up of tiny invisible blocks, each of which was eternal and immutable. He called these units 'a-toms' which means 'un-cuttable'. He outlined that the constituent parts that everything was composed of could not be divided into smaller pieces. Due to his opinion, there had to be an unlimited number and variety of atoms to combine to every matter that exists. Somehow this is still in agreement with our current understanding of matter. Mendeleev came up with the periodic table of chemical elements. Truly, if one divides these atoms into smaller parts, their chemical properties which made them unique, get lost. They become nucleus and electrons. Nuclei itself consist of neutrons and protons and even those can be subdivided into quarks. The raising question is 'Are there fundamental indivisible particles?'. The aim of modern physics is to trace back experimental observations to only a few elementary particles and interaction forces with which our entire world can be described.

This introductory outline follows the overview in reference [1]. New knowledge about elementary particles is mostly gained from the benefit of accelerator techniques. However, only charged particles can be easily accelerated. The positive and negative charge was discovered in the 18th century. In 1897, Thompson discovered the first elementary particle, the electron. This particle was defined to have negative charge and according to Stoney it was called electron, the Greek name for amber [b]. Becquerel discovered radioactivity. As a result, it was found that the radiation comes along with the transformation of an element. In 1911, Lord Rutherford experimentally proved that most of the atomic mass and its positive charge are located at a very small part at the center of the atom. He found that the hydrogen nucleus consists of an indivisible particle which he called proton.

In 1913, Bohr postulated discrete energy levels of atomic systems. The transition

[b] Amber is a gemstone that is formed from the hardened sap of trees. It attracts small objects when rubbed with fur.

between these levels occur by the emission or absorption of photons. In the first scattering experiments the light emission of the atoms of an electro-luminescence screen is used to detect nuclear reactions. Whereas such measurements are basically visual-driven, better detection apparatus were developed based on gas discharge. If a particle has enough energy to ionize a gas, the resulting emitted electrons can cause a current flow which translates to a measurable signal. In 1907, Thomson developed the first mass spectrometer based on an electromagnetic field. This apparatus is able to separate particles of the same energy but different mass, or of the same mass but different energy, which provided a very important tool for accelerator physics. In 1911, Wilson invented the cloud chamber where particle trajectories can be seen. In the presence of a magnetic field the momentum of the particle can be deduced. Such kind of experiments had an important role in the development of elementary particle physics.

So far, only radioactive sources like radium, thorium and polonium provided the basis to produce accelerated particles like alpha rays. However, the alpha rays only provide particles with energies of several MeV, thus it was necessary to develop sophisticated acceleration methods for charged particles to achieve higher energies. In 1931, van de Graaff developed the so-called Van de Graaff generator, a device which produces high voltages. Another type of accelerator is the voltage multiplier cascade developed by Cockroft and Walton. It is made up of a voltage multiplier network of capacitors and diodes to generate high voltages. Finally, in 1929, the first circular accelerator, a so-called cyclotron, was built by Lawrence.

In 1932, Chadwick discovered a new type of radiation due to a neutral particle of about the same mass as the proton, thus it was called neutron. Shortly afterwards, Heisenberg postulated that the atomic nucleus consists of protons and neutrons. As a consequence, the concept of isotope [c], which was introduced by Soddy, could be explained. Also in 1932, Anderson and Neddermeyer discovered a positively charged light particle, which had about the same mass as the electron. Cosmic rays were passed through a Wilson cloud chamber and a lead plate surrounded by a magnet. The particles were distinguished by bending differently charged particles in different directions within the magnetic field. This particle was called positron whose existence was firstly postulated in 1928 by Dirac. He claimed that for each charged particle there must also exist the antimatter counterpart with opposite charge.

Yukawa predicted, based on the successful concept of quantizing the electromagnetic field, that a massive quantum, the mediator of the strong force, must exist. This conclusion is based on the fact, that the electromagnetic mediator carries no mass and has an infinite interaction range, whereas the strong force only occurs at short distances which suggests a massive field mediator. He called this hypothetically existing particle 'meson' and predicted its mass to be about 200 MeV. In 1936, Anderson and Neddermeyer detected a particle which properties were quite similar to that of the predicted meson. However, it did not fit in all detail to the expected particle. It does not interact via the strong force. At first, this particle was called

[c] Isotopes of an element have nuclei with the same number of protons but different numbers of neutrons.

'mesotron', later then 'μ-meson' and today it is called 'muon'. Yukawa's mesons were not discovered before 1947. Occhialini, Powell and Lattes who discovered these particles called them pions (π-mesons).

In 1925, Goudsmit and Uhlenbeck postulated an intrinsic angular momentum of the electron which is commonly called spin. This implies that electrons should also have a magnetic moment [d]. Therefore it was of interest to measure this property of the electron and proton. The proton magnetic moment was measured by Stern and Frisch in 1933 and Kusch measured the magnetic moment of the electron in 1947. The predictions of the modern quark model is in full agreement to the measured values.

Cosmic rays provide high energy particles to study. In 1947, Rochester and Butler published two cloud chamber photographs of cosmic ray-induced events. They observed 'strange' particles which introduces the quantum number 'strangeness'. Later these particles were called K-meson and Lambda-hyperon. In 1952, Pais gave a theoretical explanation why these particles could only be created in pairs which corresponds to the conservation of the strangeness quantum number in the strong interaction. In 1953, Bonetti and colleagues observed a group of three particles: a neutral, a positively charged, and a negatively charged state. Due to their high masses compared to the nucleons, they called them Σ-hyperons. Additionally to the hyperons many mesons and small resonances were discovered. A whole 'zoo of particles' was established and tabulated similar to Mendelejews periodic table. This also led to the prediction of several particles which were still missing parts in the scheme suggested from Gell-Mann. Those particles were discovered later and the table could be completed.

The observation of all of these particles was only possible due to the further development of accelerator and detection techniques. In 1928, Geiger and Müller developed the Geiger-Müller tube. Inside the cylindrical tube there is a low-pressure gas. Due to ionizing radiation that passes through the tube, some of the gas molecules are ionized and thus creating positively charged ions and electrons. The center of the tube serves as the positive electrode. Electrons in their vicinity are highly accelerated and ionize themselves further gas molecules through collisions on their way to the electrode. Thus an avalanche of charged particles is produced. This results in a short and intense pulse of current which can be counted. In 1928, Bothe developed the method of coincidence. This method provides the possibility to detect two signals at the same time by the usage of the coincidence circuit which reduced the chance of a false detection significantly.

The development of the synchrotron plays an important role in accelerator physics. In 1945, Veksler and McMillan published independently the synchrotron principle and the method of phase focusing for cyclic accelerators. The synchrotron combines a magnetic and electric field such that the traveling of the particles within the synchronized fields is fixed to a circle with constant radius. The relativistic mass increase is compensated due to the variable frequency of acceleration and the varying

[d] The motion of electric charge induces a magnetic field.

of the magnetic field. Phase focusing keeps the particles which are accelerated in bunches, together. Up to the present, it is the aim of particle physics to develop such accelerators with even higher center of mass energy.

Detection techniques improved steadily as well. The development of the scintillation detector by Kallmann, Coltman and Marshall in 1947 was very considerable. A scintillator material is coupled to an electronic light sensor such as a photomultiplier tube or a photodiode. These absorb the light emitted by the scintillator and re-emit it in the form of electrons. The subsequent multiplication of those electrons results in an electrical pulse which can then be analyzed and provide information about the particle that originally struck the scintillator. In 1949, Keuffel found that the discharge between parallel plates occurs along the physical path taken by the passage of the incoming particle which led to the development of the spark chamber. In 1952, Christophilos, Courant, Livingstone and Snyder discovered the principle of the alternating-gradient focusing. It consists of a system of alternating focussing and defocussing magnetic lenses. Nontheless, as a sum the system leads to a focussing particle beam. This breakthrough concept in accelerator design allowed scientists to accelerate protons to energies that would have been otherwise unachievable. The work performed at the alternating gradient synchrotron (AGS) led to three Nobel Prizes: 1976 – The discovery of the long-lived J/ψ state by Ting, which was discovered at the same time by Richter at the National Accelerator Laboratory (SLAC). 1980 – Cronin and Fitch discovered CP violation by experimenting with Kaons. 1988 – Lederman, Schwartz and Steinberger discovered the muon neutrino.

The discovery of the J/ψ was a big surprise because until then the first quark-models of elementary particle physics were based on the assumption that all hadrons are made of three different quark types, called 'up','down' and 'strange'. Despite the impressive ability of quark-models to bring order to the 'elementary particle zoo', their status was considered something like mathematical fiction. Nontheless, the idea of Glashow, Iliopoulos, and Maiani, known as the GIM mechanism, predicted a fourth type of quark which they called 'charm'. They provided theoretical predictions of what a 'charm/anti-charm meson' would be like. Therefore the wide acceptance of the quark model began with the discovery of this predicted meson which is called J/ψ.

In the following years, more predicted particles and states were discovered. In 1975, the third generation τ-lepton was observed by a group headed by Perl. The bottom counterpart to the J/ψ, the Υ-meson was discovered at Fermilab in 1977. Gluons, the mediators of the strong force, were indirectly observed in three jet events at DESY in 1979. A very important discovery was made in 1983 by Rubbia and S. van der Meer at CERN. The massive mediators of the weak force, $W^{\pm}$ and Z^0, were discovered as it was predicted from the electroweak theory. In 1995, the third generation quark with the highest mass, the top quark, was discovered at Fermilab. In 2000, the τ lepton neutrino was also observed there. All of these observations lead to the currently accepted standard model, which consists of fundamental particles, that matter as we know it is composed of, namely quarks and leptons. However, one predicted particle is still missing. The so-called 'Higgs'-boson which is responsible for

the mass of the fundamental particles. Accelerators like the Large Hadron Collider (LHC), which is a proton-proton collider, will show whether this last missing particle of the standard model can be affirmed by experiment as well.

Not only the search for fundamental particles, but also observations of compound systems contribute to a deeper understanding of the properties of matter. In the research field of charmonia spectroscopy, the so-called 'XYZ' states have been observed in charmonium-like decay modes in the recent years [2]. Some do fit into conventional charmonia states predicted from theory. However, others like the $X(3872)$, Y(4140) and $Z^{\pm}(4430)$, do not fit into this scheme.

There are many more observed states or evidence for states, which in some cases confirm theoretical predictions while in other cases they challenge our understanding. Thus it is an exciting time to do spectroscopy in order to challenge the theory.

1.2 Basic Terminology

In particle physics there are customarily used terms. Some important conventions and terms are described in the following.

Cross Section

The interaction cross section refers to a physical quantity to describe the likelihood of an interaction between two particles. In contrast to the dimensionless quantity probability, the cross section has the unit of an area, like m^2, which corresponds to the interaction range. This can be the geometrical extention of an object but also an effective interaction area due to the force field. The number of reaction per unit time is given by

$$\frac{dN}{dt} = \sigma \cdot j \cdot n$$

where j is the number of incoming particles per unit area and time and n is the number of target particles. σ thus gives the proportionality constant. At the atomic scale typical cross sections are of the order of $10^{-20}\mathrm{m}^2$. For nuclear processes these are even smaller – around $10^{-30}\mathrm{m}^2$. Thus, it is more convenient to use the unit barn which is defined as $1\ \mathrm{b} = 10^{-24}\mathrm{cm}^2$.

Matrix Element

Quantum mechanical states are respresented by a wave function ψ. The squared value of ψ is equal to the probability density for a system to be in the state ψ. The transition between an initial state ψ_i into a final state ψ_f due to an interaction potential $\hat{O}$ is described as

$$M_{if} = \int d^3x\, \psi(x)_f^{\dagger}\, \hat{O}\, \psi(x)_i.$$

M_{if} is called the matrix element. The transition rate consists of the square of the matrix elements times the number of the possible final states in a given energy

interval dn/dE, i.e. the number of states in phase space available to the produced particles, per unit interval of the total energy. This leads to Fermi's Second Golden Rule obtained from non-relativistic perturbation theory:

$$\frac{dN_{i\to f}}{dt} = \frac{2\pi}{\hbar}|\mathcal{M}|^2 \cdot \frac{dn}{dE}.$$

As a conclusion the interaction cross section is directly proportional to the squared matrix element

$$\sigma \propto |\mathcal{M}|^2.$$

The exact calculation of the matrix elements is very difficult and mostly impossible if one really wants to consider all effects. However, the different strength of the effects are considered in the perturbation theory where effects with respect to their strength are more or less considered. The several 'orders' of perturbation correction is often used in quantum mechanics.

In the quantum field theories a similar method is used, the so-called Feynman graphs. In these diagrams the interaction processes are figuratively shown. A Feynman diagram represents a perturbative contribution to the amplitude of a quantum transition from some initial quantum state to some final quantum state. The rules of the graphical representation are obtained from the perturbative development of the quantum field theory. The diagrams thus represent the relativistically invariant description of the processes of a certain interaction force for a given order of the perturbative theory.

Decay Probability

The decay rate $dN(t)/dt$ describes the amount of decays per unit time for spontaneously occurring processes like the radioactive decay. λ is the decay constant and its inverse quantity is the so-called mean lifetime τ. Formally such a decay is described as

$$N(t) = N(t=0) \cdot e^{-\lambda t}$$

where $N(t)$ is the amount of particles which is not decayed after the time t if $N(t=0)$ is the initial number of particles. The decay rate is equal to the transition rate $dN_{i\to f}/dt$ thus

$$\lambda \propto |\mathcal{M}^2|.$$

Frequently, the decay width Γ is used which is defined as

$$\Gamma = \frac{\hbar}{\tau}.$$

Also to mention is that if there is more than one possibility for a state to decay, the full width is just the sum of the widths of all states $\Gamma = \sum_i \Gamma_i$ which is usually called the sum of the 'partial widths'.

mediated force	exchange particle	symbol	mass	couples to
electromagnetic force	photon	γ	0	electric charge
weak force	Z boson	Z^0	80 GeV/c^2	weak charge
weak force	$W^\pm$ bosons	$W^\pm$	91 GeV/c^2	weak charge
strong force	8 gluons	g	0	color charge

Table 1.1: List of the 3 fundamental Standard Model forces and the gauge bosons responsible for the mediation of the forces.

exchange particle	relative magnitude	range
photon	10^{-2}	∞
W$^\pm$, Z bosons	10^{-7}	10^{-18}m
8 gluons	1	10^{-15}m

Table 1.2: List of the fundamental exchange bosons, their relative magnitude, and range. The strength of the weak interaction force is considered for low energies compared to the $W^\pm/Z^0$ masses.

1.3 The Standard Model

The Standard Model of elementary particle physics consists of gauge theories of the electroweak and strong interactions. In nature there are four types of fundamental interactions: gravity, electromagnetism, the weak and the strong force. Gravity is responsible for the attraction between masses. Although this is the force we experience most, it is not described in the Standard Model. One reason is that compared to the other forces, its strength is so small that it can be neglected. Moreover, until now it is impossible to develop a quantum field theory based on all four forces without running into irresolvable divergences.

The three forces considered in the Standard Model are summarized in table 1.1. All of the gauge bosons, the mediators of the forces, carry the total angular momentum $J = 1$. Photons are the propagators of the electromagnetic force, gluons propagate the strong force and the $W^\pm$ and Z^0 bosons disperse the weak force. The mediation via the charged $W^\pm$ bosons is usually referred to as the charged current while the mediation via the neutral Z^0 is called the neutral current. While the massless and uncharged photons have an infinite interaction range, the gluons interaction distance is quite short due the fact that they carry themselves the color charge. Therefore, they can interact between each other which is the reason of the short force mediation range. In contrast to the electromagnetic and strong force the weak force mediators have mass. As a consequence the interaction range of the weak force is quite short. This effect becomes less pronounced at energies at the order of the $W^\pm/Z^0$ masses. The relative magnitude and interaction range of the standard model forces are summarized in table 1.2.

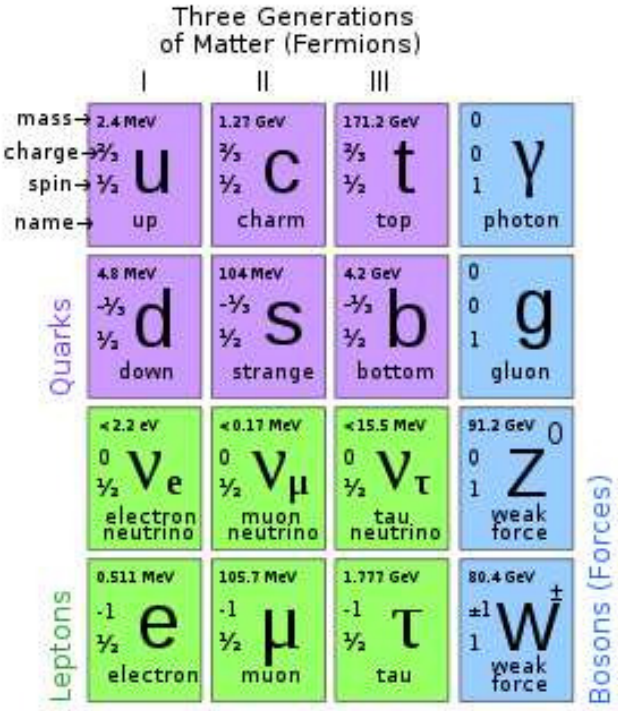

Figure 1.1: Description of the properties of the fundamental particles of the Standard Model [3].

The electroweak interaction merges the electromagnetic and weak forces. The lower the distances and the higher the energies of the interacting particles the more close get the strength of the different forces. At energies corresponding to the masses of the gauge bosons of the weak force the electromagnetic and weak interaction strength can be treated as one force. Electromagnetism is responsible for the attraction and repulsion between charged matter. The weak interaction takes place in the so-called β-decay. For instance, when a neutron decays into a proton and thereby releases a positron and an electron neutrino. The strong force holds together the nucleus in the atom.

Besides the exchange gauge bosons, the standard model also describes the quarks and leptons. The properties of the fundamental particles are summarized in figure 1.1. While the carrier of the forces are bosons, i.e. they have integer-spin and obey Bose-Einstein statistics, the fundamental particles of matter are fermions meaning that they have half-integer-spin and obey Fermi-Dirac statistics and the Pauli Exclusion Principle. Quarks and leptons can be categorized into three doublets or so-called generations. Their masses are rising with higher generation. Properties like the spin and charge remain the same.

The three generations of the leptons consists of the electron, muon and tauon which have a charge of -1 and their neutral partners, the corresponding neutrinos. Leptons do not interact via the strong force. Up-type quarks have a charge of 2/3, down-type

quarks have -1/3. All quarks have different flavors, like: up, down, charm, strange, top and bottom. Each of the quarks carry a color charge: blue, red or green. This concept had to be introduced in order to obey Pauli's Exclusion Principle which would otherwise be violated e.g. in case of the Δ^{++} resonance. [e]. The concept of color has been proven to be consistent with experimental observations. For each of the fundamental fermions exists its anti-particle. For quarks and neutrinos this is marked with a bar above its label, like up-quark (u) and anti-up-quark ($\bar{u}$). For charged leptons this is usually labeled with the corresponding charge. Our current understanding is that the leptons and quarks are fundamental and pointlike. However, it is still a puzzle why there are three generations and if there could exist more accessible at even higher energies.

Each of the interactions must obey conservation rules. The conservation of energy, momentum, angular momentum, charge, color, baryon number, and the lepton numbers for each generation separately, must be fullfilled. Charge conjugation (C) and parity (P) are conserved quantum numbers in strong and electromagnetic interactions. Furthermore, the isospin is conserved in the strong interaction. Charged current of the weak interaction can only couple to left-handed fermions and right-handed antifermions. The neutral current of the weak interaction couples with different strength to left- and right-handed fermions. Consequently, charge conjugation and parity are not conserved for the weak force. Even the combination CP does not hold here. Moreover, only the weak charged current can transform quarks into other quarks and leptons into other leptons. This leads to the fact that in contrast to the rest of the interactions the quantum numbers for the quark-flavor are not conserved in the weak interaction.

The Standard Model proves to be a theory that is in exceptional agreement with many experimental results. However, there are still puzzles in nature that can not be explained by this outstanding theory. Dark Matter and Dark Energy are one example. This in cosmology discovered phenomenon cannot be explained by the matter we know about. Another puzzle is that experimentally there are only $q\bar{q}$ and qqq compositions observed while the Standard Model only requires the formation of colorless quark compositions which would also make four quark states possible. According to our However, from a purely phenomenological point of view it is known that all observed particles can either be interpreted as a lepton or as a hadron as defined in the next paragraph.

In the constituent quark model hadrons are categorized into baryons and mesons. Baryons are composed of three quarks with different color such that they become colorless together. Due to the uneven number of spin-one-half quarks, baryons belong to the group of fermions and have therefore always half-integer spin. Protons (uud) and neutrons (udd) are examples of baryons. Mesons consist of a quark and an anti-quark. To be colorless the constituent parts are required to have color and

[e] $\Delta^{++} = uuu$ ($J = \frac{3}{2}$) requires an additional property of the quarks in order to obey Pauli's Exclusion Principle that requires that two identical fermions, in this case the u quarks, cannot occupy the same quantum state. Due to the property of color the u quarks become distinguishable and the problem is solved.

the corresponding anti-color. The even number of quarks leads to the fact that the mesons have full-integer spin which make them belong to the category of bosons. Pions (e.g. $\pi^+ = (u\bar{d})$) belong to the group of mesons. A special meson composition is the quarkonium. It consists of a quark and an anti-quark with the same quark-flavor. The up and down quarks cannot built up a quarkonium in a pure form. The first example of a quarkonium is the $s\bar{s}$ which however only appears as the vector meson ϕ. The reason for the admixture of the light quarks u, d, and s is their mass which belongs to the same order of magnitude. Due to the much higher mass of the c and b quarks it is unlikely to find them together with the lighter quarks in one state. In contrast, they build isolated pure $c\bar{c}$ (charmonium) and $b\bar{b}$ (bottomonium) systems. The masses of the quarks are listed in figure 1.1. It must be mentioned that a $t\bar{t}$ meson cannot be realized in nature because the top-quark lifetime is too short compared to the time necessary to create a bound state. The study of the quarkonia states and their excitations belongs to the research field called quarkonium spectroscopy. Bound states like quarkonia are introduced in the next section in more detail.

1.4 Bound States

Commonly known bound states are atoms. The nucleus and the electrons are bound together by the electromagnet force. The most simple one is the hydrogen atom. It consists of a proton and an electron. This system does not only have one ground state but a full spectrum of excited states, too. Due to absorption of electromagnetic rays or collisions with high energetic particles, the hydrogen atom can become excited. By contrast, the exited system can emit photons and de-excite. The energy of the emitted photons makes it possible to deduce the hydrogen spectrum. Such a spectrum can also be obtained for other bound systems. Three of them will be described in the following sections.

1.4.1 Positronium

The positronium has a hydrogen-like configuration. However, there are two main differences: the constituent parts are an electron and a positron, and the constituent particles have the same mass, in contrast to the hydrogen atom where the proton mass is about 2000 times larger than that of the electron. Furthermore, due to the closeness of a particle and its anti-particle, they annihilate so the lifetime of the positronium cannot be long. Actually, it is of the order of 10^{-10}s. It was discovered by M. Deutsch in 1951. The positronium spectrum is illustrated on the right-hand side in figure 1.2. Similarly to the existence of molecules composed of atoms, a molecule consisting of two positronium was predicted to exist in 1946 by J. A. Wheeler and subsequently studied theoretically. However, it was not observed until 2007 in an experiment done by D. Cassidy and A. Mills. The researchers made the positronium molecules by firing intense bursts of positrons into a thin film of porous

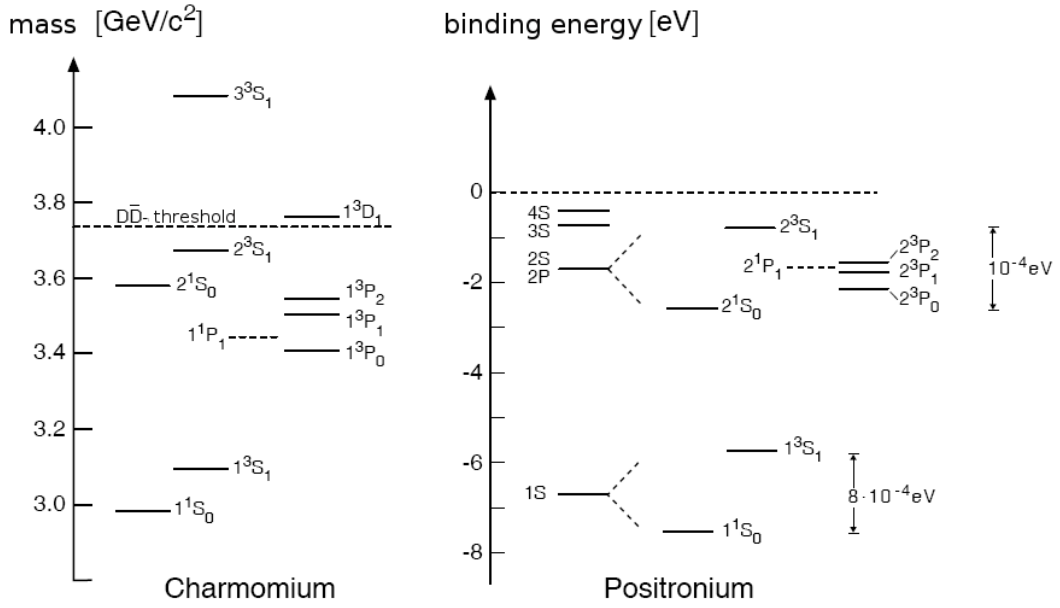

Figure 1.2: The positronium and charmonium spectra [4]. Even though the interaction force is different, the short-distance coulomb-like strong potential appears very similar to the electromagnetic potential which can be seen here: both spectra are quite similar, except of the order of magnitude of the energies.

silica. Upon slowing down in silica, the positrons captured ordinary electrons to form positronium atoms. Within the silica, they were long lived enough to interact, forming molecular di-positronium [5].

1.4.2 Charmonium

Charmonium is a bound system of a c-quark and a $\bar{c}$-quark. Compared to the positronium in this case the strong force is responsible for the binding of the constituent charm quarks. The spectra of heavy quarkonium should thus be described by the QCD. In practise there arise difficulties to do so hence one can roughly distinguish between the phenomenological and the theoretical approaches.

The theoretical approach attempts to describe heavy quarkonium with QCD based calculations. The light quarks in a meson move at relativistic speeds, since the mass of the bound state is much larger than the mass of the quark. However, the speed of the charm and the bottom quarks in their respective quarkonia is sufficiently smaller. Hence relativistic effects influence these states much less. The speed v can be roughly estimated to be 0.3 times the speed of light for charmonia and roughly 0.1 times the speed of light for bottomonia. Thus, the computation can be approximated by an expansion in powers of v/c and v^2/c^2. This technique is called non-relativistic QCD (NRQCD). There are also lattice QCD calculations which has been found to be in good agreement with the bottomonium masses [6]. However, in case of the

charmonium masses their agreement is not as good [7].

The basic tools of the phenomenological approach are models of the effective potential to calculate masses of quarkonia states. In this technique, one uses the fact that the motion of the quarks that comprise the quarkonium state is non-relativistic. It is further assumed that they move in a static potential, like non-relativistic models of the hydrogen atom. One of the most popular potential models is the so-called Cornell potential

$$V_{\mathrm{S}}(r) = -\frac{4}{3}\frac{\alpha_{\mathrm{S}}}{r} + k \cdot r.$$

The index s represents the fact that in this case the strong force is responsible for the interaction. The first term, $1/r$ corresponds to the potential induced by one-gluon exchange between the quark and its anti-quark. It is known as the Coulombic part of the potential, since its form is identical to the well-known Coulombic potential induced by the electromagnetic force. The second term is known as the confinement part of the potential, and parameterizes the poorly-understood non-perturbative effects of QCD. The potential thus is dominated by the first Coulomb-like potential term for small distances and a linear rising term for larger distances.

Generally, when using the phenomenological approach, a convenient form for the quarks wave function is taken, and then α_{S} and k are determined by fitting the results of the calculations to the masses of the well-measured quarkonium states. Corrections due to e.g. relativistic effects, fine and hyperfine splitting, retardation and annihilation effects can be incorporated into this approach by adding extra terms to the potential, in the same way that they are added for the hydrogen atom or positronium in non-relativistic quantum mechanics. This approach has no good theoretical motivation though, but it is popular because it allows for accurate predictions of quarkonia parameters without a lengthy lattice computation. Furthermore, it provides a separation between the short-distance Coulombic effects and the long-distance confinement effects that can be useful in understanding the quark/anti-quark force generated by QCD.

Due to the similar potential used for the positronium, one expects a quite similar quarkonium spectrum. The energy levels of such a system can also be calculated in analogy to the positronium by solving a non-relativistic Schrödinger equation [8].

Spectroscopy uses some special nomenclature to define the different states. In the case of the quarkonia a state is denoted by $(n+1)^{2S+1}L_J$ where

- the quantum number for radial excitation n,
- the relative orbital angular momentum between the quarks L = 0,1,2,..., denoted as S,P,D,...,
- the combined spin $S = 0, 1$ of the two quarks,
- the total angular momentum $J = L \oplus S$.

The left plot in figure 1.2 shows the charmonium spectrum. Additionally, there is also an alternative naming for the known states that assign the names after the convention of the Particle Data Group [9]. For charmonia these states are called

- η for L-even singlet states (S=0),
- ψ for L-even triplet states (S=1),
- h for L-odd singlet states (S=0),
- χ for L-odd triplet states (S=1).

The different states are also often classified according to their quantum numbers J^{PC}. J represents the total angular momentum of the particle. P and C describe the behavior of the wave-function of the state under the parity operation and the charge-parity operation. For a bound system of a spin 1/2 particle and its antiparticle they relate as follows:

$$\begin{aligned} P &= (-1)^{L+1}, \\ C &= (-1)^{L+S}. \end{aligned}$$

The lightest charmonium state is the η_c with $J^{PC} = 0^{-+}$. The two quark spins arrange to have total spin $S = 0$, i.e. they are anti-parallel. The orbital angular momentum between the quarks is $L = 0$ as well, which leads to a total angular momentum of $J = 0$. This state thus is labelled 1^1S_0 in spectroscopic notation. The other state with $L = 0$ but with parallel spin $S = 1$ is the most familiar charmonium state, the J/ψ (1^3S_1, $J^{PC} = 1^{--}$). The first radial excitations of those two states are the η_c' and the ψ', the second commonly referred to as $\psi(2S)$. In spectroscopic notation they are labelled 2^1S_0 and 2^3S_1, respectively. The vector states J/ψ and $\psi(2S)$ are easy to access in e^+e^--collider experiments due to the fact that in the annihilation process a virtual photon with the same quantum numbers is produced. Due to conservation rules the photon can directly produce only the $J^{PC} = 1^{--}$ states. The set of the lightest charmonium states with $L = 1$ are called h_c (1^1P_1, $J^{PC} = 1^{+-}$) for the spin-singlet state with $S = 0$, and χ_c for the spin triplet states with $S = 1$: χ_{c0} (1^3P_0, $J^{PC} = 0^{++}$), χ_{c1} (1^3P_1, $J^{PC} = 1^{++}$), χ_{c2} (1^3P_2, $J^{PC} = 2^{++}$).

Those are all of the unambiguously known states. Higher states have the additional property that their masses are above the $D\bar{D}$ thresholds:

- $D\bar{D}$ at a mass of $\approx 3.730\,\mathrm{GeV}/c^2$,
- $D^*\bar{D}$ at a mass of $\approx 3.875\,\mathrm{GeV}/c^2$,
- $D^*\bar{D}^*$ at a mass of $\approx 4.015\,\mathrm{GeV}/c^2$.

States with masses higher than these thresholds are kinematically allowed to decay into two D-mesons. If this decay is not suppressed for other reasons, it will become

highly dominant since it is a strong decay involving only low-energetic (so-called 'soft') gluons. The fast decay into $D\bar{D}$ translates to a broad state in mass, so that it is experimentally very difficult to isolate these states. This is not true for states which cannot decay to $D\bar{D}$ for other reasons, for example because of conservation of parity. These states can be narrow even above the $D\bar{D}$ threshold.

After the observation of the J/ψ, the search for predicted charmonium states has been started and continues until today. However, in these days, charmonium candidates have been observed which do not have the expected properties. They are called the 'XYZ' states.

In 2007, Belle reported the observation of a relatively narrow enhancement in the $\pi^+\psi(2S)$ invariant mass distribution. Their recently updated measurement reported a mass of 4433^{+15}_{-12} (stat.)$^{+19}_{-13}$ (syst.) MeV/c^2 with a significance of 6.4σ [10]. If this resonance is interpreted as a meson state then it must have an exotic structure which is already clear due to the fact that it carries charge whereas the conventional charmonium must be neutral.

The Y(4140) extends the meson search for an exotic state to c and heavy s quark decay products. It is thus searched in the final state $J/\psi\phi$ with $J/\psi \to \mu^+\mu^-$ and $\phi \to K^+K^-$. CDF II [11] reports evidence for a a narrow structure at $4143 \pm 2.9\,(\text{stat.}) \pm 1.2\,(\text{syst.})\,\text{MeV/c}^2$ near the $J/\psi\phi$ threshold with a significance estimated to be at least 3.8σ. This structure does not fit conventional expectations for a charmonium because of an expected tiny branching ratio to $J/\psi\phi$ with its mass that is above the open charm threshold of $D^*\bar{D}^*$ at a mass of $\approx 4.015\,\text{GeV}/c^2$.

Another charmonium candidate with unexpected properties is the $X(3872)$.

1.4.2.1 The $X(3872)$

In 2003 the Belle collaboration announced the discovery of a new state [12] with a measured mass of

$$m = 3872.0 \pm 0.6\ (\text{stat.}) \pm 0.5\ (\text{syst.})\ \text{MeV}/c^2.$$

The nature of the state is not clear so its mass is used to label the state. It was reconstructed in the exclusive decay[f]

$$B^\pm \to K^\pm X(3872) \to K^\pm (J/\psi\pi^+\pi^-).$$

There was a signal of 35.7 ± 6.8 observed, with a statistical significance of $10.3\,\sigma$ (see figure 1.3).

The observation of the $X(3872)$ was quickly confirmed by the CDF II collaboration [13]. A significant excess of 730 ± 90 candidates was found in the invariant $J/\psi\pi^+\pi^-$ mass spectrum (see figure 1.3). Also DØ [14] and *BABAR* [15] were soon able to confirm the state in the decay to $J/\psi\pi^+\pi^-$.

[f] If all final decay-particles are reconstructed, the decay is called 'exclusive decay'.

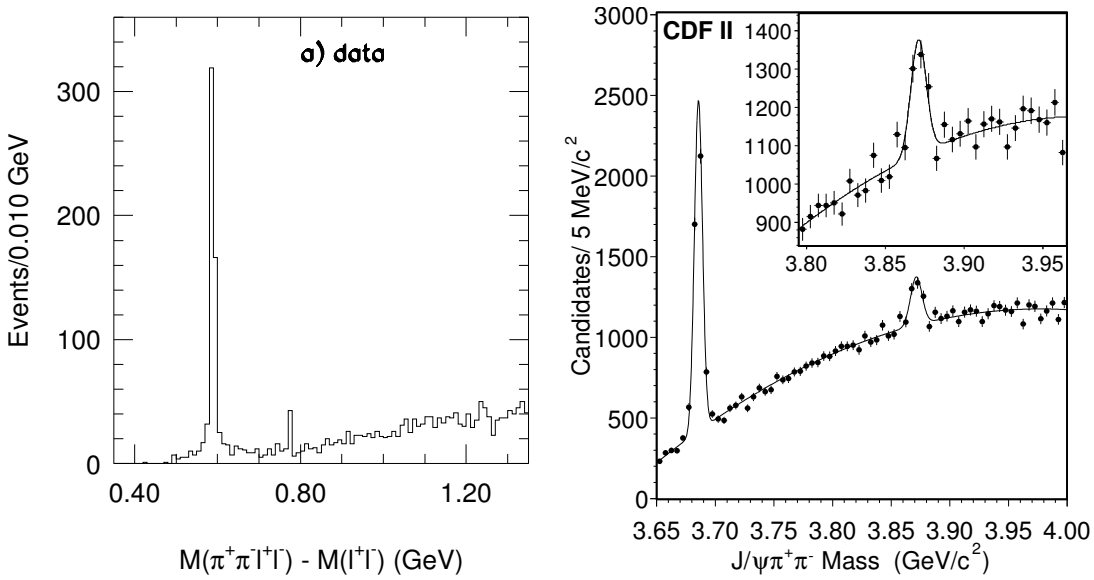

Figure 1.3: Observed spectrum of $m(J/\psi\ \pi^+\pi^-) - m(J/\psi\ )$ by Belle (left plot). The new $X(3872)$ state can be seen at $\approx 0.8\,\mathrm{GeV}/c^2$. The prominent signal at $\approx 0.6\,\mathrm{GeV}/c^2$ is the long-known charmonium state $\psi(2S)$. The right plot shows the observed spectrum of $m(J/\psi\ \pi^+\pi^-)$ by CDF with a clear signal peak at $\approx 3.87\,\mathrm{GeV/c}^2$.

The established $X(3872)$ resonance turned out to be very difficult to get categorized. Until now the true nature of the $X(3872)$ is unknown. The most natural conclusion is to assume it is a charmonium state since the final state consists of a charmonium, namely the J/ψ. Unfortunately, none of the possible candidate-states could be matched with the charmonium expectations of the $X(3872)$. E.g. experimental results show that the decay proceeds via a ρ which leads to an isospin violating strong decay if the $X(3872)$ is a charmonium state [16]. The $X(3872)$ has one outstanding property: its mass is within the errors identical to the combined mass of the D^0 and the D^{0*} mesons. This gives rise to the exotic molecule hypothesis: could the $X(3872)$ be a bound state of two D mesons? But if not, could it be something else? Anything different than a charmonium state would be unprecedented in high energy physics and would open the window for a completely new spectroscopy.

1.4.2.2 Exotic Interpretations of the $X(3872)$

There are many attempts to describe the mechanism for the $X(3872)$-production. Some of them will be shortly presented in this section.

- **Molecule Hypothesis**
  Due to the fact that the charmonium hypothesis does not fit in all detail to the observed $X(3872)$-resonance, attention soon focused on the mass of the $X(3872)$, which is in remarkable agreement with the sum of the D^0- and D^{*0}-

masses. The measured mass of the $X(3872)$-resonance [17, 18] is

$$m(X(3872)) = 3871.61 \pm 0.16 \pm 0.19\,\mathrm{MeV}/c^2$$

and the sum of the D^0- and D^{0*}-masses are according to the PDG [9]

$$\begin{aligned} m(D^0) + m(D^{0*}) &= 1864.84 \pm 0.17\,\mathrm{MeV}/c^2 \;+\; 2006.97 \pm 0.19\,\mathrm{MeV}/c^2 \\ &= 3871.81 \pm 0.36\,\mathrm{MeV}/c^2. \end{aligned}$$

It can be seen that the mass of the $X(3872)$ is within the errors identical to the sum of the D^0- and D^{0*}-masses, so that the assumption of a bound state of these two mesons suggests itself. The $X(3872)$ mass measurement can shed light into the assumption of being a molecule. If the mass was above the D^0- and D^{0*}-masses, the molecule hypothesis would be ruled out. Due to the binding energy[g] the $X(3872)$ mass is expected to be lower. The CDF II measurement is within errors consistent with the molecule hypothesis. In can be seen that the uncertainties of the measurement of the D^0 and D^{0*}-masses contribute significantly.

The basic hypothesis of a bound state of D^0 and D^{0*} is considered in different ways. Törnqvist [19] discusses a deuteron-like system, a so-called 'deuson', where the D^0 and D^{0*} mesons are bound by a long-range pion exchange. In this model only states with quantum numbers $J^{PC} = 1^{++}$ or $J^{PC} = 0^{-+}$ would be bound states. Others pion exchange is repulsive or too weak.

Swanson [20] extends Törnqvist's model by adding short-range quark/gluon interactions to the long-range pion exchange. The model predicts large decay widths into $J/\psi\pi^+\pi^-$ and $J/\psi\pi^+\pi^-\pi^0$ of similar magnitude. No $D\bar{D}$ molecules are expected, however a rich spectrum of $D^*\bar{D}^*$, $B\bar{B}^*$, and $B^*\bar{B}^*$ should exist.

- **Multiquark Hypothesis**
  A different approach to explain the $X(3872)$ is used in the multiquark hypotheses, which proposes two quarks and two anti-quarks to form a state. Multiquark states were already suggested in the 1970's [21]. The $a_0(980)$ and $f_0(980)$ states were proposed as good candidates. However, contradictory predictions and missing experimental evidence resulted in an insufficient support for this hypothesis.

  The observation of the $X(3872)$ led to a resurgence of the 4-quark model. Various different implementations of the general 4-quark model have been suggested that can accommodate the $X(3872)$ as a multiquark state containing two light quarks and two charm quarks [22–28].

  The model of Maiani et al. [22, 29], is a 'diquark-antidiquark' model which divides the four constituent quarks into a $[cq][\bar{Q}\bar{q}']$ structure with light quarks $q, q' = u, d$ and a heavy quark $Q = c, s$. The quarks are grouped into color

[g] The binding energy has to be subtracted from the sum of the energies of the constituent particles.

triplet scalar or vector clusters. The interactions between the two clusters is dominated by spin-spin interactions. Binding is achieved by the color forces of gluon exchange.

The model predicts a number of states, most importantly four states related to the $X(3872)$:

$$\begin{aligned} X^+ &= [cu][\bar{c}\bar{d}] \\ X^- &= [cd][\bar{c}\bar{u}] \\ X_u^0 &= [cu][\bar{c}\bar{u}] \\ X_d^0 &= [cd][\bar{c}\bar{d}]. \end{aligned}$$

The two neutral states mix to form the physical states X_{low} and X_{high}, described by the mixing angle θ:

$$\begin{aligned} X_{low} &= X_u^0 \cos\theta + X_d^0 \sin\theta, \\ X_{high} &= -X_u^0 \sin\theta + X_d^0 \cos\theta. \end{aligned}$$

Because of this, isospin is broken for the neutral mass eigenstates, and consequently in their strong decay as well. The mass difference between the two states is expected to be

$$m(X_{high}) - m(X_{low}) = \frac{7 \pm 2}{\cos(2\theta)}\ \mathrm{MeV}/c^2.$$

The fact that apparently only one narrow neutral state is observed at the B-factories is explained by stating that the two states X_{low} and X_{high} occur in the decay channels $B^+ \to X(3872)K^+$ and $B^0 \to X(3872)K_S^0$ differently. The ratio of these two decays is expected to be of the order of ≈ 1 [30].

The latest CDF II measurement however disfavors the hypothesis of one state [17,18].

- **Other Interpretation Possibilities**
  Charmonium Hybrid
  Hybrid mesons combine a regular meson state, in case of the $X(3872)$ a charmonium, with an excited gluonic degree of freedom. In fact, lattice gauge theory and hadron models predict a rich spectrum of charmonium hybrid mesons [31,32]. Several predictions, either using the 'flux-tube model' [33–35] or lattice calculations [36], expect $c\bar{c}g$ hybrids in the mass range of $4.0 - 4.2\,\mathrm{GeV}/c^2$. Of special interest are the states with quantum numbers $J^{PC} = 0^{+-}$, 1^{-+}, and 2^{+-} since those cannot be obtained with a simple $c\bar{c}$ charmonium model and would, if observed, unambiguously proof an unconventional state.

  Li [37] suggests the hybrid hypothesis for the $X(3872)$ and predicts a dominant decay $X(3872) \to J/\psi gg$. The $X(3872)$ should also have a sizable branching

fraction to $J/\psi\sigma$. The deviation of the measured mass of 3871.61 GeV/c^2 to the expected masses above 4.0 GeV/c^2 does not support the hybrid hypothesis. However, since no experimental 'gauge' exists to guide systematic effects, predicted masses may shift significantly.

Cusp/Threshold Effect
In contrast to exotic models, Bugg [38–40] ascribes the resonance structure of the $X(3872)$ to possibly be a threshold cusp. Cusps can appear in any process at the threshold where a coupled channel opens. The resonance-like $X(3872)$-structure is explained as randomly produced $D\bar{D}^*$ final states with low relative momentum which de-excite into open channels like $J/\psi\pi\pi$ and produce a cusp in the $J/\psi\pi\pi$ mass spectrum.

Kalashnikova [41, 42] proposes a coupled channel model of the $c\bar{c}$ system with couplings to the $D\bar{D}$ continua ($D\bar{D}$, $D\bar{D}^*$, $D^*\bar{D}^*$, ...). In the calculations for the different charmonium states χ'_{c1} stands out. In addition to the regular χ'_{c1} resonance, a virtual bound state just above the $D\bar{D}^*$ threshold is predicted, which produces a cusp in the $J/\psi\pi\pi$ final state.

Glueball
Seth [43] suggests that the observed $X(3872)$-resonance is a glueball which is a bound state containing only gluons. This model is based on the mass calculations by Morningstar and Peardon [44]. They predict a state with quantum numbers 1^{--} at a mass of $m \approx 3850$ MeV/c^2 which is already ruled out by experimental results [17].

Due to an expected small admixture of $c\bar{c}$ quark content stemming from the $\psi(2S)$, the occurrence of the decay to $J/\psi\pi^+\pi^-$ is explained. Similar to the $\psi(2S)$, also the decays $X(3872) \to J/\psi\pi^0\pi^0$ and $X(3872) \to J/\psi\eta$ are expected.

The difficulty which arises is that in the last years there are evidences and even discoveries of many of such perhaps exotic states [2]. Each of these states is a candidate for certain models, however, none of the existing exotic models can describe all of the extraordinary so-called XYZ-states together.

In order to explain the $X(3872)$, three models are favored: the charmonium, the molecule and the multiquark state. The charmonium hypothesis is strong, because it is after all a well-proven model. It however requires adjustment to explain the $X(3872)$. Moreover, it is also a probable scenario that in reality the $X(3872)$ is an admixture of some of the previously explained 'natures'. Next to the charmonium hypothesis, all other hypotheses are exotic in a sense, that they deviate from the known structures of matter in high energy physics. Be it a molecule or a multiquark state, an unambiguous identification would imply the existence of similar states in the bottom sector as well and maybe even a completely new spectrum of particles.

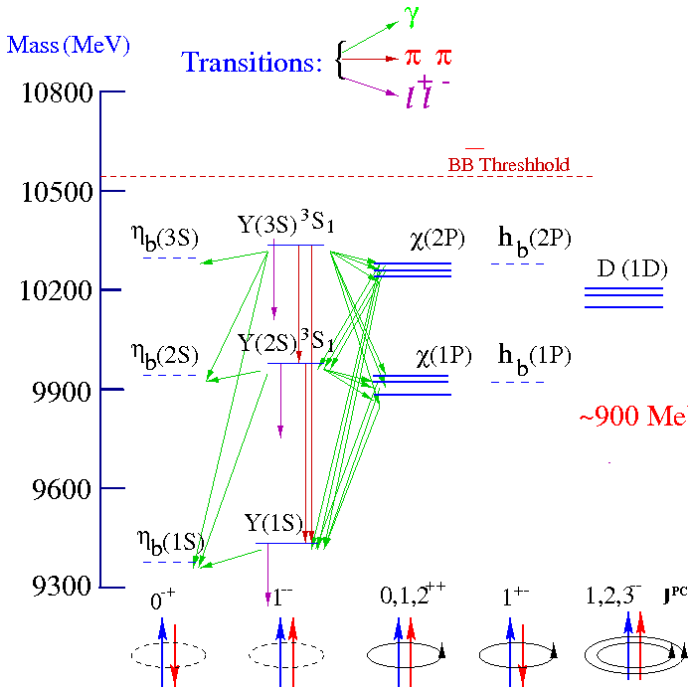

Figure 1.4: The bottomonium spectrum [45]. Observed states are labelled by a solid line, the naming scheme is explained in the text.

1.4.3 Bottomonium

The bottomonium is a bound state of a b-quark and an $\bar{b}$-quark. Again, for the composite system of two bottom quarks a full spectrum of $b\bar{b}$-states is obtained. Compared to charmonium, the bottomonium has even three vector meson states below threshold. In figure 1.4 the bottomonium spectrum is illustrated. The nomenclature that was already described in section 1.4.2 is again used here to define a state in the notation $(n+1)^{2S+1}L_J$. Theoretical predictions are in good agreement with the observed states below threshold. In addition to the spin-independent potential there are spin dependent interactions of the order of $(v/c)^2$ considered which lead to multiplet splittings. The $\Upsilon(1S) - \eta_b$ splitting is an example for the short distance $\vec{s}_q\vec{s}_{\bar{q}}$ contact interaction due to the one-gluon-exchange. The splitting of the P-wave χ_b states is a result of the spin orbit interaction.

The alternative names for the known bottomonium states are

- η_b for $L = 0$ singlet states (S=0),
- Υ for $L = 0$ singlet states (S=1),
- h_b for $L = 1$ singlet states (S=0),
- χ_b for $L = 1$ triplet states (S=1),
- $D(1D)$ for $L = 2$ triplet states (S=1).

The lightest bottomonium state is the η_b with $J^{PC} = 0^{-+}$. In spectroscopic notation it is labelled 1^1S_0. The next state with $L = 0$ but with parallel spin $S = 1$ is the most familiar upsilon state, the $\Upsilon(1S)$ (1^3S_1, $J^{PC} = 1^{--}$). The first and second radial excitations of the η_b are the $\eta_b(1S)$ and $\eta_b(2S)$. The first and second radial excitations of the $\Upsilon(1S)$ are the $\Upsilon(2S)$ and $\Upsilon(3S)$. In spectroscopic notation they are labelled 2^1S_0 and 3^1S_0, and 2^3S_1 and 3^3S_1, respectively.

The set of lightest bottomonium states with $L = 1$ are called

- $h_b(1P)$ (1^1P_1, $J^{PC} = 1^{+-}$)
- and $h_b(2P)$ (2^1P_1, $J^{PC} = 1^{+-}$)

for the spin-singlet state with $S = 0$, and χ_b for the spin triplet states with $S = 1$:

- $\chi(1P)_{b0}$ (1^3P_0, $J^{PC} = 0^{++}$),
- $\chi(1P)_{b1}$ (1^3P_1, $J^{PC} = 1^{++}$),
- $\chi(1P)_{b2}$ (1^3P_2, $J^{PC} = 2^{++}$),
- $\chi(2P)_{b0}$ (1^3P_0, $J^{PC} = 0^{++}$),
- $\chi(2P)_{b1}$ (1^3P_1, $J^{PC} = 1^{++}$),
- and $\chi(2P)_{b2}$ (1^3P_2, $J^{PC} = 2^{++}$).

The spin triplet states with $L = 1$ and $S = 1$ are:

- $D(1D)_{b0}$ (1^3D_1, $J^{PC} = 1^{--}$),
- $D(1D)_{b1}$ (1^3D_2, $J^{PC} = 2^{--}$),
- and $D(1D)_{b2}$ (1^3D_3, $J^{PC} = 3^{--}$).

Except of the η-, h- and D-states those are all of the undoubtedly experimentally observed states. Higher states have the additional property that their masses are above the $B\bar{B}$ thresholds:

- $B\bar{B}$ at a mass of $\approx 10.558\,\mathrm{GeV}/c^2$,
- $B^*\bar{B}$ at a mass of $\approx 10.604\,\mathrm{GeV}/c^2$,
- $B^*\bar{B}^*$ at a mass of $\approx 10.650\,\mathrm{GeV}/c^2$.

States with masses higher than those thresholds are kinematically allowed to decay into two B-mesons. The consequences are the same as for the charmonium case.

	$X(3872)$	X_b
quark content	charm	bottom
decay	$X(3872) \rightarrow J/\psi\pi^+\pi^-$ $J/\psi \rightarrow \mu^+\mu^-$	$X_b \rightarrow \Upsilon(1S)\pi^+\pi^-$ $\Upsilon(1S) \rightarrow \mu^+\mu^-$
quantum numbers	$J^{PC} = 1^{++}, 2^{-+}$ J/ψ: $J^{PC} = 1^{--}$	$J^{PC} = 1^{++}$ $\Upsilon(1S)$: $J^{PC} = 1^{--}$
mass	$D^0 D^{0*}$ (3.872 GeV/c^2)	$B^0 B^{0*}$ (10.604 GeV/c^2)

Table 1.3: Comparison of the bottom and charm sector relating to common properties of the $X(3872)$-state and an possibly existing bottom counterpart.

1.5 The X_b-State

The rather unusual properties of $X(3872)$ which are interpreted by theories from $D^0\bar{D}^{*0}$ molecule, 4 quark state to charmonium hybrid are still not undoubtly explained. But perhaps discovering its bottom counterpart, the X_b, could shed much light on the issue. This analysis searches for the counterpart of the $X(3872)$ in the corresponding final state $\Upsilon(1S)\pi^+\pi^-$.

1.5.1 The Possibility of a Counterpart of the $X(3872)$

Both spectra, charmonium and bottomonium, have similar properties. Consequently, there might also exist a bottom counterpart of the observed $X(3872)$. It is thus assumed that the $X(3872)$ and the X_b states have common properties that are listed in table 1.3.

Currently, $\approx$ 2300 $X(3872)$ candidates are observed in the final state $J/\psi\pi^+\pi^-$ at CDF II [46]. Thus, the bottom counterpart it searched in the corresponding final state $\Upsilon(1S)\pi^+\pi^-$. CDF II measured the quantum numbers J^{PC} of the $X(3872)$ and found that only 1^{++} or 2^{-+} are consistent with data [17,46]. The quantum numbers 1^{++} are favored from CDF II and also support, in addition to the $X(3872)$ mass, the molecule hypothesis. Thus, mass predictions for the X_b close to the $B^0\bar{B}^{*0}$ threshold are also favored to search at.

The discovery of such an analogue state would be very conclusive for current theoretical predictions because the X_b mass position could support or disfavor possible theoretical interpretations and could perhaps shed light into the unknown nature of the $X(3872)$.

Many theoretical predictions are made for the X_b state. In analogy to the $X(3872)$, several models are discussed in the following.

- **Molecule Hypothesis**
  Törnqvist [19] suggest a deuteron-like system, where the B^0 and B^{0*} mesons

are bound by a long-range pion exchange. The mass prediction for the quantum numbers 1^{++} is $\approx 10562\,\mathrm{MeV/c^2}$. According to Swanson [20] who extends Törnqvist's model a rich spectrum of $B\bar{B}^*$, and $B^*\bar{B}^*$ should exist. He predicts for the 1^{++} $B\bar{B}^*$ system a bound state of mass 10562 $\mathrm{MeV/c^2}$ in agreement with Törnqvist.

- **Multiquark Hypothesis**
  The analysis of excited tetraquark states with hidden bottom [47] in the frame of the relativistic quark model based on the quasipotential approach in quantum chromodynamics, predicts the mass of the bottom counterpart to $X(3872)$ to be 10492 $\mathrm{MeV/c^2}$.

1.5.2 Experimental Potential to observe the X_b

The Tevatron and LHC are the favored accelerators to discover the counterpart of the $X(3872)$. Due to the favored quantum numbers J^{PC} of 1^{++} and 2^{-+} hadronic machines are favored to search for the X_b. On possible expectation for the decay $X_b \to \Upsilon(1S)\pi^+\pi^-$ is ≈ 180 reconstructed events for 8 fb^{-1} [48]. The number is for roughly 3000 reconstructed $X(3872)$ per fb^{-1} and $\approx 3 \cdot 10^5$ J/ψ's. They assume further that $\approx 4400\,\Upsilon$'s are reconstructed from $77\,pb^{-1}$ where the leptonic branching fraction is taken into account.

This analysis is performed with 3.5 fb^{-1} which thus leads to an expectation of roughly 80 events. An even more conservative estimation predicts even less events for $8fb^{-1}$. However, the relative branching ratios and production fractions for the X_b relative to the $X(3872)$ are unknown. This fact makes it worth to search for the X_b and could make it accessible.

For Tevatron Run II it is suggested to benchmark the $\Upsilon(2S) \to \Upsilon(1S)\pi^+\pi^-$ process an then look for a higher mass 'bump' much like it is the case for $X(3872)$. This is a quite difficult task, however, because of two reasons. Firstly, there are many X_b mass predictions. It is self-evident to have firstly a look near the B^0-B^{0*}-threshold. However, different exotic models predict different X_b-masses [49,50]. Due to the spread of X_b mass predictions from theory, in this analysis the mass range $10.2\mathrm{GeV/c^2} \leq m_{X_b} \leq 11.2\mathrm{GeV/c^2}$ is searched for a small resonance. The second reason is the huge combinatorial background because of the pion combinatorics which makes the the search very difficult.

1.6 Υ Polarization

The polarization α of the Υ's contain important information about the Υ production mechanism. Polarizations are defined as ratios of cross-sections for the production of different spin states of the same quarkonium. The angular distribution of the decay products of the quarkonium depends on the its spin state. The polarization of the 1^{--} state can be measured from the angular distribution if the Υ decay into

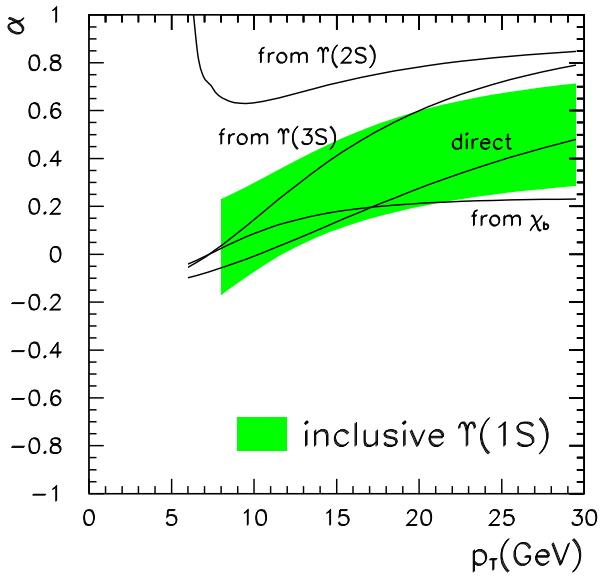

Figure 1.5: Polarization variable α for inclusive $\Upsilon(1S)$ production at the Tevatron as a function of $p_{T,\Upsilon}$. The theoretical band respresents the NRQCD factorization prediction [53].

lepton pairs. Let θ^* be the angle in the Υ rest frame between the positive lepton momentum and the chosen polarization axis then the differential cross-section has the form

$$\frac{dN}{d(\cos\theta^*)} \propto 1 + \alpha \cos^2\theta^*.$$

The limiting values $\alpha = 1$ and $\alpha = -1$ refer to the totally transverse and totally longitudinal polarizations. In this analysis the polarization information is contained in the distribution of the muon decay angle θ^*. There are different reference frames to calculate this angle. The helicity frame and the Collins Soper frame were proposed to be good orthogonal testing frames for measuring the Υ polarization [51].

1.6.1 Theoretical Predictions

The production of heavy quarkonium states at high energies is currently under intense experimental and theoretical study. NRQCD is an effective field theory that provides the formalism for calculating production rates of Υ states. Unfortunately, experimental results tend to disagree with the NRQCD predictions [52]. There are also other QCD-inspired models, e.g. the k_T-factorization model, that predict the vector meson polarization as functions of the transverse momentum p_T. Theorists emphasize that measuring the vector meson polarizations is a crucial test of NRQCD.

In reference [54] it is proposed to measure the differential cross-section

$$BR(Y(nS) \to \mu^+\mu^-) \cdot \frac{d\sigma}{dp_T dy}$$

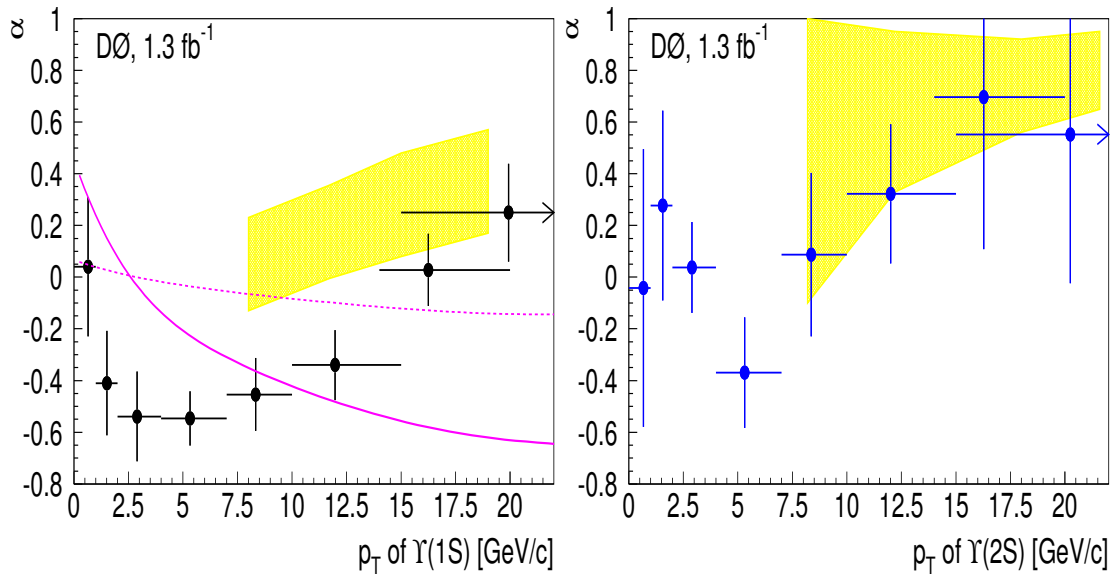

Figure 1.6: DØ ϒ polarization measurement result. The p_T-dependence of the polarization α is shown for $\Upsilon(1S)$ (left) and $\Upsilon(2S)$ (right).

as well as the polarization angle α as functions of p_T. The theoretical prediction from reference [53] for the polarization of the $\Upsilon(1S)$ is shown in figure 1.5.

1.6.2 Previous Measurements

So far DØ and CDF Run 1b performed an ϒ polarization measurement. DØ claims a significant longitudinal polarization that is dependent on p_T for $\Upsilon(1S)$ which is inconsistent with QCD [52]. Their results for $\Upsilon(1S)$ and $\Upsilon(2S)$ are shown in figure 1.6. The CDF Run 1b measurement, however, claims that the $\Upsilon(1S)$ mesons are found to be unpolarized withing the accessible range of the ϒ transverse moment p_T [55].

Recently, CDF II updated their polarization measurement but only for the $\Upsilon(1S)$. Their result is shown in figure 1.7 and is consistent with their previous measurement. As it is of crucial importance to model the ϒ's correctly to achieve the best X_b-search result, this analysis also measures the $\Upsilon(nS)$ polarization. Compared to DØ, the advantage of CDF II is the better muon momentum resolution. In figure 1.8 one can see the ϒ spectra obtained from DØ and from CDF II. Whereas DØ cannot really distinguish the three ϒ mesons, CDF II provides nicely separated resonance peaks for each ϒ vector state. However, DØ provides a higher coverage of their muon detector and has a better purity. Thus it would be very informative to get a comparison between the ϒ polarization measurement of the two experiments, soon.

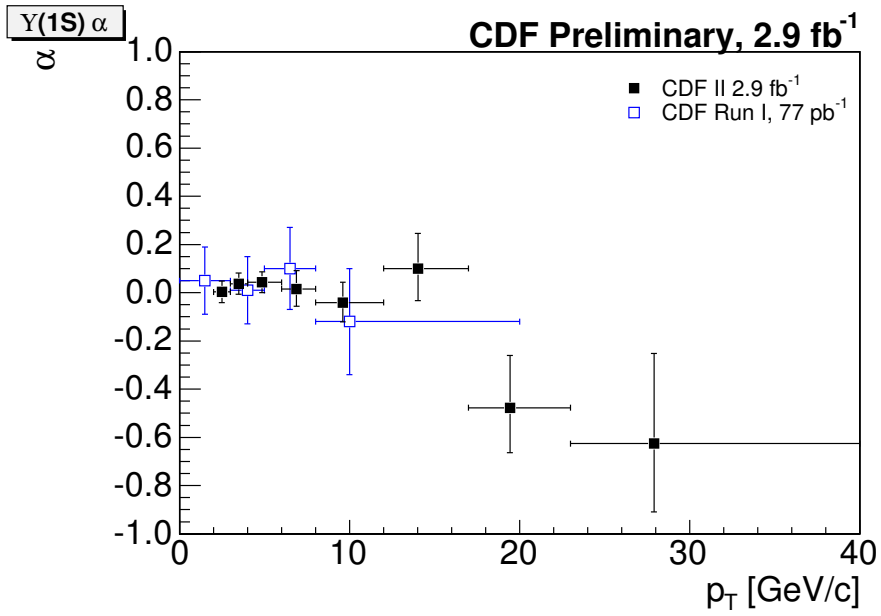

Figure 1.7: CDF II $\Upsilon(1S)$ polarization measurement result. The p_T-dependence of the polarization α is shown compared to the previous Run I measurement.

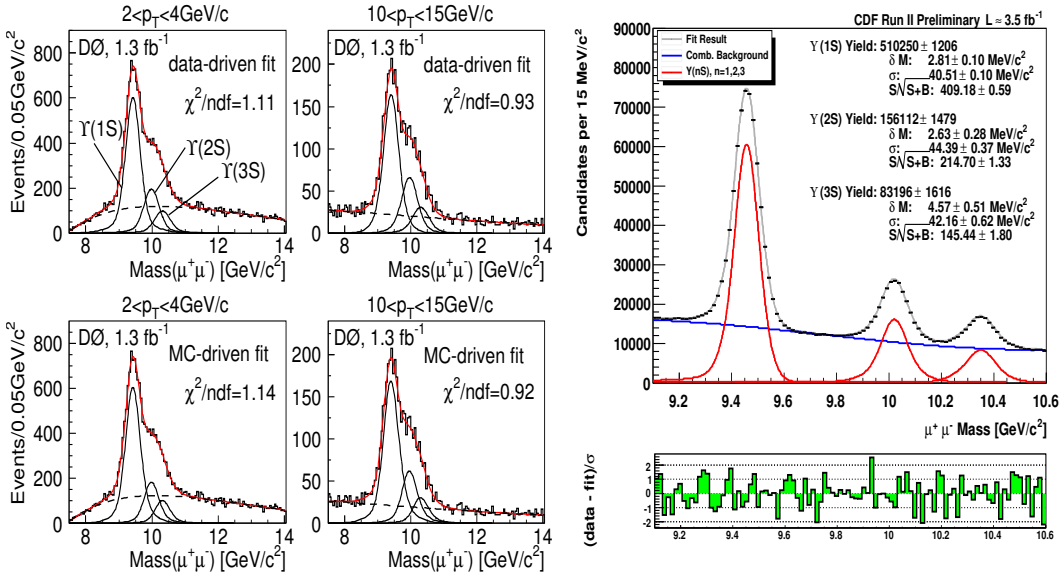

Figure 1.8: Observed invariant dimuon spectrum by the DØ experiment (left plot). The right plot shows the invariant mass spectrum from CDF II with clear and well separated signal peaks.

Chapter 2

The CDF II Experiment

Tracking and identification of tiny particles that are of interest for particle physicists, has to be performed with a particle detector which is able to identify protons, pions, kaons, photons and muons. The information obtained on a particle's propagation, energy, and electric charge help physicists to ascertain their identity. Furthermore, with this information it is possible to conclude back to the full decay chain of the finally detected particles. Such information is obtained by analyzing the data obtained from the particle detector.

For this analysis, the CDF II experiment provides such kind of information, which is referred to as 'measured data'. CDF is the abbreviation of 'Collider Detector at Fermilab' and II stands for the second running phase, which started in 2001. The experiment is hosted by the Fermi National Accelerator Laboratory, abbreviated as 'FNAL' and most commonly referred to as 'Fermilab'. Fermilab is a U.S. Department of Energy national laboratory. Figure 2.1 shows an aerial view of the main part of the Fermilab facility. The laboratory is specialized in high-energy particle physics and hosts multiple particle physics experiments. It is located in the United States, in Batavia, Illinois — 50 km west of Chicago.

2.1 The Tevatron

Physicists use high-energy accelerators to probe matter at the smallest scale. The challenge to produce such tiny particles which are not existing on our earth anymore, makes it necessary to collide high-energy particles, e.g. highly accelerated protons and antiprotons. According to Einstein, their energy can be used to create particles which were only existing some time shortly after the big bang. Fermilab hosts such a collider ring which is called Tevatron. It is a symmetric proton-antiproton collider that brings protons and antiprotons of the same energy to collision. Tevatron has been the accelerator with the highest available center-of-mass energy in the world since its start in 1995. Its successor will be the LHC — a proton-proton collider — with an even higher center-of-mass energy. Hence, the LHC will take over the position of the most powerful collider.

Figure 2.1: Aerial view of the accelerator complex at Fermilab. Tevatron itself is of course underground. However, the maintenance road in the middle of the picture, nicely indicates its course. Tevatron hosts two multipurpose detectors: CDF II and DØ.

During the first phase of operations from 1992 to 1996 — often referred to as 'Run I' — the center of mass energy of the proton-antiproton collisions was $\sqrt{s} = 1.8\,\text{TeV}$. The impressive high energy scale is responsible for the name of the accelerator ('TeV-atron'). The most outstanding measurement during Run I was the discovery of the top-quark in 1995. After upgrading the accelerator and detectors for five years, the second phase — referred to as 'Run II' — started in 2001 and is still ongoing. The Tevatron was upgraded to achieve a higher luminosity, as well as the center-of-mass energy of $\sqrt{s} = 1.96\,\text{TeV}$. Current plans are to stay in operation until the end of 2010, running longer might however still be possible and is under discussion.

2.1.1 The Accelerator Chain

The proton and antiproton acceleration are achieved in several steps. In figure 2.2, the accelerator complex is schematically shown. Fermilab uses a series of accelerators to create some of the world's most powerful particle beams. Starting with hydrogen gas, scientists create proton beams. They divert a portion of the proton beams to create antiprotons. Once they have accumulated enough antiprotons, they load them into the Tevatron, where they collide at the CDF II and DØ detectors with protons traveling in the opposite direction.

The acceleration chain starts with the production and pre-acceleration of negatively ionized hydrogen atoms in the Cockroft-Walton accelerator, where they reach an energy of 750 keV. In the Linear Accelerator ('Linac') they get speeded up to an energy of 400 MeV. The ions are then transferred into the 'Booster' which is a synchrotron of 75 m radius. At injection, the electrons of the negatively charged hydrogen atoms are passed through a carbon foil, which removes electrons from the hydrogen ions, creating protons. After further acceleration up to an energy of

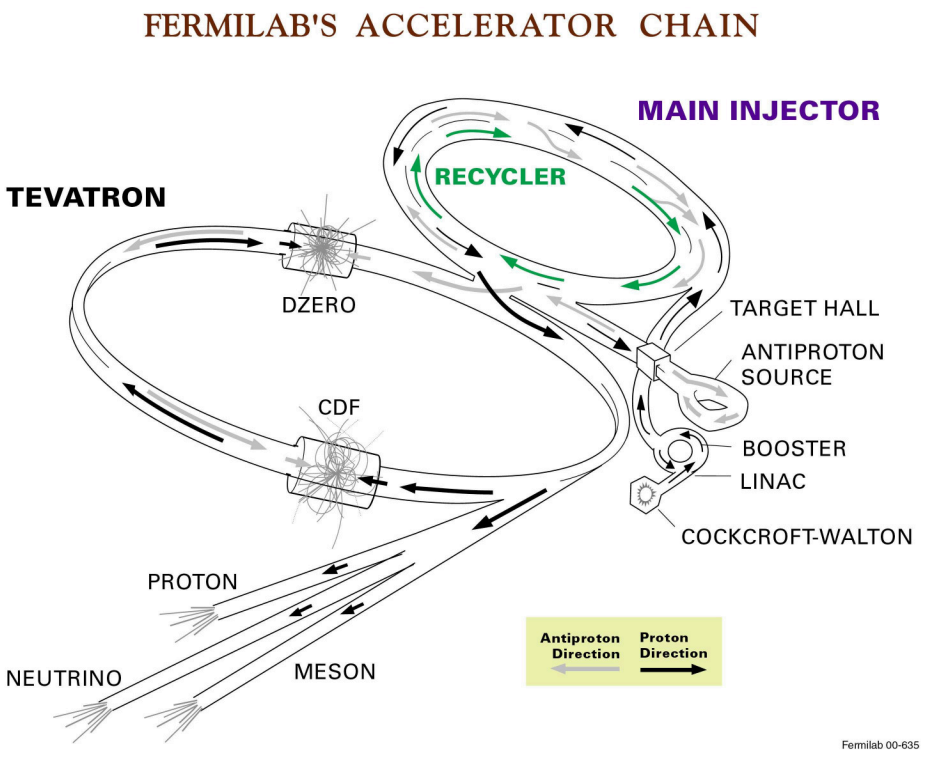

Figure 2.2: Schematic view of Tevatron's accelerator chain.

8 GeV, the protons get transferred to the 'Main Injector' which is again a circular synchrotron, however seven times larger than the Booster. The Main Injector has three functions that support the Tevatron Collider:

- Antiproton production — Protons are accelerated to an energy of 120 GeV and transfered to the antiproton source. There, the protons collide with a nickel target, producing a spray of random secondary particles including many antiprotons. From this spray, antiprotons with an energy of 8 GeV are selected and subsequently cooled in the 'Debuncher' and the 'Accumulator'. After accumulating a sufficient number of antiprotons, beam operators send them further to the 'Recycler'. This name does not reflect the role of this antiproton storage ring. While its original purpose was to gather and recycle antiprotons from $p\bar{p}$-collisions, it is now used to accumulate a large number of antiprotons before they are used for collisions. The process of antiproton production is often referred to as 'stacking'

- Acceleration — Protons and antiprotons are accelerated to an energy of 150GeV.

- Injection — Protons get injected as two bunches into the Tevatron. This is repeated 18 times, leading to 36 proton bunches. The similar procedure is applied for the antiprotons. Four bunches of antiprotons are injected from

the Recycler. This is repeated 9 times, resulting in a 36×36 bunch structure circulating in the Tevatron.

The final acceleration up to $E = 980\,\text{GeV}$ takes place in the Tevatron — an underground synchrotron with 6 km circumference. The Tevatron uses superconducting dipole magnets cooled in liquid helium at approximately 4 K, to keep the protons and antiprotons on track. Combinations of focussing and defocusing quadrupole magnets are responsible for the particle beam focusing.

Although, the Tevatron is responsible for the final acceleration, it primarily serves as a storage ring. This allows to remain in collision mode for a longer period of time. The time from filling the Tevatron until dumping the beam is referred to as a 'store'. At the beginning of a store it is necessary to clean the 'halo' of the beam because the particles from this halo usually do not take part in the collisions, but have a high probability to interact with the beam confinement material — potentially causing irreparable damage to sensitive detector parts.

The oppositely directed beams are brought to collision at two differently located interaction points along the Tevatron: B0, where the CDF II detector is located, and D0, which hosts the corresponding experiment. The whole procedure from loading protons to finally recording collisions, consists of the following steps:

- Loading protons from the Main Injector into the Tevatron ($\simeq$ 10 minutes).
- Loading antiprotons from the Main Injector into the Tevatron ($\simeq$ 45 minutes).
- Increase the beam energy to 980 GeV ('Ramping', $\simeq$ 1 minute).
- Start collisions by activating magnets, bringing the two separate beams to collision.
- Clean the beam environment ('Scraping', $\simeq$ 10 minutes).
- Power on detectors, record collisions continuously for about 16 hours.
- Dump the beam into absorber material and start over.

2.1.2 Luminosity

Luminosity is a quantity that describes the opacity of the target times the number of potential interactions per unit area per unit time. It represents the important value to characterize the performance of an accelerator.

For an intersecting storage ring collider the instantaneous luminosity $\mathcal{L}$ is given by

$$\mathcal{L} = n \cdot f \cdot \frac{N_p N_{\bar{p}}}{2\pi(\sigma_p^2 + \sigma_{\bar{p}}^2)} \cdot F.$$

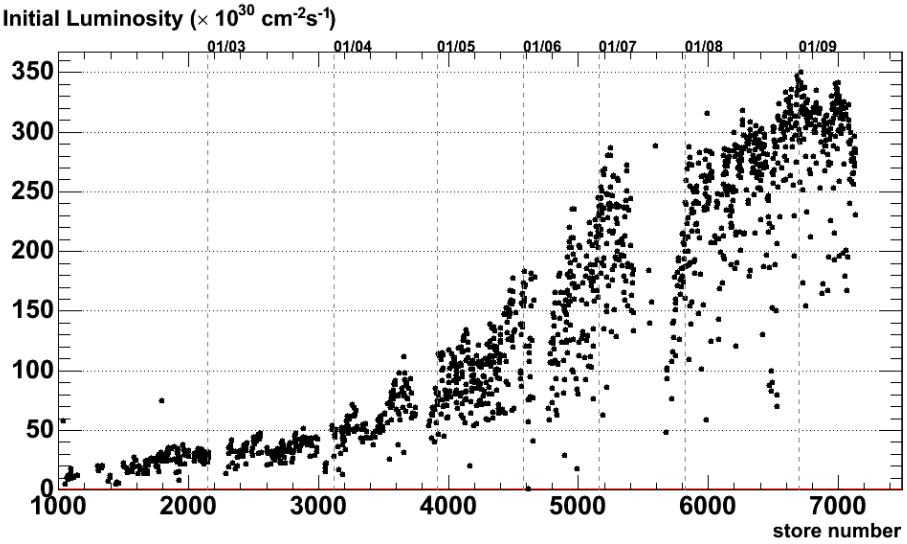

Figure 2.3: Initial luminosities over time for all stores in CDF Run II. The spread in luminosity is mainly due to the different quality of the antiproton beam, which is the limiting factor.

The quantity n is the number of bunches in one beam in the storage ring, f is the revolution frequency, and N_p ($N_{\bar{p}}$) is the number of protons (antiprotons) per bunch. σ_p ($\sigma_{\bar{p}}$) is the average transverse width of the proton (antiproton) bunch structure. Thus $2\pi(\sigma_p^2 + \sigma_{\bar{p}}^2)$ represents the cross section of the beam. F is a form factor efficiency because of the non-optimal bunch-structure, which is of the order of 70%.

The challenge of the Tevatron is to obtain a luminosity as high as possible because this results into more observable interactions at the experiments. The two important quantities connected to the number of observed interactions are the time-integrated luminosity,

$$\mathcal{L}_{int} = \int \mathcal{L}\, dt,$$

and the cross section σ of a certain physics process. The expected number of occurrences for a given process is

$$N = \sigma \cdot \mathcal{L}_{int}.$$

Usually, the unit of the cross section is 'picobarn' (pb), with 1 pb $= 10^{-12}$ b $= 10^{-36}\,\mathrm{cm}^2$. Thus, the time integrated luminosity has a dimension of inverse picobarn (pb^{-1}). The cross section for a certain process is a constant value, consequently the expected number of occurrences is directly proportional to the integrated luminosity. Since many processes of interest have very small cross sections, a high integrated luminosity is inevitable to observe a sufficient amount of events.

The time dependent instantaneous luminosity changes during a store. The luminosity at the beginning of the store is called the initial luminosity. During the store the luminosity drops roughly exponentially, since the amount of protons and an-

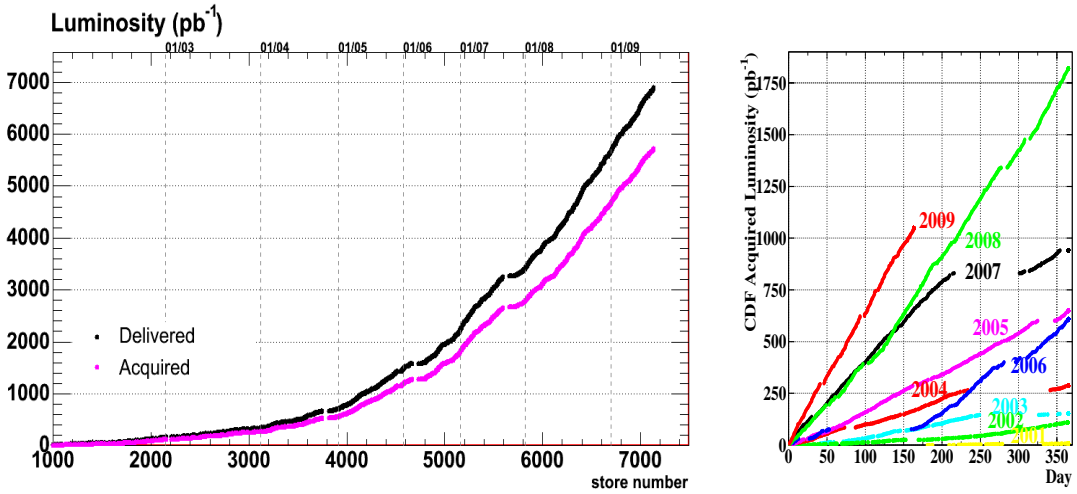

Figure 2.4: Evolution of the integrated luminosity over time for all stores in CDF Run II. The left plot shows both the delivered (black) and the acquired luminosity (magenta). The right plot shows the integrated luminosity for each year.

tiprotons is reduced at a rate proportional to their number. This decrease is caused due to collisions, losses and beam widening. After a certain amount of time it is more efficient to abort the store and start a new one, which is usually after about 16 hours. This is however also highly influenced by other operational conditions. The evolution of the initial luminosity at the CDF II interaction point over time for all stores is shown in figure 2.3. Over the course of time, the accelerator complex has become better understood and further improvements in the antiproton production has been achieved which are the reasons for the continuous rise in luminosity.

Essentially, one has to distinguish between the delivered luminosity of the Tevatron and the recorded luminosity of the experiment. Since due to technical reasons the CDF II detector is not recording data at 100% efficiency, the recorded luminosity is always lower than the Tevatron luminosity. Figure 2.4 shows the integrated luminosity for the CDF II experiment. The data taking efficiency is at a value of 80–90 %. Currently (August 2009) roughly 7 fb^{-1} have been delivered, out of which approximately 5.8 fb^{-1} have been recorded.

The CDF II instantaneous luminosity is determined with an 'Cerenkov luminosity counter' (CLC) [56] that is explained in section 2.2.5.

2.2 The CDF II Detector

The Collider Detector at Fermilab (CDF II) is a classical azimuthally and forward-backward symmetric multi-purpose detector [57–60]. Starting from the collision point in the center of the detector, it consists of a vertexing and tracking system, a particle identification system, a superconducting solenoid, the calorimeters and the

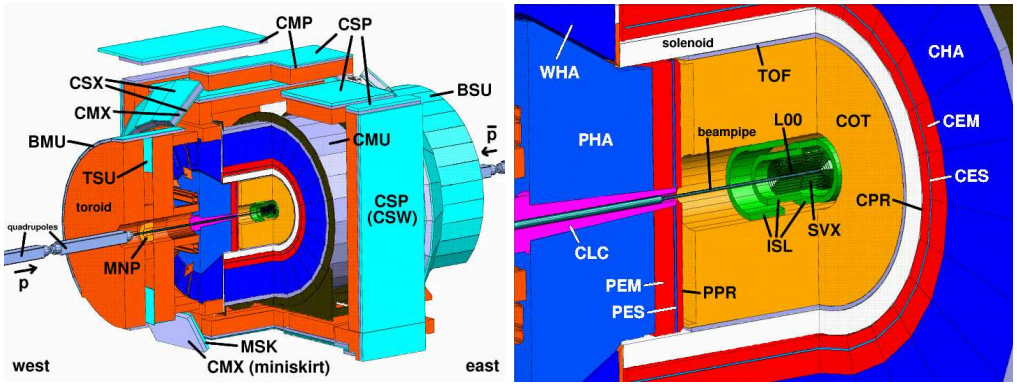

Figure 2.5: Cutaway view of the detector (left), that shows the whole detector. Only the muon systems are labelled, which make up the outermost layers of the detector. The right-hand side figure depicts a zoomed version and labels the calorimeter and tracking systems.

muon chambers. The layout of the detector in a cutaway and an elevation views are shown in figures 2.5 and 2.6.

The nominal particle interaction point is the origin of the coordinate system, which is used to describe the position of the detector components and hence the created particle's trajectories within the detector. The positive z axis is defined as the direction of proton travel, which is from west to east. The positive x-axis is defined as the direction towards the outside of the Tevatron ring, which is from south to north, and the direction of the y-axis is just bottom-up.

However, as the detector has cylindrical symmetry and collision events are basically spherical, it is more convenient to use a mixture of both with the coordinates r, ϕ and θ:

- r-coordinate — The radius r is used to denote the distance from the beam line.
- ϕ-coordinate — The azimuthal angle ϕ is measured from $\phi = 0$ towards the outside of the Tevatron ring.
- θ-coordinate — The polar angle θ is measured from the positive z-direction. Instead of the polar angle θ, one often uses the pseudorapidity $\eta = -\ln(\tan(\theta/2))$, because the production of relativistic particles with negligible mass is uniformly distributed over η.

2.2.1 Tracking System

The CDF II detector hosts a superconducting solenoid that generates a 1.4 T magnetic field parallel to the beam axis. Inside a magnetic field the bending of charged particles due to the Lorentz force is used to measured the particle's momentum.

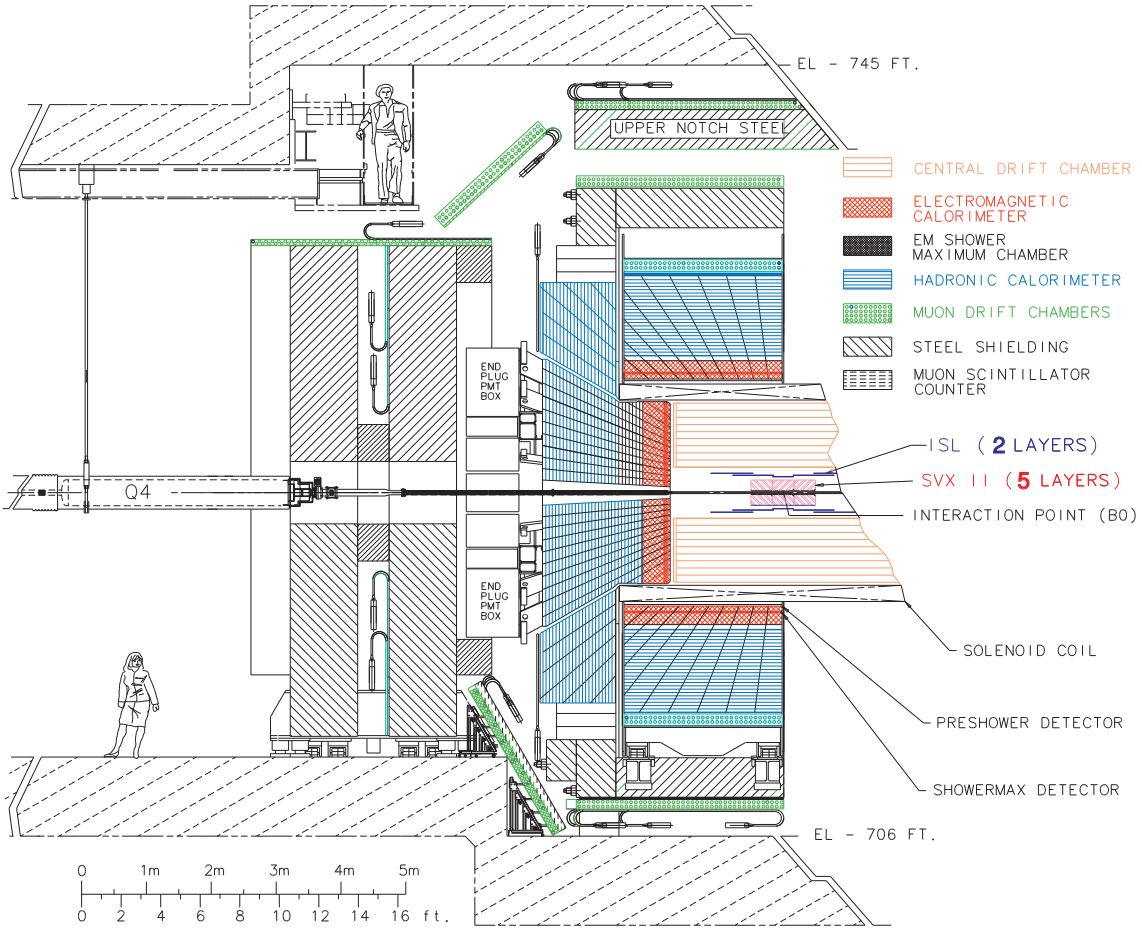

Figure 2.6: Elevation view of the CDF II detector.

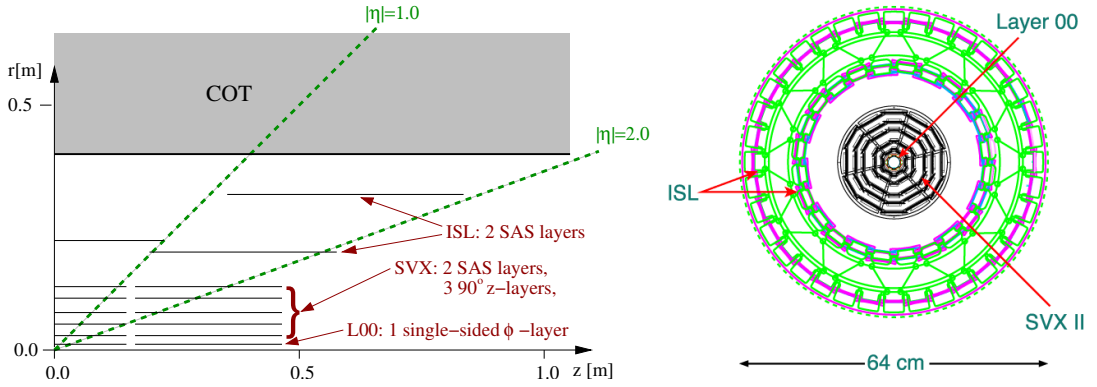

Figure 2.7: The left plot shows a schematic layer view of the silicon tracking system. The silicon microstrip detector is shown in the right-hand side plot.

Thus, the solenoid contains the tracking system which mainly consists of two subdetectors: The silicon system for precise spatial information near the interaction point and the drift chamber for good momentum resolution. Precise and efficient reconstruction of charged particles is an essential part of most analyzes studying b- or c-hadrons, e.g. to obtain a good momentum resolution, and a good signal separation from background. The left plot in figure 2.7 shows a sketch of the tracking system.

Silicon Detector

The CDF II silicon detector which is the innermost part of the tracking system, can be separated in three subsystems: 'Layer 00' (L00), the 'Silicon Vertex Detector' (SVX II), and the 'Intermediate Silicon Layers' (ISL). The right sketch in figure 2.7 shows an endview of the silicon detector which covers a radial range from 1.35 cm to 28 cm with an acceptance of $|\eta| < 2$.

- **L00** — L00 [61] is a silicon microstrip detector that adds one layer of single-sided $r-\phi$ measurements and is directly mounted onto the beam pipe. It was added during the upgrade for Run II. Its main purpose is the improvement of track measurements and taggin efficiency, but it also serves as insurance against the loss of the innermost SVX layer to radiation damage because the silicon used for L00 is less sensitive to radiation than that for the SVX. In order to avoid gaps in ϕ, the single silicon detector parts are arranged in two alternating layers, at radii $r = 1.35\,\text{cm}$ and $r = 1.62\,\text{cm}$.

- **SVX II** — This is the most important part of the silicon detector. The SVX II [62] is a double-sided silicon microstrip detector that delivers most of the silicon tracking information. Its main purpose is high-precision tracking which allows precise reconstruction of secondary vertices. The SVX II has five radially separated readout layers with Layer 0 at $r = 2.5\,\text{cm}$ and Layer 4 at

$r = 10.7\,\text{cm}$. It covers the z-range from $z = -43.5\,\text{cm}$ to $z = +43.5\,\text{cm}$, which corresponds to an acceptance of $|\eta| < 2.0$. All layers are double-sided. One side performs a measurement in the $r - \phi$ plane, while the other side provides information about the z-position. For the z-position measurement two different methods are used simultaneously. Layers 0, 1 and 3 use a 90° angle with respect to the beam axis ('stereo angle') to obtain a precise measurement. In contrast, Layers 2 and 4 use a small 1.2° stereo angle for the measurement to reduce hit combination ambiguities.

- **ISL** — The outermost part of the silicon detector are the layers of the ISL [63]. The main purpose of this double-sided silicon microstrip detector is to enhance linking of tracks between the SVX and the drift chamber. Furthermore, it also allows to perform a better tracking based only on silicon information, i.e. when no drift chamber information is available. ISL adds one extra double-sided layer at $r \approx 25\,\text{cm}$, which is divided into five overlapping 'barrels'. The central barrel at radius 22 cm covers the η range from -1 to $+1$, while the two forward and the two backward barrels with $1 < |\eta| < 21$ are located at radii of $r = 20\,\text{cm}$ and $r = 28\,\text{cm}$.

The silicon detector provides a very precise measurement of the track's impact parameter[a] and the ϕ coordinate which translates to an accurate 3-dimensional track reconstruction with a high spatial resolution.

Drift Chamber

The Central Outer Tracker (COT) [64] is a cylindrical open-cell drift chamber with an active volume from $r = 43.4\,\text{cm}$ to $r = 132.3\,\text{cm}$ with a length of 3.1 m, covering the central part of $|\eta| < 1$. The COT is located outside the silicon detector and its position is shown in figure 2.8. The drift chamber provides tracking for charged particles in the central region of the detector. Furthermore, it is able to provide a precise momentum measurement because of its large tracking volume.

The drift chamber is filled with a 50:50 mixture of argon and ethane. The COT has 96 layers of wire and altogether, 2530 cells. Each cell is a set of sense wires[b], collecting information, and potential wires, shaping the electrical field. The anode cells are separated by field panels, serving as the cathode. Due to the magnetic field, negatively charged electrons do not drift along the electrical field direction but obey the Lorenz force. To account for this, the cells are rotated by an angle ('Lorentz angle'), which for the COT at CDF II is 35°. The cells are divided into eight layers ('Superlayers'), out of which four are oriented parallel to the beam and are responsible for measurements in the $r - \phi$ plane ('axial layers'). The other four layers have a small stereo angle of 2°, providing information about the z-coordinate ('stereo layers').

[a] d_0 denotes the minimum distance of the reconstructed track to the primary vertex.
[b] An anode wire on which the avalanche of electrons is collected.

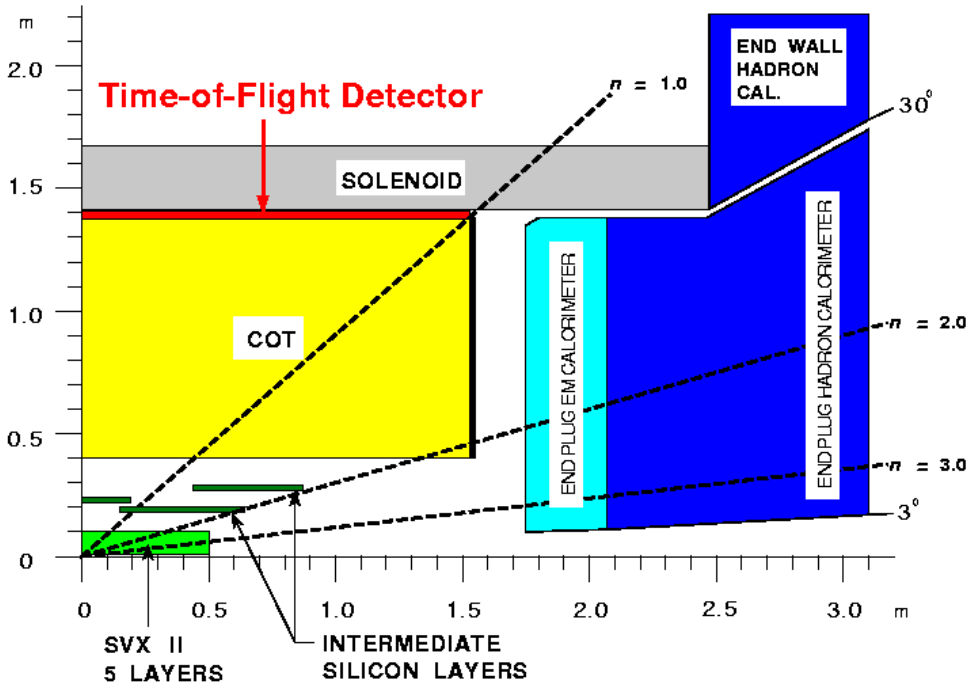

Figure 2.8: The CDF II tracking volume.

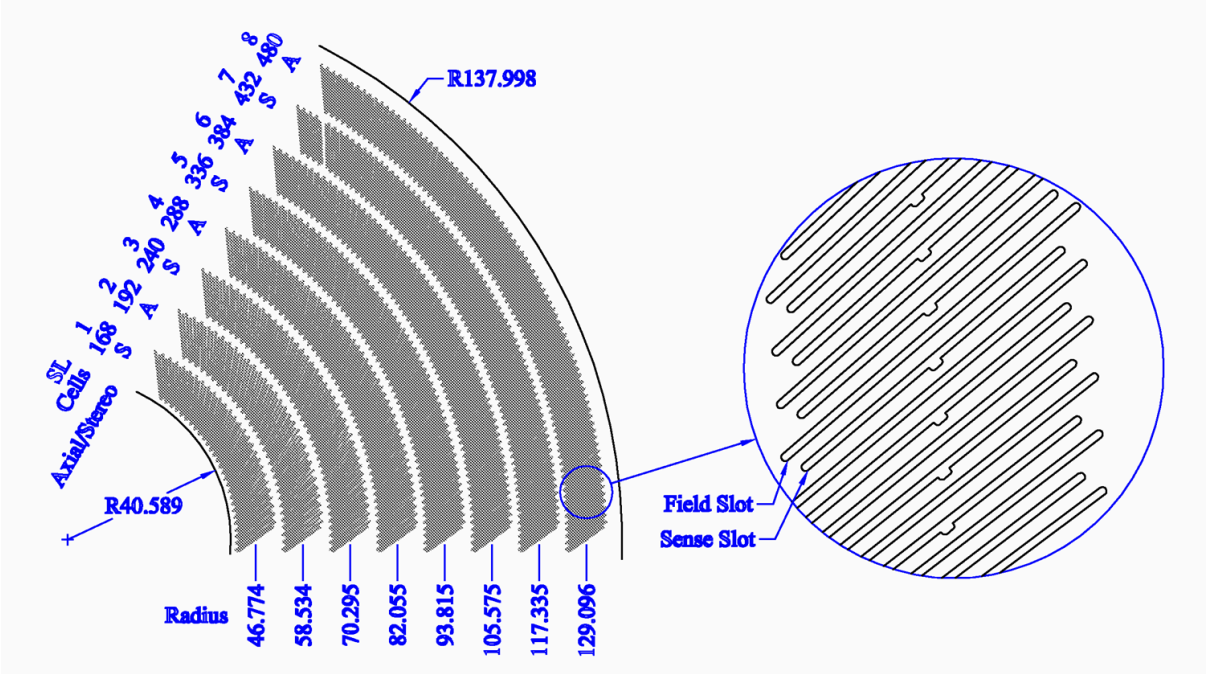

Figure 2.9: The COT cell layout. Eight superlayers are depicted, each with alternating order of field slots and sense slots, which are rotated by the Lorentz angle.

Figure 2.9 shows the cell layout of a part of the COT. The spatial resolution of the COT is of course much worse than that of the silicon detector. However, its large volume, the large number of hits, and a low track density, yield a high precision measurement of the transverse momentum in the $r-\phi$ plane, which translates to the very good momentum resolution of

$$\frac{\sigma(p_T)}{p_T} = 0.15\% \cdot p_T \frac{1}{\mathrm{GeV}/c}.$$

The identification of particles is improved by considering the particle's specific energy loss in the drift chamber. Charged particles ionize the gas mixture in the COT. The pulse width Δt on the readout chips is logarithmically proportional to the charge deposit Q, thus proportional to the ionization energy loss dE/dx:

$$\Delta t \propto \log Q \propto \frac{dE}{dx}$$

Figure 2.10 shows the separation provided by dE/dx. It reaches $\approx 1.4\,\sigma$ separation between charged kaons and charged pions for momenta greater than 2 GeV/c.

2.2.2 Time of Flight System

The 'Time of Flight' system (TOF) [65] is cylindrically located between the drift chamber and the cryostat of the super-conducting solenoid. It consists of 216 scintillator bars and photomultipliers, covering a range of $|\eta| < 1$. It measures the time t between the collision and the arrival of a particle at the scintillator, which can be combined with the momentum p and the path length L to determine the particle mass, and thus identifying the particle by

$$m = \frac{p}{c} \cdot \sqrt{\frac{(ct)^2}{L^2} - 1},$$

where p and L are measured by the tracking system. The time resolution of the TOF is about 100 ps, allowing most importantly separation of kaons from pions at low momenta. Their separation power based on their masses is at least two standard deviations for momenta smaller than $1.6\,\mathrm{GeV}/c$.

Figure 2.10 shows the time-of-flight difference between kaons and pions/protons and protons and pions. The average statistical separation in standard deviations is shown as well assuming a time-of-flight resolution of 100 ps. For comparison the separation provided by dE/dx is shown as well.

2.2.3 Calorimetry

The calorimeter system of CDF II [67–69] consists of two major systems: the electromagnetic and the hadronic calorimeter systems, which are designed to measure

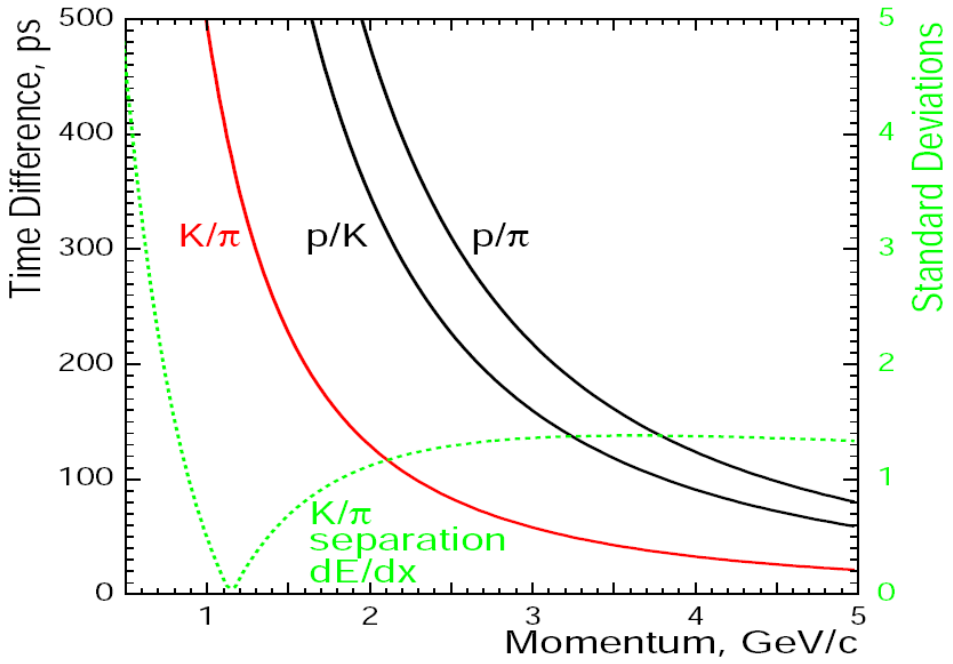

Figure 2.10: The time-of-flight difference (in ps) between kaons and pions/protons and protons and pions [66].

the energy deposit of electrons/positrons/photons and hadrons, respectively. All calorimeter systems are sampling calorimeters, meaning that they have alternating layers of active scintillator and absorber material. Both calorimeter systems are located outside the solenoid because they do not attempt to measure the curvature but the energy of the tracks. Table 2.1 lists the basic properties of the different calorimeter systems.

The hadronic calorimeter consists of the 'Central Hadron Calorimeter' (CHA), the 'Wall Hadron Calorimeter' (WHA), and the 'Plug Hadron Calorimeter' (PHA).

The electromagnetic calorimeter is composed of the 'Central Electromagnetic Calorimeter' (CEM) and the 'Plug Electromagnetic Calorimeter' (PEM). Both are supplemented with shower detectors ('Central/Plug Electromagnetic ShowerMax' chamber, CES/PES) to measure the location of the shower. The additional tracking information makes it possible to to identify electrons and photons, the transverse shower profile contributes to separate photons from neural pions, and the pulse height helps to identify electromagnetic showers.

Electromagnetic calorimeters are used to measure the energy deposit of particles that interact primarily via the electromagnetic interaction force. When a high-energy electron, positron or photon enters a material it initiates an electromagnetic shower. Thereby a cascade evolves, due to the alternating processes of pair production and the emittance of bremsstrahlung. This happens mainly in the absorber material. The scintillator plates then transform the energy-deposit of the particles that are

detector	η range	resolution	thickness
CEM	$\lvert\eta\rvert < 1.1$	$1.5\% \oplus 13.5\% \cdot f(E,\theta)$	$18\ X_0$
PEM	$1.1 < \lvert\eta\rvert < 3.64$	$1\% \oplus 16\% \cdot f(E,\theta)$	$23.2\ X_0$
CHA	$\lvert\eta\rvert < 0.9$	$3\% \oplus 50\% \cdot f(E,\theta)$	$4.7\ \lambda_0$
WHA	$0.9 < \lvert\eta\rvert < 1.3$	$4\% \oplus 75\% \cdot f(E,\theta)$	$4.7\ \lambda_0$
PHA	$1.3 < \lvert\eta\rvert < 3.64$	$5\% \oplus 80\% \cdot f(E,\theta)$	$7\ \lambda_0$

Table 2.1: Technical specifications of the CDF II calorimeter systems. The depth is given in radiation lengths X_0 and hadronic interaction lengths λ_0 [70]. The energy resolution is proportional to $f(E,\theta) = 1/\sqrt{E[\mathrm{GeV}]\sin\theta}$ with the transverse energy $E_T = E[\mathrm{GeV}]\sin\theta$.

sufficiently slow into light which is amplified by photomultipliers and then read out.

An hadronic shower is produced by a high-energy hadron such as a nucleon or a pion but also by an atomic nucleus. Due to their high mass it is unlikely that they produce bremsstrahlung since the radiation energy loss is proportional to the inverse squared mass m of the ionizing particle

$$\propto \frac{z^2}{m^2} \cdot E$$

where z denotes the charge and E the energy of the ionizing particle. In fact, they interact via the strong force with a nucleus and produce several lower-energy hadrons. This continues until all particles are stopped or absorbed in the material. Since the hadronic interaction length is much larger in case of the strong force, more absorber material is necessary. Consequently, the hadronic calorimeter is arranged behind the electromagnetic calorimeter and has a larger extent.

2.2.4 Muon Detection System

The muon detector system is placed at the outermost radius of the CDF II detector. Muons have a lifetime of about 2.2μs and decay due to the weak force. The mass of a muon is about 207 times the mass of an electron, thus their energy-loss due to Bremsstrahlung is much lower so that they can travel outside the detector. Muons have the highest probability of all long-lived particles to traverse the detector without being absorbed due to the fact that muons are minimal ionizing particles and that there is sufficient shielding within the detector which absorbs other long-lived particles like pions, kaons, and electrons, before they can reach the muon detector.

The main contribution to misidentified muons come from hadrons, either because they are high-energetic enough to punch through the shielding ('hadronic shower punchtrough') or because they decay into real muons which are not of interest for the studied process. Muons only leave small track segments in the muon system, which need to be matched to tracks from the COT. The muon system consists of several subdetectors which can also be seen figure 2.5:

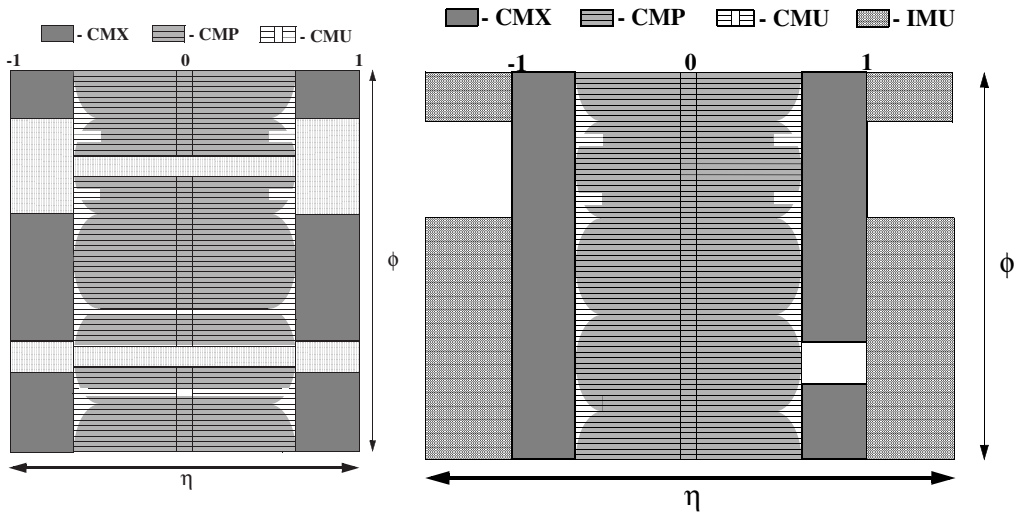

Figure 2.11: The $\eta - \phi$-coverage of the CDF muon systems for Run I (left) and Run II (right). In Run II the central part of $|\eta| < 1.0$ is completely covered, with a small exception on the eastern upper part.

	CMU	CMP	CMX	BMU
pseudorapidity coverage	$\|\eta\| < 0.6$	$\|\eta\| < 0.6$	$0.6 < \|\eta\| < 1.0$	$1.0 < \|\eta\| < 1.5$
minimum p_T [GeV/c]	1.4	2.0 – 2.2	1.4 – 1.8	2.1
maximum drift time [ns]	800	1400	1400	800

Table 2.2: Technical specifications of the CDF II muon systems.

- **CMU** — The 'Central Muon Detector' (CMU) [71] is a wire chamber and covers the central part of the detector with $|\eta| < 0.6$. The CMU does not have full coverage in the $\eta - \phi$ plane. It has gaps in ϕ because the sensitive part of the wedges only cover 12.6° out of 15°. The gap of $d = 18\,\text{cm}$ between the west and east half, which leads to the characteristic drop in acceptance for $\eta = 0$.

- **CMP** — The 'Central Muon Upgrade' (CMP) has the same $\eta - \phi$ coverage as the CMU. It consists of four layers of single-wire drift chambers. Due to the fact that the drift time can be much larger than the time between two interactions, the CMP additionally utilizes a set of scintillators ('Central Scintillator Upgrade', CSP/CSW) to provide timing information. Because of the different geometry compared to the CMU — the CMU has a shape of a rectangular box while the CMP has a cylindrical design — the CMP can partly cover for the gaps of the CMU in ϕ and z. The main purpose of the CMP however is the confirmation of muons in the CMU because the CMP is even further away from the interaction point and has an additional steel absorber shielding. As a result the rate of charged hadrons which are mistaken as muons is much smaller than that for the CMU. Together, the central muon system thus provides a very clean muon selection.

- **CMX** — The main purpose of the 'Central Muon Extension' (CMX) is to extend the coverage in $|\eta|$ from $|\eta| < 0.6$ to $|\eta| < 1.0$. It is composed of several structures. For Run I, only the easily accessible part in ϕ between collision hall floor and ceiling was covered. The bottom part had a gap of 90°, while the top part was missing 30°. Run II added structures for the remaining gaps, the so-called 'Keystone' for the western upper part[c] and the 'Miniskirt' for the bottom part, leading to almost full coverage in ϕ (see figure 2.11). The CMX uses the same drift chambers as the CMP, hence also requiring scintillators ('Central Scintillator Extension/CMX Miniskirt Scintillators' CSX/MSX) for timing information.

- **BMU** —The 'Barrel Muon Chambers' (BMU) even extend the coverage up to $|\eta| < 1.5$. The BMU drift chambers, which are of the same type as for the CMP and CMX, are installed on top of the steel toroids at both ends of the CDF II detector. Together with the scintillator systems named 'Barrel Scintillator Upgrade/Toroid Scintillator Upgrade' (BSU/TSU), the muon systems of BMU, BSU, and TSU are referred as the 'Intermediate Muon System' (IMU).

Table 2.2 summarizes the most important aspects of the different muon systems.

2.2.5 The Cerenkov Luminosity Counter

The CLC is located in the '3-degree holes' inside the endplug calorimeters in the forward and backward region which cover the $3.7 < |\eta| < 4.7$ pseudo-rapidity range. The CLC monitors the average number of inelastic $p\bar{p}$ interactions by measuring the number of particles, and their arrival time, in each bunch crossing. There are two ways to determine the luminosity.

The first method determines at which ratio the detector did not measure enough Cerenkov light signal, i.e. at which ratio a so-called 'empty bunch-crossing', a bunch-crossing without interaction took place. This rate can be used to calculate the average rate of interactions per bunch crossing μ based on the Poisson probability to get zero interactions which is $p = \exp(-\mu)$. The luminosity then can be derived as

$$\mathcal{L} = \frac{\mu\, f}{\sigma_{p\bar{p}}},$$

where f is the Tevatron bunch crossing rate and $\sigma_{p\bar{p}}$ is the $p\bar{p}$ cross-section.

The second method relates the measured number N_{meas} of actual hits in the CLC to the number that are expected for one interaction N_{exp}. The expected number must however be known from low luminosity measurements. The average rate of interactions per bunch crossing μ then simply is N_{meas}/N_{exp}. The accuracy of the luminosity measurement is about 6%.

[c] The corresponding section on the east side can not be used because it is occupied by solenoid cryogenics.

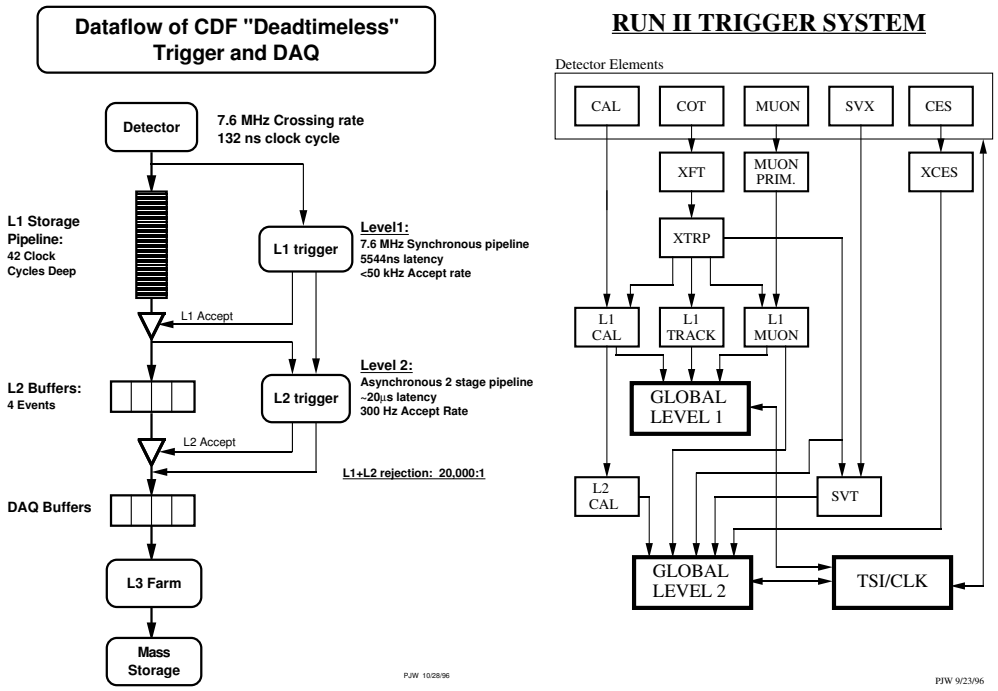

Figure 2.12: Schematics for the CDF II trigger system. The left figure shows the overall layout, while the right figure shows the information flow between the different trigger decision components.

2.2.6 Trigger System

The CDF II detector measures more information than can be processed and stored due to the large interaction rate. With approximately one interaction per bunch crossing and a rate of one crossing per 396 ns, effectively about 1.7 million events take place every second considering also empty bunches. With an estimate of about 200 kByte per detector event, this would equal a data rate of 500 GByte per second. The huge amount of data makes it impossible to collected every event. Thus physicist must select the processes they are interested in the most. Consequently, a system is required that intelligently selects the few interesting events from the huge number of events produced in every second. This is achieved by a three-level trigger system, that decides during operations which events are recorded for further analysis. Figure 2.12 shows an schematic view of the CDF II trigger data flow.

The three-level trigger system decides if an event is taken or rejected. Thereby, with increasing trigger-level the data rate decreases. Simultaneously, the available processing time and the complexity of the trigger decisions are rising. Since the trigger has to make its decisions very fast on Level-1 and Level-2, no full reconstruction of the whole detector event is possible, and the trigger has to rely on certain, quickly available quantities.

- **Level-1 trigger (L1)** — The Level-1 trigger, as the first processing unit, handles each detector event and performs decisions at a very large rate. On

average one out of 100 events is accepted, resulting in a Level-1 acceptance rate of about 25 kHz. At the Level-1 stage, three main data sources are considered: muon information, calorimeter information and tracking information from the 'extremely fast tracker' (XFT) [72], which uses COT information to get rough information about the track parameters: azimuthal angle ϕ and transverse momentum p_T. The 'extrapolator unit' (XTRP) can give additional information by matching XFT tracks to muon or calorimeter information.

- **Level-2 trigger (L2)** — Accepted events are passed on to Level-2, which has a buffer that can store 4 events. At the Level-2 stage, more time is available to process an event. More information can be processed. Most importantly for flavor physics, information from the silicon detector is used to identify events with a displaced secondary vertex. There is also enough time available to calculate more complex quantities, like the impact parameter d_0, which can be used to classify the event. If the Level-2 trigger accepts the event, which is about one out of 50, information of the whole detector is used to build an event and pass it on to the Level-3 trigger.

- **Level-3 trigger (L3)** — The input rate for the Level-3 trigger is about 500Hz. Level-3 collects all data fragments from the different detector parts and forms one single event with the so-called 'event builder'. If Level-3 accepts the event, which happens for about one out of five, it gets written on a mass storage device. The final rate is of the order of 100Hz. Level-3 finally is implemented as software on dedicated computers. The event is fully reconstructed, allowing for precise information that can be used for classification. Even complex decision processes can be realized, due to the implementation in software.

The more precise conditions for the three-level trigger are called trigger paths which can be quite different depending on the kind of analysis. In this thesis the so-called 'dimuon trigger' is used, where two reconstructed tracks are matched with hits in the muon chambers. The dimuon trigger selection for an integrated luminosity of about $360\,\mathrm{pb}^{-1}$ is shown in figure 2.13. The three resonances $\Upsilon(nS)$ with $n = 1, 2, 3$ can be seen immediately after passing the trigger requirements.

The final analysis uses the combination of CMU/CMU and CMU/CMX muons, depending on the part of the muon detector hit. Events are taken if Level 3 approves that the event is consistent with an Υ decaying into two muons.

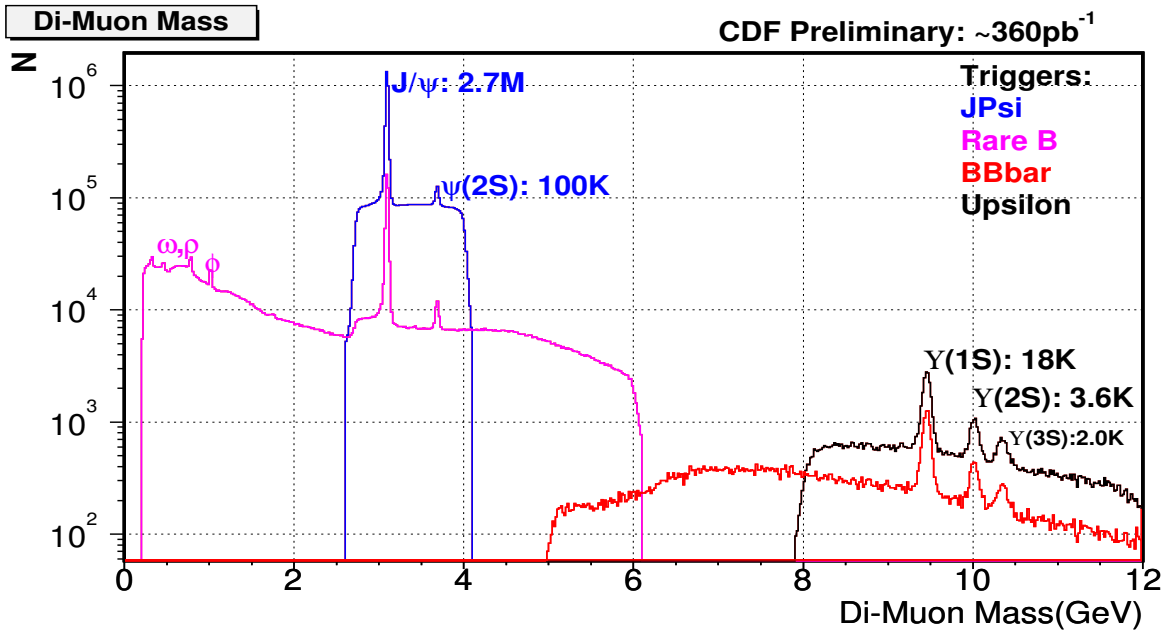

Figure 2.13: The CDF trigger systems consists of different dimuon triggers. This analysis uses the upsilon trigger (black). Although there is still a considerable amount of background, the Υ vector states below threshold are clearly visible already at trigger level.

Chapter 3

Statistical Methods

3.1 Neural Networks

The classification of measured data in signal and background candidates is requested in order to be able to study physical processes in particle physics. The aim is to remove many background candidates without losing signal at the same time. Thus, the quantities that need to be maximized are purity P and efficiency ϵ defined as

$$\text{Purity} \quad P = \frac{N_s(p_{NN} > p_{NN,cut})}{N_s(p_{NN} > p_{NN,cut}) + N_{bg}(p_{NN} > p_{NN,cut})}$$

$$\text{Efficiency} \quad \epsilon = \frac{N_s(p_{NN} > p_{NN,cut})}{N_s}$$

Purity represents the ratio between the amount of selected signal and all selected candidates, consisting of signal N_s and background N_{bg}. The selection requirements is $p_{NN} > p_{NN,cut}$ where p_{NN} denotes the signal probability and $p_{NN,cut}$ is the chosen required signal probability. Less background corresponds to a higher purity. Efficiency is a measure how many signal candidates from the full signal sample are rejected. The more signal is lost the less efficient is the selection.

Usually, for each candidate much information is available such as kinematic variables, decay angles, the vertex fit quality, and many more. The challenge is to find for each of these variables *simultaneously* the best selection requirements in order to maximize both quantities: purity and efficiency. This is no easy task as all these variables might be correlated. Neural network techniques are developed to handle such tasks.

3.1.1 Neural Network Topology

Neural networks consist of nodes grouped in multiple layers. Nodes are entities that receive a single value on their input and duplicate their value to their multiple outputs. They are thus linked together in a way depending on the network topology.

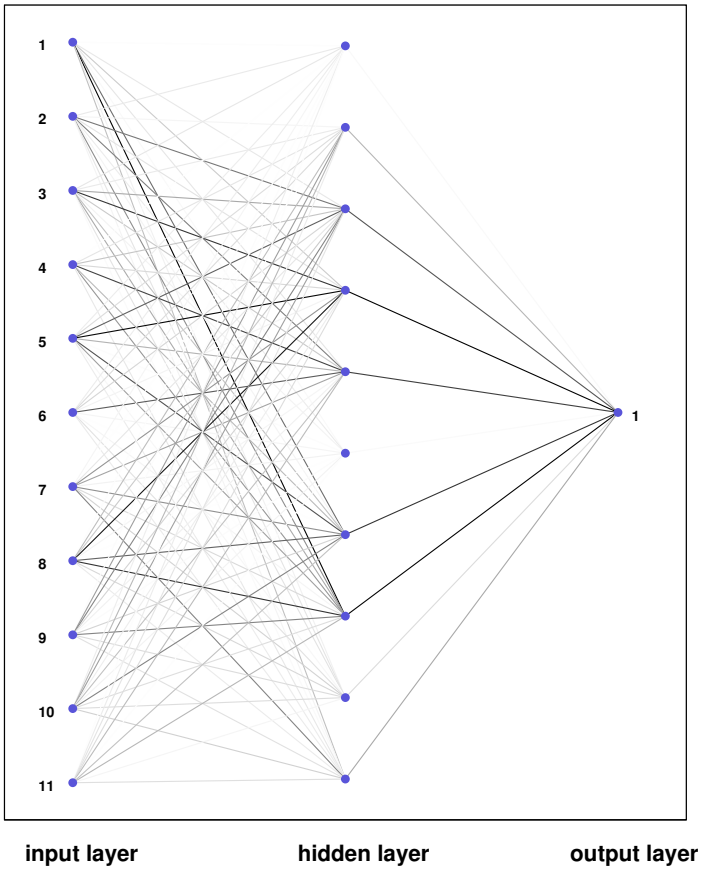

Figure 3.1: An exemplary three layer network.

In this analysis a three layer network is used which is exemplary shown in figure 3.1. It consists of the input layer, the intermediate layer and the output layer. Each layer consists of a set of nodes.

- **Input layer** — The input layer consists of a set of nodes fed by the input variables which can be kinematic quantities such as transverse momenta or decay angles but also other values which contain information to separate different classes, e.g. signal and background.
- **Intermediate layers** — Information about the correlation between the input variables becomes available due to intermediate layers. The connection between nodes is represented by weights. Zero weight corresponds to no connection and one corresponds to the fact that two input variables carry exactly the same information.

- **Final layer** — In this analysis the final layer is represented by one output node that estimates the probability to which class a input candidate belongs.

The information flow goes from the input layer via the intermediate layer to the output layer. Nodes in one layer are connected to the inputs of the nodes in the subsequent layer.

3.1.2 Neural Network Training

In case of the dimuon decay the measured data consists of combinatorial background and signal, namely the Υ resonances. Thus it is desireable to categorize each signal candidate into more 'signal-like' or more 'background-like'. Neural networks provide the likelihood for such a classification task.

Classified signal and background events serve as testing samples for the neural network training process. Thereby the neural network can 'learn' the discriminatory features of both classes.

The neural network training process identifies the difference between both testing samples. This is done by adjusting the weights that represent the connections between the variables. After each iteration the neural network can make an estimation for background or signal. As this information is available for the training samples it can readjust itself by comparing its prediction with the information to which sample the candidates really belong. The whole process is realized by minimizing an error function that represents a function of all weights between the nodes. It is of crucial importance to verify that the neural network does not learn the patterns of the training samples by heart which would lead to the fact that it would not be possible to provide a trustworthy estimation for similar but not identical patterns to the training samples.

3.1.3 Classification

After the training iterations the result is saved to a so-called expertise. Unclassified measured data can then be processed and for each candidate the probability p_{NN} for being signal is calculated based on the information obtained from the neural network training result.

Neural network techniques are a very nice tool to achieve two things: The selection is based on selection requirement on only one variable, namely the output probability and the correlations of all of the input variables are already considered. However, only with preprocessing of the input variables good results can be achieved. Therefore, it is necessary to use implementations that satisfy the challenge to obtain the best prediction probability. In this analysis the tool NeuroBayes® [73] is applied. It was developed at the university of Karlsruhe to handle common challenges in particle physics. Until today, it is applied successfully in many important CDF analyzes, e.g. the measurement of the $X(3872)$ mass [17]. Additionally to the task

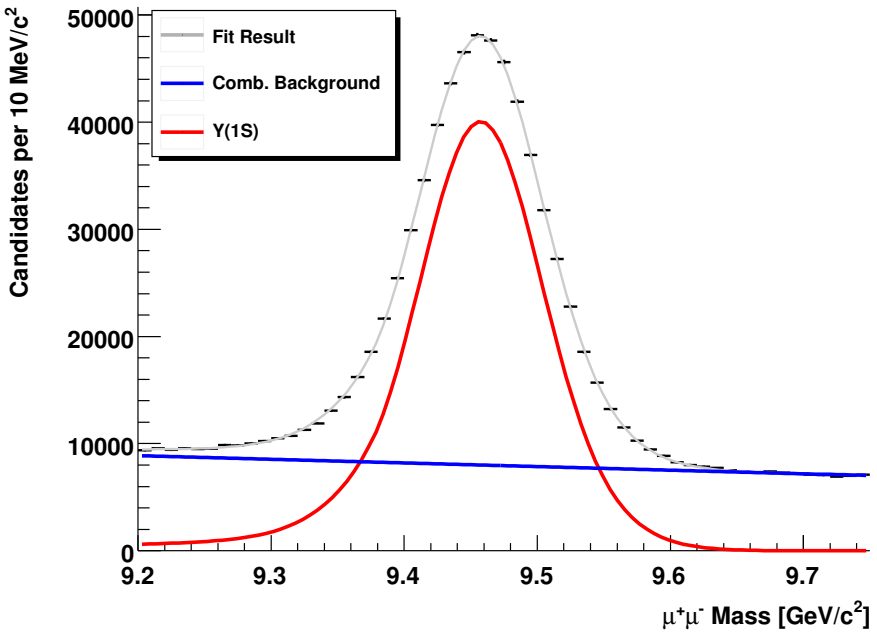

Figure 3.2: The dimuon spectrum and the fit result used to calculate the ${}_s$Plot weights. These weights are fed to the neural network to increase the discrimination power between signal and background.

of classification it also provides density functions as an output result. The very important feature of setting up an additional candidate weight during the training process makes it possible to readjust input patterns. This also provides the basis for a combination of a neural network training with so-called ${}_s$Plot weights which is described below.

3.1.4 ${}_s$Plot based Neural Network Training

A special feature of NeuroBayes® is the possibility to assign a weight to each candidate during the training process. This feature makes it possible to perform a training on unclassified measured data where signal resonances are visible already before the selection. The weights are constructed with the ${}_s$Plot formalism [74, 75].

The discrimination between signal and background can be obtained from a fit to the invariant mass spectrum consistent of a signal and background contribution. The fit result can be used to obtain the a priori probability for each candidate to be signal. Far away from the resonance this is certainly almost zero.

The dimuon invariant mass spectrum shown in figure 3.2 in the range between $9.2\,\mathrm{GeV/c^2}$ and $9.75\,\mathrm{GeV/c^2}$ consists of two kinds of candidates: combinatorial background and $\Upsilon(1S)$ signal. The two categories are simultaneously described by many variables in measured data. However, some variable distributions are known for each category separately as it is the case of the invariant mass $m_{\mu^+\mu^-}$ where obviously

the resonance peak can be seen. The distributions for signal and background are obtained by a fit described in section 5.2.2.1.

Quantities as the dimuon mass are called discriminating variables. They provide additional information to separate background and signal. In this case the dimuon invariant mass distribution takes the shape of the distributions belonging to signal and background into account. Other quantities have unknown distributions for signal and background, they represent the control variables one wants to study and separate in background and signal contribution.

The $_s$Plot weights for each signal (s) and background (bg) candidate respectively are calculated as

$$\begin{pmatrix} w_s(m) \\ w_{bg}(m) \end{pmatrix} = \frac{1}{f(m)} \cdot \mathbf{V} \cdot \begin{pmatrix} f_s(m) \\ f_{bg}(m) \end{pmatrix}$$

where $f_s(m)$ and $f_{bg}(m)$ are the probability density functions for signal and background which are obtained from the fit to the dimuon spectrum. The function $f(m)$ serves as a normalization factor defined as

$$f(m) = N_s \cdot f_s(m) + N_{bg} \cdot f_{bg}(m).$$

where N_s denotes the number of signal events and N_{bg} the number of background events, both extracted from the fit. The total number of candidates is $N = N_s + N_{bg}$. The quantity $\mathbf{V}$ is the covariance matrix of the signal and background probability density functions which is calculated as

$$\mathbf{V}^{-1}_{nj} = \sum_N \frac{f_n(m) \cdot f_j(m)}{f(m)^2}, \quad n, j = s, bg.$$

The determination of the weights requires a reasonable fit result of the discriminating variable m. By construction the sum of the signal and background weights of a certain event is one. However, the weights can be negative or larger than one. Each event is then entered into the neural network twice, once as signal and once as background with the corresponding weights.

The $_s$Plot method implies that the discriminating variables are uncorrelated from the control variables. Therefore, it is necessary to make sure that the neural network input variables are uncorrelated to the invariant dimuon mass.

3.2 The Binned Maximum Likelihood Method

Distributions are commonly represented in a histogram where the x-axis is divided into N bins which contains n_j candidates in bin j. The number of candidates inside a bin follows a Poisson distribution with the expectation value μ_j defined as

$$P(n_j|\mu_j) = \frac{\mu_j^{n_j} e^{-\mu_j}}{n_j!}.$$

The negative log likelihood function $\mathcal{L}(\vec{a})$ for a set of n independent measurements of the quantities $\vec{x}$, whose probability density function $f(\vec{x}|\vec{a})$ is known except for the parameter set $\vec{a}$ is

$$\mathcal{L}(\vec{a}) = -\sum_{i=1}^{n} \ln f(\vec{x_i}|\vec{a})$$

assuming statistically independent measurements. Considering candidates obtained from a histogram this leads to

$$\mathcal{L}(\vec{a}) = -\sum_{j=1}^{N} \ln\left(\frac{\mu^{n_j} e^{-\mu_j}}{n_j!}\right) = -\sum_{j=1}^{N} n_j \ln \mu_j + \sum_{j=1}^{N} \mu_j + \sum_{j=1}^{N} n_j!$$

For a given histogram the last term is constant and can thus be ignored. The highest probability is obtained by minimizing $\mathcal{L}(\vec{a})$.

In the limit of a large number of expected events μ the Poisson distribution can be approximated by a Gaussian distribution

$$P(n|\mu) = \frac{1}{\sqrt{2\pi}\sigma} e^{-\frac{(n-\mu)^2}{2\sigma^2}}$$

with the variance σ^2. In this case the negative log likelihood becomes

$$\mathcal{L}(\vec{a}) = -\sum_{j=1}^{N} \ln\left(\frac{1}{\sqrt{2\pi}\sigma_j} e^{-\frac{(n_j-\mu_j)^2}{2\sigma_j^2}}\right) = -\frac{1}{2}\sum_{j=1}^{N} \frac{(n_j-\mu_j)^2}{\sigma_j^2} + \text{constant.}$$

As a result, $2\mathcal{L}(\vec{a})$ follows a χ^2 distribution with $ndof$ degrees of freedom which corresponds to the difference between the number of bins N and the number of free parameters N_a in the likelihood function. The ratio $\chi^2/ndof$ is a figure of merit for the fit performance and should be approximately 1 if the probability density function $f(\vec{x}|\vec{a})$ describes the histogram distribution well.

3.3 Slicing Method and Sideband Subtraction

The 'slicing method' is a common way of extracting signal variable distributions. If a resonance is clearly visible and provides enough statistics it is possible to perform a fit to the invariant mass spectrum. The distribution e.g. of the transverse momentum of the $\Upsilon(1S)$ in the range between 0 GeV/c and 30 GeV/c is obtained by dividing the measured data samples into bins of $p_{T,\Upsilon}$ and extracting the signal contribution from a fit applied to each subsample. The obtained signal yield is then plotted over the transverse momentum of the $\Upsilon(1S)$ and represents the pure signal distribution in measured data for $p_{T,\Upsilon}$. This method is mostly used in this analysis to extract signal distributions from data.

Another common method is the 'sideband subtraction'. Two areas of the invariant mass spectrum are selected. The signal area contains signal as well as background.

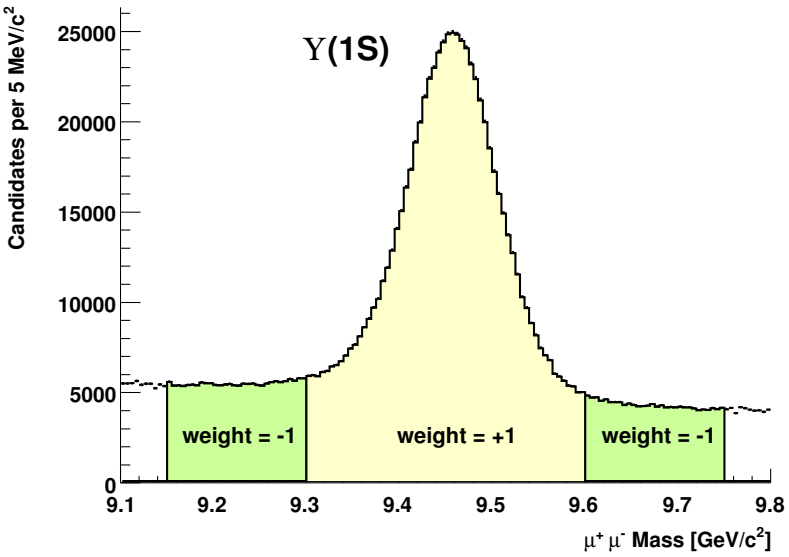

Figure 3.3: The areas for the sideband subtraction method are illustrated exemplary for the $\Upsilon(1S)$ invariant mass spectrum. The green area is defined as the sideband. The bright yellow area represents the signal region, which consists of signal and background.

The background only area consistent of pure background is usually taken from the left-hand side and from the right-hand side of the signal area. In case for the $\Upsilon(1S)$ resonance these areas are shown in figure 3.3. and are chosen such that the amount of background in the signal area is the same as the amount in the background area. Measured data of both areas enter a histogram but with different weights. Signal area candidates have weight $= 1$ and background area candidates have weight $= -1$. The idea is that the sideband distribution of a variable is subtracted from the distribution within the signal region and as a result only the signal distribution remains. In this analysis the sidebands belong to the ranges of $[9.15, 9.3]$ GeV/c^2 and $[9.6, 9.75]$ GeV/c^2. The signal range is within $[9.3, 9.6]$ GeV/c^2. The defined ranges are obtained by a fit to the spectrum, and chosen such that the areas below each region just cancel for the background contribution. This method is only used to extract a scatter plot distribution considering only the signal distribution.

Chapter 4

Monte Carlo Simulation

The simulation of signal patterns of which physicists are interested in, are of essential importance. They provide the possibility to compare measured data with predicted models. Moreover, due to detector simulation it is possible to obtain efficiencies and training patters to find suppressed signals in low-statistic measured data samples. Expectations for signal yields in measured data as well as resolution of the detector are also calculated based on information determined from the simulation.

4.1 Event Generation and Detector Acceptance

For the Υ polarization measurement, the simulated samples are generated with the standard CDF II full simulation software. Three high statistics samples are created for each $\Upsilon(nS) \rightarrow \mu^+\mu^-$, $(n = 1, 2, 3)$ decay, respectively. The generation process occurs in the following steps:

1. Values of transverse momentum for the $\Upsilon(nS)$ are generated according to a distribution obtained from measured data of roughly 2.4 fb^{-1}. The distribution parameterization that serves as an input distribution for the simulation is

$$\frac{d\sigma}{dp_T} \propto \frac{(p_T[\mathrm{GeV/c}])^{0.763}}{(6.819^2\ \mathrm{GeV}^2/c^2 + (p_T[\mathrm{GeV/c}])^2)^{2.857}}$$

   It is modelled in the p_T range from 0 GeV/c to 30 GeV/c. The comparison between the input p_T and the distribution of measured data is shown in figure 4.1. Acceptance leads to slight deviations between measured data and simulated candidates. Between the three resonance there is also a clear trend from $\Upsilon(1S)$ to $\Upsilon(3S)$ visible. Thus the polarization measurement is done in bins of p_T where the momentum distribution can be considered to be flat and unbiased of a possible polarization dependence.

2. The generation uses a world average mass $\bar{m}$ [9] for the generated Υ.

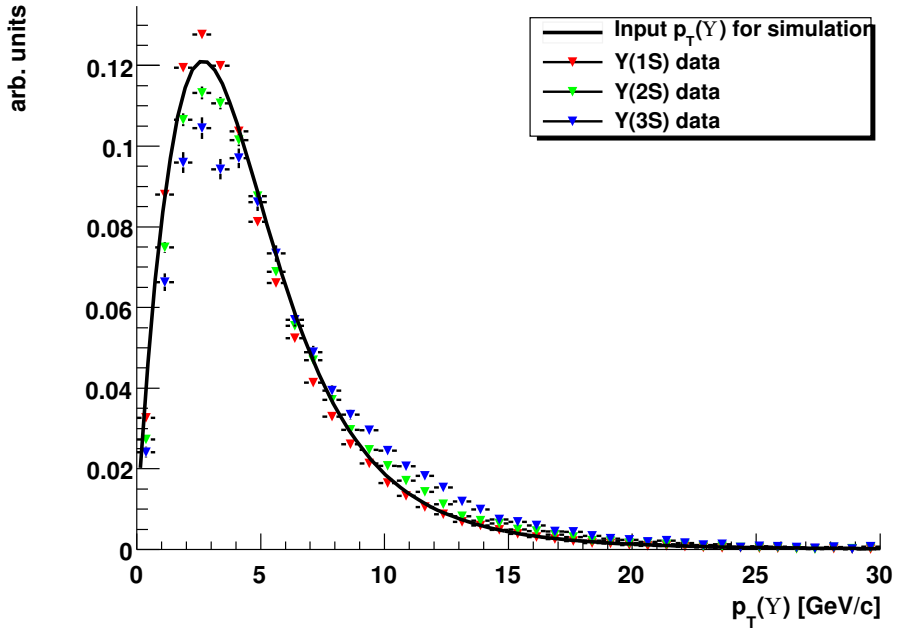

Figure 4.1: The acceptance corrected input transverse momentum function is compared to signal obtained from measured data with the slicing method.

3. Assuming an unpolarized production events are uniformly generated in rapidity $y = 1/2 \cdot \ln \frac{E+p_L}{E-p_L}$ where p_L is the component of the momentum along the beam direction.

4. The azimuthal angle ϕ is generated uniformly between 0 and 2π.

5. The `EvtGen` package [76] creates the decay into the final state. The decay is simulated as an unpolarized phase-space decay.

6. Simulated events are required to have $|\eta(\mu^{\pm})| < 1.5$ and $p_T(\mu^{\pm}) \geq 1.2$ GeV/c^2.

7. The CDF II detector response to the final particles is modelled by the full `GEANT` -based simulation of the CDF detector [77, 78].

8. The reconstruction process is applied in the same way as it is done for real measured events.

There are about 10 M $\Upsilon(1S)$ and $\Upsilon(2S)$ produced for each of them and about 20 M $\Upsilon(3S)$.

Each track has to pass some the following preselection criteria:

- Only opposite sign muons are selected.
- Tracks are taken from the central region of the detector, i.e. $|\eta_{\mu^{\pm}}| < 1$ and the average pseudorapidity of both muons is required to be smaller than 0.8.

- The reconstructed Υ-mass needs to be in the mass range $8.5\,\mathrm{GeV}/c^2 < m_{\mu\mu} < 11.5\ \mathrm{GeV}/c^2$. The uncertainty on the reconstructed mass has to be less than 70 MeV.
- The muon transverse momentum has to be larger than $1.8\ \mathrm{GeV}/c^2$.
- A pair of muon candidates is required to have a high vertex fit probability that corresponds to a χ^2 less than 60.
- To avoid hadrons misidentified as muons the minimum of the two muon likelihoods [79] need to be larger than 0.01 and the maximum has to be larger than 0.02.
- The impact parameter d_0 for both muons has to fullfill two requirements. The absolute value of the impact parameter significance d_0/σ_{d_0} is less than 9, and the minimum impact parameter significance of the two muons has to be less than 6.
- L_{xy} is the distance of the reconstructed decay vertex to the primary vertex in the x-y-plane and L_z is this distance in the z direction. Muon tracks are required to have $L_{xy} < 1$ cm and $L_z < 0.8$ cm. The absolute significance $|L_{xy}/\sigma_{L_{xy}}|$ where $\sigma_{L_{xy}}$ is the uncertainty of L_{xy} has to be less than 10.
- Z_0 is the z position of the primary vertex. The difference ΔZ_0 of both muons z position has to be less than 1.8 cm.

For the X_b search, the simulated sample candidates are generated with the standard CDF II full simulation software as it is done for the Υ's samples. However, in this case only one sample for a certain invariant mass $m_{\Upsilon(1S)\pi^+\pi^-} = m_{X_b}$ range is produced. The generation process occurs in the following steps:

1. Values of transverse momentum for the X_b are generated alike it is done for the Υ's in the polarization measurement. It is assumed that the X_b would also have the same distribution as the $\Upsilon(2S)$ in the same channel but due to the low statistics the dimuon channel is used to obtain the transverse momentum distribution.
2. The generation uses a full mass range instead of one mass position, for the generated X_b candidates that is $9.9\ \mathrm{GeV/c^2} \leq m_{X_b} \leq 11.3\ \mathrm{GeV/c^2}$.
3. Detector events are uniformly distributed in rapidity y_{X_b}.
4. The azimuthal angle ϕ is generated uniformly between 0 and 2π.
5. The `EvtGen` package [76] creates the decay into the final state. At this stage a phase-space decay is simulated. However, due to the three-body-decay with intermediate states it will be later necessary to reweight the candidates according to the quantum numbers J^{PC}.

6. Simulated events are required to have $|\eta_{Xb}| < 6$, $|\eta(\mu^{\pm})| < 1.5$ and $p_T(\mu^{\pm}) \geq 1.2$ GeV/c^2.

7. The CDF II detector response to the final particles is modelled by the full `GEANT` -based simulation of the CDF detector [77, 78].

8. The reconstruction process is applied in the same way as it is done for real measured events.

During the event generation the four-momenta of the decaying particle are deduced. There are about 500 M X_b candidates generated that corresponds to roughly 330 k candidates per MeV/c^2 due to the fact that they were produced flatly in mass.

They are additional selection requirements described in the following:

- The full selection criteria of the Υ polarization analysis is applied here as well except for the $_s$Plot based neural network selection.
- Only opposite sign muons and pions are selected.
- Pion tracks are required to have ≥ 10 COT hits and ≥ 2 SVX hits.
- Combined tracks are required to have a high vertex fit probability that corresponds to a $\chi^2_{X_b}$ of less than 55 for the X_b and $\chi^2_{\Upsilon(1S)}$ of less than 10 for the $\Upsilon(1S)$.
- The reconstructed X_b-mass needs to be in the mass range $9.9\,\mathrm{GeV}/c^2 \leq m_{X_b} \leq 11.2\,\mathrm{GeV}/c^2$.

Additionally, pion quality selection requirements are applied that are described below:

- The pion transverse momenta are required to have $p_{T,\pi^{\pm}} \geq 0.4$ GeV/c.
- Tracks are taken from the central region of the detector, i.e. $|\eta_{\pi^{\pm}}| < 1$.
- Both pions are required to lie in a cone around the X_b momentum vector with $\Delta R < 0.7$. $\Delta R = \sqrt{(\Delta\phi)^2 + (\Delta\eta)^2}$, here $\Delta\phi$ is the azimuthal angle and $\Delta\eta$ is the pseudorapidity of the pion with respect to the X_b candidate momentum vector.

Pions decay in a frame boosted relative to the detector frame. Thus they are distributed in a cone around the flight direction of the X_b. Cutting on the cone size ΔR is motivated by the fact that the pions are mostly distributed close the X_b in the $\eta - \phi$ plane because they do not obtain much kinetic energy compared to the momentum of the X_b in the laboratory frame. Their available kinetic energy for the considered invariant mass range can vary between 330 MeV/c^2 up to 1.74 GeV/c^2. For the $\Upsilon(2S)$ their available energy is around 560 MeV/c^2, in case of the $\Upsilon(3S)$ it is

around $900\,\mathrm{MeV/c^2}$ and for a hypothetical X_b mass of $10.604\,\mathrm{GeV/m^2}$ their available energy would be around $1.14\,\mathrm{GeV/c^2}$.

p_T requirements remove badly measured tracks. Only very few well-measured pions can reach the COT with a transverse momentum less then 0.4 GeV/c because of the detector geometry and magnetic field strength.

4.2 Simulation Verification

The comparison between signal in measured data and simulated candidates can only be done for the dimuon sample because in their invariant mass spectrum the three high statistical resonance are available. Simulated distributions can thus be compared to signal from data obtained by the slicing method described in section 3.3.

The simulations of the three Υ's are supposed to describe measured data. It is of crucial importance to take care that the Monte Carlo simulation really provides this information and does not describe distributions wrongly. Therefore there are three main simulation verifications necessary for this analysis:

- Comparison of the distributions for the different muons. There are CMU, CMP and CMX muons depending on in which muon chamber the muon is located. Therefore the first check is the comparison between the distributions of the different muon combinations.
- Comparsion of the p_T distribution between signal in data and simulated candidates.
- Comparison of neural network input variables. The neural network training requires well described signal patterns from the simulation. Thus, it is unavoidable to verify, that neural network input variables describe the Υ resonance good enough.

In the following comparisons only the high statistic $\Upsilon(1S)$ resonance is used to compare distributions with the corresponding simulation if not stated otherwise.

4.2.1 Comparison of CMU and CMX muons

Both muons can be categorized into two main samples. One containts only CMU muons ('CMU only'; $\approx 63\%$ of selected data), i.e. both muons are detected in the CMU subdetector. The second one consists of the combination that one muon comes from the CMU and the other one from the CMX subdetector ('CMU/CMX'; $\approx 33\%$ of selected data). The missing 4% contribute from other possible combinations which are removed from the final sample.

The categories had to be chosen like this because there is no CMP information available on the simulation. The $\eta - \phi$ distributions of the sideband subtracted measured

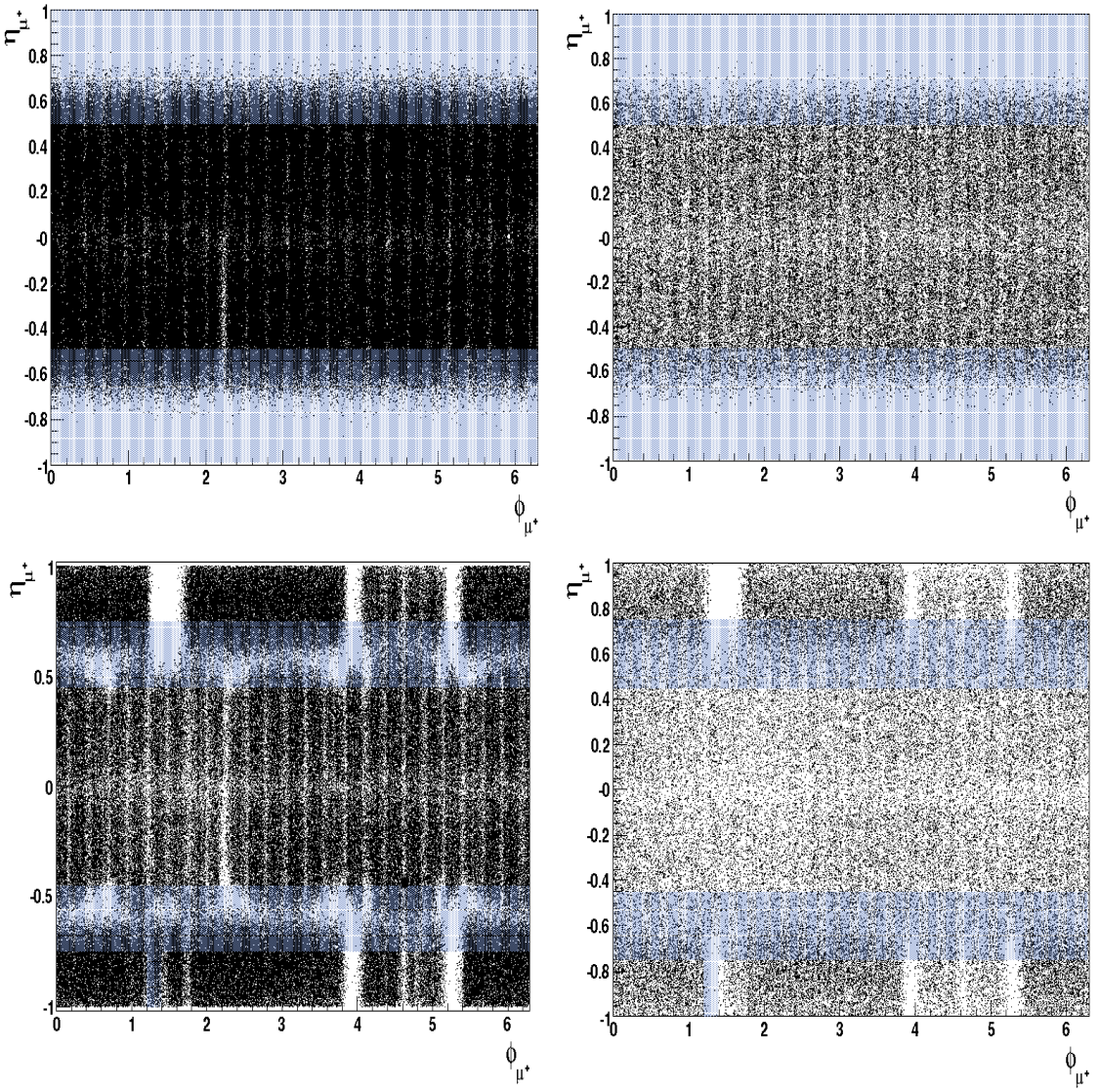

Figure 4.2: Qualitative $\eta - \phi_{\mu^+}$ comparison between data (left plots) and simulation (right plots). The upper row shows the distribution for only CMU muons. The lower row shows the plots for the combination of one CMU and one CMX muon. The blue shaded area is removed in the final selection.

data candidates and of the simulation for the $\Upsilon(1S)$ for each of the three samples are shown in figure 4.2. Measured data consists of signal as well as combinatorial background. By using the sideband substraction method described in section 3.3, combinatorial background is removed and measured data can be compared to the simulation.

In the first row of plots in figure 4.2 no obvious discrepancy is visible, however, the comparison of the η_{μ^+} distribution, described in the following, leads to the removal of the candidates within the shaded area. The middle row obviously shows a discrepancy which is due to the missing modelling of CMP muons. There is an additional mismatch in the simulated acceptance of the muons. In the region of $\eta_{\mu^\pm} < -0.6$ and $1.2 < \phi_{\mu^\pm} < 1.4$, there is a gap simulated which does not appear in measured data. The shaded areas are removed from the data sample due to their mismatch.

The muon η distribution comparison which is shown in figure 4.3 is based on the slicing method. Only for the combination of an CMU and an CMX muon there is a difference in the range $0.45 < |\eta_\mu| < 0.7$ visible. Obviously, the CMP shape shown in figure 2.11, is not well modelled in that region. The same occurs for μ^-, of course. The shaded area corresponds to regions which are removed in the final selection. Additionally, for the 'CMU only' muons a selection of $|\eta_\mu| < 0.5$ must be required due to the missing CMP modelling in the simulation.

The muon transverse momentum does also not fit well enough for low $p_{T,\mu^\pm}$ in both categories which can be seen in the left plots in figures 4.4, 4.5 and 4.6. Thus, for the 'CMU only' muons a selection of $p_{T,\mu^\pm} > 3\,\mathrm{GeV/c}$ and for the CMU/CMX combination a selection of $p_{T,\mu^\pm} > 4\,\mathrm{GeV/c}$ is required. The resulting $p_{T,\mu^\pm}$ distributions after reweight and all applied selection cuts is shown in the right plots of figures 4.4, 4.5 and 4.6. After all the applied cuts, the distribution of the simulated candidates matches measured signal in data better.

4.2.2 Comparison of the p_T Distribution

The measured $p_{T,\Upsilon}$ distribution is obtained from a fit in equal bins of $p_{T,\Upsilon}$ with fixed shape, width and mass. However, the resolution is rising with $p_{T,\Upsilon}$, thus the resolution is fixed to the value evaluated for the certain $p_{T,\Upsilon}$ bin in data according to the fitted functions shown in figure 4.7.

The obtained p_T distributions of data and simulation are shown in figure 4.8. In order to remove the remaining discrepancies the simulated events are reweighted such that both distributions match. As different trigger paths can have different Υ transverse momentum distributions the two categories of 'CMU only' muons and CMU/CMX combined muons are reweighted separately as well.

In order to correct the distributions a function is fitted to the ratio between measured data and simulated candidates with respect to $p_{T,\Upsilon}$. The ratio distribution, the parameterization and the resulting fit parameters are shown in figure 4.9. The finally reweighted Υ transverse momentum is compared after all selection cuts to

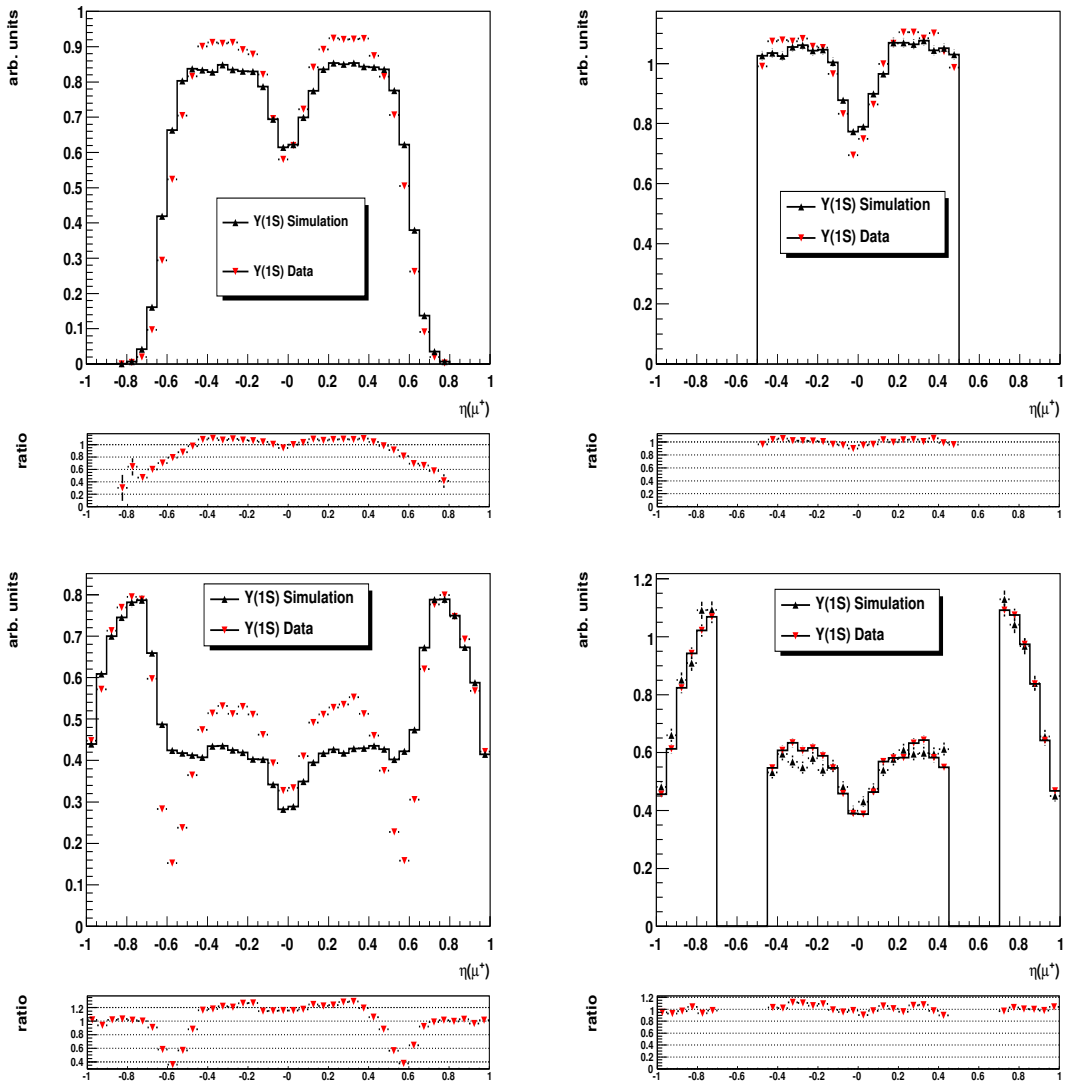

Figure 4.3: η_{μ^+} comparison between $\Upsilon(1S)$ data (red) and $\Upsilon(1S)$ simulation (black). The upper row shows the distribution for CMU only muons and the lower row for the combination of CMU/CMX muons. The left plots show the distribution without the $\eta(\mu)$ and $p_{T,\mu}$ selection while on the right plots the in the text described selection is applied.

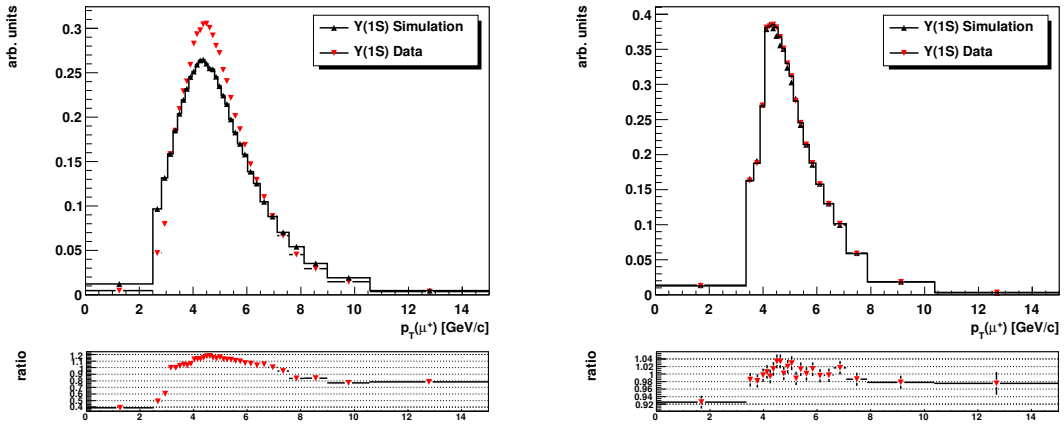

Figure 4.4: Comparison of the $p_T(\mu^+)$ distributions obtained from measured data and simulation after applied selection cuts for the full sample. The left plots shows the distribution without $p_T(\mu^+)$ selection requirements.

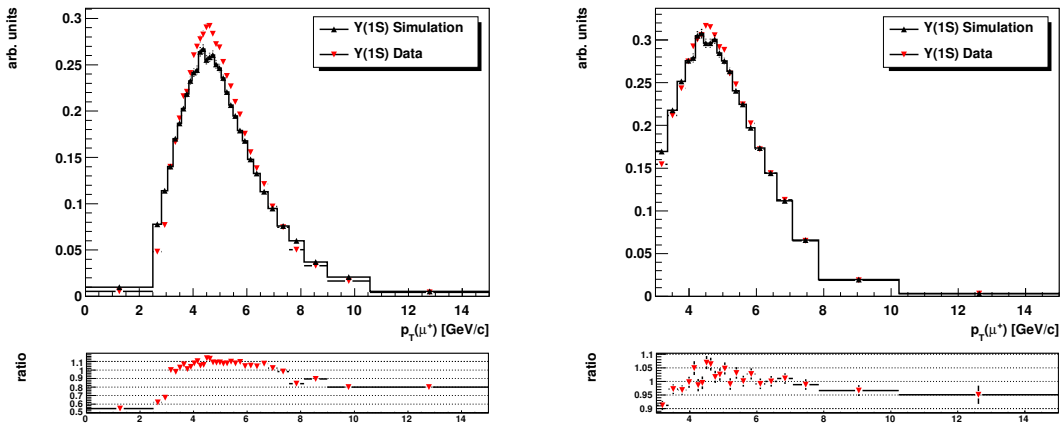

Figure 4.5: Comparison of the $p_T(\mu^+)$ distributions obtained from measured data and simulation after applied selection cuts for 'CMU only' muons. The left plots shows the distribution without $p_T(\mu^+)$ selection requirements. The right plot requires $p_{T,\mu^\pm} > 3\,\mathrm{GeV/c}$.

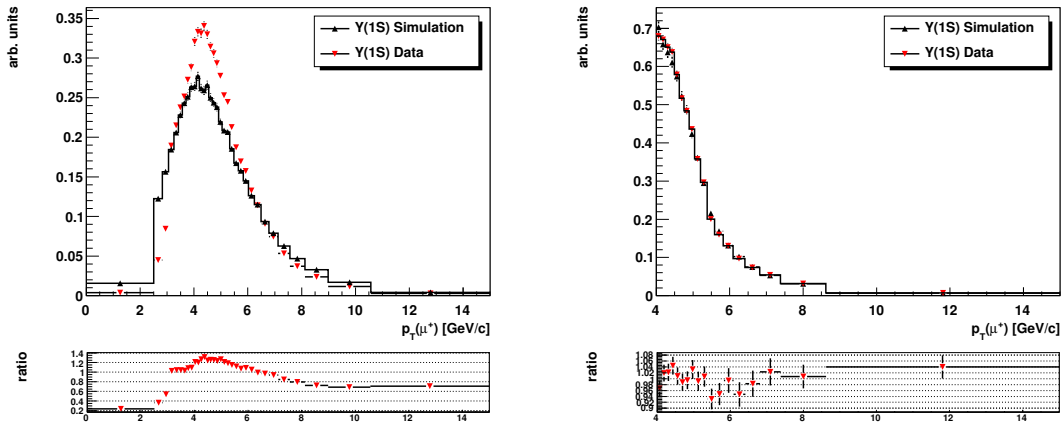

Figure 4.6: Comparison of the $p_T(\mu^+)$ distributions obtained from measured data and simulation after applied selection cuts for the CMU/CMX muons. The left plots shows the distribution without $p_T(\mu^+)$ selection requirements. The right plot requires $p_{T,\mu^\pm} > 4$ GeV/c.

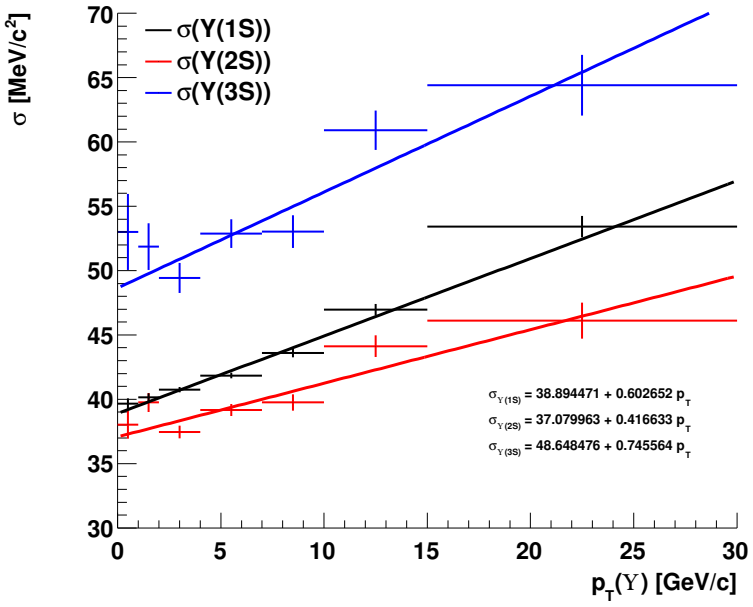

Figure 4.7: Resolution obtained from data with respect to $p_{T,\Upsilon}$. A linear function is fitted and used for the evaluation of $p_{T,\Upsilon}$ in measured data and the simulation. The result is used to obtain the correction weights w_p for the resulting simulated Υ transverse momentum.

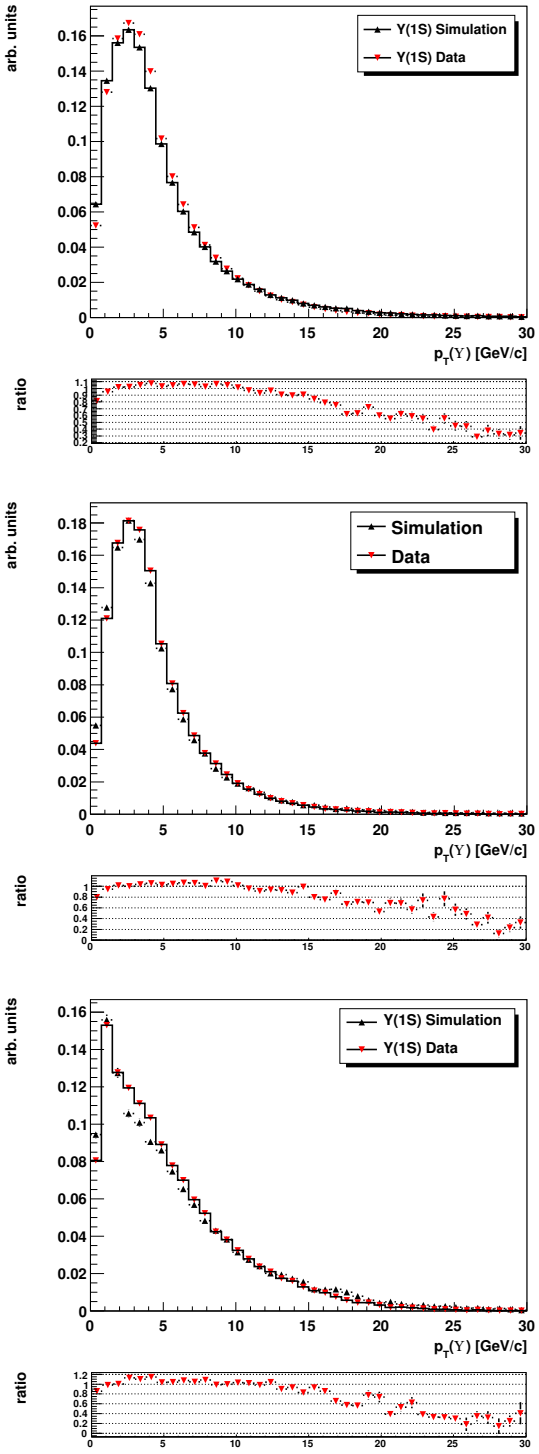

Figure 4.8: $p_{T,\Upsilon}$ distributions of measured data compared to simulation after all selection cuts. The left plot corresponds to the full sample, while the middle and right plot correspond to the CMU only and CMU/CMX muon combinations.

signal in measured data in figure 4.10. The reweight functions are also sufficient to describe the $\Upsilon(2S)$ and $\Upsilon(3S)$ states.

After the preselection and removal of the not good enough described muon pseudo-rapidity range, the p_T weights to correct the simulated distribution, are determined from the distributions of the $\Upsilon(1S)$. The reason is the highly available statistics for this state.

Simulated X_b candidates are reweighted with the same p_T weights obtained from the dimuon sample. However, in this case the p_T correction weight obtained from the full sample is used because the information about the muons if they are detected in the CMU or CMX detector is not available in a generated toy simulation necessary for the efficiency estimation.

4.2.3 Comparison of Input Variables

The comparison between signal in data and the simulation for several variables which will later serve as input variables for the neural network, is shown in figure 4.11. Of course, the same selection criteria as described above are applied to the simulation and measured data. The simulation is also reweighted according to correct the p_T distribution. The data distributions are obtained by fits in bins of equal amounts of simulated candidates. The mass and width are kept fixed in the fit. There are only slight differences visible. The muon likelihood seems to have some mismatch in the last bins. Anyhow, as a result it is found that the simulation describes the signal well enough providing as input pattern for the neural network training.

4.3 Dimuon Sample

4.3.1 Detector Resolution

The simulation provides the information about the detector resolution. For the $\Upsilon(nS), (n = 1, 2, 3)$ the invariant mass spectra after the final selection is shown in figure 4.12. Obviously, the combination of a Crystall Ball and a Gaussian function matches very good. Each resonance is thus described as

$$f_{\Upsilon(nS)}(m) = \mathrm{N}_{\Upsilon(nS)} \cdot [f_{\mathrm{norm}} \cdot CB(m) + (1 - f_{\mathrm{norm}}) \cdot G(m)]$$

and $\mathrm{N}_{\Upsilon(nS)}$ denotes the $\Upsilon(nS)$ signal yield and f_{norm} defines the proportion of the Crystal Ball function. The definition of the Crystal Ball function is

$$CB(m; \bar{m}, \sigma, \alpha, n) = \begin{cases} e^{-\frac{m-\bar{m}}{2\cdot\sigma^2}} & , \frac{m-\bar{m}}{\sigma} > -\alpha \\ A \cdot (B - (\frac{m-\bar{m}}{\sigma})^{-n}) & , \frac{m-\bar{m}}{\sigma} \leq -\alpha \end{cases}$$

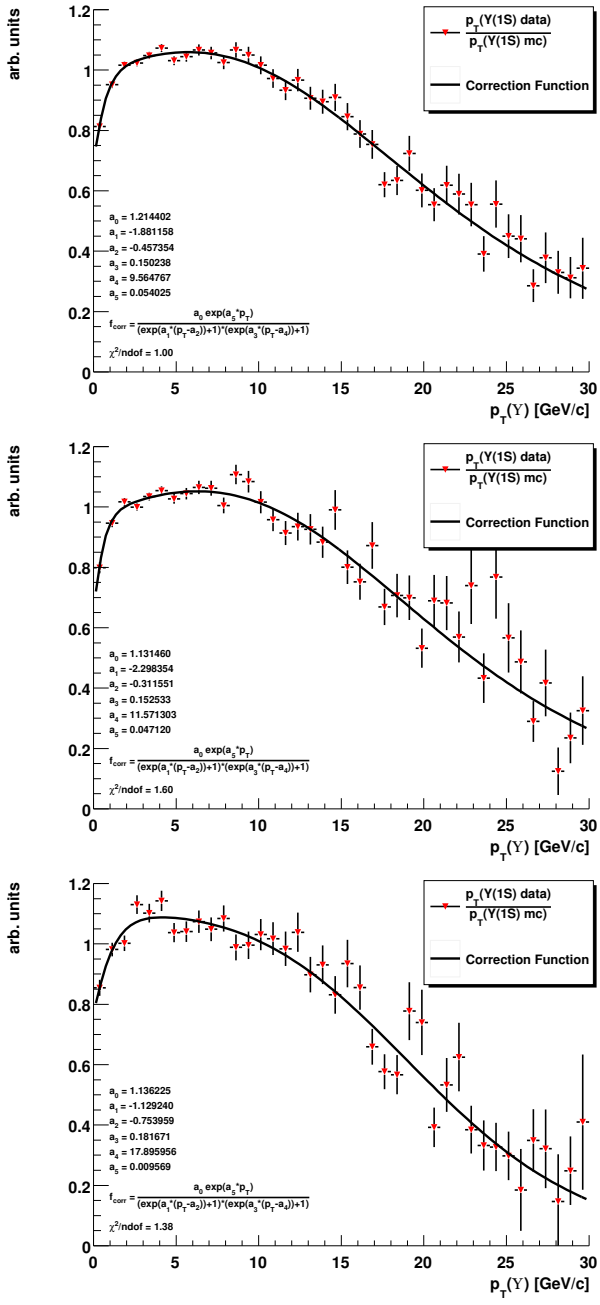

Figure 4.9: The applied correction function with respect to $p_{T,\Upsilon}$ is shown. Again, the middle and the right plot show the CMU only and CMU/CMX combinations, while the left plot is just the sum.

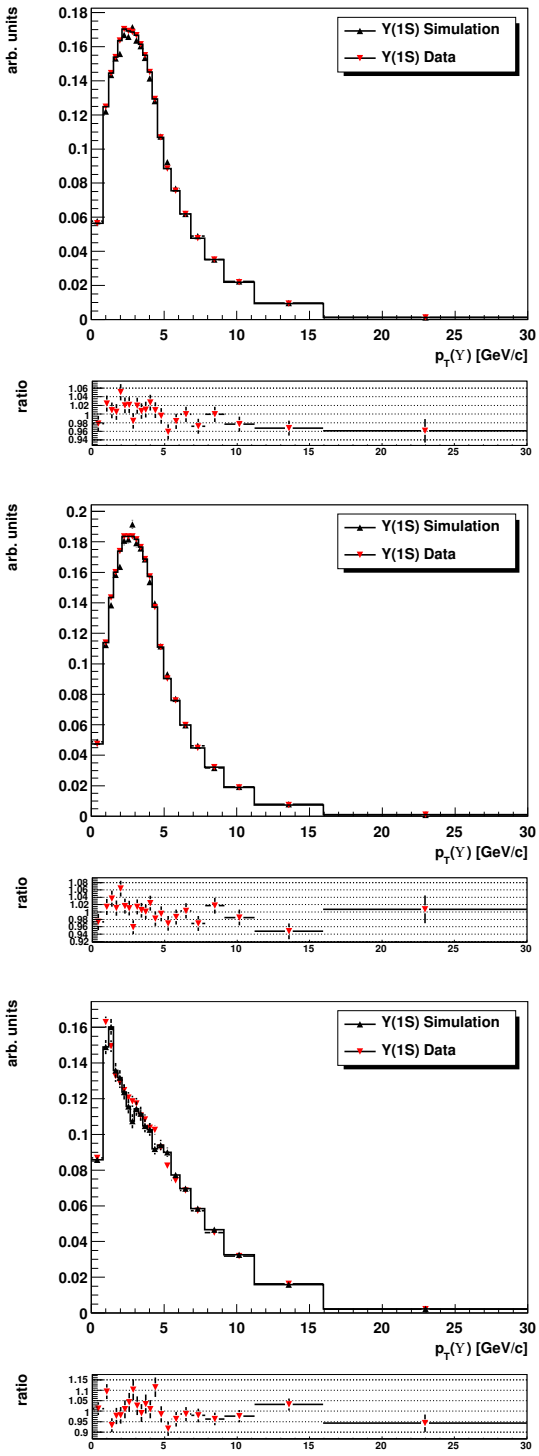

Figure 4.10: Measured data $p_{T,\Upsilon}$ distributions compared to simulation reweighted and after all selection cuts. The middle and the right plot show the CMU only and CMU/CMX combinations, while the left plot is just the sum.

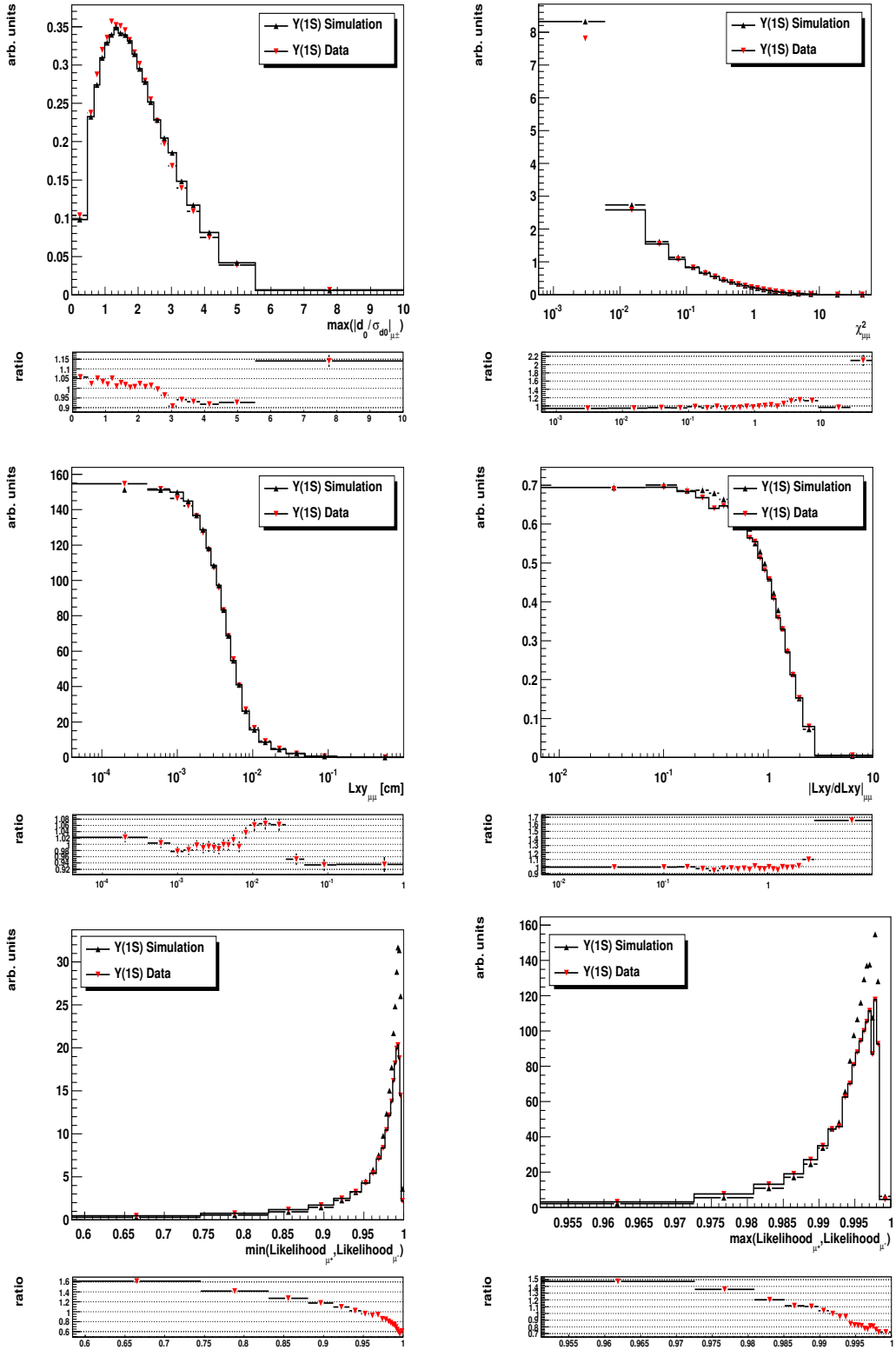

Figure 4.11: Comparison of the neural network input variables of simulated and measured $\Upsilon(1S)$ data.

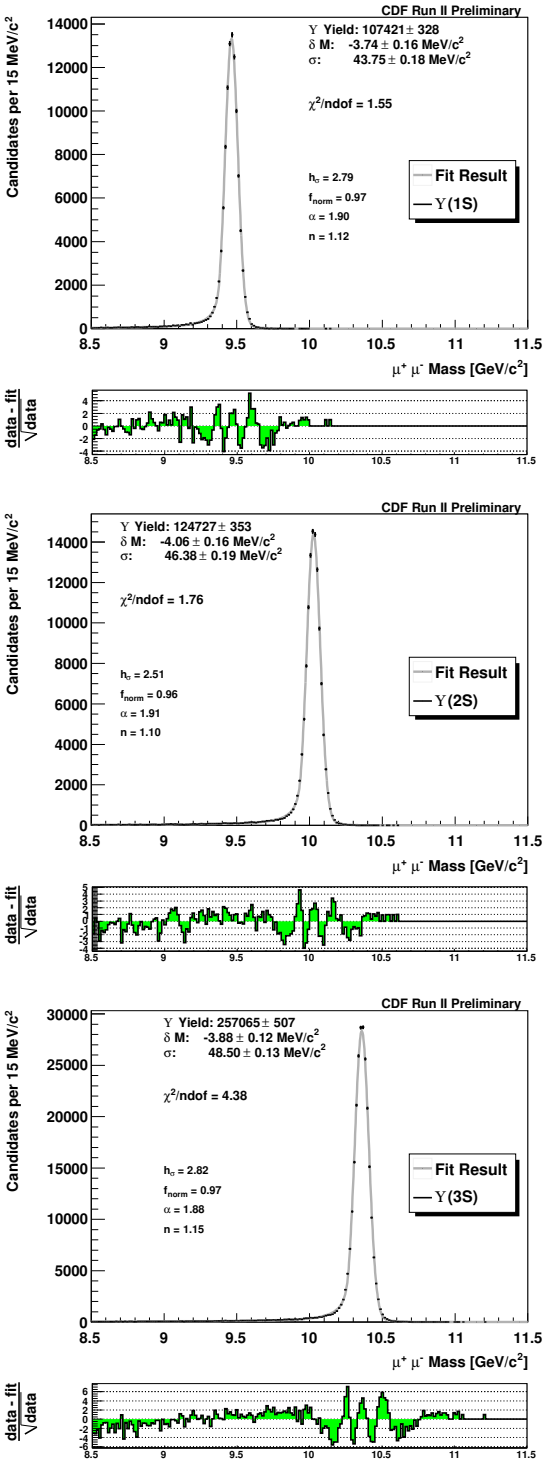

Figure 4.12: Dimuon invariant mass spectra from the simulation after all applied selection cuts.

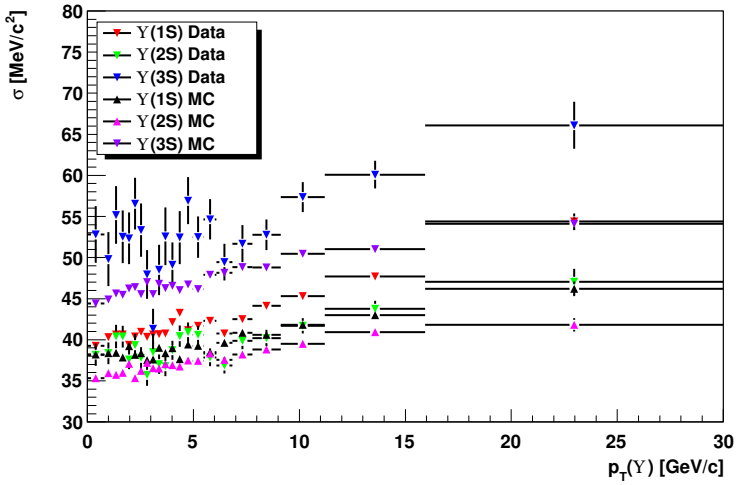

Figure 4.13: The resolution for the Υ states obtained from the final sample and after $p_{T,\Upsilon}$ reweight are compared between measured data and simulation.

and $\bar{m}$ denotes the mean mass value. The parameters A and B are given as

$$A = (\frac{n}{|\alpha|})^n \cdot e^{-\frac{|\alpha|^2}{2}},$$
$$B = \frac{n}{|\alpha|} - |\alpha|,$$

where α, n, σ and $\bar{m}$ are parameters which are fitted to data. The Gaussian function is described as

$$G(m; \bar{m}, \sigma_G) = \frac{1}{\sigma_G\sqrt{2\pi}} \cdot e^{-\frac{m-\bar{m}}{2\sigma_G^2}}$$

where $\sigma_G = h_\sigma \cdot \sigma$. The parameter σ denotes the width of the Crystal Ball function. Together both functions describe the detector resolution and the radiative tail of the Υ's which happens when the muons also radiate photons thus leading to a lower invariant mass because of the undetected low energy photons.

The resolution with respect to the Υ transverse momentum is shown in figure 4.13. This serves as a crosscheck that the tendency of the simulated resolution is consistent with signal from data. The simulated resolution is slightly underestimated, however for the polarization measurement the resolution obtained from a fit to measured data is used.

4.3.2 Efficiency

The efficiency of the dimuon Υ decay is of crucial importance for the X_b search analysis. Efficiency is the ratio between the finally selected simulated events and

selection stage	$\Upsilon(1S)$	$\Upsilon(2S)$	$\Upsilon(3S)$
produced	9.9	9.9	20
accepted	0.359 (3.6%)	0.345 (3.48%)	0.701 (3.5%)
+ after preselection	0.310 (3.13%)	0.327 (3.3%)	0.640 (3.2%)
+ ${}_s$Plot selection	0.307 (3.1%)	0.324 (3.27%)	0.635 (3.18%)
+ muon cuts (η/p_T)	0.107 (1.1%)	0.125 (1.3%)	0.259 (1.3%)

Table 4.1: List of simulated candidates (in M) at certain selection stages. These numbers of course hold for the unpolarized simulation. Considering polarization would lead to different efficiencies.

the produced events:

$$\epsilon = \frac{N(\text{accepted})}{N(\text{produced})}$$

The calculated efficiencies in per cent and for each selection stage are listed in table 4.1. Due to the fact that the simulation is produced unpolarized the resulting efficiencies will differ for different polarization assumptions.

Reweighting of simulated samples must be done very carefully. In case of the muons it is not easily possible to reweight for detector acceptance because efficiency would then become unknown due to the different missing overall normalization between trigger paths. However, a weight in order to correct the slightly different input transverse momentum compared to signal in data and a weight to consider the possible polarizations of the Υ can be used to reweight simulated candidates. The efficiency for reweighted simulated candidates is obtained by

$$\epsilon(\Upsilon(nS) \to \mu^+\mu^-) = \frac{N(\text{accepted})}{N(\text{produced})} = \frac{\sum_{i=1}^{N_{acc}} w_i}{\sum_{i=1}^{N_{prod}} w_i} = \frac{\sum_{i=1}^{N_{acc}} w_i}{N_{prod} \cdot \langle w \rangle}$$

where w denotes the weight according to $p_{T,\Upsilon}$ and polarization. In the case of weighted samples, instead to sum over accepted candidates it is summed over the weights for each signal candidate. N_{acc} refers to the accepted number of signal candidates. In the production stage the weights are also not considered thus the number of produced candidates N_{prod} has to be multiplied by the mean weight $\langle w \rangle$. In case of the Υ analysis the weight w is the product of the Υ transverse momentum weight w_p and the polarization weight w_α. w_p is chosen such that $\sum_{i=1}^{N_{acc}} w_{p,i} = N_{acc}$. Thus the mean weight $\langle w_p \rangle$ becomes one. Consequently, this weight does not need to be considered in the calculation because it does not change the produced and accepted candidates. This is not the case for the polarization weight w_α. The unpolarized simulation produces a flat $\cos(\theta^*)$ distribution before considering detector acceptance. Polarized $\cos(\theta^*)$ distributions before considering acceptance follow a shape

proportional to the weight

$$w_\alpha = 1 + \alpha \cdot \cos^2(\theta^*)$$

Thus the efficiency can be calculated as

$$\epsilon(\Upsilon(nS) \to \mu^+\mu^-) = \frac{\sum_{i=1}^{N_{acc}}(1 + \alpha \cos^2 \theta_i^*)}{N_{prod} \cdot \langle(1 + \alpha \cos^2 \theta^*)\rangle}$$

Usually, in order to obtain the mean weight, it is necessary to produce a 'toy simulation' which does not account for the detector acceptance. This simulation can be reweighted and the mean weight calculated. However, in case of the polarization the mean weight w_α can be obtained analytically as

$$\langle w_p(x)\rangle = \langle(1 + \alpha \cos^2 \theta^*)\rangle = \frac{1}{N_{prod}} \cdot \sum_{i=1}^{N_{prod}}(1 + \alpha \cos^2 \theta_i^*) = \frac{1}{\Delta x} \cdot \int_{-1}^{1}(1 + \alpha x^2)dx = 1 + \frac{1}{3}\alpha.$$

Efficiencies, calculated according to

$$\epsilon(\Upsilon(nS) \to \mu^+\mu^-) = \frac{\sum_{i=1}^{N_{acc}}(1 + \alpha \cos^2 \theta_i^*)}{N_{prod} \cdot (1 + \frac{1}{3}\alpha)}$$

for five different polarizations for the final selection and are listed in table 4.2. The calculated efficiencies are only slightly different for both frames. In figure 4.14 the efficiencies with respect to the transverse momentum of the Υ states for the final selection are shown. Different curves correspond to different assumed polarization in the corresponding frame.

4.4 X_b Sample

4.4.1 Detector Resolution

The fit model of the resonances in the final state $\Upsilon(1S)\pi^+\pi^-$ are obtained from the simulation as well. The three states, X_b, $\Upsilon(2S)$ and $\Upsilon(3S)$, have different quantum numbers J^{PC} and are thus accordingly reweighted. The weights are derived as described later in section 6.1. The simulation study shows that a double Gaussian function $f_{X_b}(m)$ describes the resonance best which is exemplary shown in figure 4.15. Each resonance is thus described as

$$f_{X_b}(m) = \mathrm{N}_{X_b} \cdot [f_{\mathrm{norm}} \cdot G_1(m) + (1 - f_{\mathrm{norm}}) \cdot G_2(m)]$$

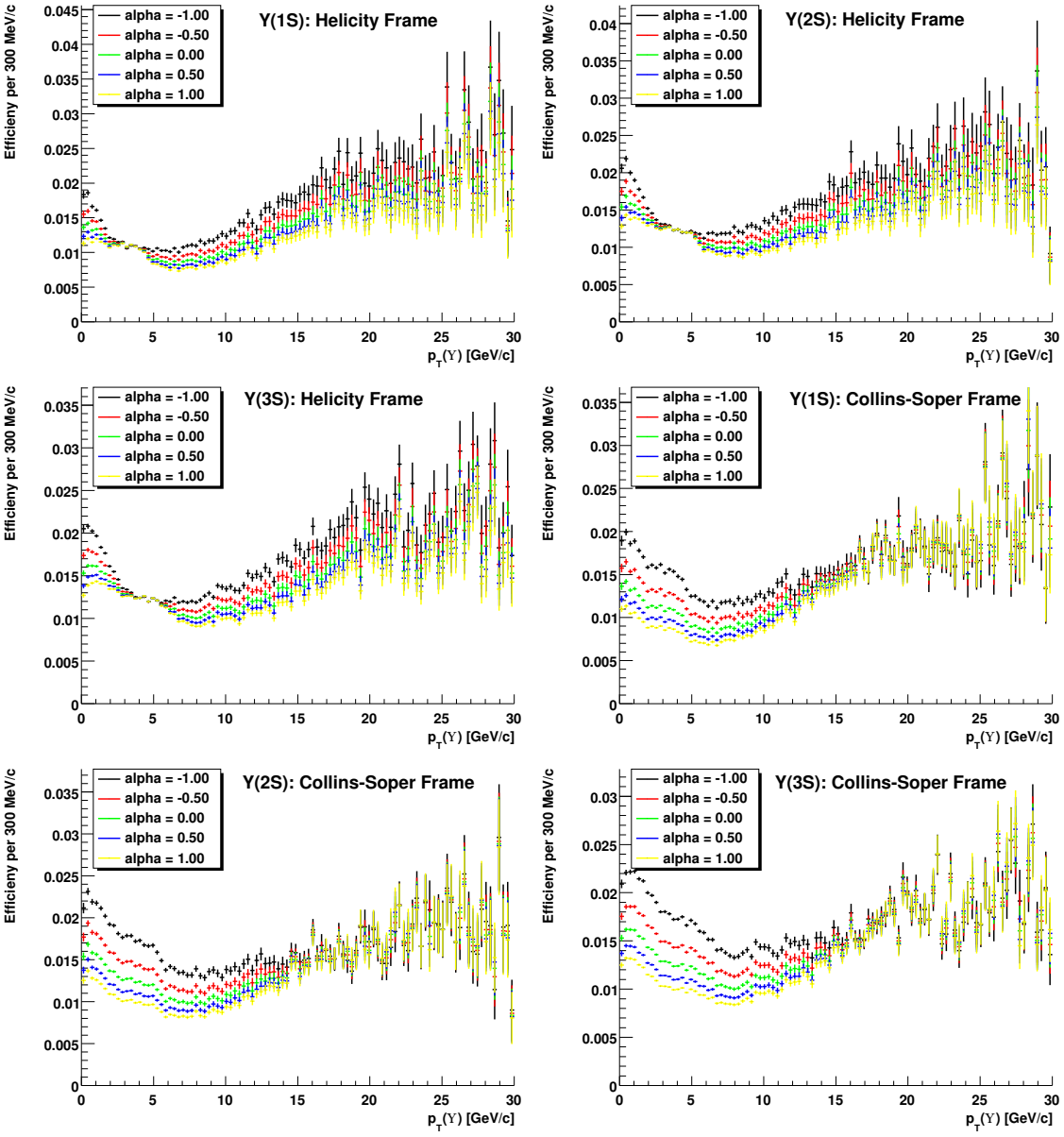

Figure 4.14: Efficiency for different polarization assumptions in the two frames with respect to $p_{T,\Upsilon}$. The plots in the first row correspond to the angle θ^* calculated in the helicity frame while in the second row the angle is calculated in the Collins-Soper frame.

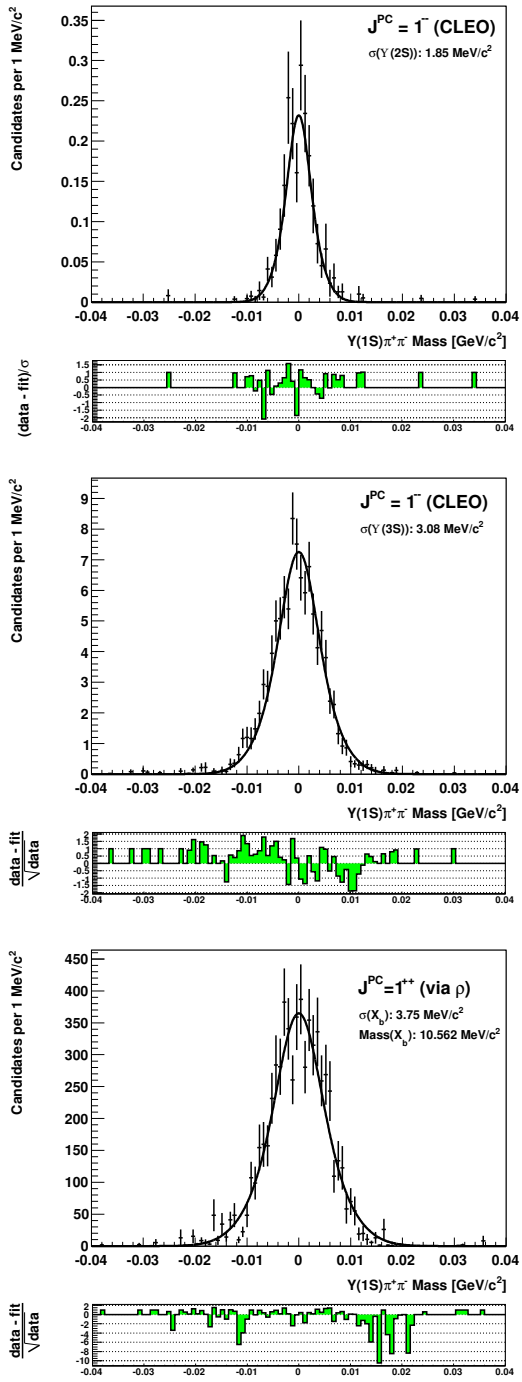

Figure 4.15: The simulated resolution for $\Upsilon(2S)$, $\Upsilon(3S)$ and the X_b for a hypothetical mass of 10.562 GeV/c^2.

	efficiency (Helicity)	efficiency (Collins-Soper)	accepted (Helicity)	accepted (Collins-Soper)	produced events	α
	0.0122	0.0147	81,270	97,749	9,975,629	-1
	0.0135	0.0123	94,341	102,581		-0.5
$\Upsilon(1S)$	0.0108	0.0108	107,413	107,413		0
	0.0104	0.0096	120,485	112,245		0.5
	0.01	0.0088	133,556	117,076		1
	0.014	0.017	92,978	113,270	9,975,629	-1
	0.0131	0.0143	108,853	118,999		-0.5
$\Upsilon(2S)$	0.0125	0.0125	124,727	124,727		0
	0.0121	0.0112	140,601	130,455		0.5
	0.0118	0.0102	156,476	136,184		1
	0.0143	0.0175	190,335	232,800	19,957,057	-1
	0.0135	0.0147	223,698	244,972		-0.5
$\Upsilon(3S)$	0.0129	0.0129	257,059	257,059		0
	0.0125	0.0116	290,419	269,145		0.5
	0.0122	0.0106	323,781	281,237		1

Table 4.2: Efficiencies of the Υ states for different assumed polarizations α with respect to the angle θ^* in the two frames: Helicity and Collins-Soper Frame.

with

$$G_1(m;\bar{m},\sigma) = \frac{1}{\sigma\sqrt{2\pi}} \cdot e^{-\frac{m-\bar{m}}{2\sigma^2}}$$

and

$$G_2(m;\bar{m},\sigma_2) = \frac{1}{\sigma_2\sqrt{2\pi}} \cdot e^{-\frac{m-\bar{m}}{2(\sigma_2)^2}}$$

where $\sigma_2 = h_\sigma \cdot \sigma$. The parameters $h_\sigma = 1.79$ and $f_{\text{norm}} = 0.343$ are fixed in this analysis.

The resolution is obtained from p_{T,X_b} and J^{PC} reweighted simulated candidates and is evaluated for several reconstructed invariant mass ranges. For each interval the deviation between the true and the reconstructed mass, $m_{true} - m_{rec}$, is fitted. The mean mass deviation $\delta\bar{m}$ is fixed to zero. The obtained resolutions for different selection requirements are shown in figure 4.16. The left plot shows the dependence after preselection requirements while the right plot shows the resolution after additionally applied pion quality cuts. The resolutions differ only slightly for the different J^{PC} assumptions. The resolutions are fitted for the X_b case and the fit results are evaluated for the certain masses. In case of the $\Upsilon(2S)$ and $\Upsilon(3S)$ the widths are fixed values due to the known masses of these two resonance.

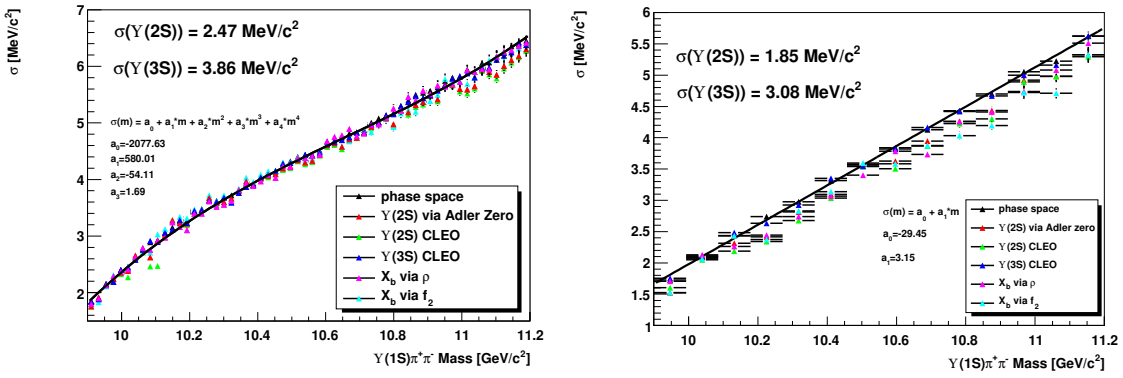

Figure 4.16: The expected resolution with rising invariant mass. Simulated candidates are reweighted with p_{T,X_b} weight and according to the corresponding resonance quantum numbers J^{PC}. The left plot shows the dependence after preselection requirements while the right plot shows the resolution after additionally applied pion quality cuts.

4.4.2 Efficiencies and Expectation

Efficiencies are calculated the same way as it is done for the polarization measurement. Due to the fact that simulated candidates are reweighted for p_{T,X_b} with the weight w_p and for J^{PC} with the weight w_{JPC}, the following formula is used

$$\epsilon(\Upsilon(nS) \to \mu^+\mu^-\pi^+\pi^-) = \frac{N(\text{accepted})}{N(\text{produced})} = \frac{\sum_{i=1}^{N_{acc}} w_i}{N_{prod} \cdot \langle w \rangle},$$

where w denotes the weight $w = w_p \cdot w_{JPC}$. In this case, the mean weight $\langle w \rangle$ can neither be derived analytically nor is it chosen such that the $\langle w \rangle = 1$. Thus, a toy simulation is generated, alike the full simulation, i.e. the same input transverse momentum distribution for the X_b is taken as well as the dimuon requirements: $p_{T,\mu^\pm} > 1.2$ GeV/c and $|\eta| < 1.5$. Phase-space decays with flat rapidity y are generated. The toy simulation of course does not consider detector acceptance. For each candidate the corresponding weights are calculated. As a result the mean weight $\langle w \rangle$ is obtained according to

$$\langle w \rangle = \frac{1}{N_{prod}} \sum_{i=1}^{N_{prod}} w_i.$$

Efficiencies for the $\Upsilon(2S)$ and $\Upsilon(3S)$ with respect to the neural network selection criterion and after required pion quality selection is shown in figure 4.17. For the X_b whose mass is unknown, the efficiency for the best significance selection with respect to the possible mass position is shown in figure 4.18. The uncertainties are calculated by assuming that the selected candidates are binomial distribution.

The expected signal candidates of the states $\Upsilon(2S)$ and $\Upsilon(3S)$ are derived by a simulation study. The cross-section of the corresponding state can be calculated by

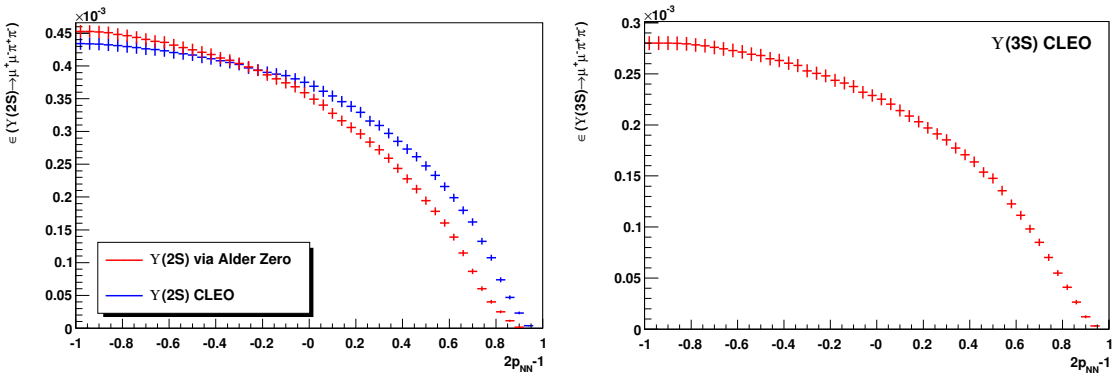

Figure 4.17: The left plot shows the dependence of the obtained $\Upsilon(2S)$ efficiency to the network probability for the quantum numbers $J^{PC} = 1^{--}$ calculated with an two different dipion propagators. The left plot shows the dependence of the obtained $\Upsilon(3S)$ efficiency.

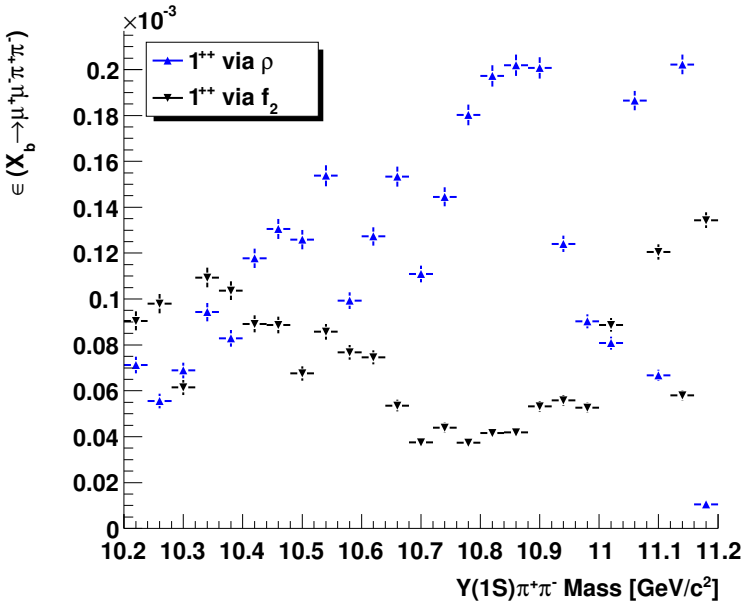

Figure 4.18: The X_b efficiency with respect to the network probability for two different dipion propagators ρ and f_2.

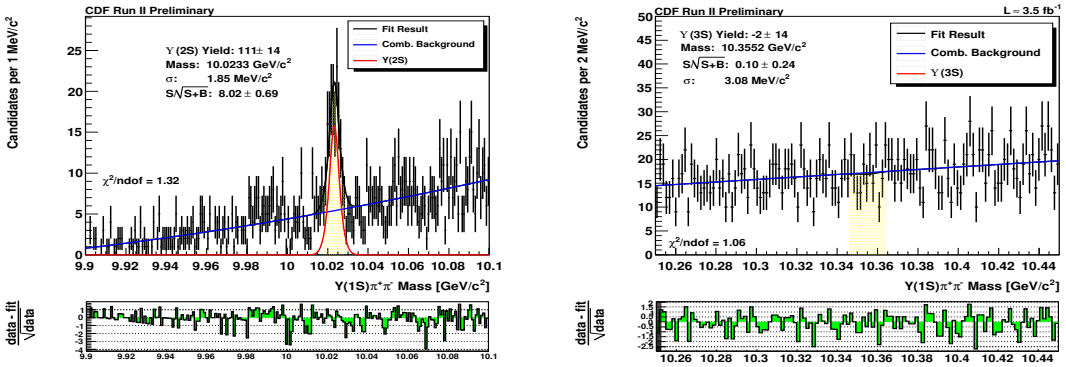

Figure 4.19: $\Upsilon(2S)$ and $\Upsilon(3S)$ fitted candidates.

	Fit Result	Expectation
$\Upsilon(2S)$	111.14 ± 13.6	83.6 ± 5.9
$\Upsilon(3S)$	-2.39 ± 13.88	24.74 ± 0.83

Table 4.3: List of fitted and expected $\Upsilon(2S)$ and $\Upsilon(3S)$ candidates.

$$\sigma_{\Upsilon(nS)} = \frac{N(\Upsilon(nS) \to \mu^+\mu^-)}{\epsilon(\Upsilon(nS) \to \mu^+\mu^-) \cdot \mathcal{L}_{int} \cdot BR(\Upsilon(nS) \to \mu^+\mu^-)}$$

$$\sigma_{\Upsilon(nS)} = \frac{N(\Upsilon(nS) \to \mu^+\mu^-\pi^+\pi^-)}{\epsilon(\Upsilon(nS) \to \mu^+\mu^-\pi^+\pi^-) \cdot \mathcal{L}_{int} \cdot BR(\Upsilon(nS) \to \mu^+\mu^-\pi^+\pi^-)}$$

Thus the expectation is obtained with

$$N(\Upsilon(nS) \to \mu^+\mu^-\pi^+\pi^-) = N(\Upsilon(nS) \to \mu^+\mu^-) \cdot BRQ \cdot effQ$$

where the efficiency ratio $effQ$ and the ratio of the branching fractions BRQ are defined as

$$effQ = \frac{\epsilon(\Upsilon(nS) \to \mu^+\mu^-\pi^+\pi^-)}{\epsilon(\Upsilon(nS) \to \mu^+\mu^-)}$$

$$BRQ = \frac{BR(\Upsilon(nS) \to \Upsilon(1S)\pi^+\pi^-) \cdot BR(\Upsilon(1S) \to \mu^+\mu^-)}{BR(\Upsilon(nS) \to \mu^+\mu^-)}$$

The integrated luminosity $\mathcal{L}_{int}$ cancels due to the fact that the dimuon sample as well as the X_b candidate sample are obtained from datasets of same luminosities.

The derived fitted $\Upsilon(2S)$ candidates obtained from a optimized selection without applying the pion quality requirements is only half the amount of the estimated value. This is due to the fact that the simulation overestimates pion tracks with $p_{T,\pi^\pm} \leq 0.4\,\mathrm{GeV/c}$.

Efficiency and expectations for the $\Upsilon(2S)$ and $\Upsilon(3S)$ for the chosen neural network selection are compared to the measured yields in table 4.3. The corresponding fits

are shown in figure 4.19. The expectation is of the order of the fit result though slightly underestimates $\Upsilon(2S)$ in measured data. There $\Upsilon(3S)$ expectation is not supported by the corresponding fit result.

Chapter 5

Υ Polarization

The measurement of polarization of the $\Upsilon(1S)$, $\Upsilon(2S)$ and $\Upsilon(3S)$ states is presented in this chapter. There are different predictions [80, 81] and measurements [52] that are contradictory. In order to verify the simulation it is important to find out if the Υ states with respect to their transverse momentum are polarized or not. This is of high importance for the X_b-search analysis as well where no obvious high statistic resonance can be seen in the invariant mass spectrum on which a simulation verification could be investigated. The X_b would decay into a pair of pions and an $\Upsilon(1S)$ which thereupon decays into two muons. The part of the simulation which describes the $\Upsilon(1S)$ simulation is scrutinized based on the Υ resonances in the dimuon spectrum. As a byproduct of testing the dimuon simulation reliability the Υ polarization is analyzed as well.

Section 5.1 describes the decay topology and important properties and observables of the Υ resonances. The selection process for the measured data sample is exposed in section 5.2. In section 5.3 the Υ polarization will be measured based on the finally selected samples on which measured data are described consistently by the simulation. In section 5.4 systematic uncertainties are investigated. Finally, the result is presented in section 5.5.

5.1 Decay Topology

The $\Upsilon(nS)$ vector states, with $n = 1, 2, 3$, can decay due to annihilation of their quark and anti-quark pair via a virtual photon or three gluons. Figure 5.1 shows the two processes illustrated by Feynman graphs. The single gluon decay is forbidden because of the color-charge and the two gluon decay is not allowed due to parity conservation. Consequently, only the annihilation via a subsequent virtual photon or three gluons is possible. However, the decay into two opposite-sign muons is only possible via the electromagnetic interaction, i.e. via a photon exchange. The decay is described as

$$\Upsilon(nS) \rightarrow \mu^+\mu^-.$$

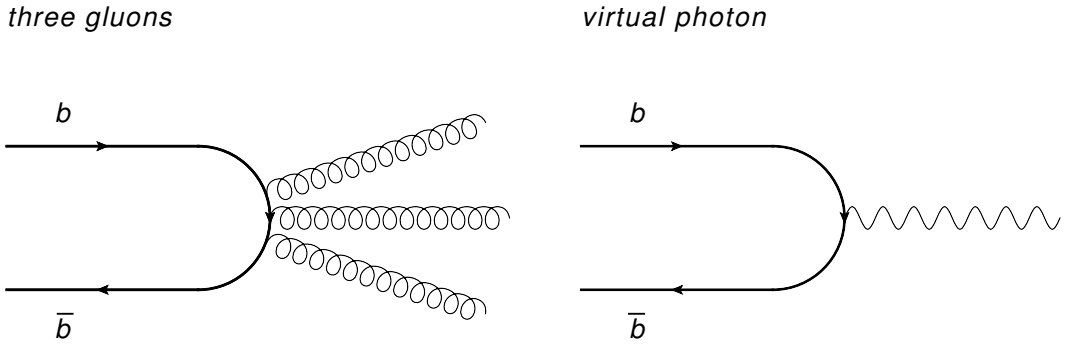

Figure 5.1: Annihilation processes of Υ vector states.

resonance	$\Upsilon(1S)$	$\Upsilon(2S)$	$\Upsilon(3S)$
mass [MeV/c^2]	$9,460.30 \pm 0.26$	$10,023.26 \pm 0.31$	$10,355.2 \pm 0.5$
J^{PC}	1^{--}	1^{--}	1^{--}
width [keV/c^2]	54.02 ± 1.25	31.98 ± 2.63	20.32 ± 1.85
BR($\Upsilon(nS) \to \mu^+\mu^-$) [%]	2.48 ± 0.05	1.93 ± 0.17	2.18 ± 0.28
BR($\Upsilon(nS) \to \Upsilon(1S)\pi^+\pi^-$) [%]	—	18.8 ± 0.6	4.48 ± 0.21

Table 5.1: $\Upsilon(nS)$ properties [9].

This decay channel is the most promising one to study Υ resonances at the Tevatron because muons are well detectable at CDF II, as it is described in section 2.2.4. Since about 2.5% of the $\Upsilon(1S)$-states decay into two muons this is a good decay channel to obtain high statistics. Due to the lifetime of the Υ states of about $1.2 \cdot 10^{-20}$ s it is impossible to find a displaced decay vertex from the vector state itself. In fact, the decay happens immediately on scale of the detector resolution. Because of the invariant mass reconstruction of two combined and oppositely charged muons

$$m(\mu^+\mu^-) = \sqrt{(E_{\mu^+} + E_{\mu^-})^2 - (p_{\mu^+} + p_{\mu^-})^2}$$

which arise from one common origin, it is possible to trace back to the so-called 'mother' particle, which possibly produced them. Thus the signature to search for such kind of resonances is to find two opposite-sign muons which come from one origin or rather from one so-called vertex. The invariant mass spectrum should then show a peak at the mass position of the corresponding Υ state.

Some important properties of the Υ resonances are listed in table 5.1. The determination of the Υ polarization crucially depends on the reference frame [51]. A full understanding of the polarization phenomenon requires measurements obtained in two orthogonal frames, such as the Collins-Soper and helicity frame.

These two frames are illustrated in figure 5.2 and table 5.2 lists the definition of the certain axis in the corresponding frames.

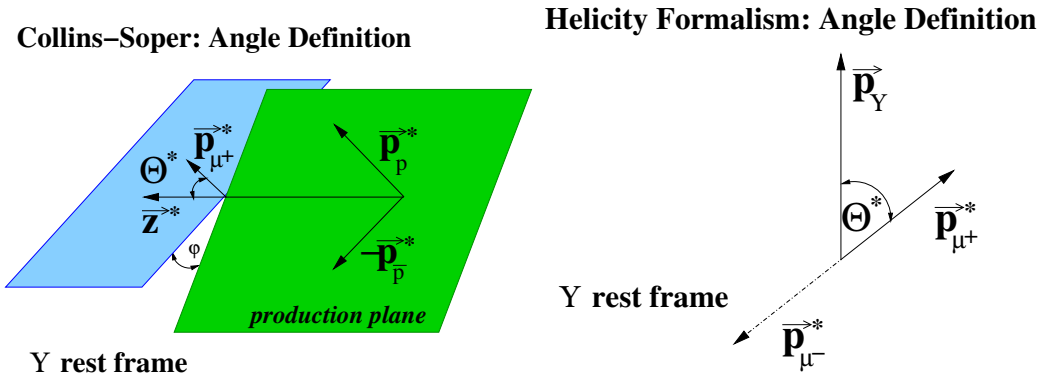

Figure 5.2: The left plot illustrates the Collins-Soper frame. The right plot illustrates the helicity frame.

	helicity frame	Collins-Soper frame
decay	$\Upsilon(nS) \to \mu^+\mu^-$	$\Upsilon(nS) \to \mu^+\mu^-$
angle	θ^*_Υ	$\theta^*_{\Upsilon,CS}$
daughter momentum	$\vec{p}^*_{\mu^+}$ (in Υ cms)	$\vec{p}^*_{\mu^+}$ (in Υ cms)
polarization axis	$\vec{p}_\Upsilon$ in the laboratory frame	direction of the bisector vector of the colliding protons in the Υ cms

Table 5.2: Momenta and vectors used for the helicity and Collins-Soper angle calculation. θ is defined as the angle between the muon momentum and polar axis.

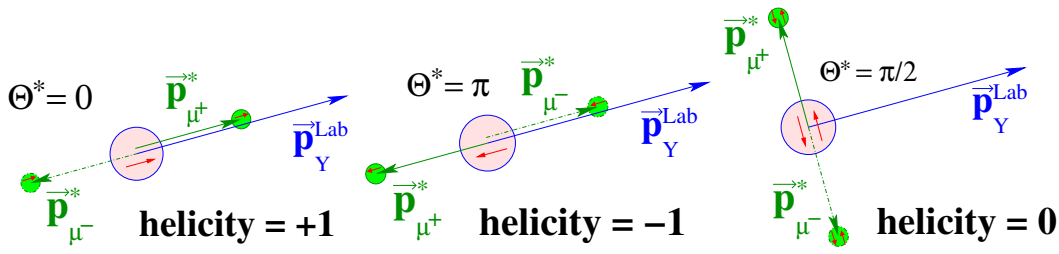

Figure 5.3: Diagrams of helicity polarization angles θ^* with three different helicity states. The red arrows label the spin projections of the particles. Equally populated helicity states corresponds to zero polarization.

- **Helicity Frame:**
  In the helicity frame the polar axis coincides with the flight direction of the Υ in the center-of-mass frame ('cms') of the colliding hadrons, which at CDF II is the laboratory system. This is illustrated in the left plot in figure 5.2. The polarization axis is defined as the flight direction of the Υ in the laboratory system, $\vec{p}_\Upsilon$. The polarization axis, for each frame respectively, and the direction of the positive muon momentum $\vec{p}^*_{\mu^+}$ in the Υ rest frame define the corresponding polarization angle. The helicity angle θ^*_Υ is defined as the angle between the polarization axis and flight direction of the positive muon in the center-of-mass frame of the Υ.

- **Collins-Soper Frame:**
  A very different approach is implied in the definition of the Collins-Soper frame. Here the polarization axis reflects, on average, the direction of the relative velocity of the colliding partons in the center-of-mass frame of the Υ. This is illustrated in the left plot in figure 5.2. The bisector $\vec{z}^*$ of the proton and negative antiproton momenta, $\vec{p}^*_p$ and $-\vec{p}^*_{\bar{p}}$, both in the Υ rest frame, defines the polarization axis. The Collins-Soper angle $\theta^*_{\Upsilon,CS}$ is defined as the angle between the polarization axis and flight direction of the positive muon in the Υ rest frame.

In the rest frame of the Υ the two daughter particles decay 'back-to-back' so that $\vec{p}^*_{\mu^+} = -\vec{p}^*_{\mu^-}$. which is illustrated in the right plot of figure 5.2. They move along an axis, rotated by a polar angle θ^* with respect to the momentum direction of the mother particle in the laboratory frame. This direction is given by the momentum of the positive muon. The mother particle is characterized by its spin J and spin projection J_z along an arbitrarily chosen quantization axis. It decays into two opposite-sign muons with helicities λ_+ and λ_-. Helicity is defined as the projection of the spin eigenstate vector on the momentum axis: $\lambda = \vec{s} \cdot \frac{\vec{p}}{|\vec{p}|}$. Taking the direction of the positive muon as the new spin quantization axis, the total combined angular momentum projection is $\lambda = \lambda_+ + (-\lambda_-)$. There is no orbital angular momentum contribution because, due to $\vec{L} = \vec{r} \times \vec{p}$, any orbital angular momentum is perpendicular to the quantization axis (given by $\vec{p}$), so that the projection on the axis is zero.

The three different helicity states are shown in figure 5.3. In the Collins-Soper frame the same approach is used, only the polarization axis $\vec{p}^{Lab}_Y$ must be replaced by the Collins Soper polarization axis $\vec{p}^{CS}_Y$. Equal population of all three types corresponds to unpolarized production.

5.2 Candidate Selection

This analysis uses all data taken until August 2008 which corresponds to the run number range from 138425 to 266513 and an integrated luminosity of about $3.5\,\mathrm{fb}^{-1}$. For the primary data selection on trigger-level the dimuon trigger is used which

combines two muons to one vertex. More precisely, the upsilon trigger is applied because we are interested in the decay $\Upsilon(nS) \rightarrow \mu^+\mu^-$.

In measured data background contributes about a half. Most of it comes from combining two opposite sign muons to one vertex which are essentially produced uncorrelated. This is the so-called combinatorial background. It is the first task to remove obvious background from the sample while maintaining high signal efficiency. To select a reasonable amount of signal candidates and simultaneously remove many background candidates, a good quantity to maximize is

$$S_{NN} = \frac{\mathbf{S}\text{ignal}}{\sqrt{\mathbf{S}\text{ignal} + \mathbf{B}\text{ackground}}} = \frac{S}{\sqrt{S+B}}$$

where S denotes the signal expectation value of the Poisson random variable N=S+B, the total number of observations, and $\sigma_N = \sqrt{S+B}$ refers to the corresponding standard deviation.

It is the first challenge to have a sample that achieves the highest S_{NN} based on which the Υ polarization can be measured.

5.2.1 Preselection Cuts

The selection criteria listed in section 4.1 must be fullfilled in order to remove obvious background. Υ candidates are obtained by fitting opposite-charge muon candidate tracks to a common vertex using the `CTVMFT` fitter [82]. Figure 5.4 shows the Υ mass distribution for measured data recorded to tape which contains about 13 M candidates within the dimuon mass range of $8.5\,\mathrm{GeV/c^2}$ and $11.5\,\mathrm{GeV/c^2}$. Figure 5.5 shows the spectrum that fullfills the preselection criteria. For the $\Upsilon(1S)$ and $\Upsilon(2S)$ the 3σ range around the mean dimuon mass is used while for the $\Upsilon(3S)$ the 2σ range is used due the larger mass resolution. Roughly 21 % of the candidates remain while only about 6 % of the $\Upsilon(1S)$ signal is lost.

5.2.2 Final Selection Optimization

The final selection criteria are determined in the following steps:

1. The measured invariant mass spectrum after preselection is fitted in order to prepare for the ${}_s$Plot-based neural network training.

2. All neural network input variables are required to be independent of the input invariant mass distribution, which supplies the basis for the ${}_s$Plot weight calculation that is fed to the neural network. Additionally, the input variables need to be well modelled in order to calculate a reasonable ${}_s$Plot-based likelihood for simulation and measured data. The Υ's are generated unpolarized, therefore all input variables which are highly dependent on the polarization angle must be removed in order to do the final polarization comparison between simulation and measured data unbiased.

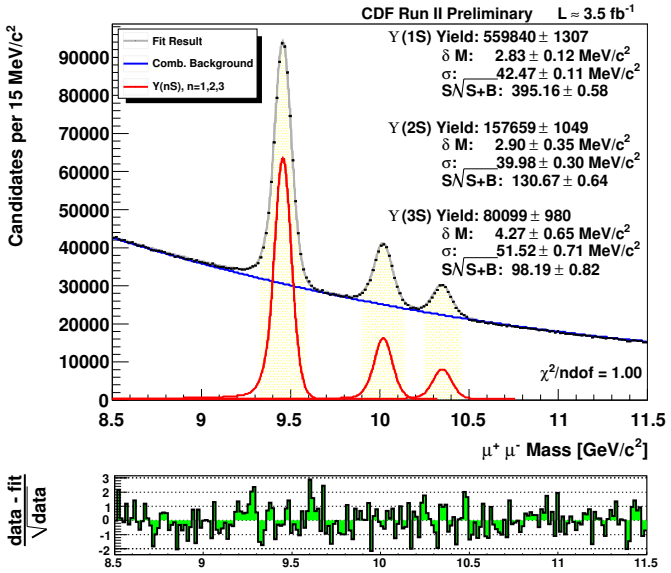

Figure 5.4: The upper plot shows the distribution of the reconstructed dimuon mass. Even the full sample without any selections shows clearly all three vector ϒ resonances. The yellow area refers to the dimuon mass range for which the quantity significance is calculated. The lower plot shows the deviation between data points and fit result for each bin.

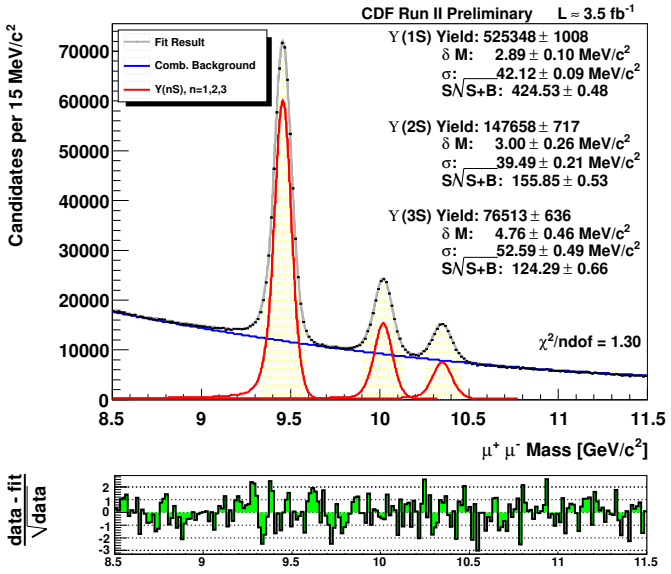

Figure 5.5: Distribution of the reconstructed dimuon mass for candidates that fullfill the selection criteria described in section 4.1. Although only 21 % of the dataset candidates without preselection are left, almost no signal is lost.

resonance	$\Upsilon(1S)$	$\Upsilon(2S)$	$\Upsilon(3S)$
h_σ	1.42	1.47	1.72
f_{norm}	0.56	0.32	0.85
α	1.62	1.53	1.9
n	1.28	0.67	0.97

Table 5.3: $\Upsilon(nS)$ shape parameters are estimated from a fit to the measured and preselected invariant mass spectrum.

3. The optimal requirement on the likelihood of the neural network based estimation is found by maximizing the fit-based calculated significance.

4. Finally, this selection criterion on the likelihood is applied to simulated events and measured data. These represent the final samples on which the Υ polarization measurement is performed.

5.2.2.1 Signal Extraction

In order to provide the discrimination variable for the ${}_s$Plot based neural network training it is necessary to fit the invariant dimuon spectrum. In the range between $m_l = 8.5\,\text{GeV/c}^2$ and $m_h = 11.5\,\text{GeV/c}^2$ it is obvious that there are the contributions of the three resonances $\Upsilon(1S)$, $\Upsilon(2S)$ and $\Upsilon(3S)$, and the combinatorial background. The Monte Carlo simulation study shows that a Crystal Ball function $CB(m)$ plus a Gaussian function $G(m)$ is required to model the mass distribution of the Υ states as described in section 4.3.1.

The background contribution is modelled by a third order polynomial function described as

$$f_{\text{bg}}(m) = \text{N}_{\text{bg}} \cdot \frac{2}{(x_h - x_l)} \cdot (1/2 + a(x(m)^2 - 1/3) + x(m)(b + cx^2)).$$

The number of background candidates is N_{bg}. The nominal mass range $[m_l, m_h]$ is transformed into the range $[-1, 1]$ by

$$x(m) = -1 + \frac{2}{m_h - m_l} \cdot (m - m_l).$$

Simultaneously for each contribution, the fitting of the function $f(m)$ with respect to the invariant mass m is applied to the whole invariant dimuon spectrum represented by

$$f(m) = f_{\Upsilon(1S)}(m) + f_{\Upsilon(2S)}(m) + f_{\Upsilon(3S)}(m) + f_{\text{bg}}(m).$$

The shape parameters of the distribution are obtained from measured data after preselection. This is possible because of the high statistics sample. However, for

#	variable	description	NN signi. [73]
1	training target	signal=1, background=0	
2	$\max(\lvert d_0/\sigma_{d_0}\rvert_{\mu^+}, \lvert d_0/\sigma_{d_0}\rvert_{\mu^-})$	maximum impact parameter significance	129.43
3	$\chi^2_{\mu^+\mu^-}$	Υ candidate vertex fit quality	70.1
4	$L_{xy,\mu^+\mu^-}$	transverse decay length	173.77
5	$\lvert L_{xy}/\sigma_{L_{xy}}\rvert_{\mu^+\mu^-}$	transverse decay length significance	12.17
6	$\min(\text{Like}_{\mu^+},\text{Like}_{\mu^-})$	minimum of muon likelihood	248.8
7	$\max(\text{Like}_{\mu^+},\text{Like}_{\mu^-})$	maximum of muon likelihood	70.91

Table 5.4: List of the input variables of the $_s$Plot-based neural network.

the $\Upsilon(3S)$ statistics are not sufficient enough so that in this case the shape parameters are calculated based on its simulation. The resulting parameters are listed in table 5.3. These are the parameters that are kept fixed in all fits.

The resolution and the mean mass parameters are left free in the fits. Due to effects like detector calibration there is a mass shift observed in the simulation. Thus the fit $\delta m = m_{PDG} - \bar{m}_{fit}$ is used instead of the central mass value where m_{PDG} is fixed to the mass value from the PDG [9].

The $_s$Plot based neural network training uses the $\Upsilon(1S)$ resonance to calculate the $_s$Plot weights. Due to similar properties of all three resonances, the resulting likelihood also holds for the other two resonances.

5.2.2.2 Neural Network Input Variables

The neural network input variables are listed in table 5.4. All input variable distributions obtained from the simulation have to properly describe the corresponding signal distributions of measured data. The comparison is already investigated in section 4.2.3. It was checked that the mass resolution is independent of the neural network variables so that in all fits the mass and the mass resolution are fixed to the values obtained from the fit to the invariant mass spectrum obtained from measured data which is shown in figure 5.9. Additionally, simulated candidates are reweighted in order to correct slight differences in the $p_{T,\Upsilon}$ distribution which is described in section 4.2.2.

The final comparison between simulation and measured data leads to the polarization angle. Therefore it is important to leave information about θ^* out of the selection process. Otherwise the selection criterion for the simulation, that is produced unpolarized, wouldn't hold. As a consequence, θ^* cannot be taken as an input variable and shouldn't be correlated to any of them. As a cross-check the correlation between the input variables and θ^* is investigated and shown figure 5.6. There are only slight correlations to the input variables. While the Colins-Soper angle is

almost uncorrelated, the helicity angle is slightly correlated to some of neural network variables. The highest correlation is seen to transverse decay length $L_{xy,\mu^+\mu^-}$. However, it is not possible to achieve a full θ^* independence. Even the trigger requirements could have an effect on the polarization. All neural network variables are uncorrelated to the dimuon mass as it is required for the $_s$Plot training.

As a result, the the estimation based on the data driven $_s$Plot training can be applied to the simulation as well. However, the slight θ^* dependence and the difference in the likelihood distribution have to be considered in the systematics later.

5.2.2.3 Training Result and Significance Maximization

The $_s$Plot based neural network training result is then applied to unclassified measured data after preselection. For each Υ candidate a probability p_{NN} for being signal is estimated. However, what is the probability required at least to achieve a reasonable selection? As explained before the quantity to maximize is the quantity

$$\frac{S(p_{NN} > p_{NN,cut})}{\sqrt{S(p_{NN} > p_{NN,cut}) + B(p_{NN} > p_{NN,cut})}}.$$

Hereby, step by step a certain probability $p_{NN,cut}$ is required and then the fit for the selected signal and background candidates, S and B, of measured data evaluated. Probability is a quantity that is defined to the range between $[0, 1]$. The value 0 means it is certainly background and 1 means it is signal. Mostly, for each candidate a value in between is obtained.

The question is how much probability is required to obtain the maximum significance. Therefore many requirements on the neural network probabilities, in case of the $\Upsilon(1S)$, 100 out of the interval $[0, 1]$ in equidistant steps are evaluated for significance. The probability which provides the highest significance is then chosen to be the at least required probability. Due to the fact that the mass resolution is independent of the network probability which is shown in the right plot of figure 5.7, the mass resolution as well as the mass are fixed during the scanning. The significance with respect to the network output variable $(p_{NN} \cdot 2 - 1)$ is shown in the left plot of figure 5.7. The best $\Upsilon(1S)$ selection is obtained at a probability of $p_{NN} = 14\%$. Υ candidates that passes the all selection requirements including the $_s$Plot based requirement, are shown in figure 5.8. The selection keeps 17% of the data candidates on tape while only 7.8% $\Upsilon(1S)$ of the signal is removed.

In figure 5.9 the dimuon spectrum of the finally selected measured data sample, including the muon requirements for η_μ and $p_{T,\mu}$ described in section 4.2.1, is shown. About 53% of the $\Upsilon(1S)$ signal is lost compared to the selection after the applied neural network cut. Based on this finally selected samples the Υ polarization will be measured. The efficiency of the selection summarized in table 5.5.

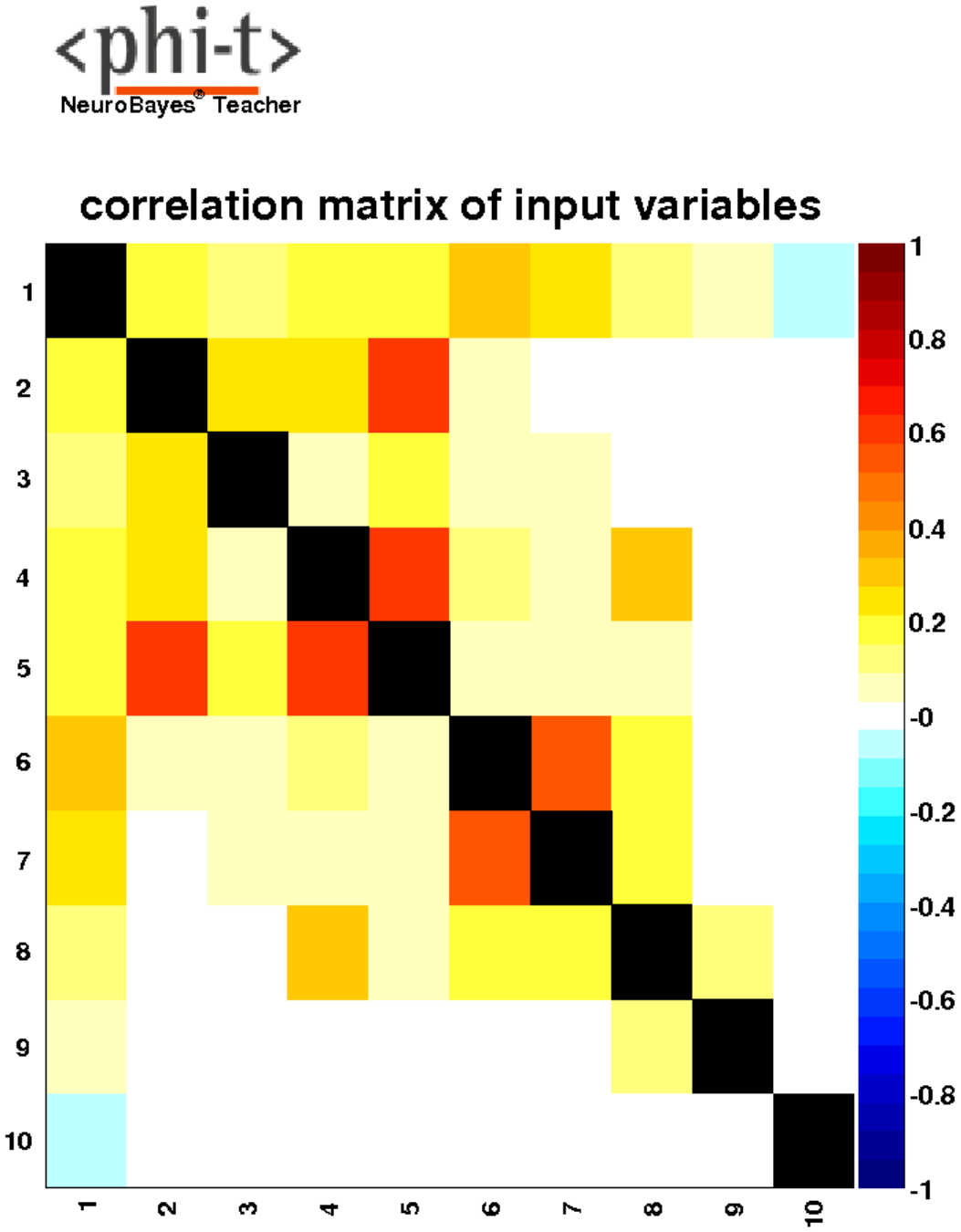

Figure 5.6: Correlations of neural network the input variables (2-7), the helicity angle θ^* (8), the Colins-Soper angle θ^*_{CS} (9) and the dimuon mass (10) are illustrated. The labelling of the input variables are defined in table 5.4.

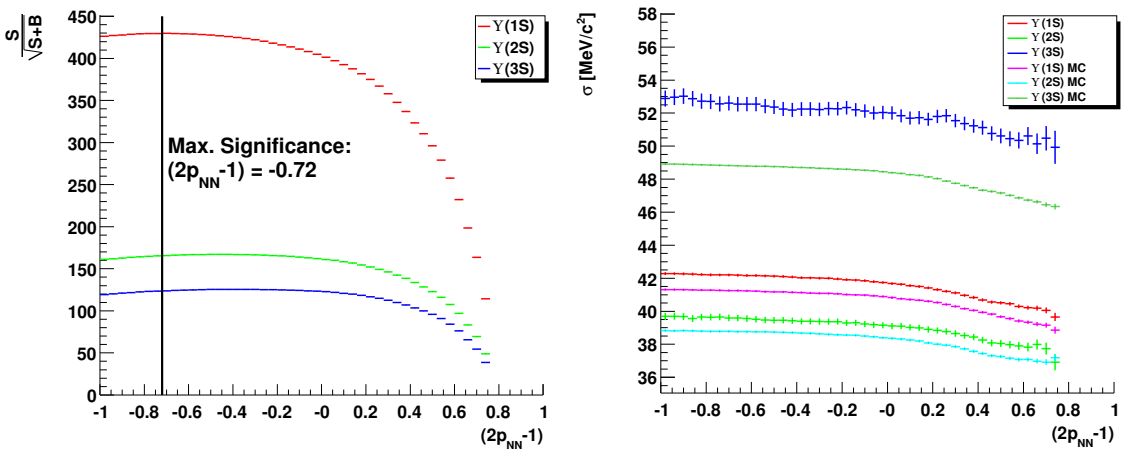

Figure 5.7: The $\Upsilon(nS)$ significance and mass resolution for different neural network probability requirements is plotted. The network output selection with the maximal $\Upsilon(1S)$ significance is at $2p_{NN} - 1 = -0.72$ and is represented as the black vertical line in the left plot. The right plot shows that the mass resolution only slightly decreases with higher neural network cuts.

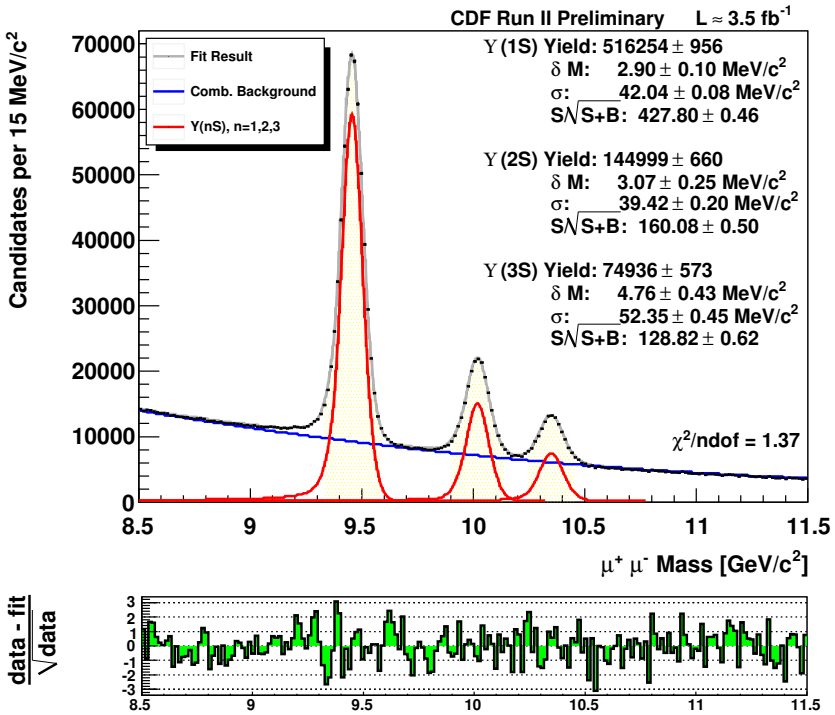

Figure 5.8: Distribution of the reconstructed invariant mass. The preselection criteria and the $_s$Plot based neural network probability for maximized $S/\sqrt{S+B}$ are required.

selection stage	candidates	$\Upsilon(1S)$	$\Upsilon(2S)$	$\Upsilon(3S)$
on tape	13	0.56	0.158 M	0.08
+ after preselection	0.27 (2.1%)	0.525 (94%)	0.148 (94%)	0.077 (96%)
+ $_s$Plot selection	0.226 (1.7%)	0.516 (92%)	0.145 (92%)	0.075 (94%)
+ muon cuts (η/p_T)	0.109 (0.84%)	0.263 (47%)	0.079 (50%)	0.042 (53%)

Table 5.5: List of measured data candidates and Υ signal yields in $10^6 = M$ for several selection stages.

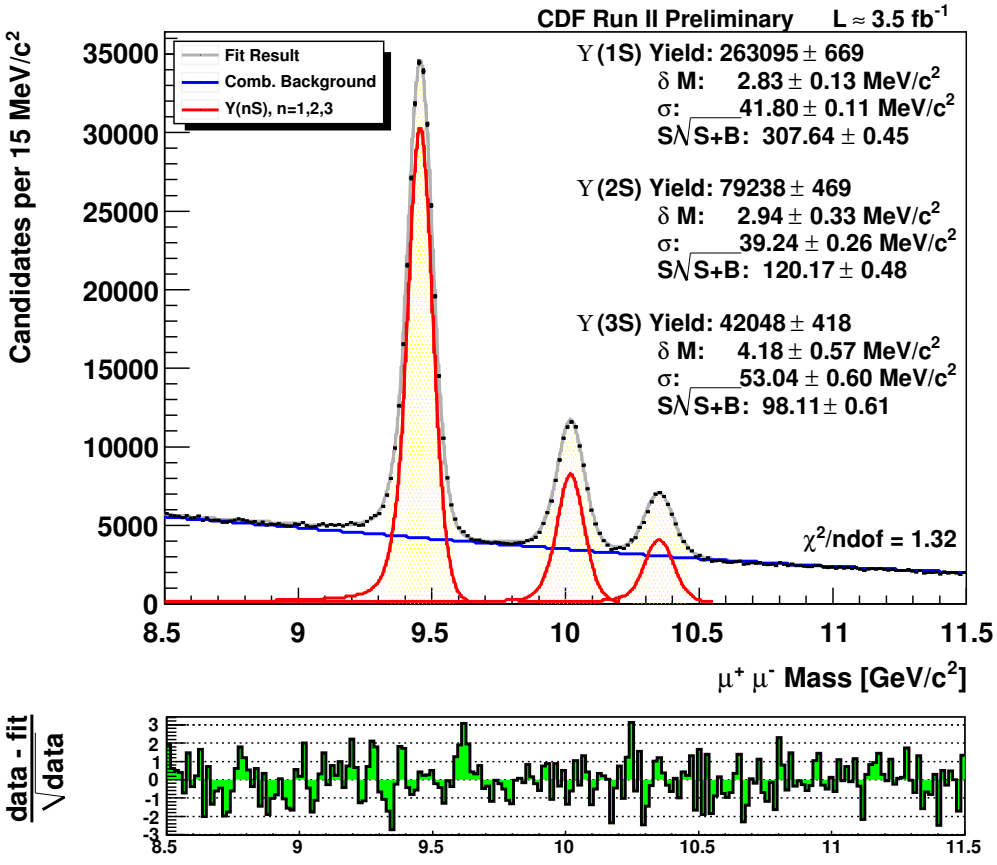

Figure 5.9: Distribution of the reconstructed invariant dimuon mass for candidates that fullfill all selection criteria.

5.3 Υ Polarization Measurement

The aim of this analysis is to measure the Υ polarization α based on the acceptance corrected $\cos(\theta^*_{\Upsilon(nS)})$ distribution that is expected to be flat in case of no polarization, i.e. equally population of all helicity states.

5.3.1 Analysis Steps

The analysis proceeds in the following steps:

- Divide sample into seven $p_{T,\Upsilon}$ bins.
- Obtain the parameters σ and δm from a fit to the invariant mass spectrum of each $p_{T,\Upsilon}$ bin. The obtained values are kept fixed in the following.
- Divide the sample into bins of $\cos(\theta^*)$.
- For each $p_{T,\Upsilon}$ and $\cos(\theta^*)$ bin a fit is applied where only the signal yield $N_{\Upsilon(nS)}$ and background yield N_{bg} are left free as well as the shape parameters for the background, a, b and c, with the parameters are already introduced in section 5.2.2.1.
- Due to detector acceptance and efficiencies the measured data sample has to be adjusted based on the full Monte Carlo simulation in order to obtain the corrected distribution.
- The resulting $\cos(\theta^*)$ distributions are fitted for each $p_{T,\Upsilon}$ bin to the theoretical predicted shape $1 + \alpha \cos^2\theta^*$ with the χ^2 minimization method.

The probability that an event leads to some measured value is called the detection efficiency ϵ. In case of the polarization measurement, the measured and simulated signal yields are obtained from a fit which is described in section 5.2.2.1. Thus the $\cos\theta^*$ distribution obtained from measured data, denoted as $g(\cos\theta^*)$, needs to be corrected for acceptance effects, described by the acceptance efficiency $\epsilon(\cos\theta^*)$, in order to obtain the true distribution $f_{corr}(\cos\theta^*)$ by

$$f_{corr}(\cos\theta^*) = \frac{g(\cos\theta^*)}{\epsilon(\cos\theta^*)}.$$

The simulation generates N candidates. After considering all detector effects n candidates are left over, thus the total efficiency is $\epsilon = n/N$. The total number of generated events N is distribution according to the input $p_{T,\Upsilon}$ distribution. In each $\cos\theta^*$ bin the generated distribution is flat due to the unpolarized simulated Υ candidates. For each $\cos\theta^*$ bin i the efficiency corrected distribution is obtained by

$$f_{corr,i} = \frac{N_{\Upsilon,i}}{\epsilon_i}.$$

bin	range [GeV/c]		$\Upsilon(1S)$	$\Upsilon(2S)$	$\Upsilon(3S)$
1	$[0,1]$	Mass [GeV/c^2]	9.4574	10.02	10.349
		Resolution [MeV/c^2]	39.65	38.016	53.007
2	$[1,2]$	Mass [GeV/c^2]	9.4579	10.021	10.351
		Resolution [MeV/c^2]	40.163	39.754	51.854
3	$[2,4]$	Mass [GeV/c^2]	9.457	10.02	10.352
		Resolution [MeV/c^2]	40.743	37.462	49.435
4	$[4,7]$	Mass [GeV/c^2]	9.458	10.021	10.351
		Resolution [MeV/c^2]	41.842	39.171	52.871
5	$[7,10]$	Mass [GeV/c^2]	9.4574	10.02	10.35
		Resolution [MeV/c^2]	43.587	39.752	53.027
6	$[10,15]$	Mass [GeV/c^2]	9.4572	10.018	10.35
		Resolution [MeV/c^2]	46.964	44.12	60.914
7	$[15,30]$	Mass [GeV/c^2]	9.4576	10.021	10.353
		Resolution [MeV/c^2]	53.422	46.109	64.413

Table 5.6: List of resolution and mass values for each $p_{T,\Upsilon}$ bin. The values are obtained from a fit to measured data of the final selected sample in the corresponding $p_{T,\Upsilon}$ bin.

where $N_{\Upsilon,i}$ denotes the number of measured signal candidates obtained from the fit to the invariant mass spectrum in the i-th bin and ϵ_i is the efficiency in the i-th $\cos\theta^*$ bin. In this analysis $p_{T,\Upsilon}$ is divided in seven bins. The $\cos\theta^*$ distribution for each $p_{T,\Upsilon}$ bin is obtained from several fits in bins of $\cos\theta^*$ chosen such that an equal number of simulated candidates are contained.

All fits use fixed shape parameters as listed in table 5.3. The mass resolution depends on $p_{T,\Upsilon}$ as shown in figure 4.13. Thus the mass resolution as well as the central mass value are fixed in each $p_{T,\Upsilon}$ bin separately. The values, listed in table 5.6, are obtained by a fit to measured data in the finally selected sample for each $p_{T,\Upsilon}$ bin. The fit results are shown in figure 5.11. The background parameterization is left free due to the fact that the background shape can change significantly for different bins which is exemplary shown in figure 5.10.

By accepting n candidates out of N independent events, the quantity n is binomial distributed. Thus the relative error $\sigma_{i,rel,\epsilon}$ of the efficiency ϵ_i in each $\cos\theta^*$ bin i is

$$\sigma_{i,rel,\epsilon} = \frac{\sigma_{i,\epsilon}}{\epsilon_i} = \sqrt{\frac{1-\epsilon_i}{n_i}}.$$

This follows from the fact that the expectation value for a binomial distributed quantity n is $E[n] = N\epsilon$ and the corresponding error is $\sigma_n = \sqrt{N\epsilon(1-\epsilon)}$. Thus the efficiency $\epsilon = n/N$ has the error $\sigma_\epsilon = \sigma_n/N$. The relative error of the measured

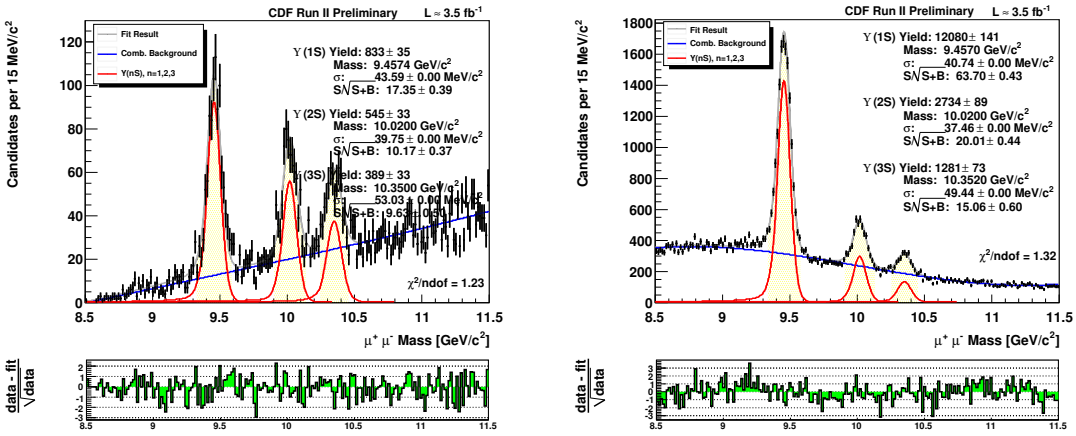

Figure 5.10: Two examples of fitted dimuon spectra for the first $\cos\theta^*$ bin of the third (right) and fifth (left) $p_{T,\Upsilon}$ bin.

distribution $g(\cos\theta^*)$ in each $\cos\theta^*$ bin i is

$$\sigma_{i,rel,g} = \frac{\sigma_{N_\Upsilon,i}}{N_{\Upsilon,i}}.$$

The uncertainty $\sigma_{N_{\Upsilon,i}}$ is obtained from the error of the fitted signal value $N_{\Upsilon,i}$ in the corresponding $\cos\theta^*$ bin. The errors of the corrected distribution $f_{corr}(\cos\theta^*)$ are thus

$$\sigma_{i,f} = \frac{\sigma_{N_\Upsilon,i}}{\epsilon_i}\sqrt{1+\left(\frac{N_{\Upsilon,i}}{\sigma_{N_\Upsilon,i}}\right)^2\left(\frac{N_{MC,i}}{\sigma_{N_{MC},i}}\right)^2}.$$

The result is obtained by using the error propagation for uncorrelated quantities given as

$$f(x) = \frac{g(x)}{\epsilon};\quad df(x) = \sqrt{(\frac{df}{dg}\Delta g)^2 + (\frac{df}{d\epsilon}\Delta\epsilon)^2}.$$

The number of simulated candidates $N_{MC,i}$ in each $\cos\theta^*$ bin as well as the corresponding uncertainty $\sigma_{N_{MC},i}$ is obtained from a fit applied in the same way as it is done for signal in measured data. Using the derived formula, the corrected $\cos\theta^*$ distributions for each $p_{T,\Upsilon}$ bin is obtained for the three resonances $\Upsilon(1S)$, $\Upsilon(2S)$ and $\Upsilon(3S)$. The distributions are then fitted to extract the polarization of the corresponding $p_{T,\Upsilon}$ bin. The parameterization of the fit function is

$$f(x) = p_0 \cdot \frac{1+\alpha(\cos\theta^*)^2}{2\cdot(1+\frac{1}{3}\alpha)}.$$

It is chosen such that p_0 serves as the normalization parameter because the remaining part of the function is normalized to one. The fitting is done by using the χ^2 minimization method.

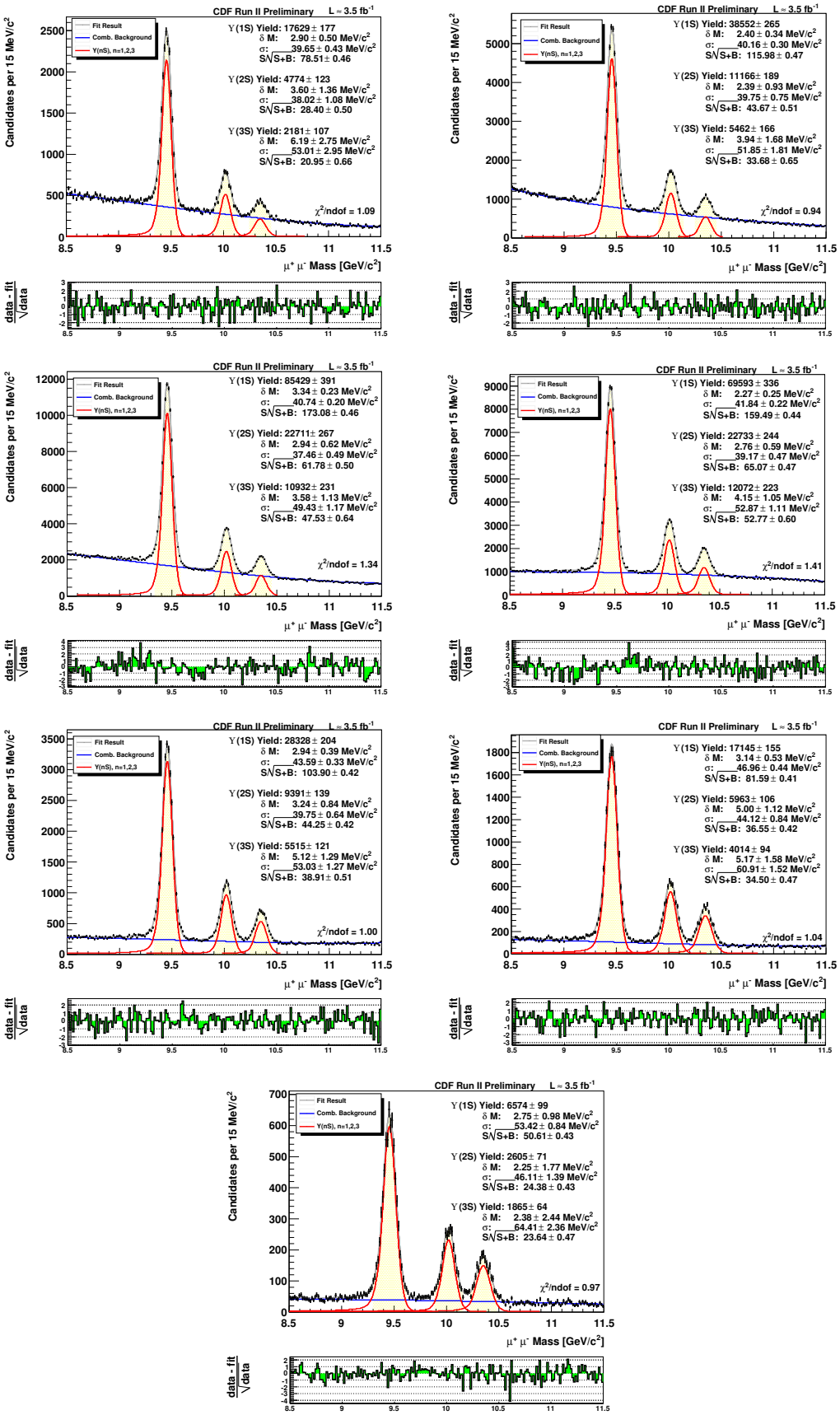

Figure 5.11: Fitted dimuon invariant mass spectra for $p_{T,\Upsilon}$ bins.

$p_{T,\Upsilon}$ range [GeV/c]	$\alpha(\Upsilon(1S))$	$\alpha(\Upsilon(2S))$	$\alpha(\Upsilon(3S))$
$[0,1]$	-0.027± 0.078	0.122 ± 0.144	-0.231± 0.200
$[1,2]$	0.028 ± 0.043	0.208 ± 0.082	0.247 ± 0.128
$[2,4]$	-0.072± 0.024	-0.159± 0.039	-0.186± 0.062
$[4,7]$	-0.047± 0.029	0.050 ± 0.044	0.089 ± 0.065
$[7,10]$	-0.128± 0.057	0.028 ± 0.079	-0.108± 0.091
$[10,15]$	-0.098± 0.075	0.086 ± 0.115	-0.017± 0.111
$[15,30]$	0.023 ± 0.111	0.012 ± 0.147	0.069 ± 0.161

Table 5.7: Measured Υ polarization and statistical uncertainty. The angle θ^* is calculated in the helicity frame.

$p_{T,\Upsilon}$ range [GeV/c]	$\alpha(\Upsilon(1S))$	$\alpha(\Upsilon(2S))$	$\alpha(\Upsilon(3S))$
$[0,1]$	0.046 ± 0.121	0.183 ± 0.157	-0.109± 0.225
$[1,2]$	0.006 ± 0.110	-0.010± 0.127	0.091 ± 0.186
$[2,4]$	0.012 ± 0.036	-0.023± 0.057	0.057 ± 0.087
$[4,7]$	-0.077± 0.036	-0.132± 0.051	0.103 ± 0.080
$[7,10]$	-0.176± 0.062	-0.044± 0.094	-0.161± 0.123
$[10,15]$	0.064 ± 0.066	0.108 ± 0.102	-0.176± 0.099
$[15,30]$	0.017 ± 0.096	-0.196± 0.106	-0.056± 0.122

Table 5.8: Measured Υ polarization and statistical uncertainty. The angle θ^* is calculated in the Collins-Soper frame.

5.3.2 Fit Results

The resulting fits for the finally selected sample are shown in figures A.1 and A.2 for the helicity frame and in figures A.4 and A.5 for the Collins-Soper frame. The summarized polarizations α for each $p_{T,\Upsilon}$ bin are listed in tables 5.7 and 5.8. So far, only statistical uncertainties are considered.

Figure 5.12 shows exemplary the $\cos\theta^*$ distributions for the $\Upsilon(1S)$ resonance in the first $p_{T,\Upsilon}$ bin. θ^* is the polar angle calculated in the helicity frame. Figure 5.13 shows the corresponding plots for the $\Upsilon(2S)$ and $\Upsilon(3S)$ states.

In contrast to the result of DØ, the Υ's seem to be produced unpolarized. The polarization with respect to the Υ transverse momentum for each frame is shown in figure 5.14.

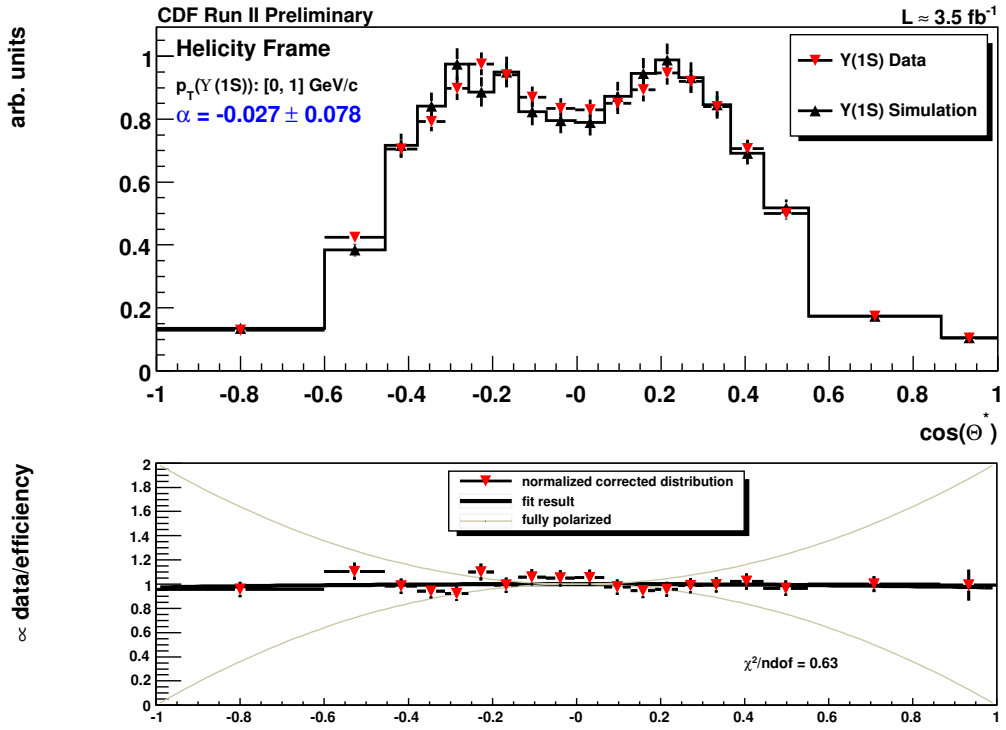

Figure 5.12: The upper plot shows the normalized distributions obtained from measured data and the simulation. The lower plot corresponds to the normalized corrected distribution on which the polarization fit is applied. The grey lines illustrate the distribution with fully transversal and longitudinal polarization.

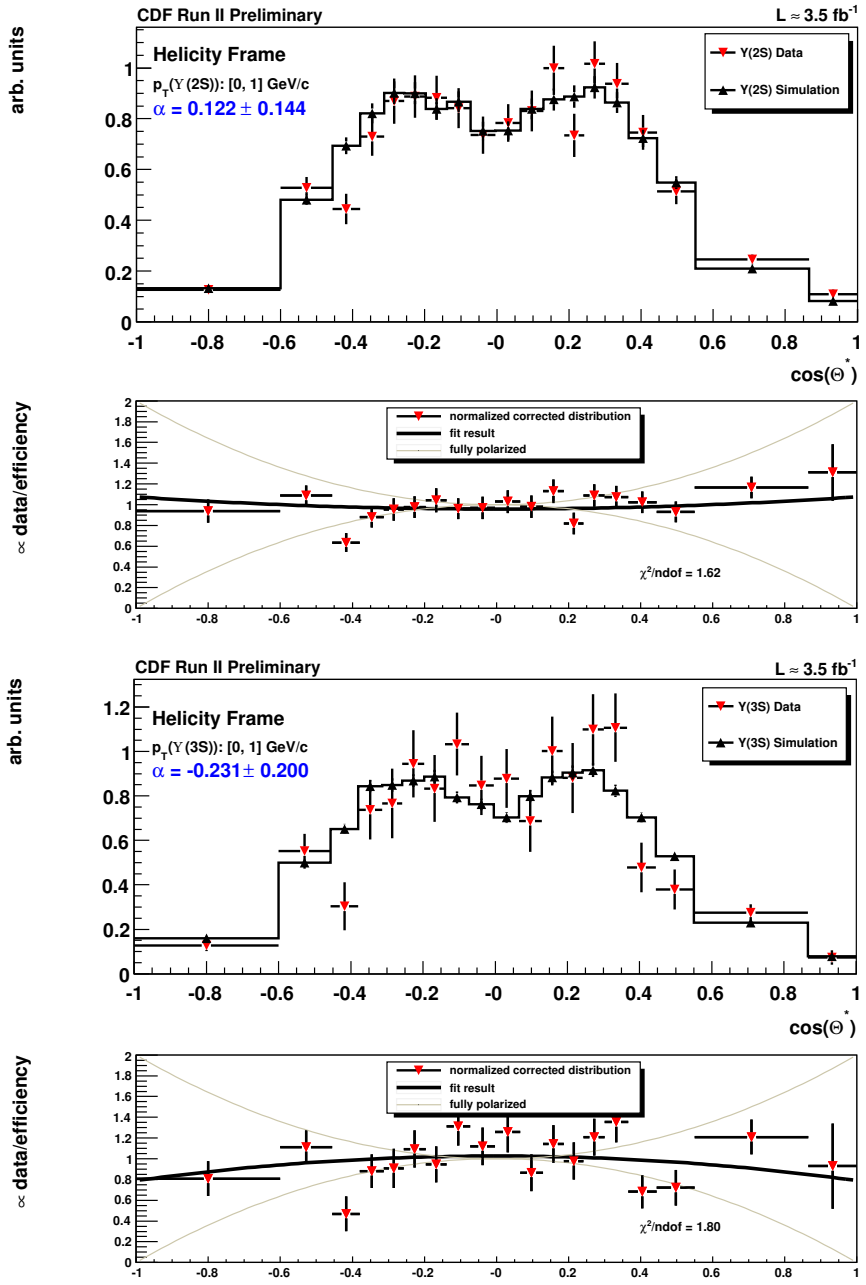

Figure 5.13: Polarization fit to the $\Upsilon(2S)$ and $\Upsilon(3S)$ states in the first $p_{T,\Upsilon}$ bin.

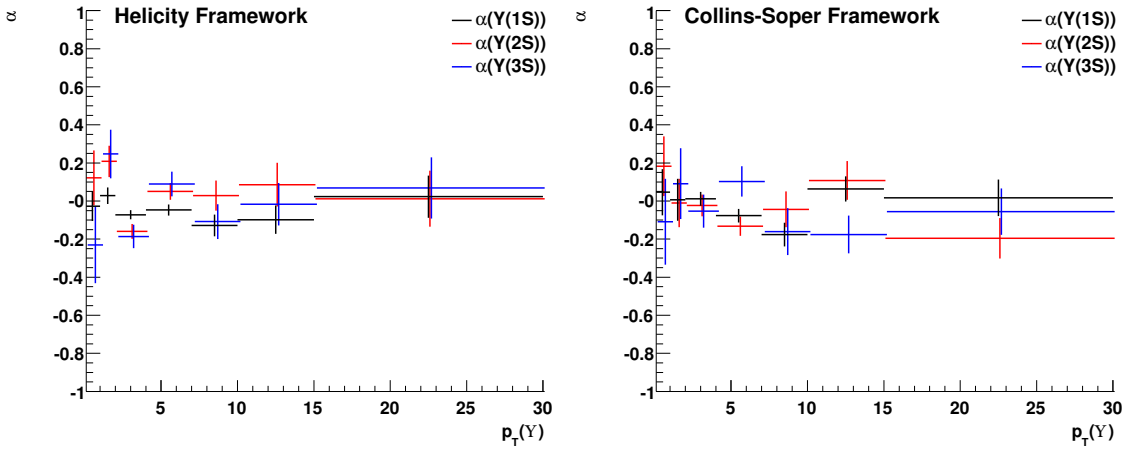

Figure 5.14: Polarization α with respect to $p_{T,\Upsilon}$ for the two frames and for the three Υ states.

5.4 Crosschecks and Systematics

5.4.1 Consistency Checks

Results of this analysis are based on the assumption that the Υ production is understood correctly. In order to proof some aspects of the simulation the following additional checks are investigated.

The resulting distribution of $p_{T,\Upsilon}$ in the simulation is reweighted according to the true result obtained from measured data. The weights are then applied and the $p_{T,\Upsilon}$ distributions between the reweighted simulation and measured data is compared which is shown in figure 4.10. As a result, the reweight procedure is found to be consistent with measured data.

During the analysis it is found out that the simulation does not describe the signal correctly for the $\eta - \phi$ and p_T distributions of the two muons. It is not possible to reweight the simulation accordingly because in this case acceptance would be changed and the corresponding efficiency would not be accessible anymore. Therefore, a selection criterion is required in order to chose only those parts of the simulation that describe the signal well enough. The comparison of the distributions after the selection is shown in figures 4.3, 4.4, 4.5 and 4.6. For this selection the simulation matches signal of measured data very good.

The mass resolution with respect to $\cos\theta^*$ for each $p_{T,\Upsilon}$ bin is evaluated and found to be constant. This is exemplary shown for the first $p_{T,\Upsilon}$ bin in figure 5.15. The highest deviation results of course from the low statistic $\Upsilon(3S)$ resonance. As the simulation yields, which are also obtained by a fit with the same shape parameters as in data, shows the same tendency as in data, no systematic uncertainty due to resolution is applied. The same is done with the Υ mass $\bar{m}$. No $\cos\theta^*$ dependence is found.

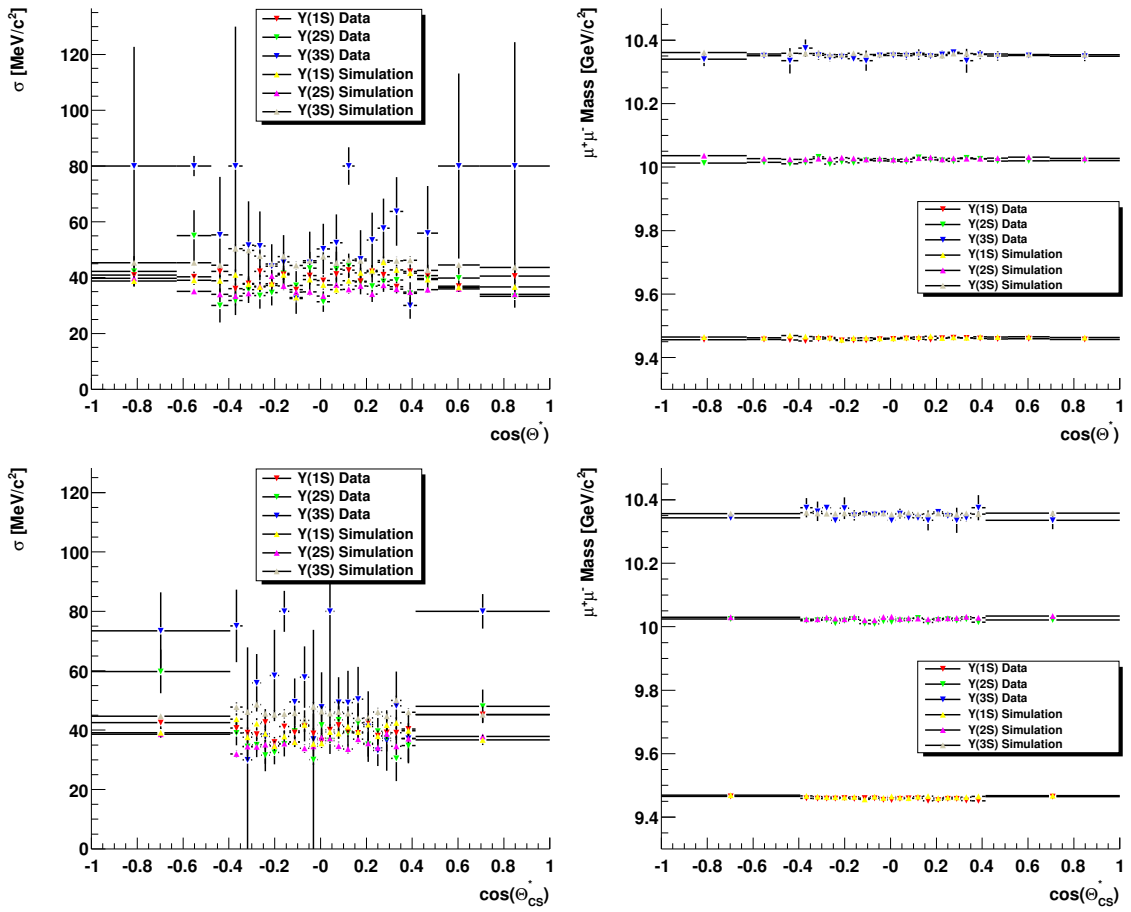

Figure 5.15: The dependence of the resolution and mass as a function of $\cos\theta^*$ is checked for all $p_{T,\Upsilon}$ bins and found to be constant. The plots show exemplary the result for the first bin for $\Upsilon(1S)$, $\Upsilon(2S)$ and $\Upsilon(3S)$.

5.4.2 Systematic Uncertainties

There are two kinds of uncertainties: statistical and systematic. While statistical uncertainties are due to random effects and become lower with higher statistics the latter is due to uncertainties of the used method, e.g. wrong assumptions. Usually systematic uncertainties do not decrease with higher statistics. The statistical uncertainty of the polarization measurement has thus to be added by the systematics which are investigated in the following.

There are three potential source of systematic uncertainties investigated in this analysis as listed below

- **Input $p_{T,\Upsilon}$ Distribution** — In order to study effect of the reweight of the $p_{T,\Upsilon}$ distribution, the polarization is also measured without reweighting $p_{T,\Upsilon}$. The obtained systematic uncertainties are listed in tables 5.9 and 5.10.
- **Muon Acceptance** — The effect of the missing simulation of CMP muons is studied by performing the polarization measurement with the loser $p_{T,\mu^\pm}$ requirements of $p_{T,\mu^\pm} > 2.5\text{GeV/c}$ for CMU muons only and $p_{T,\mu^\pm} > 3.5\text{GeV/c}$. The obtained systematic uncertainties are listed in tables 5.9 and 5.10.
- **Neural Network Selection** — The neural network based selection depends on the fact how well the input variables are described in the simulation. This consistency check is shown figure 4.11. Only the muon likelihood seem to have some mismatch. Due to this, the polarization measurement is also performed without the neural network selection. The obtained systematic uncertainties are also listed in tables 5.9 and 5.10.

The deviation to the final result are added quadratically in order to obtain the systematic uncertainties.

5.5 Results

The final results of the $\Upsilon(1S)$, $\Upsilon(2S)$ and $\Upsilon(3S)$ polarization measurement considering statistical and systematic uncertainties are shown in figure 5.14 for each frame. The resulting values for the polarization α are listed in tabels 5.11 and 5.12.

In the helicity frame there are only slight deviations to zero polarization in the $p_{T,\Upsilon}$ range of $[1,4]\,\text{GeV/c}^2$ while the rest is consistent with unpolarized Υ's. The $\Upsilon(1S)$ and $\Upsilon(3S)$ are consistent to be unpolarized except for the $p_{T,\Upsilon}$ range of $[2,4]\,\text{GeV/c}^2$ where there is a small longitudinal polarization observed. The $\Upsilon(2S)$ shows an small transversal polarization in the $p_{T,\Upsilon}$ range of $[1,2]\,\text{GeV/c}^2$ while in $[2,4]\,\text{GeV/c}^2$ it is observed to be slightly longitudinal polarized.

In the Collins-Soper frame slight deviations from zero polarization are observed in the $p_{T,\Upsilon}$ range of $[4,15]\,\text{GeV/c}^2$. All deviations show small longitudinal polarizations.

	bin	range [GeV/c]	$\Upsilon(1S)$	$\Upsilon(2S)$	$\Upsilon(3S)$
no p_T Reweight	1	$[0, 1]$	-0.035	-0.015	0.032
	2	$[1, 2]$	0.029	0.065	0.056
	3	$[2, 4]$	0.014	0.016	0.005
	4	$[4, 7]$	0.028	0	-0.024
	5	$[7, 10]$	0.003	-0.005	-0.008
	6	$[10, 15]$	0.025	0.017	-0.067
	7	$[15, 30]$	0.209	0.093	-0.029
no NN selection	1	$[0, 1]$	0.023	0.039	-0.112
	2	$[1, 2]$	-0.029	-0.008	0.03
	3	$[2, 4]$	-0.02	-0.02	0.058
	4	$[4, 7]$	-0.013	-0.034	0.017
	5	$[7, 10]$	-0.019	-0.021	-0.009
	6	$[10, 15]$	-0.015	-0.009	-0.056
	7	$[15, 30]$	-0.026	0.002	0.037
loser muon p_T	1	$[0, 1]$	0.198	0.227	0.225
	2	$[1, 2]$	0.083	0.077	0.049
	3	$[2, 4]$	0.028	-0.008	-0.036
	4	$[4, 7]$	0.292	0.244	0.164
	5	$[7, 10]$	0.343	0.345	0.177
	6	$[10, 15]$	0.435	0.408	0.123
	7	$[15, 30]$	0.532	0.397	0.247

Table 5.9: List of systematic uncertainties per $p_{T,\Upsilon}$ in the helicity frame.

	bin	range [GeV/c]	$\Upsilon(1S)$	$\Upsilon(2S)$	$\Upsilon(3S)$
no p_T Reweight	1	$[0,1]$	-0.046	-0.185	-0.052
	2	$[1,2]$	-0.206	-0.102	-0.121
	3	$[2,4]$	-0.035	-0.036	-0.075
	4	$[4,7]$	-0.027	-0.058	-0.003
	5	$[7,10]$	0.016	0.004	0.02
	6	$[10,15]$	0.075	0.131	0.072
	7	$[15,30]$	0.154	0.203	0.201
no NN selection	1	$[0,1]$	0.012	-0.099	-0.007
	2	$[1,2]$	-0.052	0.08	0.098
	3	$[2,4]$	0.012	-0.027	0.024
	4	$[4,7]$	0.003	0.056	-0.021
	5	$[7,10]$	0.014	0.009	0.002
	6	$[10,15]$	0.007	-0.03	-0.001
	7	$[15,30]$			
loser muon p_T	1	$[0,1]$	0.717	0.803	0.892
	2	$[1,2]$	0.464	0.387	0.4
	3	$[2,4]$	0.154	0.168	0.08
	4	$[4,7]$	0.032	0.083	0.241
	5	$[7,10]$	0.069	0.034	0.039
	6	$[10,15]$	0.063	0.002	0.086
	7	$[15,30]$	0.048	-0.007	0.072

Table 5.10: List of systematic uncertainties per $p_{T,\Upsilon}$ in the Collins-Soper frame.

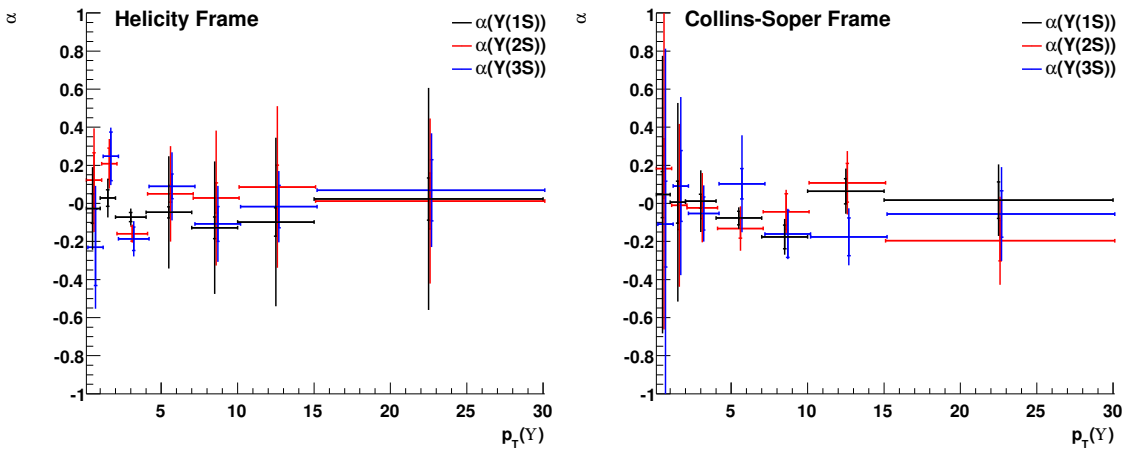

Figure 5.16: Polarization α with as a functio of $p_{T,\Upsilon}$ for the two frames and for the three Υ states considering statistical and systematic uncertainties.

$p_{T,\Upsilon}$ range [GeV/c]	$\alpha(\Upsilon(1S))$	$\alpha(\Upsilon(2S))$	$\alpha(\Upsilon(3S))$
[0, 1]	-0.027±0.078±0.139	0.122±0.144±0.128	-0.231±0.2±0.123
[1, 2]	0.028±0.043±0.059	0.208±0.082±0.048	0.247±0.128±0.023
[2, 4]	-0.072±0.024±0.020	-0.159±0.039±0.008	-0.186±0.062±0.030
[4, 7]	-0.047±0.029±0.266	0.05±0.044±0.206	0.089±0.065±0.114
[7, 10]	-0.128±0.057±0.291	0.028±0.079±0.276	-0.108±0.091±0.108
[10, 15]	-0.098±0.075±0.367	0.086±0.115±0.3093	-0.017±0.111±0.076
[15, 30]	0.023±0.111±0.472	0.012±0.147±0.286	0.069±0.161±0.138

Table 5.11: Measured Υ polarization and statistical uncertainty. The angle θ^* is calculated in the helicity frame.

$p_{T,\Upsilon}$ range [GeV/c]	$\alpha(\Upsilon(1S))$	$\alpha(\Upsilon(2S))$	$\alpha(\Upsilon(3S))$
[0, 1]	0.046±0.121±0.608	0.183±0.157±0.688	-0.109±0.225±0.696
[1, 2]	0.006±0.11 ±0.412	-0.01±0.127±0.3	0.091±0.186±0.282
[2, 4]	0.012±0.036±0.126	-0.023±0.057±0.125	-0.053±0.087±0.061
[4, 7]	-0.077±0.036±0.021	-0.132±0.051±0.066	0.103±0.08±0.175
[7, 10]	-0.176±0.062±0.032	-0.044±0.094±0.021	-0.161±0.123±0.009
[10, 15]	0.064±0.066±0.053	0.108±0.102±0.064	-0.176±0.099±0.051
[15, 30]	0.017±0.096±0.092	-0.196±0.106±0.125	-0.056±0.122±0.124

Table 5.12: Measured Υ polarization and statistical uncertainty. The angle θ^* is calculated in the Collins-Soper frame.

Chapter 6

X_b Search

Motivated by the observed resonance $X(3872)$ in the final state $J/\psi\pi^+\pi^-$, this analysis presents the search for a resonance in the corresponding decay channel $\Upsilon(1S)\pi^+\pi^-$ of the bottom sector. In the following this hypothetical state is called X_b. The label b represents the fact that this resonance is searched in the final state with bottom quark content. It cannot be labeled with a certain mass though, as it is the case for the $X(3872)$. Due to the unknown nature of the $X(3872)$ it is not possible to unambiguously predict the mass of the X_b. Furthermore, it is even unsure if the counterpart of the $X(3872)$ in the bottom sector exists at all.

In this analysis the X_b search is performed in the following steps. At first a phase space simulation is used in order to model the decay $X_b \rightarrow \Upsilon(1S)\pi^+\pi^-$. The simulation is already described in chapter 4. The X_b is assumed to have the quantum numbers $J^{PC} = 1^{++}$, thus the simulation has to be reweighted accordingly. The decay topology and calculation of the quantum number weights is described in the first section. The reconstruction and selection of the measured CDF II data in the final state $\Upsilon(1S)\pi^+\pi^-$ are presented in the second section. Efficiencies and yield expectations are tested by the $\Upsilon(2S)$ state. The same selection method is then applied to the $\Upsilon(3S)$ and the X_b. The neural network based selections are presented in the third section. At first it is searched for the $\Upsilon(3S)$. Because there it is not significantly observed an upper limit relative to the $\Upsilon(2S)$ is set on the ratio of the corresponding cross sections $\sigma_{\Upsilon(3S)}/\sigma_{\Upsilon(2S)}$ at a credibility level of 95%. This is then checked by the ratio obtained from the decay into two muons. The fitting procedure in order to obtain the upper limit is described in the fourth section. The search for the X_b is performed in the mass range $10.2\,\mathrm{GeV/c^2} \leq m_{X_b} \leq 11.2\,\mathrm{GeV/c^2}$. An mass dependent optimized selection is required and the result is fitted for several mass positions in order to obtain an mass dependent upper limit on the ratio of the cross sections of the X_b and the $\Upsilon(2S)$ times the unknown branching ratio of the X_b at a credibility level of 95%. In the fifth section the results are presented. Finally, systematic uncertainties are discussed.

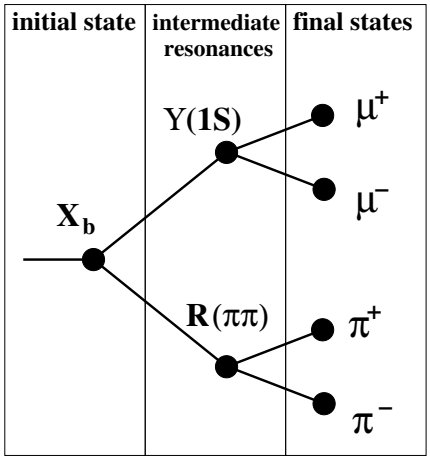

Figure 6.1: Decay Topology of the X_b. The decay proceeds in three sequential two-body decays.

6.1 Decay Topology

In analogy to the $X(3872)$, the X_b is searched for in the three-body decay channel

$$X_b \to \Upsilon(1S)\pi^+\pi^-$$

where the $\Upsilon(1S)$ is reconstructed in its decay to two muons. This decay chain is modelled as a sequence of three two-body decays. It is thus necessary to construct the X_b decay amplitudes in order to be able to simulate the decay correctly.

$$X_b \to \Upsilon(1S)R(\pi\pi),$$

$$\Upsilon(1S) \to \mu^+\mu^-,$$

$$R(\pi\pi) \to \pi^+\pi^-.$$

Hereby the two opposite charged pions in the final state decay via an intermediate dipion resonance $R(\pi\pi)$.

In figure 6.1 the decay chain is schematically shown. As already described in section 1.2, the cross section is proportional to the squared absolute matrix element $|\mathcal{M}|^2$ which is deduced from the decay amplitudes. At the Tevatron, the momentum distribution of the X_b is assumed to be independent of its quantum numbers, since the state is assumed to be produced unpolarized in the fragmentation of the collision products. Information about the quantum numbers J^{PC} is however contained in the mass distribution $m_{\pi\pi}$ of the dipion resonance, since the X_b quantum numbers affect both the resonance nature of the intermediate dipion resonance and the mass dependence of the decay.

The two-body decay of a mother particle I into its daughter particles F_1 and F_2 can be written as

$$\begin{aligned} I &\rightarrow F_1 F_2 \\ J_I^{P_I C_I} &\rightarrow J_1^{P_1 C_1} J_2^{P_2 C_2}. \end{aligned}$$

The total angular momentum J is conserved. The total final-state angular momentum J_F is determined by combining the spins J_1 and J_2 of the final-state particles to a common spin S_F, which in turn is combined with the relative angular momentum L_F between the two final state particles to the total final-state angular momentum J_F.

$$\begin{aligned} S_F &= J_1 \oplus J_2, \\ J_F &= L_F \oplus S_F. \end{aligned}$$

The X_b decay and each of its sub-decays are assumed to be electromagnetic or strong decays. Because of this, C-parity and parity P are conserved quantities as well. The conservation rules are:

$$\begin{aligned} J_I &= J_F, \\ P_I &= P_F = P_1\, P_2 \times (-1)^{L_F}, \\ C_I &= C_F. \end{aligned}$$

In order to determine the final state C-parity C_F the nature of the daughter particles needs to be considered. C_F is given by:

- $C_F = C_1\, C_2$ for a system of neutral daughter particles,
- $C_F = (-1)^{L_F+S_F}$ for a neutral system of two charged particles.

The decay amplitudes of the X_b are constructed using the helicity formalism. This allows a straightforward treatment of sequential two-body decays. In this analysis the conventions by Richman [83] are used. The components of the complete decay matrix element consist of three vertex decay matrix elements describing the three two-body decays and two propagator terms describing the time evolution of the intermediate resonances. This is written as

$$\begin{aligned} \mathcal{M}_{total} = &\mathcal{M}(X_b \rightarrow \Upsilon(1S) R(\pi\pi)) \\ &\times \Upsilon(1S)\text{-Propagator} \times \mathcal{M}(\Upsilon(1S) \rightarrow \mu^+\mu^-) \\ &\times R(\pi\pi)\text{-Propagator} \times \mathcal{M}(R(\pi\pi) \rightarrow \pi^+\pi^-). \end{aligned}$$

In the helicity formalism the angles describing the decay direction are defined in the rest frame of a decaying particle. The definition of the decay angles in the sequential two-body decay chain of the X_b is illustrated in figure 6.2. The polar

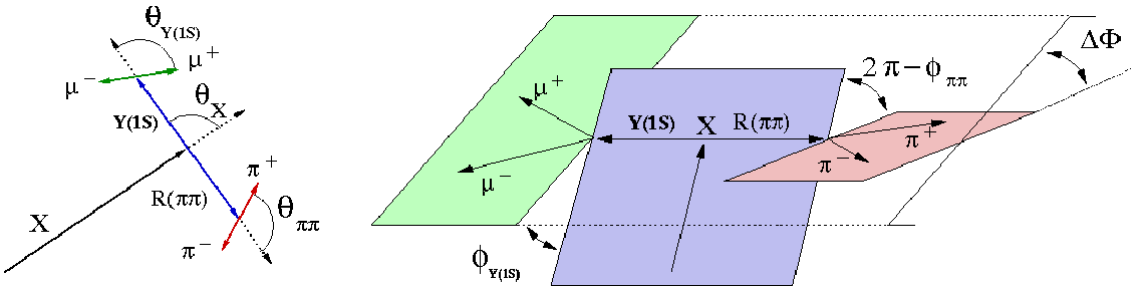

Figure 6.2: Definition of the angles, used to describe the particle momenta.

decay	$X_b \to \Upsilon(1S)R(\pi\pi)$	$\Upsilon(1S) \to \mu^+\mu^-$	$R(\pi\pi) \to \pi^+\pi^-$
angles	θ_{X_b}, ϕ_{X_b}	$\theta_{\Upsilon(1S)}$, $\phi_{\Upsilon(1S)}$	$\theta_{\pi\pi}$, $\phi_{\pi\pi}$
mother momentum	$\vec{p}_X$	$\vec{p}_{\Upsilon(1S)}$ in X_b cms	$\vec{p}_{\pi\pi}$ in X_b cms
daughter momentum	$\vec{p}_{\Upsilon(1S)}$ in X_b cms	$\vec{p}_{\mu^+}$ in $\Upsilon(1S)$ cms	$\vec{p}_{\pi^+}$ in $R(\pi\pi)$ cms
reference vector	beam axis	$\vec{p}_{X_b}$	$\vec{p}_{X_b}$

Table 6.1: Momenta and vectors, used for the angle calculation. θ is the angle between the mother and one daughter momentum. ϕ is the angle between the two planes, one spanned by the daughter momentum and the mother momentum and the other spanned by the mother momentum and the reference vector.

angles θ are defined as the angle between the mother particle momentum direction and the momentum of one of the daughter particles in the mother rest frame. Since in the mother rest frame both daughter particles are 'back-to-back', it does not matter which particle is chosen, but this arbitrary selection needs to be applied consistently. The definition of an azimuthal angle ϕ needs an additional independent reference vector in order to define a proper $\phi = 0$ reference. Used is either the proton beam axis or the X_b momentum, depending on the decay. The momenta used for the angle calculations are listed in table 6.1.

The decay matrix element of a single vertex is determined by the momenta of the incoming and outgoing particles, and by the involved spins. Since the matrix element is constructed in the helicity formalism, the decay is examined in the mother particle rest frame. The angular dependence of such a single decay vertex is given by the Wigner rotation functions $D^J_{J_z,\lambda}(\theta,\phi)$. For low spins J they are listed in [84]. The Wigner functions give a quantitative answer to the question 'Given a state with spin J and spin projection J_z along a quantization axis, what is the amplitude to find the spin projection λ with a new quantization axis, turned by (θ,ϕ)?' The two-body decay of a particle with spin J and helicity λ_I into two daughter particles with helicities λ_1 and λ_2 and momentum magnitude k^* each is described by the decay matrix element, that under angular change (θ,ϕ) of the quantization axis is given

by:

$$\mathcal{M}(|J,\lambda_I\rangle \to |L,S,\lambda_1,\lambda_2,k^*,\theta,\phi\rangle) \quad \propto \quad c_{LS}(\lambda_1,\lambda_2)\; D^J_{\lambda_I,\lambda_1-\lambda_2}(\theta,\phi)\; {k^*}^L f_L(k^*).$$

where k^* is the three-momentum magnitude of one of the two daughter particles in the decay which is completely determined by the involved masses and $f_L(k^*)$ is a form factor used to avoid divergences of the matrix elements for higher momenta. This analysis uses a widely used model of Blatt and Weisskopf [85]. The form factors for $L \leq 1$ are:

$$f_{L=0}(k^*) \propto 1 \ ,$$
$$f_{L=1}(k^*) \propto \sqrt{\frac{r^2}{1+(k^*r)^2}} \ .$$

For the interaction radius r the common value of $r = 1$ fm is used. The coefficients $c_{LS}(\lambda_1,\lambda_2)$ are determined for the case when $\phi = \theta = 0$. The LS-frame then coincides with the helicity frame and the quantization axes are the same. The values $c_{LS}(\lambda_1,\lambda_2)$ are obtained [86, 87] by

$$c_{LS}(\lambda_1,\lambda_2) = \left(\begin{array}{cc|c} J_1 & J_2 & S \\ \lambda_1 & -\lambda_2 & \lambda_1-\lambda_2 \end{array}\right) \times \left(\begin{array}{cc|c} L & S & J \\ 0 & \lambda_1-\lambda_2 & \lambda_1-\lambda_2 \end{array}\right)$$

as a product of two Clebsch-Gordan coefficients. The first coefficient describes the coupling of the two daughter particles to the combined spin S. The second coefficient describes the combination of L and S to the total angular momentum J. The orbital angular momentum does not contribute, since in the chosen frame any orbital momentum is perpendicular to the quantization axis.

To simulate the transition rate T, the matrix element will be used to reweight pure phase space simulation events according to Fermi's golden rule

$$T(X_b \to \mu^+\mu^-\pi^+\pi^-) = \frac{2\pi}{\hbar}|\mathcal{M}_{total}|^2 \ \text{PS}.$$

The description of the phase space PS will be handled by the event generator. In order to form a weight w_{JPC} from the matrix element, the matrix element needs to be squared and summed over all possible helicities, since those are not measured. This leads to

$$w_{JPC} \propto \frac{1}{2J+1} \sum_{\lambda_{X_b}} \sum_{\lambda_{\mu^+}} \sum_{\lambda_{\mu^-}} \sum_{\lambda_{\pi^+}} \sum_{\lambda_{\pi^-}} \left| \sum_{\lambda_{\Upsilon(1S)}} \sum_{\lambda_{\pi\pi}} \mathcal{M}_{total} \right|^2 ,$$

where averaging over all initial state helicities λ_{X_b}, incoherently summing over all final state helicities and coherently summing over all intermediate state helicities is done. This looks like a very tedious calculation, however, this general equation is simplified significantly by exploiting specific properties of the analyzed decay. It should be noted that the decay weight will be exclusively used to reweight neural network input candidates. Any overall normalization from global factorizing constants or coefficients is neglected.

6.1.1 $\Upsilon(1S) \to \mu^+\mu^-$ Decay

The quantum numbers of the $\Upsilon(1S)$ are $J^{PC} = 1^{--}$, the muons have $J = 1/2$. Muons are point-like particles and are defined with positive intrinsic parity for particles and negative for antiparticles. Their mass is $\approx 105\,\mathrm{MeV/c^2}$. The decay time of the $\Upsilon(1S)$ is so large that the uncertainty in energy spread Γ is very small and can be neglected. Thus the intermediate dimuon system is treated as a $\Upsilon(1S)$ with the world average mass listed in table 5.1. As a result

$$k^*_{\Upsilon(1S)} = \frac{c}{2}\sqrt{m^2_{\Upsilon(1S)} - 4m^2_\mu} \approx 4.73\,\mathrm{GeV}/c$$

is constant, thus any momentum dependence can be ignored.

The decay is dominated by the annihilation of the two bottom quarks of the $\Upsilon(1S)$ into a virtual photon which transforms into two muons. The massless photon cannot have helicity 0, i.e. it is transversely polarized [a]. So from the $2 \times 2 = 4$ possible helicity combinations only those with $\lambda_{\mu^+} - \lambda_{\mu^-} = \pm 1$ need to be considered.

For those two terms, the helicity couplings $A(+\frac{1}{2}, -\frac{1}{2})$ and $A(-\frac{1}{2}, +\frac{1}{2})$ occur. The helicity couplings $A(\lambda_1, \lambda_2)$ are related to the LS-couplings by a linear combination of different LS-couplings:

$$A_{hel}(\lambda_1, \lambda_2) = \sum_i c_{LS_i}(\lambda_1, \lambda_2)\; B(LS_i)$$

It can be shown [83] that parity relates two couplings $A(\lambda_1, \lambda_2)$ and $A(-\lambda_1, -\lambda_2)$ by the relation

$$A(\lambda_1, \lambda_2) = \eta \;\times\; A(-\lambda_1, -\lambda_2).$$

η is the so-called 'naturality', defined as

$$\eta = P\, P_1\, P_2 \times (-1)^{J - J_1 - J_2}.$$

P, P_1, and P_2 are the intrinsic parities of the involved particles.

Since the quantum numbers of the $\Upsilon(1S)$ are 1^-, the combined parity of two muons is (-1), and the muon spin is $1/2$, it follows that the naturality is $\eta = (-1) \times (-1) \times (-1)^{1-1/2-1/2} = +1$. As a consequence only one independent helicity coupling $c(\lambda_{\mu^+}, \lambda_{\mu^-})$ remains. It can be treated as an overall constant and can be ignored.

The simplified matrix element thus reads:

$$\mathcal{M}(\Upsilon(1S) \to \mu^+\mu^-) \propto\; D^1_{\lambda_{\Upsilon(1S)}, \underbrace{\lambda_{\mu^+} - \lambda_{\mu^-}}_{=\pm 1}}(\theta_{\Upsilon(1S)}, \phi_{\Upsilon(1S)}).$$

[a] This is not completely true here, because the photon is virtual and off-shell and thus also can have a mass, but in the limit where the decaying particle is much heavier than the muon, the transversality is still a very good approximation.

6.1.2 $R(\pi^+\pi^-) \to \pi^+\pi^-$ Decay

Charged pions have $J^P = 0^-$ and because they have charge they are not eigenstates of the charge parity operation C. The quantum numbers J^{PC} of the dipion system can be constrained. It is assumed that the X_b quantum numbers are $J^{PC} = 1^{++}$ and that the decay proceeds via a ρ that corresponds to a 1^{--}-dipion system with the relative angular momentum between the two pions of $L_{\pi\pi} = 1$. This assumption is based on the fact that the $X(3872)$ could be a molecule and that measurements are consistent with $J^{PC} = 1^{++}$ [17] as also predicted from theory if the $X(3872)$ is a molecule [19, 20]. Furthermore, it is also measured that the intermediate dipion system of the decay X(3872)$\to J/\psi\pi^+\pi^-$ proceeds via ρ [16]. In case of the $\Upsilon(2S)$ and $\Upsilon(3S)$ the decay proceeds via an S-wave, i.e. a 0^{++}-dipion system with $L_{\pi\pi} = 0$.

However, it must be mentioned that since the allowed dipion mass range for possible X_b masses up to 11.2 GeV/c^2 is

$$\begin{aligned} 2m_\pi < m_{\pi\pi} < m_{X_b} - m_{\Upsilon(1S)}, \\ 280\ \mathrm{MeV}/c^2 < m_{\pi\pi} < 1740\ \mathrm{MeV}/c^2, \end{aligned}$$

also higher dipion resonances are possible like the $f_2(1270)$ resonance with $L_{\pi\pi} = 2$ and the $\rho_3(1690)$ with $L_{\pi\pi} = 3$.

The final state pions have spin 0, thus the sum over the final state helicities of the pions are completely removed. Because the combined pion spin is 0 as well, $L_{\pi\pi}$ must be identical to $J_{\pi\pi}$. The quantum numbers of a state, decaying into two charged pions, are thus completely determined by their relative angular momentum:

$$\begin{aligned} J_{\pi\pi} &= L_{\pi\pi}, \\ P_{\pi\pi} &= (-1)^{L_{\pi\pi}}, \\ C_{\pi\pi} &= (+1) \times (-1)^{L_{\pi\pi}}. \end{aligned}$$

Consequently, the helicity coupling $A(\lambda_{\pi^+} = 0, \lambda_{\pi^-} = 0)$ only considers the momentum dependence ${k^*_{\pi\pi}}^{L_{\pi\pi}} f_{L_{\pi\pi}}(k^*_{\pi\pi})$. As a result, the vertex matrix element is given by

$$\mathcal{M}(R(\pi\pi) \to \pi^+\pi^-) \propto\ D^{J_{\pi\pi}}_{\lambda_{\pi\pi},0}(\theta_{\pi\pi}, \phi_{\pi\pi})\ {k^*_{\pi\pi}}^{J_{\pi\pi}} f_{J_{\pi\pi}}(k^*_{\pi\pi}).$$

Therefore, the dependence on $k^*_{\pi\pi}$ is in practise a dependence on $m_{\pi\pi}$. Since the pion masses are identical and constant, one simply obtains

$$k^*_{\pi\pi} = \frac{c}{2}\sqrt{m^2_{\pi\pi} - 4m^2_\pi}.$$

6.1.3 Propagator Terms

The $\Upsilon(1S)$ propagator is only a constant since the intermediate dimuon state is treated as a resonance with fixed world average $\Upsilon(1S)$ mass not allowing for any mass deviations. Thus this propagator term can be ignored. This is however not

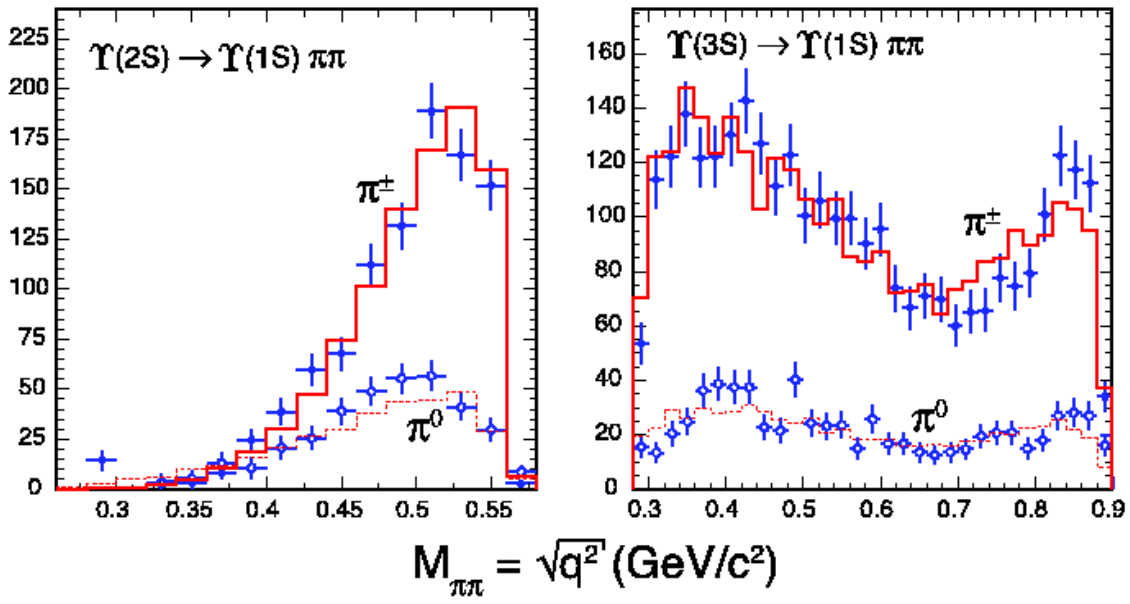

Figure 6.3: Dipion spectra for the decays $\Upsilon(2S) \to \Upsilon(1S)\pi^+\pi^-$ and $\Upsilon(3S) \to \Upsilon(1S)\pi^+\pi^-$ from CLEO [88]. The plots show overlaying projections of the data (points with error bars) and the fit result (histograms) onto the $m_{\pi\pi}$ variable.

the case for the dipion system. Depending on the initial state that decays into $\Upsilon(1S)\pi^+\pi^-$ the dipion dynamics is assumed differently. This is discussed in the following for each decay accordingly.

6.1.4 $\Upsilon(2S) \to \Upsilon(1S)\pi^+\pi^-$ Decay

In case of the reference state $\Upsilon(2S)$ two models of the matrix elements are used. The first calculation is based on the measurement of di-pion transitions among $\Upsilon(3S)$,$\Upsilon(2S)$ and $\Upsilon(1S)$ states from CLEO [88]. They use the di-pion mass parameterization of the form

$$\frac{d\sigma}{dm_{\pi\pi}} \propto PS \times (\mathcal{A} \cdot (m^2_{\pi\pi} - 2m^2_{\pi}) + \mathcal{B} \cdot E_{\pi^+}E_{\pi^-})^2$$

where $E_{\pi^\pm}$ denotes the energies of the pions in the parent rest frame and the quantities $\mathcal{A}$ and $\mathcal{B}$ are form factors which are assumed to be complex constants. Their measurement results for the decay $\Upsilon(2S) \to \Upsilon(1S)\pi^+\pi^-$

$$\mathcal{B}/\mathcal{A} = -0.753 \pm 0.064 + i(\pm 0.000 \pm 0.108).$$

The fit result compared to data from CLEO is shown in the left plot of figure 6.3. Only the charged modes are of interest in this analysis.

Another approach is the 'Adler-zero' model of Voloshin and Zhakarov [89]. Their

di-pion mass parameterization is of the form

$$\frac{d\sigma}{dm_{\pi\pi}} \propto PS \times (m_{\pi\pi}^2 - \lambda m_{\pi}^2)^2,$$

where λ is a free parameter which is usually set to 4. For the $\psi(2S)$ this parameter is precisely measured by BES [90]:

$$\lambda = 4.35 \pm 0.06 \pm 0.17.$$

In this analysis the value of $\lambda = 4$ is used since λ is not measured for the $\Upsilon(2S)$.

In addition, the k^* dependences are fixed to the correct description for the $J^{PC} = 1^{--}$ case. This leads to $L_{\Upsilon(2S)} = 0$ and $L_{\pi\pi} = 0$. With the fixed mass dependence and the di-pion dependence as

$$\frac{d\sigma}{dm_{\pi\pi}} \propto PS \times (\mathcal{P}_{\pi\pi})^2.$$

The generic angular matrix element for the $\Upsilon(2S)$ is then given by:

$$\begin{aligned} M_{total,\Upsilon(2S)} \propto\ & c_{LS}(\lambda_{\Upsilon(1S)}, \lambda_{\pi\pi})\ D^{J_{\Upsilon(2S)}}_{\lambda_{\Upsilon(2S)},\lambda_{\Upsilon(2S)}-\lambda_{\pi\pi}}(\theta_{\Upsilon(2S)}, \phi_{\Upsilon(2S)}) \\ & \times (\mathcal{P}_{\pi\pi}) \\ & \times D^{J_{\pi\pi}}_{\lambda_{\pi\pi},0}(\theta_{\pi\pi}, \phi_{\pi\pi}) \\ & \times D^{1}_{\lambda_{\Upsilon(1S)},\lambda_{\mu^+}-\lambda_{\mu^-}}(\theta_{\Upsilon(1S)}, \phi_{\Upsilon(1S)}) \quad . \end{aligned}$$

6.1.5 $\Upsilon(3S) \to \Upsilon(1S)\pi^+\pi^-$ Decay

The transition $\Upsilon(3S) \to \Upsilon(1S)\pi^+\pi^-$ is known to defy the straightforward predictions by displaying a peculiar double-peaked $m_{\pi\pi}$ spectrum which is shown in the right plot of figure 6.3. Therefore the 'Adler-zero' model cannot be applied here.

Again, the CLEO [88] result for the di-pion mass prediction of the form already described in case for the $\Upsilon(2S)$ transition is used here. Their measured parameters for the decay $\Upsilon(3S) \to \Upsilon(1S)\pi^+\pi^-$ are

$$\mathcal{B}/\mathcal{A} = -2.523 \pm 0.031 + i(\pm 1.189 \pm 0.051).$$

The generic angular matrix element for the $\Upsilon(3S)$ decay is the same as for the $\Upsilon(2S)$ but with the above parameters.

6.1.6 $X_b \to \Upsilon(1S)R(\pi\pi)$ Decay

It is important to determine the allowed combinations of combined spin S_X and relative angular momentum L_X in the X_b decay. While the possible combinations

J^{PC}_X	$J^{PC}_{\Upsilon(1S)}$	$J^{PC}_{\pi\pi}$	S	parity-allowed LS
1^{++}	1^{--}	1^{--}	0,1,2	01, 21, 22
1^{++}	1^{--}	2^{++}	1,2,3	10, 11, 12, 32, 33
1^{++}	1^{--}	3^{--}	2,3,4	22, 23, 43, 44
1^{--}	1^{--}	0^{++}	1	01, 21

Table 6.2: Parity-allowed LS combinations in the decay to $\Upsilon(1S)R(\pi\pi)$. The X_b is assumed to have the quantum numbers $J^{PC} = 1^{++}$ and the $\Upsilon(2S)$ and $\Upsilon(3S)$ have $J^{PC} = 1^{--}$. Listed are possible J^{PC} hypotheses, the daughter quantum numbers, and their allowed combinations of combined spin S_X and relative angular momentum L_X.

are given by angular momentum conservation, the additional conservation of parity reduces the allowed combinations to combinations with either odd or even relative angular momentum L_X. Table 6.2 lists some of the allowed possibilities in the decay to $\Upsilon(1S)R(\pi\pi)$ for each considered quantum number hypothesis. In this analysis only the X_b decay via a $\rho(770)$ and the $f_2(1270)$ resonance is studied.

The mass behavior of the dipion system is given by a relativistic Breit-Wigner function,

$$R(\pi\pi)\text{-Propagator} = BW_r(m_{\pi\pi}) = \frac{1}{m^2_{\pi\pi} - m^2_r + i m_r \Gamma_r}.$$

The quantity m_r is the world average ρ (775.8 MeV/c^2 [9]) or f_2 (1.2754 GeV/c^2 [9]) mass respectively. Since these resonances are broad, kinematic behavior changes over its mass range. This is reflected in an energy-dependent width [91], modifying the nominal width Γ_r as a function of the dipion mass $m_{\pi\pi}$:

$$\Gamma_r(m_{\pi\pi}) = \Gamma_{r,0} \times \left(\frac{k^*_{\pi^+}(m_{\pi\pi})}{k^*_{\pi^+}(m_{\pi\pi} = m_r)}\right)^{(2L_{\pi\pi}+1)} \frac{m_r}{m_{\pi\pi}} \frac{f^2_{L_{\pi\pi}}(k^*_{\pi^+}(m_{\pi\pi}))}{f^2_{L_{\pi\pi}}(k^*_{\pi^+}(m_{\pi\pi} = m_r))}.$$

The used nominal width are $\Gamma_{\rho,0} = 150.3$ MeV/c^2 and $\Gamma_{f_2,0} = 185.2$ MeV/c^2 [9]. The Blatt-Weisskopf form factors enter with the same interaction radius choice as already proposed.

As a result, the simulation is reweighted according to the assumed quantum numbers of the initial state and the intermediated dipion resonance. The $\Upsilon(2S)$ and $\Upsilon(3S)$ have $J^{PC} = 1^{--}$ and their dipion resonance modelled according to a measurement obtained from CLEO. The X_b is assumed to have $J^{PC} = 1^{++}$. In this case two dipion models are considered: the ρ and the f_2.

6.2 Data Reconstruction

For the X_b search all data taken until August 2008 is used which corresponds to the run number range from 138425 to 266513 and an integrated luminosity of about 3.5fb^{-1}. The corresponding dataset names are `xbmm0d, xbmm0h, xbmm0i, xbmm0j, xbmmij, xbmmik` and `xbmmfm`. The data is selected by the dimuon upsilon trigger,

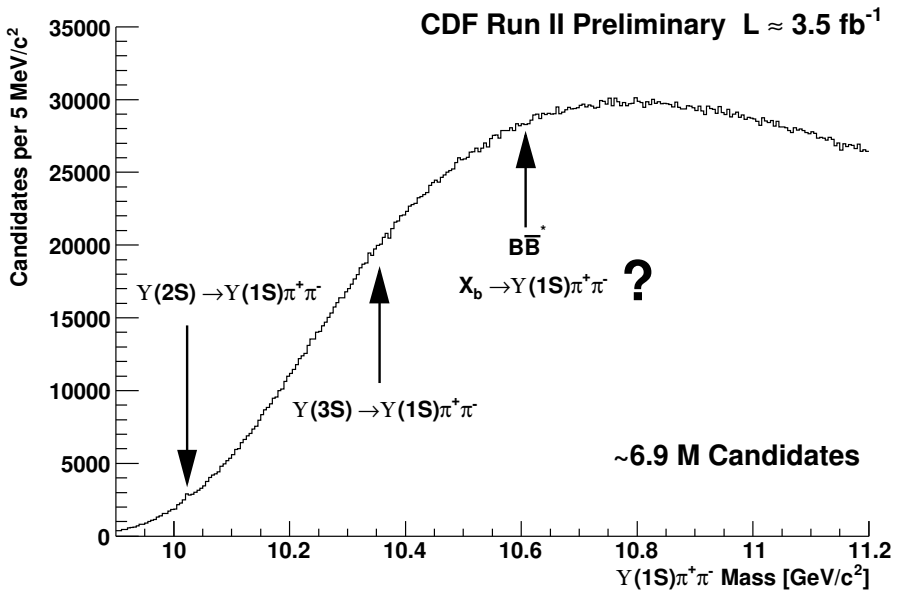

Figure 6.4: The preselected $\Upsilon(1S)\pi^+\pi^-$ mass spectra without required pion quality selection. None of the resonances are clearly visible at the preselection stage.

leading to a sample of $\Upsilon(1S)$ candidates that are subsequently combined with pions to form the X_b candidates.

6.2.1 Preselection Cuts

The basic preselection cuts are chosen in order to remove obvious background from data. The requirements are already described in section 4.1. Candidates that fullfill the all requirements are shown in figure 6.5 and candidates without required pion quality selection are shown in figure 6.5. For low mass candidates the pions are very slow. Consequently, due to their highly curved tracks, it is not possible for the detector to 'see' them all and reconstruct them correctly. This acceptance effect leads to the rising shape of the invariant mass at the left-hand side of the distribution. The shape of the right-hand side results from trigger requirements.

Usually more selection requirements have to be fullfilled like the pion quality cuts described in section 4.1. There are two reasons why the pion quality selection requirements are not demanded: Firstly, obviously in order to not remove low p_T pions which can be combined to possible $\Upsilon(2S)$ candidates which is produced close to the threshold and secondly, because the neural network based selection method is tested for efficiencies and yield expectations on the $\Upsilon(2S)$.

In this analysis the pion quality cuts are only applied in case for the $\Upsilon(3S)$ and X_b neural network trainings. The final selection as well as the calculated efficiencies and yield expectations are however calculated for $p_{T,\pi^\pm} \geq 0.4$ GeV/c because the simulation otherwise overestimates the detector acceptance.

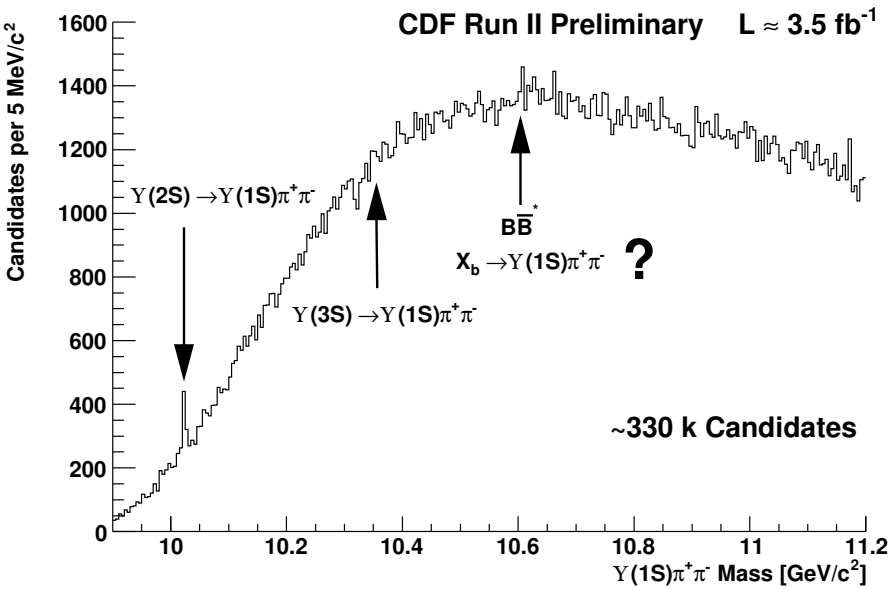

Figure 6.5: The preselected $\Upsilon(1S)\pi^+\pi^-$ mass spectra with required pion quality selection. After required pion quality cuts the $\Upsilon(2S)$ state is clearly visible.

6.2.2 Final Selection Optimization

The finally used selection criterion is based on the usage of the already described neural network technique. The resonances $\Upsilon(2S)$ and $\Upsilon(3S)$ serve as a cross-check of the analysis method. Both resonances are known to decay to $\Upsilon(1S)\pi^+\pi^-$ Furthermore, the study of the dimuon spectra shows clearly that all three resonances are produced in the CDF II detector. Thus there are also $\Upsilon(2S)$ and $\Upsilon(3S)$ decays into the final $\Upsilon(1S)\pi^+\pi^-$ state. The analysis steps are described in the following listing.

- **Cross-check with** $\Upsilon(2S)$ — The $\Upsilon(2S)$ state serves as a testing resonance for the cross-check of the analysis strategy applicability. The resonance is already visible when all preselection and pion quality requirements are fullfilled. However, at the preselection stage this resonance is not clearly visible. The selection method thus is applied to these candidates. If the $\Upsilon(2S)$ can be extracted by the used final selection criterion efficiencies and yield expectations can be cross-checked. If the result is consistent the same method can be applied to the $\Upsilon(3S)$ which is not visible even after all preselection and pion quality cuts.

- **Search for** $\Upsilon(3S)$ — The same selection method as applied to the $\Upsilon(2S)$ is used in order to search for the $\Upsilon(3S)$. Because no significant resonance is observed, an upper limit on the $\Upsilon(3S)$ cross section relative to the $\Upsilon(2S)$ cross section is set. This is then cross-checked with the ratio obtained from the decays to $\mu^+\mu^-$.

- **Search for X_b** — In contrast to the known $\Upsilon(2S)$ and $\Upsilon(3S)$ resonances, the invariant mass of the X_b is unknown. Thus, the mass range of $10.2\,\mathrm{GeV/c^2} \leq m_{X_b} \leq 11.2\,\mathrm{GeV/c^2}$ is analyzed. In $200\,\mathrm{MeV/c^2}$ ranges, neural network trainings are performed in order to obtain a selection criterion. The selected candidates are then evaluateded for setting an mass dependent upper limit relative to the $\Upsilon(2S)$, the same as it is done for the $\Upsilon(3S)$, however not for one mass position but with respect to several mass positions in steps of $10\,\mathrm{MeV/c^2}$.

The neural network training is performed with a simulated resonance sample considering detector acceptance (signal pattern) and measured data (background pattern) serving as the combinatorial background sample. In contrast to the simulated resonance sample for the $\Upsilon(nS)$ polarization measurement, in this case the simulation is done for the full mass range of $9.9\,\mathrm{GeV/c^2} \leq m_{X_b} \leq 11.2\,\mathrm{GeV/c^2}$. The Monte Carlo simulation is described in more detail in section 4. Because no signal is visible at the preselection stage, all measured data candidates are treated as combinatorial background. The amount of real signal inside is considered to be very small and can thus be neglected.

The advantages of a neural network training within a full mass range instead of only one mass position are the following. In case of the X_b the mass position is unknown thus it is not necessary to perform a neural network training at each mass position separately. Furthermore, it is not necessary to avoid any correlations of the input variables to the invariant mass m_{X_b}. The important task is that the neural network approach does not create an artificial signal peak. Usually the training is performed such that signal pattern is only used for the certain mass position and background pattern is taken from sidebands. By learning any mass dependence the neural network would just find out that at the certain mass position all candidates are signal and outside of that mass position everything is background and thus would fake a signal peak. Due to the fact, that the neural network training is done in a full mass range for both samples, it is harmless if the neural network learns any mass dependence as well.

Simulated phase space candidates are reweighted according to the full decay quantum numbers as previously described. Additionally, it is assumed that the p_{T,X_b} distribution is the same as for the $\Upsilon \to \mu^+\mu^-$. Thus X_b candidates have to be reweighted due to the slight difference of the input $p_{T,\Upsilon}$ distribution compared to the measured $p_{T,\Upsilon}$ distribution. The same weight $w_{p_{T,X_b}}$ as used for the simulated Υ candidates described in section 4.2.2, is applied to the X_b candidates as well. An additional weight is used for each simulated candidate depending on the invariant mass m_{X_b} bin where it belongs to, that accounts for the different mass shapes between data and simulated candidates. It is given as

$$w_{shape,\, m_{X_b} bin} = \frac{N(\mathrm{data})_{\ m_{X_b}\, bin}}{N(\mathrm{MC})_{\ m_{X_b}\, bin}}.$$

This weight is necessary because the neural network must not learn the different mass shapes of measured data and the simulation because, due to the fact that

the simulation is done for a full mass range the shape itself provides no usefull information. It is only an arbitrary normalization for each mass position.

The weights need to be considered in the neural network trainings and are thus given to the neural network as a weighted simulated candidate with

$$w_{NN} = w_{p_{T,X_b}} \cdot w_{J^{PC}} \cdot w_{shape,\, m_{X_b} bin}$$

The neural network input variables are listed in table 6.3. The approximated significances are obtained from the training with the from CLEO proposed dipion propagator. The dipion mass is the most important input variable.

variable	description	NN signi. [73]
training target	signal=1, background=0	
$p_{NN,\mu\mu}$	dimuon network probability	2.57
$\chi^2_{X_b}$	X_b candidate vertex fit quality	71.52
$\chi^2_{\Upsilon(1S)}$	$\Upsilon(1S)$ candidate vertex fit quality	3.11
$m_{\Upsilon(1S)}$	$\Upsilon(1S)$ reconstructed mass	15.27
$\max(p_{T,\pi^\pm})$	maximum of the pion transverse momentum	18.47
$\min(p_{T,\pi^\pm})$	minimum of the pion transverse momentum	38.6
$m_{\pi^+\pi^-}$	dipion mass	161.48
$\Theta_{\pi^+\pi^-}$	Dipion polar helicity angle	8.75
L_{xy,X_b}	X_b transverse decay length	10.62
$w_{J^{PC}}$	quantum numbers weight	1.06
$p_{T,\Upsilon(1S)}$	$\Upsilon(1S)$ transverse momentum	4.69
$L_{xy,\Upsilon(1S)}$	$\Upsilon(1S)$ transverse decay length	5
$\lvert L_{xy}/\sigma_{L_{xy}}\rvert_{\Upsilon(1S)}$	$\Upsilon(1S)$ transverse decay length significance	4.6
Δm_{X_b}	X_b mass uncertainty	5.65
$\max(\text{Like}_{\mu^+},\text{Like}_{\mu^-})$	maximum of muon likelihood	19.25
$\min(\text{Like}_{\mu^+},\text{Like}_{\mu^-})$	minimum of muon likelihood	54.08
$\max(\lvert d_0/\sigma_{d_0}\rvert_{\Upsilon(1S)}, \lvert d_0/\sigma_{d_0}\rvert_{\Upsilon(1S)})$	$\Upsilon(1S)$ maximum impact parameter significance	7.88
$\min(\lvert d_0/\sigma_{d_0}\rvert_{X_b}, \lvert d_0/\sigma_{d_0}\rvert_{X_b})$	X_b maximum impact parameter significance	6.49
$\max(\lvert d_0/\sigma_{d_0}\rvert_{X_b}, \lvert d_0/\sigma_{d_0}\rvert_{X_b})$	X_b maximum impact parameter significance	11.05

Table 6.3: List of the input variables of the neural networks.

Neural network training results are then used to classify measured data candidates. In case of the $\Upsilon(2S)$ resonance the selection requirement is obtained by maximizing

$$S_{NN,\Upsilon(2S)} = \frac{N(\mathrm{MC}, 1^{--}, p_{NN} > p_{NN,cut})}{\sqrt{N(\mathrm{BG}, p_{NN} > p_{NN,cut})}}$$

in the $\pm 3\sigma$ range around the $\Upsilon(2S)$ world average mass. The quantity $S_{NN,\Upsilon(2S)}$ is evaluated for 50 different required probabilities $p_{NN,cut}$. The probability with the highest $S_{NN,\Upsilon(2S)}$ is then chosen as the selection requirement.

The number of simulated candidates $N(\mathrm{MC}, 1^{--})$ is obtainted from the p_T and $J^{PC} = 1^{--}$ reweighted candidates. The number of background candidates $N(\mathrm{BG})$ within the same range is obtained from a fit to the invariant mass spectrum of measured data. The fit is performed in the mass range between 9.9 GeV/c^2 and 10.1 GeV/c^2. It has a signal and a background contribution. The signal parameterization for the $\Upsilon(2S)$ is a double Gauss with fixed parameters according to the simulation study that is already described in section 4.4.1. Only the signal yield is a floating parameter. The background model is parameterized as a second order polynomial

$$f_{\mathrm{bg}}(m) = \mathrm{N_{bg}} \cdot \frac{2}{(x_h - x_l)} \cdot (1/2 + a(x(m)^2 - 1/3) + bx(m)).$$

The number of background candidates is $\mathrm{N_{bg}}$. The nominal mass range $[m_l, m_h]$ is transformed into the range $[-1, 1]$ by

$$x(m) = -1 + \frac{2}{m_h - m_l} \cdot (m - m_l).$$

The fit function thus is

$$f(m) = f_{X_b}(m) + f_{\mathrm{bg}}(m).$$

The background parameters are left free in all fits.

In case of the $\Upsilon(3S)$ and the X_b where there is no significant signal visible. Thus the selection requirement is obtained by maximizing

$$S_{NN} = \frac{N(\mathrm{MC}, J^{PC}, p_{NN} > p_{NN,cut})}{3/2 + \sqrt{N(\mathrm{data}, p_{NN} > p_{NN,cut})}}$$

This quantity is also evaluated in a 3σ range around the central mass value. $N(\mathrm{data})$ denotes the candidates obtained from measured data in the corresponding mass range. Again it is assumed that in measured data the real signal contribution is very few thus approximated to be only background. The 3/2 is a term that Punzi [92] suggested in order to aim for a signal with the significance of 3σ.

6.3 Neural Network Selection Results

Efficiencies and yield expectations are tested with the $\Upsilon(2S)$ resonance. Thus it is the first task to optimize the $\Upsilon(2S)$ candidate selection.

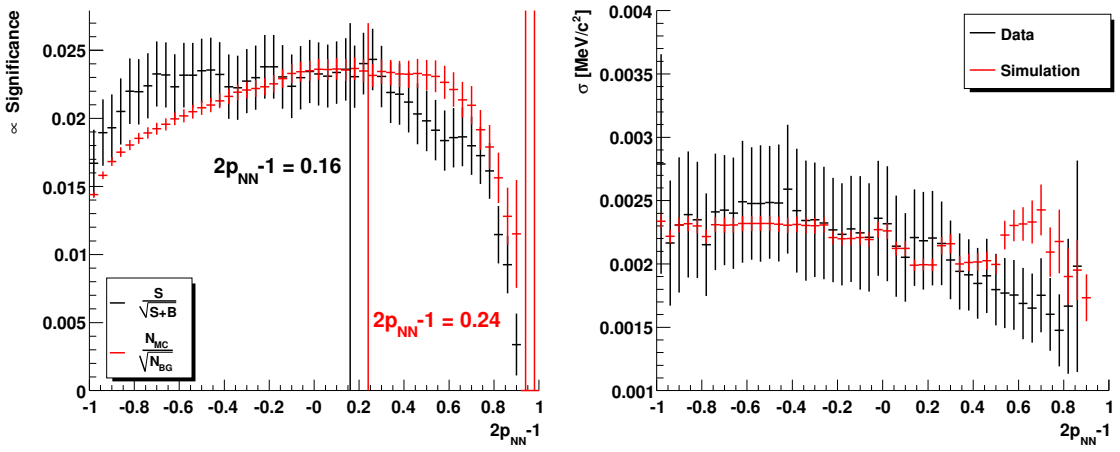

Figure 6.6: The left plot shows the $\Upsilon(2S)$ significance for several selection requirements. The right plot shows the mass resolution.

6.3.1 $\Upsilon(2S)$ Selection

Within the invariant mass range between $9.9\,\mathrm{GeV/c^2}$ and $10.1\,\mathrm{GeV/c^2}$ the optimized selection method based on the training result of neural network trainings is applied to the $\Upsilon(2S)$ resonance. The fit result to the invariant mass spectrum can also be used to derive the quantity $S/\sqrt{(S+B)}$ in the 3σ range around the $\Upsilon(2S)$ world average mass.

In figure 6.6 the selection requirements are shown. The left plot shows the quantity $S/\sqrt{(S+B)}$, obtained from the fit result, for a given selection and the quantity $N(MC)/\sqrt{N(BG)}$ where only the background candidates $N(BG)$ are obtained from the fit result and the signal is estimated from selected simulated candidates. This is a cross-check to test if the selection criterion based on simulated candidates is consistent with the results obtained from measured data. There are slight differences, however, both selection requirements of $(2p_{NN}-1)$ give similar results. As a result, it is found that the optimization of $N(MC)/\sqrt{N(BG)}$ can be used in order to estimate the required neural network probability if no signal is visible in the invariant spectrum which is the case for the $\Upsilon(3S)$ and X_b.

The dependence of the mass resolution compared between measured data and simulated signal candidates for a given selection is shown in the right plot in figure 6.6. The simulation describes the trends seen in signal candidates of measured data well.

In the right plot in figure 6.7 measured candidates after required preselection and pion quality selection criteria is shown. Even without the neural network selection the $\Upsilon(2S)$ can be observed.

The neural network trainings are performed under different assumptions to have a cross-check for the different models that are used to reweight simulated candidates.

- **Phasespace Training** — Though, no quantum numbers J^{PC} considered,

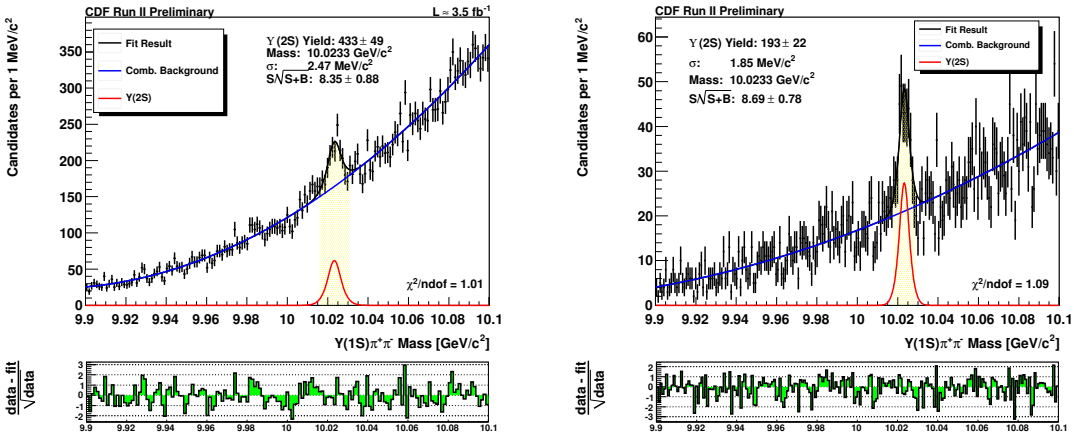

Figure 6.7: Invariant mass spectra. The left plot shows the $\Upsilon(2S)$ fit result with the neural network based optimized selection. The right plot shows the result after required preselection and pion quality criterion.

	Fit Result	Expectation
no neural network selection	193.03 ± 21.6	183 ± 8.8
phase space	165.165 ± 18.81	175.83 ± 8.63
'Alder Zero'	129.82 ± 15.13	98.26 ± 6.44
'CLEO'	111.14 ± 3.6	83.6 ± 5.9

Table 6.4: List of fitted and expected $\Upsilon(2S)$ candidates. Pion quality requirements are

phase space properties already provide information to achieve a reasonable $\Upsilon(2S)$ selection. The selected candidates are shown in the left plot of figure 6.7.

- $J^{PC} = 1^{--}$ **Training via 'Adler Zero' dipion propagator and** p_{T,X_b} **reweighting** — The 'Alder Zero' dipion model is used at first because it serves as a cross-check for the selection method. The resulting fit to the invariant mass spectrum for the best selection requirement is shown in the left plot of figure 6.8.

- $J^{PC} = 1^{--}$ **Training via 'CLEO' dipion propagator and** p_{T,X_b} **reweighting** — The selected invariant mass spectrum is shown in the right plot of figure 6.8. This result is consistent with the 'Adler Zero' approach.

In table 6.4 the fitted signal yields are compared to the yield expectations. The numbers are obtained from candidates which are required to fullfill the pion quality selection criteria. Though the approaches with considering the dipion propagators deviate slightly from the fitted signal yields, all results are found to be consistent within 2σ. The dipion model from 'CLEO' sufficiently describes the signal and is thus accordingly used for the $\Upsilon(3S)$.

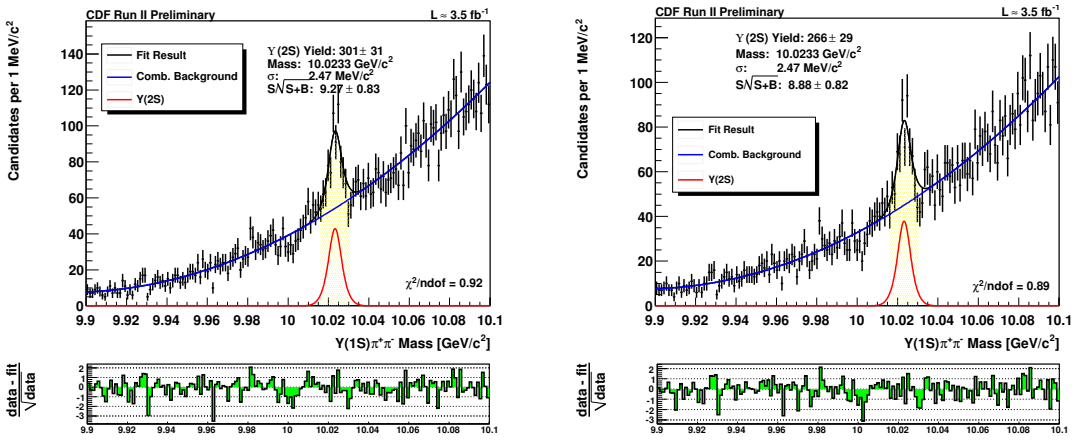

Figure 6.8: Invariant mass spectra. The left plot shows the $\Upsilon(2S)$ fit result with the neural network based optimized selection considering the p_T reweight and the quantum numbers $J^{PC} = 1^{--}$ via a pion propagator modelled by an Alder zero. The right plot shows the best result assuming the result from CLEO for the dipion propagator.

6.3.2 $\Upsilon(3S)$ Selection

In case of the $\Upsilon(3S)$ the neural network training is performed within the invariant mass range between 10.25 GeV/c^2 and 10.45 GeV/c^2 using the same neural network setup as it is done for $\Upsilon(2S)$. The only difference is that in this case the dipion propagator for the $\Upsilon(3S)$ is considered in the weight w_{JPC} and the the pion quality requirements are demanded as well. The required neural network probability selects the measured candidates shown in the left plot in figure 6.9. No signal is visible. The right plot shows the dependence on the selection requirement of the optimized quantity $N(MC)/(3/2 + \sqrt{N(data)})$.

6.3.3 X_b Selection

Neural network trainings are performed in five 200 MeV/c^2 invariant mass regions between 10.2 GeV/c^2 and 11.2 GeV/c^2. This has two reasons: firstly, such a mass range provides a reasonable results for the $\Upsilon(2S)$ state and secondly, to avoid to mislead the neural network training result due to different properties of background and signal at distant invariant masses positions. Again the pion quality selection criteria is required in order to obtain reasonable efficiencies.

For each of the ranges the required network probability for the highest $N(MC)/(3/2+\sqrt{N(data)})$ is evaluated. The result is shown in figure 6.10. In this case the evaluation of $N(MC)/(3/2 + \sqrt{N(data)})$ is performed at 25 mass positions starting at 10.22 GeV/c^2 in steps of 40 MeV/c^2.

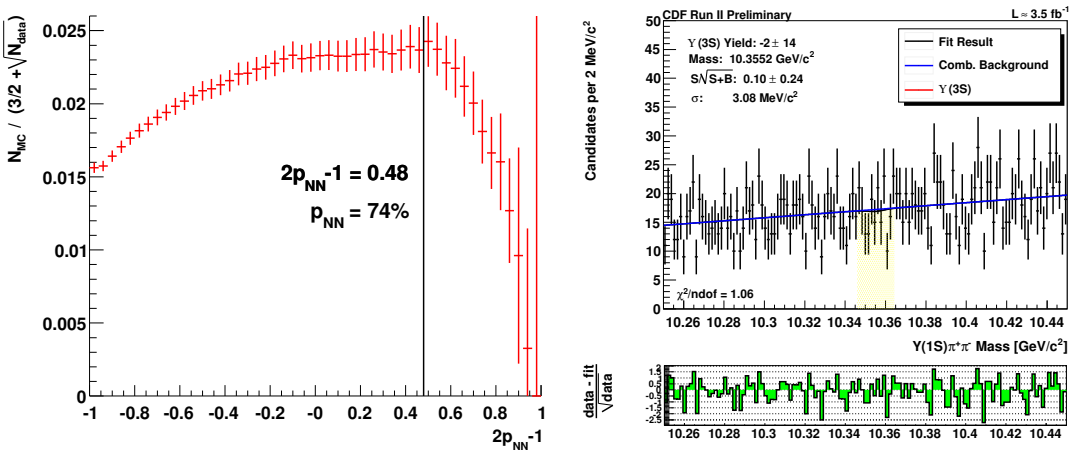

Figure 6.9: The right plot shows the invariant mass spectrum of selected $\Upsilon(3S)$ candidates in data. The left plot shows the significance dependence for several selection requirements.

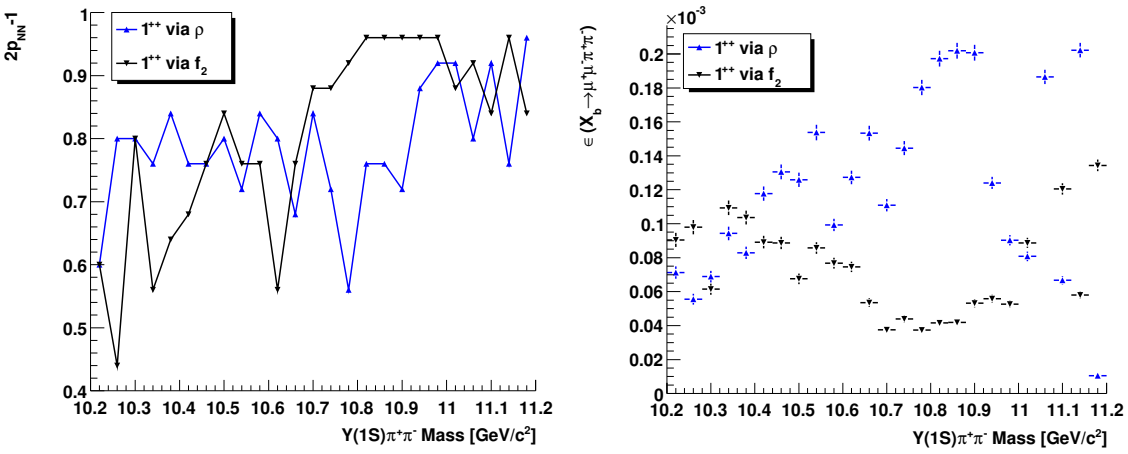

Figure 6.10: The left plot shows the obtained required neural network probability. The right plot shows the corresponding efficiency.

6.4 Upper Limit and Fit Description

6.4.1 Upper Limit

The purpose of this analysis is to search for a new particle, the possibly existing X_b. This implies that the data yield at a certain mass is significantly above background. In such a case a discovery can be claimed. However, if the signal yield is consistent with zero, then the result is reported by giving an upper limit at a credibility level of 95% on the quantity R defined as

$$R(m_{\Upsilon(1S)\pi^+\pi^-}) = \frac{\sigma_{X_b}}{\sigma_{\Upsilon(2S)}} \cdot BR(X_b \to \Upsilon(1S)\pi^+\pi^-).$$

The limit on the ratio R is dependent on the invariant mass $m_{\Upsilon(1S)\pi^+\pi^-}$ because it is not known at which mass position the hypothetical X_b can be found. Also the branching fraction $BR(X_b \to \Upsilon(1S)\pi^+\pi^-)$ is unknown.

The $\Upsilon(2S)$ state is the only resonance visible in this decay channel therefore it is of advantage to present an upper limit relative to that state. Consequently, some of the systematic uncertainties due to the usage of the similar selection method, should cancel in the ratio. Additionally, the integrated luminosity cancels as well.

6.4.2 The Likelihood Function

In order to obtain the value $R(m_{\Upsilon(1S)\pi^+\pi^-})$ an binned maximum likelihood fit to the invariant mass distribution of the data sample is performed. The used fitter is built using the MINUIT [93] minimizer provided by the ROOT [94] package. The likelihood function is given by

$$L = \prod_{\text{all bins}} f_i^{n_i} \frac{e^{-f_i}}{n_i!}$$

where f_i denotes the expectation in bin i which is represented by the the integral of the function f_i over the width of the bin i and n_i is the corresponding bin content of the histogram.

In the fit the negative log likelihood to minimize is defined as

$$\mathcal{L} = -2 \cdot \ln L_{\Upsilon(2S)} - 2 \cdot \ln L_{X_b} + \frac{1}{2}\left(\frac{\epsilon_R - \epsilon_{R,MC}}{\sigma_{\epsilon_R}}\right)^2.$$

where the last term represents the Gaussian constraint to the efficiency ratio ϵ_R which is defined as

$$\epsilon_R = \frac{\epsilon_{X_b}}{\epsilon_{\Upsilon(2S)}} = \frac{\epsilon(X_b \to \mu^+\mu^-\pi^+\pi^-)}{\epsilon(\Upsilon(2S) \to \mu^+\mu^-\pi^+\pi^-)}.$$

and is floating in the fit.

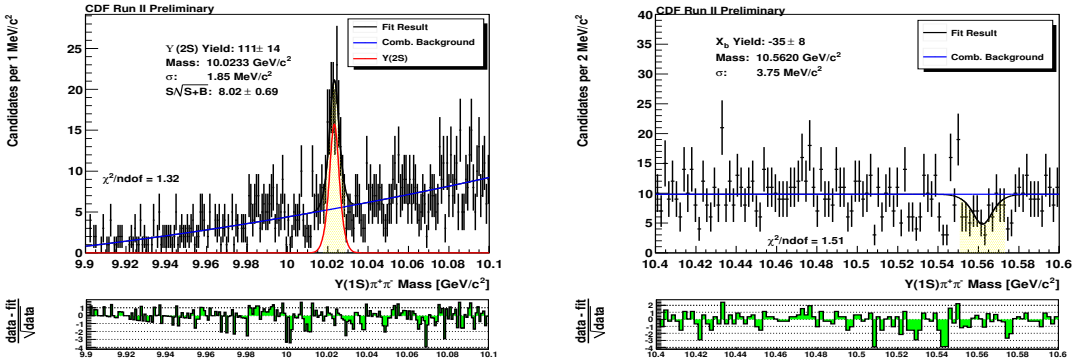

Figure 6.11: Invariant mass spectra of the $\Upsilon(2S)$ selected candidates and an exemplary selection of X_b candidates for an assumed mass of 10.562 GeV/c^2 and a selection based on the assumption of an ρ propagator.

There are two contributions: The first term $-\ln L_{\Upsilon(2S)}$ is the negative log likelihood obtained from the fit to the selected $\Upsilon(2S)$ invariant mass spectrum in order to obtain an estimation of the number of signal candidates. Thus also the pion quality selection criterion is required. The background contribution is modelled as a first order polynomial. The fit function thus is

$$f(m)_{\Upsilon(2S)} = \mathrm{N}_{\Upsilon(2S)} \cdot [f_{\mathrm{norm}} \cdot G_1(m) + (1 - f_{\mathrm{norm}}) \cdot G_2(m)] + \mathrm{N}_{\mathrm{bg}} \cdot p_{1,\mathrm{norm}},$$

where only the background parameters and the number of $\Upsilon(2S)$ signal candidates are left free in the fit. The signal contribution is already described in section 4.4.1. The resulting invariant mass spectrum is shown in the left plot of figure 6.11.

The second term belongs to the fits to the X_b spectrum that is simultaneously performed with the $\Upsilon(2S)$ fit described in the first term. In this case a constant is used to describe the background. An exemplary X_b selection for an assumed invariant mass of 10.562 GeV/c^2 and intermediate ρ dipion propagator is shown in the right plot of figure 6.11. However, in the simultaneous fit the signal contributions are required to be positive. In order to fit for the value R the fit function is given as

$$f(m)_{X_b} = \frac{R \cdot \mathrm{N}_{\Upsilon(2S)} \cdot \epsilon_R}{BR(\Upsilon(2S) \to \Upsilon(1S)\pi^+\pi^-)} \cdot [f_{\mathrm{norm}} \cdot G_1(m) + (1 - f_{\mathrm{norm}}) \cdot G_2(m)]$$
$$+\mathrm{N}_{\mathrm{bg}} \cdot p_{0,\mathrm{norm}}.$$

The invariant mass range used for the fit depends on the assumed mass position. The invariant mass range which belongs to the corresponding X_b neural network training is taken. The ratio of the efficiencies ϵ_R is floating in the fit within an Gaussian constraint. The efficiencies are of the order of 10^{-4} and the uncertainties are of the order of 10^{-5} which are shown for several assumed X_b masses in figure 4.18. The number of $\Upsilon(2S)$ candidates $\mathrm{N}_{\Upsilon(2S)}$ is simultaneously fitted.

The Bayesian limit on the ratio R is calculated with the fit function described above. In order to set the limit a fit to the selected X_b candidates is performed where the

parameter R is left free in the fit. The obtained negative log likelihood value $\mathcal{L}_0$ serves as the result from the reference fit. Then a set of consecutive fits is done where the parameter R is fixed to values corresponding to rising number of N_{X_b} candidates, starting from zero. Each fit returns a negative log likelihood value $\mathcal{L}$ as defined above. The obtained values are transformed back into the likelihood value ΔL as

$$\Delta L = \exp\left(\frac{\mathcal{L}_0 - \mathcal{L}}{2}\right)$$

The Bayesian posterior probability density function is

$$p(\vec{a}|\vec{x}) = \frac{\Delta L(\vec{x}|\vec{a})\pi(\vec{a})}{\int \Delta L(\vec{x}|\vec{a})\pi(\vec{a})d\vec{a}}$$

where $\pi(\vec{a})$ is the prior probability density function. It is assumed to be flat for all $\vec{a}$: $\pi(\vec{a}) = 1$. In this analysis $\vec{a}$ is only one parameter namely the ratio R which is required to be higher or equal to zero. The credibility interval can be determined for a given fraction $(1 - \beta)$ of the probability by

$$1 - \beta = \int_0^{R_{up}} p(R|\vec{x})dR$$

where R_{up} denotes the upper obtained upper limit. In this analysis the credibility level of $1 - \beta = 95\%$ is chosen.

6.5 Results

6.5.1 $\Upsilon(3S)$ Significance

The selected invariant mass spectrum of $\Upsilon(3S)$ candidates is fitted in order to obtain the significance to observe a signal. Again to cross-check the simulation 50 neural network selection requirements with equidistant increase in the range between $[0, 1]$ for the probability p_{NN} are evaluated for signal significance. The significance of an observed signal is obtained from

$$\sqrt{2 \cdot (LL - LL_0)}$$

where LL_0 is the negative log-likelihood extracted from fits with floating signal yield and LL is the negative log-likelihood extracted from fits considering only background. The background shape from the $\Upsilon(3S)$ candidates is assumed as a first order polynomial. The signal shape is used as explained in section 4.3.1. Only the the number of signal candidates N_{sig} is floating in the fit to obtain log likelihood LL_0.

The resulting signal significance with respect to the selection requirement is shown in figure 6.12. No significant $\Upsilon(3S)$ is observed. The highest significance is 1.56σ standard deviation. The corresponding fit is shown in figure 6.13.

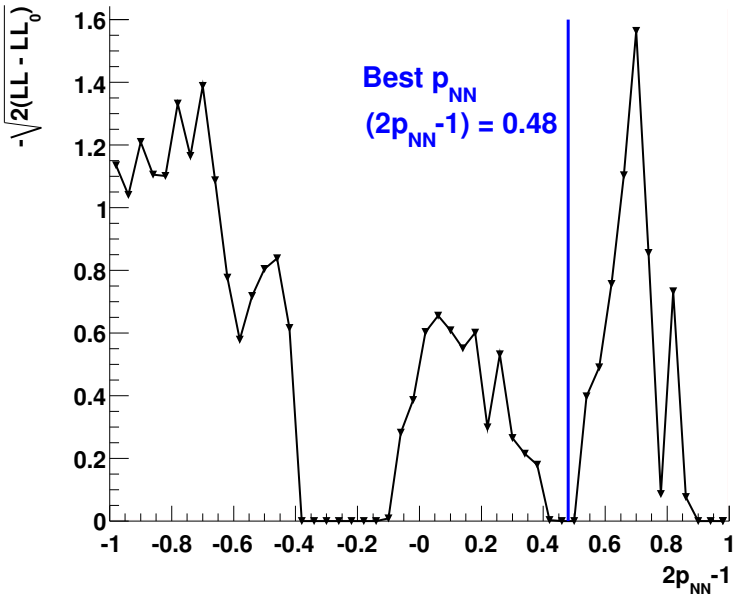

Figure 6.12: $\Upsilon(3S)$ signal significance for different selection requirements on p_{NN}.

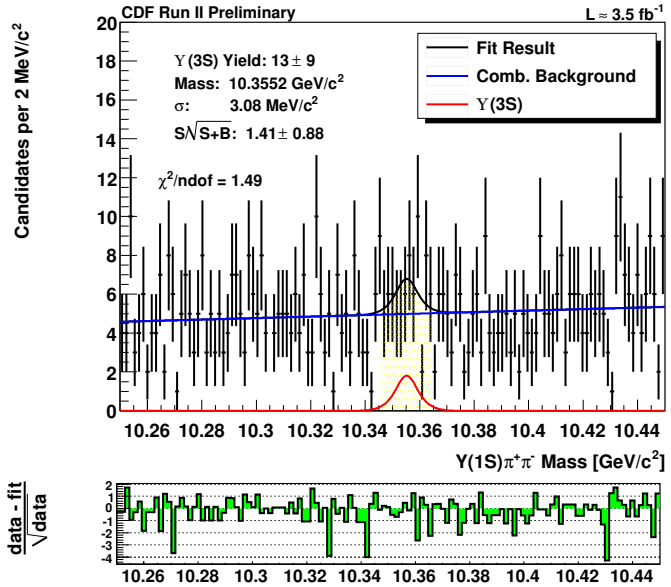

Figure 6.13: $\Upsilon(3S)$ result obtained from the fitted invariant mass spectrum with the selection requirement the yields the highest signal significance.

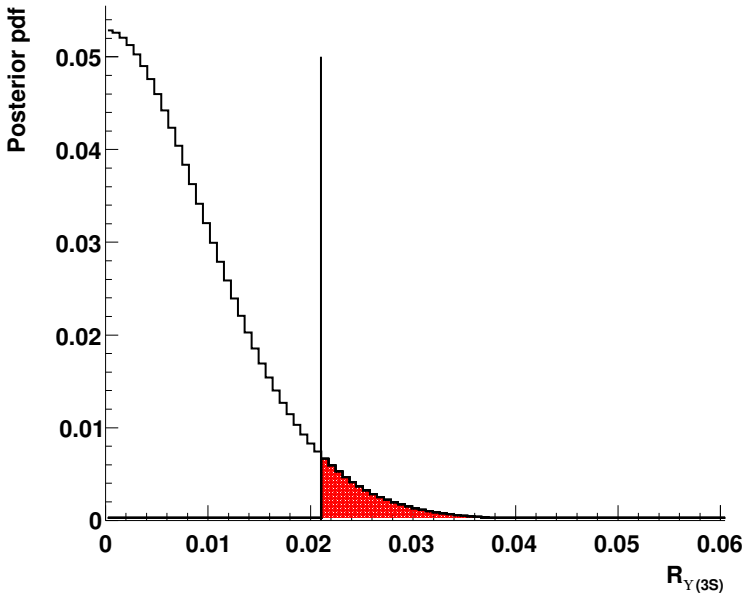

Figure 6.14: The $\Upsilon(3S)$ posterior probability density function as a function of $R_{\Upsilon(3S)}$.

6.5.2 $\Upsilon(3S)$ Upper Limit

The upper limit on the ratio $R_{\Upsilon(3S)}$ of the $\Upsilon(3S)$ at a credibility level of 95% is derived by the method described in section 6.4.2. The mean mass of $\Upsilon(3S)$ is fixed to the world average mass [9]. The mass resolution is fixed to the value described in section 4.3.1. A Bayesian limit is set on $R_{\Upsilon(3S)}$. It is calculated assuming a flat prior for R which implies that the number of $\Upsilon(3S)$ signal candidates cannot be negative. The resulting upper limit at a credibility level of 95% is

$$R_{\Upsilon(3S)} < 0.021.$$

The probability is evaluated up to $R = 0.271$. By taking into account the known branching fraction $BR(\Upsilon(3S) \to \Upsilon(1S)\pi^+\pi^-)$ given in table 5.1 this translates to

$$\frac{\sigma_{\Upsilon(3S)}}{\sigma_{\Upsilon(2S)}} < 0.469.$$

The posterior probability density function is shown in figure 6.14.

The result is consistent with cross section ratio obtained from the decay $\Upsilon \to \mu^+\mu^-$ which is

$$\frac{\sigma_{\Upsilon(3S)}}{\sigma_{\Upsilon(2S)}} = 0.453 \pm 0.006$$

by considering the efficiencies described in section 4.3.2, the obtained signal yields in that decay and the branching fractions. It is also consistent with the result obtained

by using the expected yields in the decay to $\Upsilon(1S)\pi^+\pi^-$ and the corresponding branching ratios and efficiencies which is

$$\frac{\sigma_{\Upsilon(3S)}}{\sigma_{\Upsilon(2S)}} = 0.4879 \pm 0.05$$

6.5.3 X_b Significance

The selected X_b and $\Upsilon(2S)$ spectra are fitted simultaneously in steps of 50 neural network selection requirements with equidistant increase in the range between $[0, 1]$ for the probability p_{NN}. The significance of an observed signal is again obtained from

$$\sqrt{2 \cdot (LL - LL_0)}$$

where LL_0 is the negative log-likelihood extracted from fits with floating signal and LL is the negative log-likelihood extracted from fits considering only background. The background shape from the X_b candidates is assumed to be a first order polynomial. The signal shape is used as explained in section 4.3.1.

Only the number of the ratio R_{X_b} is a floating parameter in the fit to obtain LL. In case of the X_b the scan is performed at 100 mass position of the invariant mass range $[10.2, 11.2]\,\mathrm{GeV/c^2}$ starting from $10.205\,\mathrm{GeV/c^2}$. The signal significance is then evaluated for each mass position at several neural network selection requirements. The resulting maximum signal significance as a function of the invariant mass is shown in figure 6.15 for the two obtained selection criterion obtained from the neural network trainings considering different dipion propagators, ρ and f_2. No significant signal is observed.

The significance is also evaluated for candidates for the optimized selection based on the maximized quantity $N(MC)/(3/2+\sqrt{N(data)})$. This approach is unbiased as it demand a selection based on the best selection of simulated candidates. The results are shown in figure 6.16 only one value with a significance of 3.08σ standard deviation at the invariant mass $10.385\,\mathrm{GeV/c^2}$ is obtained. The corresponding invariant mass spectrum is shown in the right plot of figure 6.17. However, if one also consideres the additional degree of freedom since the X_b mass position is unknown, the significance decreases according to

$$Prob(\chi^2 \; = \; 2(LL - LL_0), ndof \; = \; 2)$$

which translates in this case to a significance of 2.62σ standard deviations. As a result, no evidence for the X_b is obtained.

In the left plot of figure 6.16 the selected invariant mass spectrum based on the ρ assumption is shown for the maximal obtained significance of 2.78σ standard deviation. The corresponding mass is $10.295\,\mathrm{GeV/c^2}$.

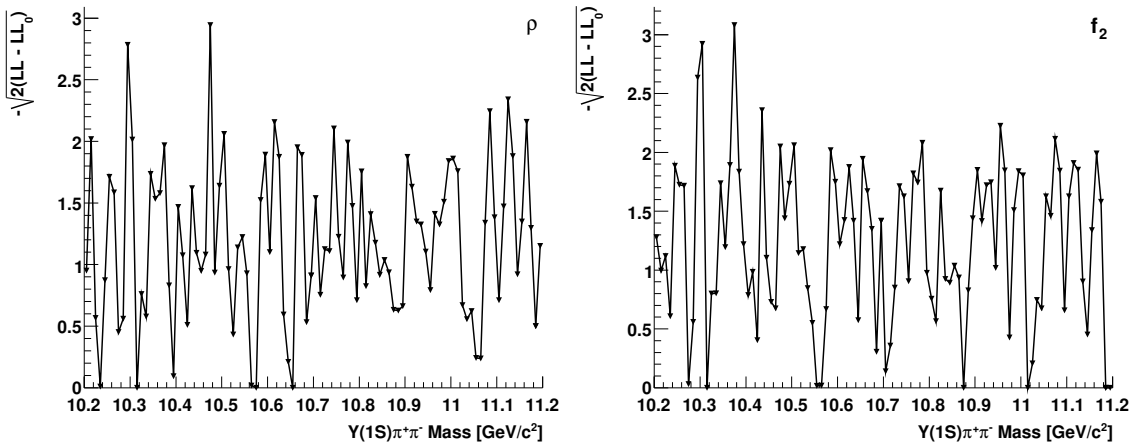

Figure 6.15: X_b significance for each mass position. The left plot shows the obtained significance assuming a ρ dipion propagator and the right plot shows the result assuming a f_2 propgator.

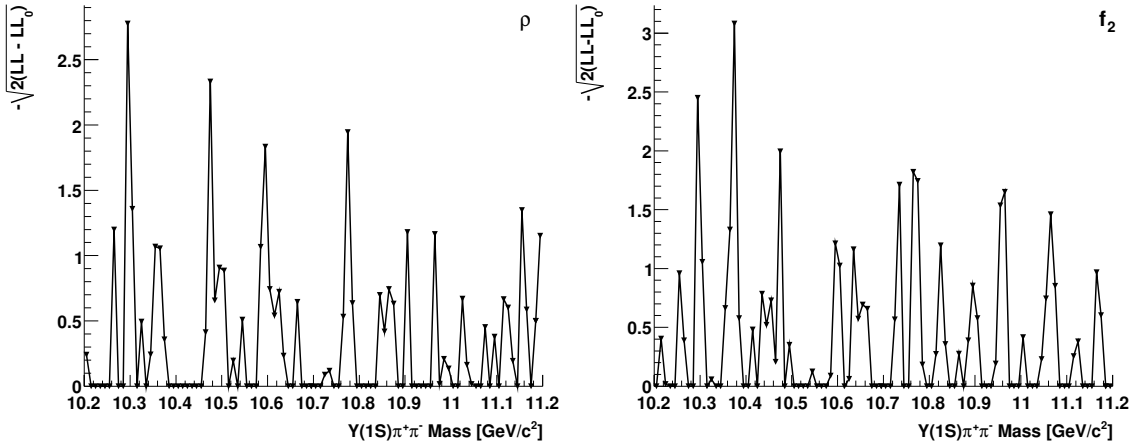

Figure 6.16: X_b significance for each mass position. The left plot shows the obtained significance assuming a ρ dipion propagator and the right plot shows the result assuming a f_2 propgator for the selection. Only selection requirements for maximized quantity $N(MC)/(3/2 + \sqrt{N(data)})$ are considered.

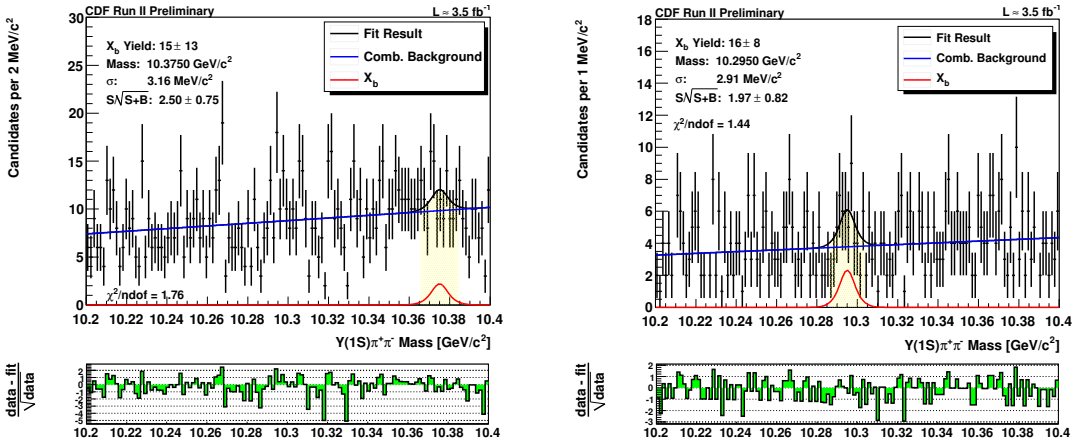

Figure 6.17: X_b spectra for highest significances. The left plot shows the best selection based on the f_2 dipion propagator, the right plot shows the best selection based on the ρ dipion propagator.

6.5.4 X_b Upper Limit

The upper limit on the ratio R_{X_b} of the X_b is derived by the method described in section 6.4.2. An upper limit is calculated for several mass position, starting from 10.205 GeV/c^2 in steps of 10 MeV/c^2. The resolution as a function of the mass and is fixed to the value obtained from the corresponding fit described in section 4.3.1. A Bayesian limit is set on $R_{X_b}(m)$ depending on the invariant mass at a credibility level of 95%. It is again calculated assuming a flat prior for R which implies that the number of $\Upsilon(3S)$ signal candidates cannot be negative. The probability is evaluated up to $\Delta L(\vec{x}|R)\pi(R) = 10^{-6}$.

Figure 6.18 shows the resulting ratio R as a function of the mass for two neural networks trained on simulated candidates with weights for the assumed dipion propagators.

The highest value R_{X_b} is obtained at the mass position of 10.295 GeV/c^2 with $R < 0.0264$ for an assumed ρ dipion propagator and $R < 0.0312$ at the mass of 10.375 GeV/c^2. The corresponding selected candidates are shown in figure 6.19.

6.6 Systematic Uncertainties

Consistency checks for efficiencies and yield expectations are performed based on the $\Upsilon(2S)$ and a reasonable result is obtained as shown in table 6.4. This is expected to be the largest source of uncertainties. Thus, as a preliminary estimation, the systematic uncertainties are expected to be mostly consistent with zero. The systematic uncertainties are expected to be small compared to the statistical uncertainties and are thus neglected in the analysis.

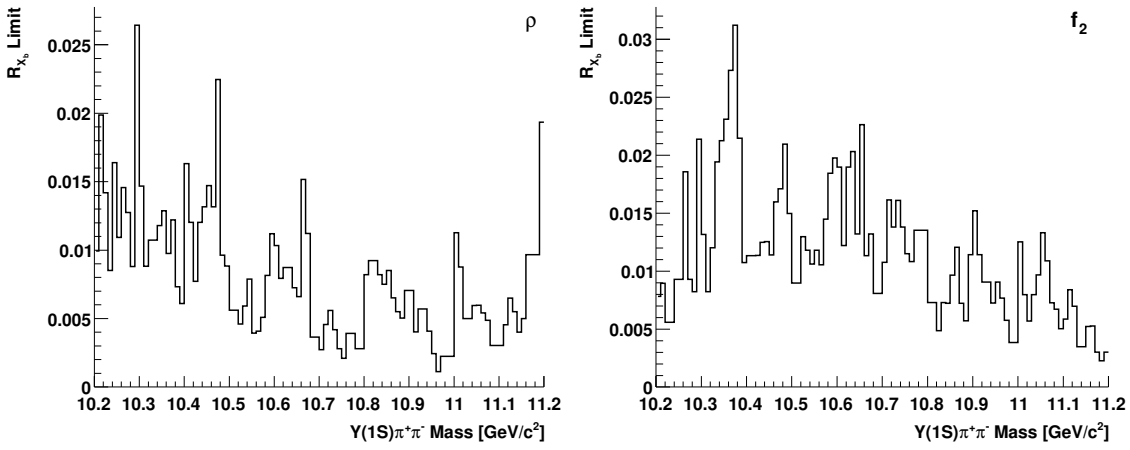

Figure 6.18: X_b ratio R for each mass position. The left plot shows the obtained significance assuming a ρ dipion propagator and the right plot shows the result assuming a f_2 propgator.

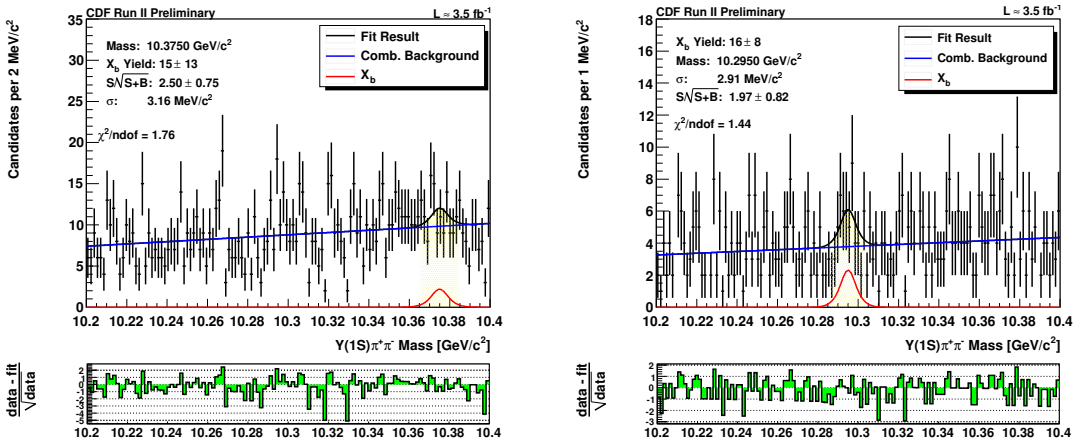

Figure 6.19: X_b spectra for the highest R_{Xb} limit. The left plot shows the best selection based on the f_2 dipion propagator, the right plot shows the best selection based on the ρ dipion propagator.

Chapter 7

Conclusion and Outlook

There are two studies presented in this analysis. The first one is the measurement of the $\Upsilon(1S)$, $\Upsilon(2S)$ and $\Upsilon(3S)$ polarization in two orthogonal frames: the helicity and the Collins-Soper frame. The second is the search for a possible bottom counterpart of the $X(3872)$ which would show up as a narrow resonance in the $\Upsilon(1S)\pi^+\pi^-$ final state.

The data samples were collected with the CDF II detector and correspond to an integrated luminosity of $3.5\,\mathrm{fb}^{-1}$. The selection was performed using neural networks. The requirements were chosen such that the signal significance being generally defined as a function of the number of simulated events and of background events, was maximized.

The analysis result is consistent with mostly unpolarized Υ's for the considered $p_{T,\Upsilon}$ range of $[0, 30]$ GeV/c in both frames. There are previous Υ polarization measurements from CDF Run I [55] and DØ [52]. Recently, CDF also updated their $\Upsilon(1S)$ polarization measurement [95]. The results from the measurement obtained in this thesis is consistent with the CDF Run I result and the independent CDF Run 2 $\Upsilon(1S)$ polarization measurement. This analysis is not consistent with the result from the DØ collaboration. They observe a significant $p_{T,\Upsilon}$-dependent longitudinal polarization for the $\Upsilon(1S)$. For the $\Upsilon(2S)$ they measure a transversal polarization for $p_{T,\Upsilon} > 7$ GeV/c which is however still consistent with zero. It is the first time that the polarization was measured in the Collins-Soper frame at collider experiments, thus the result of this analysis in that frame cannot be compared.

This measurement is consistent with the NRQCD factorization prediction [53] for $p_{T,\Upsilon} < 10\,\mathrm{GeV/c}$ which argues that the fragmentation mechanism does not dominate until relative large values of $p_{T,\Upsilon}$ are reached and hence the polarization is predicted to be small for $p_{T,\Upsilon}$ below about 10 GeV/c [96]. However, for larger values of $p_{T,\Upsilon}$ this measurement is also consistent with zero but still does not exclude the NRQCD prediction which favors transverse polarization at large values of $p_{T,\Upsilon}$.

In the second part the X_b search was performed. In order to verify that the simulation efficiencies are reasonable, at first the $\Upsilon(2S)$ was selected and yields were compared to the expectation. As a result, this was found to be consistent within

$\pm 2\sigma$ standard deviations.

The same approach was used for the $\Upsilon(3S)$. In contrast to the $\Upsilon(2S)$ no significant $\Upsilon(3S)$ resonance was observed in the final selection. Therefore an Bayesian limit at a 95% credibility level was set on the ratio $R_{\Upsilon(3S)}$ defined as

$$R_{\Upsilon(3S)} = \frac{\sigma_{\Upsilon(3S)}}{\sigma_{\Upsilon(2S)}} \cdot BR(\Upsilon(3S) \to \Upsilon(1S)\pi^+\pi^-) < 0.021.$$

Using the known branching ratio $BR(\Upsilon(3S) \to \Upsilon(1S)\pi^+\pi^-) = 0.0448 \pm 0.0021$ this translates to the ratio of the corresponding cross-sections

$$\frac{\sigma_{\Upsilon(3S)}}{\sigma_{\Upsilon(2S)}} < 0.469 \pm 0.022$$

The ratio obtained from the corresponding decays to the final state $\mu^+\mu^-$ where the Υ signals are clearly visible, results a ratio of $\sigma_{\Upsilon(3S)}/\sigma_{\Upsilon(2S)} = 0.453 \pm 0.006(\text{stats.})$. The ratio obtained from the yield expectation to the final state $\Upsilon(1S)\pi^+\pi^-$ was calculated to be $\sigma_{\Upsilon(3S)}/\sigma_{\Upsilon(2S)} = 0.4879 \pm 0.05(\text{stats.})$. Both ratios are consistent, though should also lead to some excess in the $\Upsilon(3S)$ invariant mass spectrum which was however not observed.

The X_b search was done in the invariant mass range 10.2 GeV/c^2 $\leq m_{X_b} \leq$ 11.2 GeV/c^2. In the search it was assumed that the X_b quantum numbers are $J^{PC} = 1^{++}$. The dipion propagators are either modelled as a ρ dipion propagator or an f_2 dipion propagator. No significant signal was observed. Thus an mass dependent upper limit on

$$R(m_{\Upsilon(1S)\pi^+\pi^-}) = \frac{\sigma_{X_b}}{\sigma_{\Upsilon(2S)}} \cdot BR(X_b \to \Upsilon(1S)\pi^+\pi^-)$$

was set at 95% credibility level. The highest value was obtained at the mass position of 10.295 GeV/c^2 with $R < 0.0264$ for an assumed ρ dipion propagator and $R < 0.0312$ at the mass of 10.375 GeV/c^2 for an assumed f_2 dipion propagator.

There are still no theoretical predictions of the cross section and branching ratio of the X_b. If the branching fraction is assumed to be 100% this would lead for the highest R value to a ratio of the cross sections of $\sigma_{X_b}(10.375\ \text{GeV/c}^2)/\sigma_{\Upsilon(2S)} < 0.0312$.

The relative cross section times the branching ratio of the $X(3872)$ at CDF II is estimated to be $R_{X(3872)} \approx 0.055$. The number is obtained from considering the corresponding yields taken from reference [17] and an assumed relative efficiency between the $X(3872)$ and $\psi(2S)$ of one. The branching ratio of the $\psi(2S)$ is taken from reference [9]. The largest measured value of R_{X_b} is less than $R_{X(3872)}$ which leads to the conclusion that the X_b in relation to the $\Upsilon(2S)$ is produced less than the $X(3872)$ in relation to the $\psi(2S)$ or that it has a lower branching ratio as the $X(3872)$ if the X_b state exists at all.

Appendix A

Polarization Measurement: Fit Results

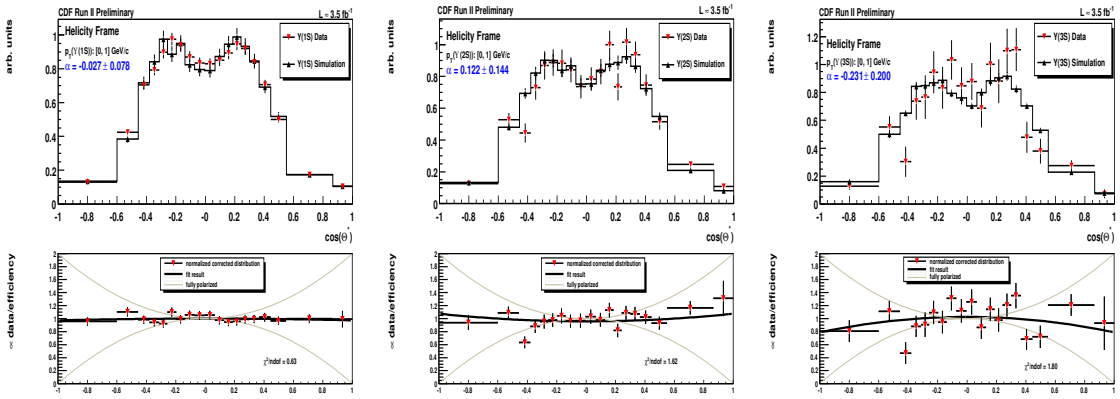

Figure A.1: Fit in bins of $p_{T,\Upsilon}$. The columns refer to the states $\Upsilon(1S)$, $\Upsilon(2S)$ and $\Upsilon(3S)$. Rows of two plots show the obtained distribution from measured data and simulation and below the resulting corrected and normalized distribution with the applied fit to obtain the polarization α (Helicity frame). Each row corresponds to a certain $p_{T,\Upsilon}$ bin.

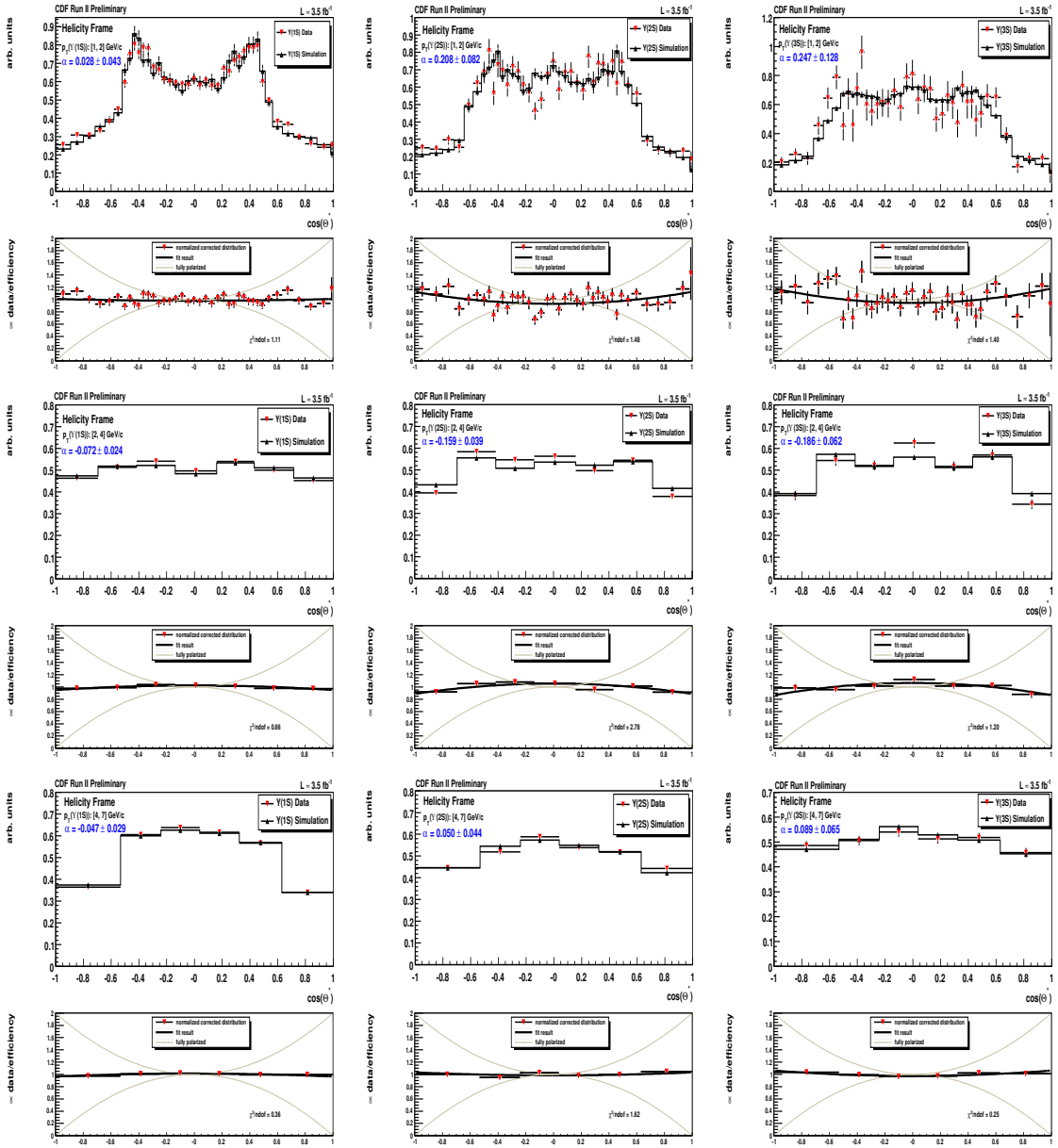

Figure A.2: Fit in bins of $p_{T,\Upsilon}$. The columns refer to the states $\Upsilon(1S)$, $\Upsilon(2S)$ and $\Upsilon(3S)$. Rows of two plots show the obtained distribution from measured data and simulation and below the resulting corrected and normalized distribution with the applied fit to obtain the polarization α (Helicity frame). Each row corresponds to a certain $p_{T,\Upsilon}$ bin.

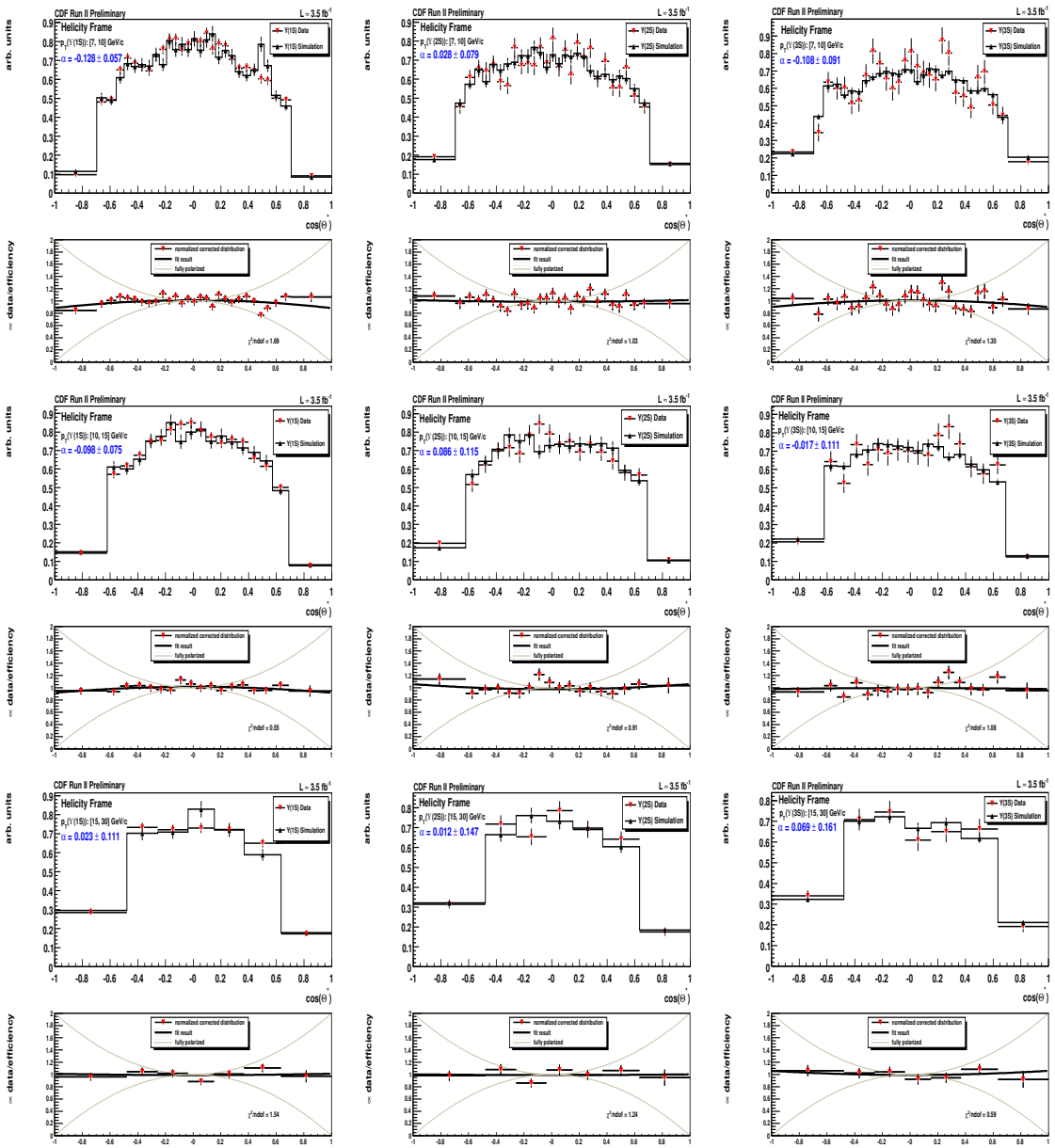

Figure A.3: Fit in bins of $p_{T,\Upsilon}$. The columns refer to the states $\Upsilon(1S)$, $\Upsilon(2S)$ and $\Upsilon(3S)$. Rows of two plots show the obtained distribution from measured data and simulation and below the resulting corrected and normalized distribution with the applied fit to obtain the polarization α (Helicity frame). Each row corresponds to a certain $p_{T,\Upsilon}$ bin.

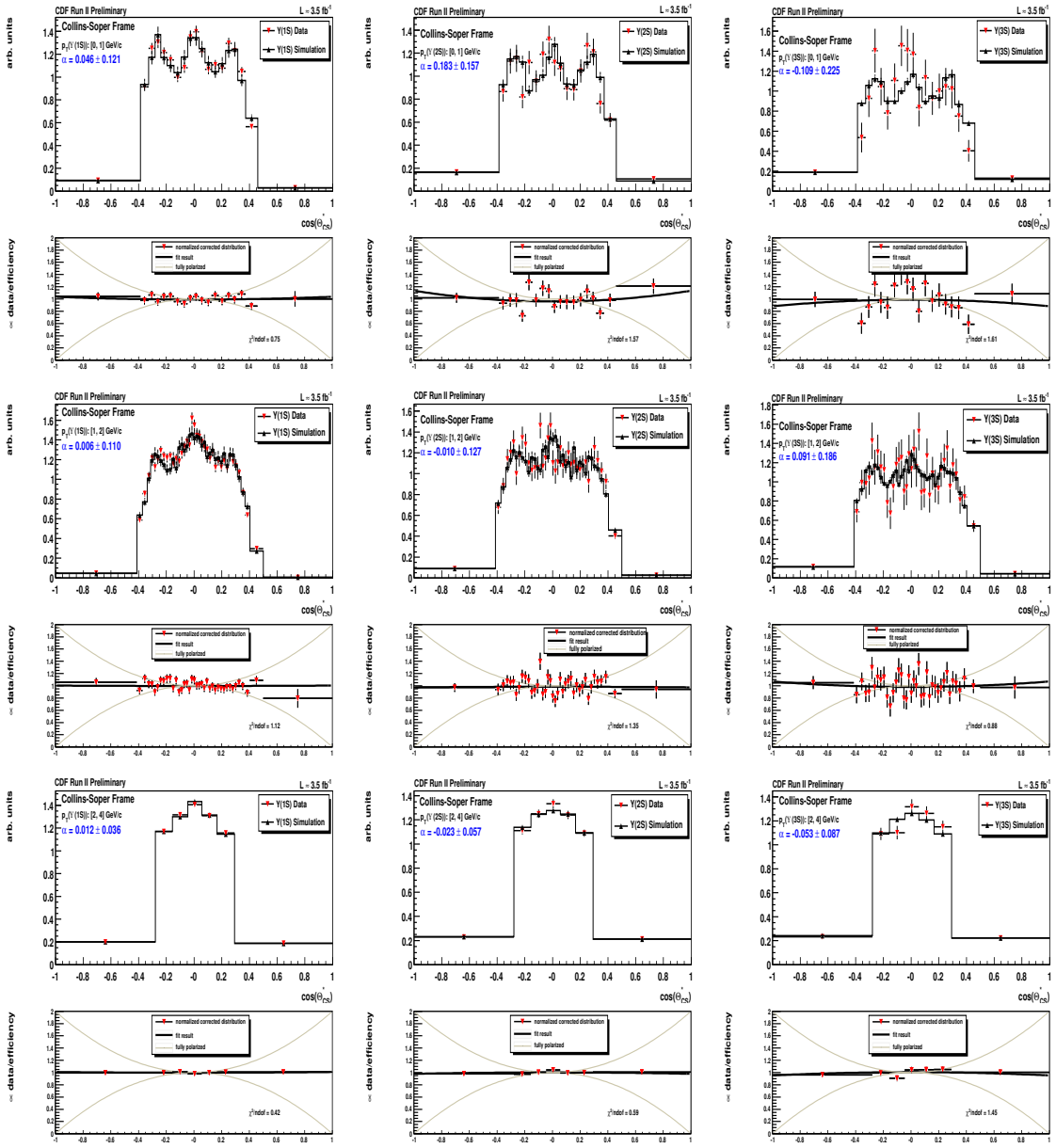

Figure A.4: Fit results in bins of $p_{T,\Upsilon}$. The columns refer to the states $\Upsilon(1S)$, $\Upsilon(2S)$ and $\Upsilon(3S)$. Rows of two plots show the obtained distribution from measured data and simulation and below the resulting corrected and normalized distribution with the applied fit to obtain the polarization α (Collins-Soper frame). Each row corresponds to a certain $p_{T,\Upsilon}$ bin.

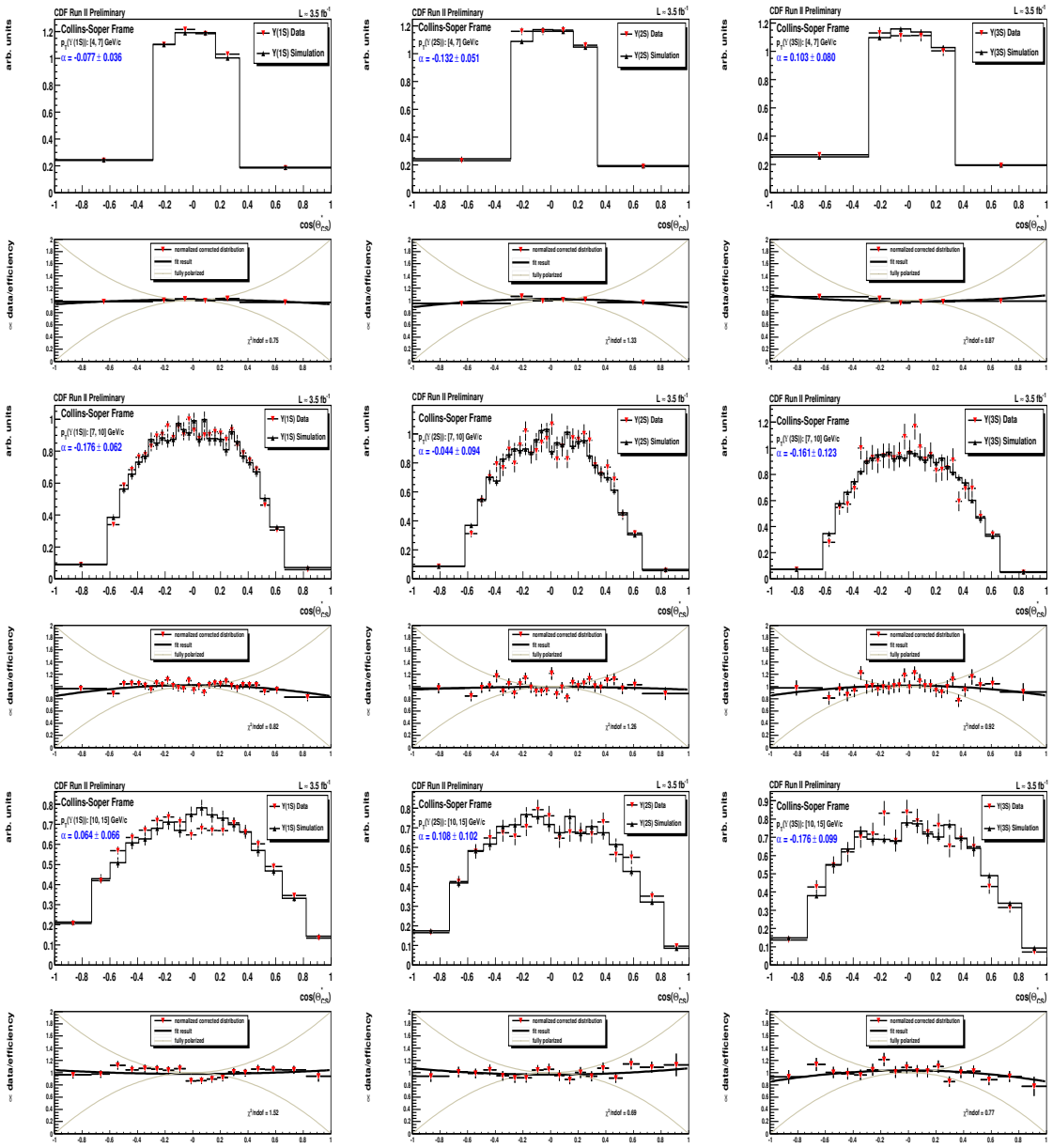

Figure A.5: Fit results in bins of $p_{T,\Upsilon}$. The columns refer to the states $\Upsilon(1S)$, $\Upsilon(2S)$ and $\Upsilon(3S)$. Rows of two plots show the obtained distribution from measured data and simulation and below the resulting corrected and normalized distribution with the applied fit to obtain the polarization α (Collins-Soper frame). Each row corresponds to a certain $p_{T,\Upsilon}$ bin.

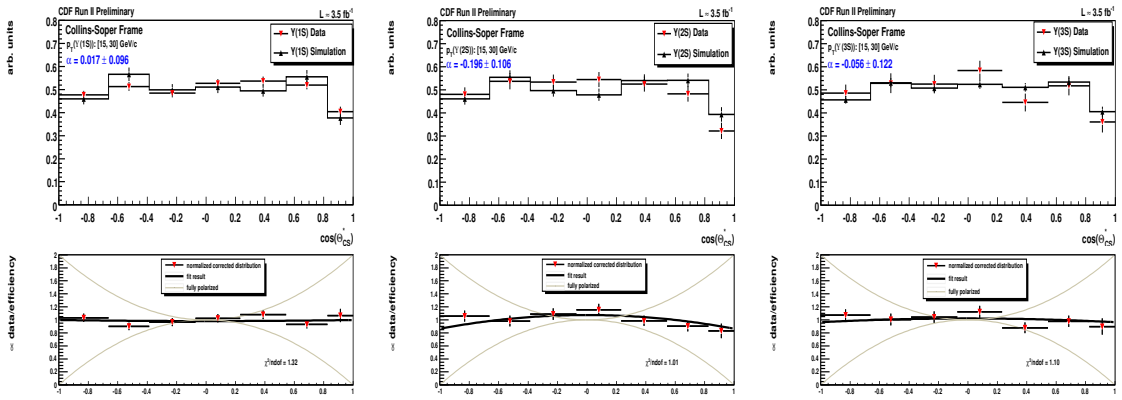

Figure A.6: Fit in bins of $p_{T,\Upsilon}$. The columns refer to the states $\Upsilon(1S)$, $\Upsilon(2S)$ and $\Upsilon(3S)$. Rows of two plots show the obtained distribution from measured data and simulation and below the resulting corrected and normalized distribution with the applied fit to obtain the polarization α (Collins-Soper frame). Each row corresponds to a certain $p_{T,\Upsilon}$ bin.

Appendix B

$\Upsilon(1S)$ Acceptance Corrected $p_{T,\Upsilon}$ Distribution

The given simulation input transverse momentum distribution provides the possibility to calculate the distribution which should serve as the simulation input. The comparison between the input and output distribution offers the possibility to calculate the correction functions which is shown in figure B.1.

Finally, the resulting input transverse momentum for the Υ is fitted to the corrected distribution. However, the above described parameterization, does not sufficiently describes the distribution. Anyhow, the obtained parameters for this parameterization in case of the $\Upsilon(1S)$ is the following:

$$\frac{d\sigma}{dp_T} \propto \frac{p_T^{0.86987}}{\left(3.804493^2\ \mathrm{GeV}^2/c^2 + {p_T}^2\right)^{1.982066}}.$$

The corresponding fit is shown in figure B.2.

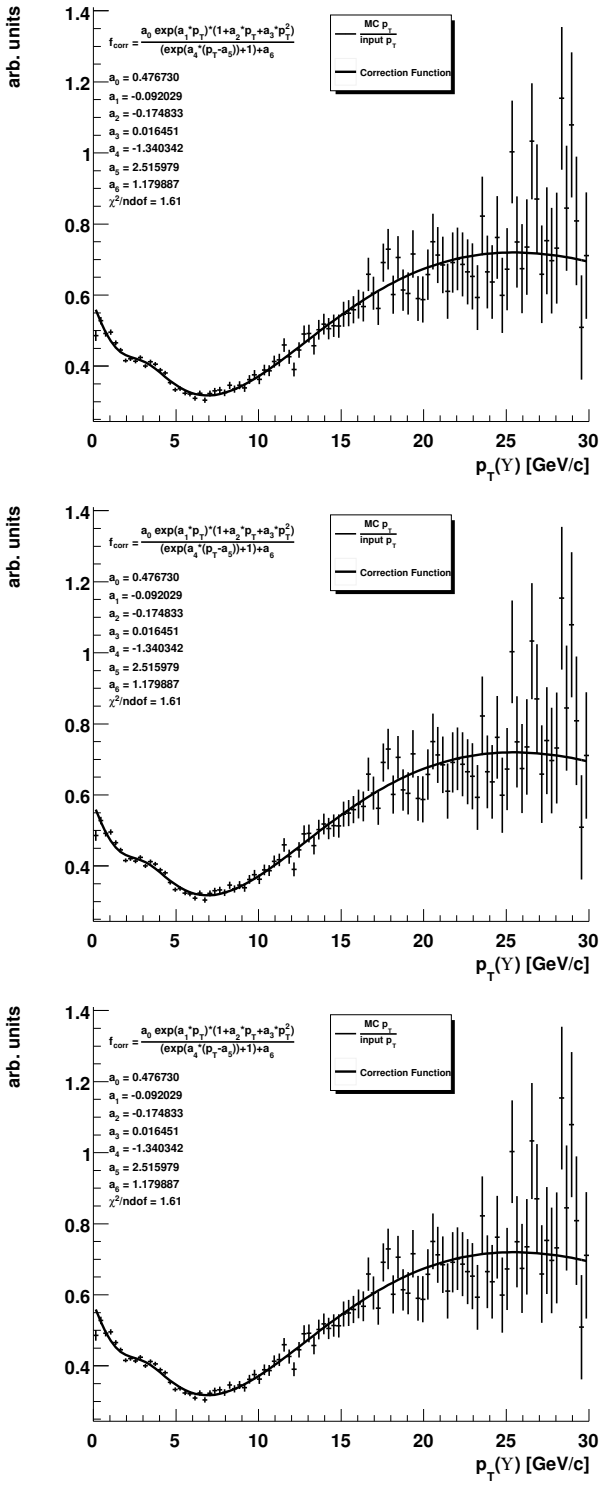

Figure B.1: The ratio between the input transverse momentum distribution and the output leads to the correction function which can be applied to correct the measured data distribution in order to obtain the according to data correct simulation input distribution. The middle and lower plots are the result for the CMU only and CMU/CMX combinations while the upper plot is the sum of both.

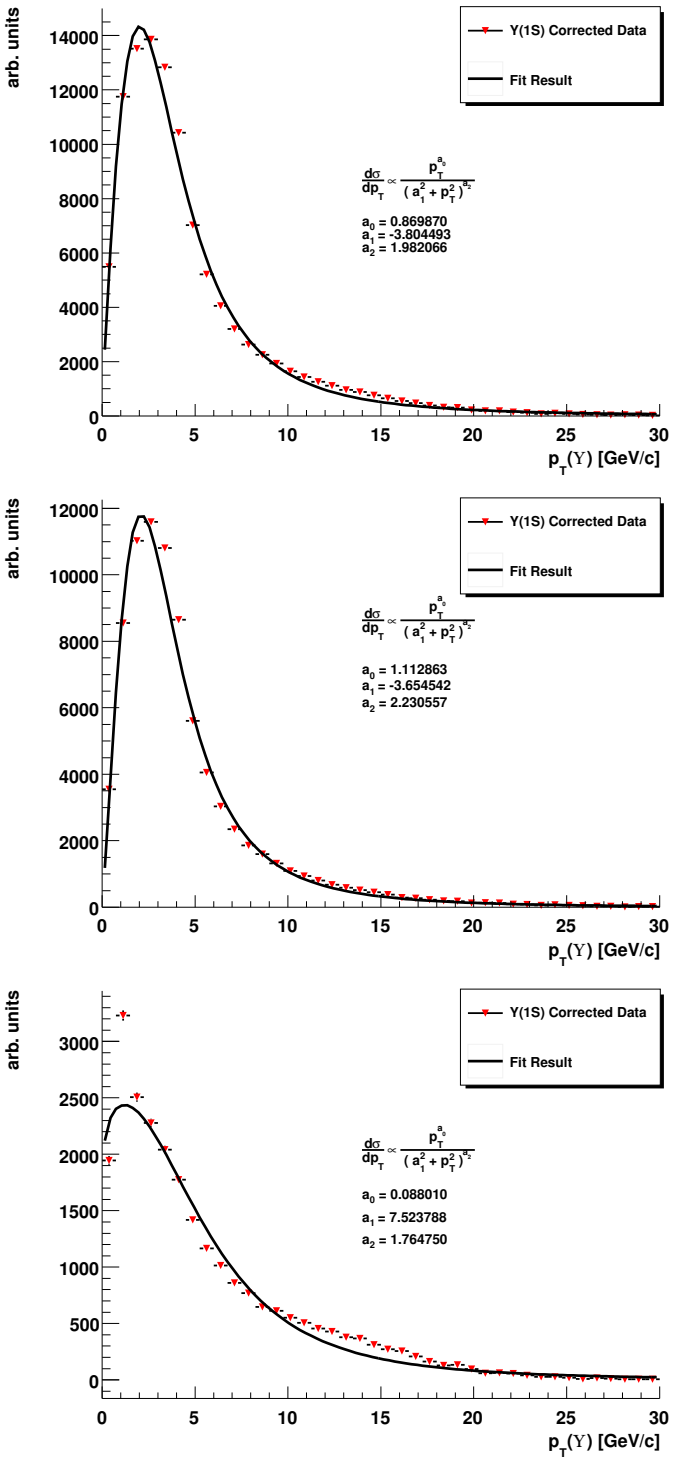

Figure B.2: The red dots correspond to the distribution obtained from measured data of the finally selected sample and corrected by the $p_{T,\Upsilon}$ correction function. The black line is the fit result with the parameterization described in the text. The middle and lower plots are the result for the CMU only and CMU/CMX combinations while the upper plot is the sum of both.

List of Figures

List of Tables

Bibliography

[1] Klaus Bethge, Ulrich E. Schröder. Elementarteilchen und ihre Wechselwirkungen: Eine Übersicht, 3., überarb. u. erw. Auflage. ISBN: 978-3-527-40587-9.

[2] Stephen Godfrey and Stephen L. Olsen. The Exotic XYZ Charmonium-like Mesons. 2008. arXiv:0801.3867 [hep-ph].

[3] http://www-cdf.fnal.gov/.

[4] Bogdan Povh, Klaus Rith, Christoph Scholz, Frank Zetsche. Teilchen und Kerne: Eine Einführung in die physikalischen Konzepte. Springer, 2009.

[5] D.B. Cassidy and Jr A.P. Mills. The Production of Molecular Positronium. Nature, 2007. http://dx.doi.org/10.1038/nature06094.

[6] Stefan Meinel. The Bottomonium Spectrum from Lattice QCD with 2+1 Flavors of Domain Wall Fermions. Physical Review D, 79:094501, 2009.

[7] J. J. Dudek, R. G. Edwards, N. Mathur, and D. G. Richards. Charmonium Excited State Spectrum in Lattice QCD. Physical Review D, 77:034501, 2008. doi:10.1103/PhysRevD.77.034501.

[8] S. Godfrey and Nathan Isgur. Mesons in a Relativized Quark Model with Chromodynamics. Phys. Rev., D32:189–231, 1985.

[9] C. Amsler et al. (Particle Data Group). Physics Letters B667, 1, 2008.

[10] R. Mizuk and for the Belle Collaboration. Dalitz analysis of $B \to K\pi\psi'$ decays and the $Z(4430)^+$. Physical Review D, 80:031104, 2009. arXiv:0905.2869 [hep-ph].

[11] Kai Yi for the CDF Collaboration. Properties of Exotic Charmonium-like States at CDF. 2009. arXiv.org:0906.4996 [hep-ph].

[12] S. K. Choi et al. Observation of a New Narrow Charmonium State in Exclusive $B^{\pm} \to K^{\pm}\pi^+\pi^- J/\psi$ Decays. Phys. Rev. Lett., 91:262001, 2003.

[13] Darin E. Acosta et al. Observation of the Narrow State $X(3872) \to J/\psi\pi^+\pi^-$ in $\bar{p}p$ Collisions at $\sqrt{s} = 1.96$ TeV. Phys. Rev. Lett., 93:072001, 2004.

[14] V. M. Abazov et al. Observation and Properties of the $X(3872)$ Decaying to $J/\psi\pi^+\pi^-$ in $p\bar{p}$ Collisions at $\sqrt{s} = 1.96$ TeV. Phys. Rev. Lett., 93:162002, 2004.

[15] B. Aubert et al. Study of the $B \to J/\psi K^-\pi^+\pi^-$ Decay and Measurement of the $B \to X(3872)K^-$ Branching fraction. Phys. Rev., D71:071103, 2005.

[16] A. Abulencia et al. Measurement of the Dipion Mass Spectrum in $X(3872) \to J/\psi\pi^+\pi^-$ decays. Phys. Rev. Lett., 96:102002, 2006. hep-ex/0512074.

[17] Joachim Heuser. Measurement of the Mass and the Quantum Numbers J^{PC} of the X(3872) State. 2008. http://www-ekp.physik.uni-karlsruhe.de/pub/web/thesis/iekp-ka2008-16.pdf.

[18] The CDF Collaboration: T. Aaltonen. Precision Measurement of the X(3872) Mass in $J/\psi\pi^+\pi^-$ Decays. 2009. arXiv.org:0906.5218.

[19] Nils A. Tornqvist. Isospin Breaking of the Narrow Charmonium State of Belle at 3872 MeV as a Deuson. Phys. Lett., B590:209–215, 2004.

[20] Eric S. Swanson. Short Range Structure in the $X(3872)$. Phys. Lett., B588:189–195, 2004.

[21] Robert L. Jaffe. Multi-Quark Hadrons. 2. Methods. Phys. Rev., D15:281, 1977.

[22] L. Maiani, F. Piccinini, A. D. Polosa, and V. Riquer. Diquark-Antidiquarks with Hidden or Open Charm and the Nature of $X(3872)$. Phys. Rev., D71:014028, 2005.

[23] H. Hogaasen, J. M. Richard, and P. Sorba. A Chromomagnetic Mechanism for the $X(3872)$ Resonance. Phys. Rev., D73:054013, 2006.

[24] D. Ebert, R. N. Faustov, and V. O. Galkin. Masses of Heavy Tetraquarks in the Relativistic Quark Model. Phys. Lett., B634:214–219, 2006.

[25] N. Barnea, J. Vijande, and A. Valcarce. Four-quark Spectroscopy Within the Hyperspherical Formalism. Phys. Rev., D73:054004, 2006.

[26] Ying Cui, Xiao-Lin Chen, Wei-Zhen Deng, and Shi-Lin Zhu. The Possible Heavy Tetraquarks $qQ\bar{q}\bar{q}$, $qq\bar{Q}\bar{Q}$ and $qQ\bar{Q}\bar{Q}$. High Energy Phys. Nucl. Phys., 31:7–13, 2007.

[27] R. D. Matheus, S. Narison, M. Nielsen, and J. M. Richard. Can the $X(3872)$ be a 1^{++} Four-quark State? Phys. Rev., D75:014005, 2007.

[28] Ting-Wai Chiu and Tung-Han Hsieh. Pseudovector Meson with Strangeness and Closed-charm. Phys. Rev., D73:111503, 2006.

[29] L. Maiani, A. D. Polosa, and V. Riquer. Indications of a Four-Quark Structure for the $X(3872)$ and $X(3876)$ Particles from Recent Belle and *BABAR* Data. Phys. Rev. Lett., 99:182003, 2007.

[30] Belle Collaboration. Study of X(3872) in B meson decays. 2008. arXiv.org:0809.1224.

[31] D. Horn and J. Mandula. A Model of Mesons with Constituent Gluons. Phys. Rev., D17:898, 1978.

[32] F. E. Close and Stephen Godfrey. Charmonium Hybrid Production in Exclusive B Meson Decays. Phys. Lett., B574:210–216, 2003.

[33] Nathan Isgur and Jack E. Paton. A Flux Tube Model for Hadrons in QCD. Phys. Rev., D31:2910, 1985.

[34] Ted Barnes, F. E. Close, and E. S. Swanson. Hybrid and Conventional Mesons in the Flux Tube Model: Numerical Studies and Their Phenomenological Implications. Phys. Rev., D52:5242–5256, 1995.

[35] John Merlin and Jack E. Paton. Spin Interactions in the Flux Tube Model and Hybrid Meson Masses. Phys. Rev., D35:1668, 1987.

[36] X. Liao and T. Manke. Excited Charmonium Spectrum from Anisotropic Lattices. 2002. hep-lat/0210030.

[37] Bing An Li. Is $X(3872)$ a Possible Candidate of Hybrid Meson. Phys. Lett., B605:306–310, 2005.

[38] D. V. Bugg. Reinterpreting Several Narrow 'Resonances' as Threshold Cusps. Phys. Lett., B598:8–14, 2004.

[39] D. V. Bugg. The $X(3872)$ and the 3941 MeV Peak in $\omega J/\psi$. Phys. Rev., D71:016006, 2005.

[40] D. V. Bugg. How Resonances Can Synchronise with Thresholds. 2008. arXiv:0802.0934 [hep-ph].

[41] Yu. S. Kalashnikova. Coupled-channel Model for Charmonium Levels and an Option for (3872). Phys. Rev., D72:034010, 2005.

[42] C Hanhart, Yu. S Kalashnikova, Alexander E. Kudryavtsev, and A. V Nefediev. Reconciling the $X(3872)$ with the Near-threshold Enhancement in the $D^0\bar{D}^{*0}$ Final State. Phys. Rev., D76:034007, 2007.

[43] Kamal K. Seth. An Alternative Interpretation of $X(3872)$. Phys. Lett., B612:1–4, 2005.

[44] Colin J. Morningstar and Mike J. Peardon. The Glueball Spectrum from an Anisotropic Lattice Study. Phys. Rev., D60:034509, 1999.

[45] Hanna Mahlke. Heavy Quarkonia Spectroscopy and Decays. 2003. arXiv.org:0309015 [hep-ex].

[46] CDF Collaboration. Analysis of the Quantum Numbers J^{PC} of the X(3872) Particle. Physical Review Letters, 98:132002, 2007.

[47] Zhi-Gang Wang. Reanalysis of the Mass Spectrum of the Scalar Hidden Charm and Hidden Bottom Tetraquark States. 2009. arXiv.org:0908.1266.

[48] George W. S. Hou. Search for Bottom Counterparts of X(3872) and Y(4260) via $\pi^+\pi^-\Upsilon$. 2006. arXiv.org:hep-ph/0611153.

[49] Gui-Jun Ding, Jia-Feng Liu, and Mu-Lin Yan. Dynamics of Hadronic Molecule in One-Boson Exchange Approach and Possible Heavy Flavor Molecules. Physical Review D, 79:054005, 2009.

[50] D. Ebert, R. N. Faustov, and V. O. Galkin. Relativistic Model of Hidden Bottom Tetraquarks. MOD.PHYS.LETT.A, 24:567, 2009.

[51] Pietro Faccioli, Carlos Lourenco, Joao Seixas, and Hermine Woehri. J/ψ Polarization from Fixed-target to Collider Energies. 2009. arXiv.org:0902.4462.

[52] D0 Collaboration: V. M. Abazov. Measurement of the polarization of the $\upsilon(1s)$ and $\upsilon(2s)$ states in $p\bar{p}$ collisions at $\sqrt{s}$ =1.96 tev. Physical Review Letters,.

[53] Jungil Lee. Polarization of Prompt J/ψ and $\Upsilon(nS)$. ACTA PHYS.POLON.B, 33:3237, 2002. arXiv.org:0208238 [hep-ph].

[54] S. P. Baranov and N. P. Zotov. Production and Polarization of Upsilon mesons in the k_T-factorization Approach in more Detail. 2008. arXiv.org:0810.4928.

[55] D. Acosta et al. Υ Production and Polarization in $p\bar{p}$ Collisions at $s = 1.8TeV$. Phys. Rev. Lett., 88(16):161802, Apr 2002.

[56] D. Acosta et al. The Performance of the CDF Luminosity Monitor. Nucl. Instrum. Meth., A494:57–62, 2002.

[57] R. Blair et al. The CDF II detector: Technical Design Report. FERMILAB-PUB-96-390-E.

[58] Darin E. Acosta et al. Measurement of the J/ψ Meson and $b-$hadron Production Cross Sections in $p\bar{p}$ Collisions at $\sqrt{s} = 1960$ GeV. Phys. Rev., D71:032001, 2005.

[59] Darin E. Acosta et al. Measurement of the $t\bar{t}$ Production Cross Section in $p\bar{p}$ Collisions at $\sqrt{s} = 1.96$ TeV Using Lepton + Jets Events with Secondary Vertex $b-$tagging. Phys. Rev., D71:052003, 2005.

[60] A. Abulencia et al. Measurements of Inclusive W and Z Cross Sections in p-pbar Collisions at $\sqrt{s} = 1.96$ TeV. J. Phys., G34:2457–2544, 2007.

[61] Christopher S. Hill. Operational Experience and Performance of the CDF II Silicon Detector. Nucl. Instrum. Meth., A530:1–6, 2004.

[62] A. Sill. CDF Run II Silicon Tracking Projects. Nucl. Instrum. Meth., A447:1–8, 2000.

[63] Anthony A. Affolder et al. Intermediate Silicon Layers Detector for the CDF Experiment. Nucl. Instrum. Meth., A453:84–88, 2000.

[64] Anthony Allen Affolder et al. CDF Central Outer Tracker. Nucl. Instrum. Meth., A526:249–299, 2004.

[65] D. Acosta et al. A Time-of-flight Detector in CDF II. Nucl. Instrum. Meth., A518:605–608, 2004.

[66] CDF. The Time of Flight Detector at CDF. http://ppd.fnal.gov/experiments/e907/TOF/ cdf5501_The_TOF_Detector.pdf.

[67] L. Balka et al. The CDF Central Electromagnetic Calorimeter. Nucl. Instrum. Meth., A267:272, 1988.

[68] S. Bertolucci et al. The CDF Central and Endwall Hadron Calorimeter. Nucl. Instrum. Meth., A267:301, 1988.

[69] M. G. Albrow et al. The CDF Plug Upgrade Electromagnetic Calorimeter: Test Beam Results. Nucl. Instrum. Meth., A480:524–546, 2002.

[70] A. Bhatti et al. Determination of the Jet Energy Scale at the Collider Detector at Fermilab. Nucl. Instrum. Meth., A566:375–412, 2006.

[71] G. Ascoli et al. CDF Central Muon Detector. Nucl. Instrum. Meth., A268:33, 1988.

[72] Evelyn J. Thomson et al. Online Track Processor for the CDF Upgrade. IEEE Trans. Nucl. Sci., 49:1063–1070, 2002.

[73] M. Feindt and U. Kerzel. The NeuroBayes Neural Network Package. Nucl. Instrum. Meth., A559:190–194, 2006.

[74] Muriel Pivk and Francois R. Le Diberder. sPlot: a Statistical Tool to Unfold Data Distributions. NUCL.INSTRUM.METH.A, 555:356, 2005.

[75] Muriel Pivk. sPlot: A Quick Introduction. 2006. arXiv.org:physics/0602023.

[76] D. J. Lange. The EvtGen Particle Decay Simulation Package. Nucl. Instrum. Meth., A462:152–155, 2001.

[77] `http://www-cdf.fnal.gov/cdfsim/cdfsim_main.html`.

[78] E. Gerchtein and M. Paulini. CDF Detector Simulation Framework and Performance. 2003. physics/0306031.

[79] The CDF Collaboration. Muon B Flavour Tagging, A Likelihood Approach. www-cdf.fnal.gov/physics/new/bottom/.../blessed-like-mu-tag.ps.

[80] D. Acosta et al. CDF Collaboration. Measurement of the J/ψ Meson and b-Hadron Production Cross Sections in $p\bar{p}$ Collisions at $\sqrt{s} = 1960\,\text{GeV}$. Physical Review D, 71:032001, 2005.

[81] F. Abe et al. CDF Collaboration. J/ψ and $\psi(2S)$ Production in $p\bar{p}$ Collisions at $\sqrt{s} = 1.8\,\text{TeV}$. Physical Review D, 79:572, 1997.

[82] J. Marriner. Secondary Vertex Fit with Mass and Pointing Constraints `CTVMFT`. Public CDF Note 1996 (unpublished), 1993.

[83] Jeffrey D. Richman. An Experimenter's Guide to the Helicity Formalism. CALT-68-1148.

[84] W. M. Yao et al. Review of Particle physics. J. Phys., G33:1–1232, 2006.

[85] J. M. Blatt and V. F. Weisskopf. Theoretical Nuclear Physics. New York, John Wiley, 1952.

[86] Michael Feindt. An Amplitude Construction Primer for Experimentalists. (unpublished).

[87] M. Nikolic. Analysis of Scattering and Decay. New York, USA: Gordan and Breach (1968) 332p.

[88] CLEO Collaboration: D. Cronin-Hennessy. Study of Di-Pion Transitions Among Upsilon(3S), Upsilon(2S), and Upsilon(1S) States. Physical Review D, 76:072001, 2007.

[89] Mikhail B. Voloshin and Valentin I. Zakharov. Measuring QCD Anomalies in Hadronic Transitions Between Onium States. Phys. Rev. Lett., 45:688, 1980.

[90] J. Z. Bai et al. $\psi(2S) \to \pi^+\pi^- J/\psi$ Decay Distributions. Phys. Rev., D62:032002, 2000.

[91] H. Albrecht et al. A Partial Wave Analysis of the Decay $D^0 \to K^0(s)\pi^+\pi^-$. Phys. Lett., B308:435–443, 1993.

[92] Giovanni Punzi. Sensitivity of Searches for New Signals and its Optimization. 2003. arXiv.org:physics/0308063.

[93] F. James. MINUIT, Function Minimization and Error Analysis. CERN Program Library Long Writeup D, 506, 1998.

[94] F. Rademakers R. Brun. ROOT - An Object Oriented Data Analysis Framework. AIHENP'96 Workshop, Lausane, Nucl. Inst. & Meth. in Phys. Res. A, 389:81–86, 1997.

[95] CDF Collaboration. Measurement of $\Upsilon(1S)$ Polarization. 2009. http://www-cdf.fnal.gov/physics/new/bottom/090903.blessed-Upsilon1S-polarization/blessed_plots.html.

[96] N. Brambilla et al. Heavy quarkonium physics. 2004. hep-ph/0412158.

Acknowledgments

I would like to thank my supervisor Prof. Dr. Michael Feindt for the guidance through the course of this PHD work. His deep knowledge about physics were essential for all of the work during this study.

Also I would like to thank Prof. Dr. Günter Quast for co-supervising this thesis. As well I would like to thank Prof. Dr. Thomas Müller for his work in his function as head of the institute.

Without the advice and work of Dr. Michal Kreps and Dr. Thomas Kuhr this thesis would not have been possible. Therefore many thanks to them especially for carefully reading and commenting on this manuscript.

It was a great experience to work in an atmosphere like that of the B group. Thus, many thanks to each member of that group and also to the entire EKP group.

I would like to thank all members of the EKP admin team to keep everything running. As well I would like to thank our secretaries.

I would like to especially thank Gernot and Stephie Riedel for supporting me.

Special thanks are dedicated to my mother. Without her support all of this work would not have been possible.